

**SYNTHETIC, STRUCTURAL, SPECTROSCOPIC AND
COMPUTATIONAL STUDIES OF METAL-DITHIOLATES AS
MODELS FOR PYRANOPTERINDITHIOLATE MOLYBDENUM AND
TUNGSTEN ENZYMES: DITHIOLATE FOLDING EFFECT**

by

Hemant Kumar Joshi

A Dissertation Submitted to the Faculty of the

DEPARTMENT OF CHEMISTRY

In Partial Fulfillment of the Requirements
For the Degree of

DOCTOR OF PHILOSOPHY

In the Graduate College

THE UNIVERSITY OF ARIZONA

2003

UMI Number: 3119957

INFORMATION TO USERS

The quality of this reproduction is dependent upon the quality of the copy submitted. Broken or indistinct print, colored or poor quality illustrations and photographs, print bleed-through, substandard margins, and improper alignment can adversely affect reproduction.

In the unlikely event that the author did not send a complete manuscript and there are missing pages, these will be noted. Also, if unauthorized copyright material had to be removed, a note will indicate the deletion.

UMI[®]

UMI Microform 3119957

Copyright 2004 by ProQuest Information and Learning Company.

All rights reserved. This microform edition is protected against unauthorized copying under Title 17, United States Code.

ProQuest Information and Learning Company
300 North Zeeb Road
P.O. Box 1346
Ann Arbor, MI 48106-1346

THE UNIVERSITY OF ARIZONA ®
GRADUATE COLLEGE

As members of the Final Examination Committee, we certify that we have read the
dissertation prepared by Hemant K. Joshi

entitled Synthetic, Structural, Spectroscopic and Computational Studies of

Metal-Dithiolates as Models for Pyranopterindithiolate Molybdenum and

Tungsten Enzymes: Dithiolate Folding Effect

and recommend that it be accepted as fulfilling the dissertation requirements for the

Degree of Doctor of Philosophy

<u>John H. Enemark</u> Professor John H. Enemark	<u>10/29/2003</u> Date
<u>Dennis L. Lichtenberger</u> Professor Dennis L. Lichtenberger	<u>10/29/2003</u> Date
<u>Richard S. Glass</u> Professor Richard S. Glass	<u>10/29/03</u> Date
<u>Robin Polt</u> Professor Robin Polt	<u>29 Oct 2003</u> Date
<u>Katrina M. Miranda</u> Professor Katrina M. Miranda	<u>10/29/03</u> Date

Final approval and acceptance of this dissertation is contingent upon the candidate's
submission of the final copy of the dissertation to the Graduate College.

I hereby certify that I have read this dissertation prepared under my direction and
recommend that it be accepted as fulfilling the dissertation requirement.

<u>John H. Enemark</u> Dissertation Director, Professor John H. Enemark	<u>11/10/2003</u> Date
--	---------------------------

STATEMENT BY AUTHOR

This dissertation has been submitted in partial fulfillment of requirements for an advanced degree at The University of Arizona and is deposited in the University Library to be available to borrowers under rules of the Library.

Brief quotations from this dissertation are allowable without special permission, provided that accurate acknowledgement of the source is made. Request for permission for extended quotation from or reproduction of this manuscript in whole or in part may be granted by the head of the major department or the Dean of the Graduate College when in his or her judgment the proposed use of the material is in the interests of scholarship. In all other instances, however, permission must be obtained from the author.

SIGNED: 

ACKNOWLEDGMENTS

This research would not have been possible without the aid of a number of people. I want to acknowledge the following people for their support, patience and understanding during my graduate research work and my stay in Tucson.

First of all I want to thank my mentor Prof. John H. Enemark, for nurturing the chemist in me over the last few years. He has not only taught me many of the core and elective courses but has also been my dissertation supervisor. He has tried his best to expose me to new ideas, perspectives and standards, and to the values and norms of the chemical profession. His enthusiasm for science is my perennial source of inspiration.

I want to thank my dissertation committee members for interesting discussions; Drs. D. L. Lichtenberger, R. S. Glass, R. Polt, F. A. Walker and K. M. Miranda, some of whom have also taught me several core or elective courses.

Dr. Frank E. Inscore kept feeding me the idea that molybdenum chemistry is hot; he not only trained me in modern inorganic synthesis, but also influenced my thinking as a scientist. Drs. Michael D. Carducci and Nadine E. Gruhn taught me a variety of instrumental aspects, troubleshooting and maintenance of X-ray Crystallography and Photoelectron Spectroscopy instruments, respectively. Dr. J. J. A. Cooney has read and edited my manuscripts and helped me improve my scientific writing. He has been successful in reaffirming my belief that computers are cool. Dr. C. Feng has been answering my biological chemistry related queries. Thanks to all, for being so patient and for your valuable time.

I have used some data from the following, either for comparative purposes or it has been refitted and refined in the light of the latest findings. I want to thank previous and current graduate/ undergraduate students: Dr. B. L. Westcott, Dr. I. K. Dhawan, T. G. Bill, M. E. Arvin, J. T. Schirlin and P. Bernardson, post doctoral fellows; Dr. F. E. Inscore and Dr. J. J. A. Cooney. Many of them have been coauthors in my scientific papers and have been a great team. I have made appropriate references as required in the text.

I thank my granny, parents, siblings and their spouses for their constant emotional support and love. Chand, my better half, I have cherished our sweet courtship for years, and I have been waiting for this moment to come. They might have matched us in heaven but I found you here.

I thank Dona Myers, Dr. M. Lynn and Dr. J. English for all their help. Thanks, my friends; Laura, Tonja, Liliya, Brian, Jake, host families Gail and Bob's, Chandolas and Kulbes, and the Desi gang Bhaskar, Tapan, Abhishek, Srivats, Vinod, Rakesh, Amar, Sonal and Bithika and others for all the fun filled times we have spent together.

You will all be in my memories.

To

Mom and Papa

Their blessings have always paved my way...

TABLE OF CONTENTS

LIST OF TABLES	11
LIST OF FIGURES	13
ABSTRACT	19
CHAPTER 1: Introduction	21
1.1 Bioavailability of molybdenum and tungsten.....	22
1.2 The Mo/W enzymes and pyranopterindithiolate cofactor.....	22
1.3 The sulfite oxidase (SO) and xanthine oxidase (XO) active sites.....	23
1.4 Proposed catalytic mechanism for SO and XO.....	25
1.5 Bioinorganic modeling of SO and XO	26
1.6 References.....	35
CHAPTER 2: Experimental Section	38
1.0 Synthesis of Compounds	39
1.1 Abbreviations.....	39
1.2 General.....	39
1.3 Synthesis of (Tp*)MoOX ₂ (X = F, Cl, Br) Complexes.....	40
1.4 Synthesis of (Tp*)MoO(S-S) Complexes	41
1.5 Synthesis of (Tp*)Mo(NO)(S-S) Complexes.....	41
1.6 Synthesis of Cp ₂ M(S-S) Complexes	42
2.0 Gas-Phase Photoelectron Spectroscopy.....	42
2.1 Data Collection.	42

2.2 Data Analysis	44
3.0 X-ray Crystallography.....	45
4.0 Theoretical Methods	46
5.0 References.....	51

CHAPTER 3: Electronic Structures of Hydrotris(pyrazol-1-yl)borates and Ene-1,2-dithiolenes Ligands 52

2.0 Experimental.....	58
2.1 General.....	58
2.3 Photoelectron spectroscopy.....	59
2.4 Theoretical Methods	60
3.0 Results and Discussions.....	61
3.1 Gas-Phase Photoelectron Spectroscopy Studies of Scorpionate Ligands	61
4.0 Conclusions	68
5.0 References.....	81

CHAPTER 4: Experimental and Theoretical Evaluation of Metal- Halide Interactions in (Tp*)MoOX₂ Compounds (X = F, Cl, Br, I) by Gas-Phase Photoelectron Spectroscopy and Density Functional Theory; Molecular Structure of (Tp*)MoOBr₂..... 85

1.0 Introduction	86
2.0 Experimental and Theoretical Section.....	91
2.1 Abbreviations	91
2.2 Synthesis	91
2.3 X-Ray Crystal Structure Determination.....	91
2.4 Photoelectron Spectroscopy	92
2.5 Computational details	93
3.0 Results.....	94
3.1 X-ray Crystal Structure of (Tp*)MoOBr ₂	94
3.2 Gas-Phase Photoelectron Spectroscopy: Valence Ionizations	95
3.4 Computational Results	96
4.0 Discussion.....	97
5.0 Conclusions	100
6.0 References.....	110

CHAPTER 5: Structural Studies of Active Site Models: Metal Dithiolates with and without a Terminal Oxo Ligand 116

1.0 Introduction	117
2.0 X-Ray Crystal Structure Determinations	118

3.0 X-ray Structure Analysis.....	119
3.1 Structure of (Tp*)MoO(bdtCl ₂)·1/2(C ₆ H ₁₄)	119
3.2 Structure of (Tp*)MoO(qdt)	122
3.3 Structure of (Tp*)WO(bdt)	128
3.4 Structure of Cp ₂ Mo(bdt)	130
4.0 Geometric and Electronic Structural Correlation:.....	131
5.0 References.....	152

CHAPTER 6: Electronic Structure Comparison to Ionization Potential of Oxo-Mo/W Ene-1, 2-dithiolate Compounds: Experimental and Theoretical Evaluation of the Second Coordination Effects..... 155

1.0 Introduction	156
2.0 Experimental Section	162
2.1 Abbreviations.....	162
2.2 Synthesis and characterization	163
2.3 Theoretical	164
3.0 Results.....	166
3.1 Gas-Phase Photoelectron Spectroscopy	166
3.1.1 (Tp*)MoO(S-S) Compounds: Remote Ligand Substitution Effect.....	166
3.1.2 (Tp*)MO(bdt) (M = Mo, W) Compounds: Metal Effect	167
3.1.3 Computational Study.....	167
4.0 Discussion.....	168
4.1 Gas-phase Photoelectron Spectroscopy	168
4.2 Computational Study	169
5.0 Conclusions	171
6.0 References.....	183

CHAPTER 7: Six-Coordinate Molybdenum Nitrosyls with a Single Ene-1,2-Dithiolate Ligand..... 188

1.0 Introduction	189
2.0 Experimental Section	192
2.1 General.....	192
2.2 Synthesis of (Tp*)Mo(NO)(bdt)	193
2.3 Synthesis of (Tp*)Mo(NO)(tdt)	195
2.4 Synthesis of (Tp*)Mo(NO)(bdtCl ₂)	196
2.5 X-Ray Crystal Structure Determinations:	196
2.6 Photoelectron Spectroscopy:.....	197
2.7 Theoretical	198
3.0 Results and Discussion:.....	199
3.1 Synthesis and Physical Properties of Tp*Mo(NO)(S-S) Compounds:.....	199
3.2 Molecular Structure Analysis of (Tp*)Mo(NO)(S-S) compounds:.....	201
3.3 Photoelectron Spectroscopy.....	207
3.4 Computational Study	209

4.0 Conclusions	209
5.0 References.....	226
CHAPTER 8: Spectroscopic and Computational Investigation of Metal–Dithiolate Fold Angle Effects and the Significance of Unsaturation in the Metallacycle: its Implication to Pyranopterindithiolate Enzymes	232
1.0 Introduction	233
2.0 Materials and Methods	238
2.1 Synthesis of Compounds.....	238
2.2 Photoelectron spectroscopy.....	239
2.3 Theoretical Methods	240
3.0 Results and Discussions.....	241
3.1 Photoelectron Spectra	241
3.2 Effect of Metal and Enedithiolate Coordination	243
3.3 Significance of Unsaturation (C=C) in the Metallacycle	244
3.4 Computational Results	245
4.0 Conclusions	247
5.0 References.....	259
CHAPTER 9: Geometrical Control of the Active Site Electronic Structure of Pyranopterin Enzymes by Metal-Sulfur Interactions: Aldehyde Oxidase (MOP) .	264
1.0 Introduction	265
2.0 References.....	274
CHAPTER 10: Conclusions and Future Directions	276
1.0 Model Chemistry.....	277
2.0 Implications for Enzymes.....	283
3.0 Future Directions.....	285
4.0 References.....	286
APPENDIX-A1: Structural parameters for (Tp*)MoO(halide)₂	288
APPENDIX-A2: [Mo(IV)(mnt)₂(SPh)₂][PPh₄]₄.....	289
1.0 Structural Studies.....	289
2.0 Theoretical Studies	295
2.1 Methods	295
3.0 Results.....	295

<i>4.0 References</i>	296
APPENDIX-A3: The Structure of (Tp*)MoO₂(SCH₂Ph)	298
APPENDIX A4. Photoelectron Spectra of (Tp*)VO(dtc)	303

LIST OF TABLES

Table 1.1. Some reactions catalyzed by molybdenum containing enzymes. Nitrogenase, although a molybdenum containing enzyme, is not a pyranopterindithiolate containing enzyme. A general reaction scheme for a pyranopterindithiolate containing enzyme is shown.	29
Table 2.1. Experimental details of the photoelectron spectroscopic studies.....	47
Table 2.2. Experimental details of the crystallographic studies.....	50
Table 3.1. Experimental ionization energies (I.E.), calculated absolute orbital eigenvalues (- ϵ_i) and calculated Δ SCF first ionization energies and experimental ionization energies (all values in eV).....	70
Table 4.1. Crystal data and structure refinement for (Tp*)MoOBr ₂	102
Table 4.2. Experimental ionization energies (I.E.), calculated absolute orbital eigenvalues (- ϵ_i) and calculated Δ SCF first ionization energies (all values in eV).....	103
Table 4.3. Ionization energies and areas of Gaussian fits.	104
Table 5.1. Crystal data and structure refinement parameters for (Tp*)MoO(bdtCl ₂).....	133
Table 5.2. Important bond lengths [\AA] and angles [$^\circ$] for (Tp*)MoO(bdtCl ₂).	134
Table 5.3. Crystal data and structure refinement parameters for (Tp*)MoO(qdt).....	135
Table 5.4. Important bond lengths [\AA] and angles [$^\circ$] for (Tp*)MoO(qdt).....	136
Table 5.5. Important mean bond lengths [\AA] and angles [$^\circ$] for (Tp*)MoO(qdt), (Tp*)MoO(bdt) and (Tp*)MoO(bdtCl ₂)	137
Table 5.6. Crystal data and structure refinement for (Tp*)WO(bdt).	138
Table 5.7. Important bond lengths [\AA] and angles [$^\circ$] for (Tp*)WO(bdt).	139
Table 5.8. Crystal data and structure refinement for Cp ₂ Mo(bdt)	140
Table 5.9. Important bond lengths [\AA] and angles [$^\circ$] for Cp ₂ Mo(bdt).....	141

Table 6.1. Experimental ionization energies (I.E.), calculated absolute orbital eigenvalues ($-\epsilon_i$) and calculated Δ SCF first ionization energies (all values in eV).	173
Table 7.1. Crystal data and structure refinement	213
Table 7.2. Selected bond lengths (\AA), bond angles ($^\circ$) and torsion angles ($^\circ$) (esd's in parentheses).....	215
Table 7.3. Ionization energies (± 0.02 eV) of frontier orbitals in HeI gas phase photoelectron spectra for (Tp*)Mo(E)(S-S) systems.	216
Table 7.4. Ionization energies (± 0.02 eV) of frontier orbitals in HeI gas phase photoelectron spectra for (Tp*)Mo(E)(S-S) systems.....	216
Table 8.1. Metal-dithiolate Fold Angles in Representative Mo Enzymes.	250
Table 8.2. Experimental and calculated Δ SCF and orbital ionization energies (eV) for the ionizations from sulfur antisymmetric (S_π^-), sulfur symmetric (S_π^+) and metal in-plane (M_{ip}) orbitals.	251
Table A1.1. Structural parameters for (Tp*)MoOX ₂ (X= F, Cl, Br) defining the coordination environment of Mo (lengths in (\AA) and angles in ($^\circ$)).....	288
Table A2.1. Crystal data and structure refinement for [Mo(IV)(mnt) ₂ (SPh) ₂][PPh ₄] ₄ . .	290
Table A2.2. Important bond lengths (\AA) and angles ($^\circ$) for [Mo(IV)(mnt) ₂ (SPh) ₂][PPh ₄] ₄	291
Table A2.3. Atomic coordinates ($\times 10^4$) and equivalent isotropic displacement parameters ($\text{\AA}^2 \times 10^3$). U(eq) is defined as one third of the trace of the orthogonalized U ^{ij} tensor.	292
Table A3.1. Crystal data and structure refinement for (Tp*)MoO ₂ (SCH ₂ Ph).	298
Table A3.2. Important bond lengths (\AA) and angles ($^\circ$) for (Tp*)MoO ₂ (SCH ₂ Ph).	299
Table A3.3. Atomic coordinates ($\times 10^4$) and equivalent isotropic displacement parameters ($\text{\AA}^2 \times 10^3$). U(eq) is defined as one third of the trace of the orthogonalized U _{ij} tensor.	300

LIST OF FIGURES

- Figure 1.1. Classification of the pyranopterindithiolate containing enzymes. Also shown is a schematic representation of the pyranopterindithiolate cofactor..... 30
- Figure 1.2. The proposed catalytic mechanism for sulfite oxidase. Mo(VI) on left hand side is the resting state of the enzyme. During catalysis the metal center undergoes electronic configurations changes that involve d^0 , d^2 and d^1 states. 31
- Figure 1.3. The proposed mechanism of aldehyde oxidase (MOP) involves a hydride atom transfer to the the terminal sulfido group that reduces Mo (VI) center to Mo(IV) and is considered to be an important step during catalysis..... 32
- Figure 1.4. Modeling of the active site of sulfite oxidase. Breakdown of the active site into more manageable features that can be incorporated into minimal molecular models. 33
- Figure 1.5. Active site models that contain one enedithiolate. 34
- Figure 3.1. (a) A generic tripodal scorpionate ligand hydrotris(pyrazol-1-yl)borate; KTp. (b) Examples of substitutions at the 3 and 4 positions of the pyrazole ring. These substitutions retain the C_3 symmetry of the adducts. (c) A generic aryldithiolate ligand..... 71
- Figure 3.2. The He I full photoelectron spectra of the potassium salts of hydrotris(3,5-dimethylpyrazol-1-yl)borate, Tp* and hydrotris(3,5-bis(trifluoromethyl)pyrazol-1-yl)borate, Tp^{(CF₃)₂}. Both of the spectra have three general features labeled as bands A, B and C in the lower energy region. These bands are assigned as A: pyrazole- π ; B, B': σ_N of the pyrazole nitrogen orbitals; C: σ_{BH} of the trispyrazole borate ligands. 72
- Figure 3.3. The He I close up photoelectron spectra of KTp*; and KTp^{(CF₃)₂}. Bands A, B and C are assigned as in Figure 3.2..... 73
- Figure 3.4. The He I and He II close up spectra of KTp*. Ionizations associated with molecular orbitals with hydrogen contributions decrease in relative intensity in the He II source. 74
- Figure 3.5. He I close-up photoelectron spectra of Na(Tp^{(CF₃)₂}) (top) and K(Tp^{(CF₃)₂}) (bottom). The bands are assigned as A: pyrazole- π ; B, B': σ_N (*e*-symmetric and *a* symmetric combinations, respectively) of the pyrazole nitrogen orbitals; C: σ_{BH} of the trispyrazole borate ligand. 75

- Figure 3.6. Molecular orbital plots (at 0.05 cutoff levels unless stated) of KTp. (a) Lowest occupied molecular orbital (LUMO) is primarily metal in character (at 0.03 cutoff levels). (b) The highest occupied molecular orbital (HOMO) is primarily pyrazole- π in character. (c) HOMO-1 is again pyrazole- π in character. (d) An example of the pyrazole σ -donor (σ_N) molecular orbital (at 0.008 cutoff levels). (e) The hydrotris(pyrazol-1-yl)borate σ_{BH} molecular orbital. 76
- Figure 3.7. Comparison of the highest occupied molecular orbitals (HOMO), σ_N (*a*-symmetric) and σ_{BH} orbitals (at 0.05 cutoff levels)..... 77
- Figure 3.8. The He I full photoelectron spectra of 1, 2-benzenedithiolate (H_2bdt) and 3, 6-dichloro-1,2-benzenedithiolate (H_2bdtCl_2). Both of the spectra have four first ionizations labeled as bands 1, 2, 2', 1' in the lower energy region. These bands are assigned as 1, 1': bonding and antibonding orbitals of $S\pi^+$; 2, 2': bonding and antibonding orbitals of $S\pi^-$ (where $S\pi^+$ and $S\pi^-$ = symmetric and antisymmetric combinations of dithiolate out of plane orbitals) 78
- Figure 3.9. The molecular orbital diagram of 1, 2-benzenedithiol. The $S\pi^+$ orbital is raised in energy due to an effective overlap from C=C π -orbital of benzene. 79
- Figure 3.10. The one-to-one correlation of first four ionization bands with theoretically calculated frontier molecular orbitals of 1, 2-benzenedithiol. Bands 1, 1', 2, 2' have been assigned as described in Figure 3.8. 80
- Figure 4.1. (a) Systematic representation of $(Tp^*)MoOX_2$ ($X = F, Cl, Br, I$). (b) Simplified molecular orbital scheme for orbitals in the *xy* plane showing metal and halide interaction..... 105
- Figure 4.2. ORTEP representation of $(Tp^*)MoOBr_2$ at 50% probability level. Hydrogen atoms are made arbitrarily small for comparison. A rotational disorder can be viewed along the pseudo three fold axis. 106
- Figure 4.3. The stack plot of the He I photoelectron spectra of $(Tp^*)K$, $(Tp^*)MoOF_2$, $(Tp^*)MoOCl_2$ and $(Tp^*)MoOBr_2$ 107
- Figure 4.4. The He I and He II photoelectron spectra of $(Tp^*)MoOF_2$, $(Tp^*)MoOCl_2$, $(Tp^*)MoOBr_2$ 108
- Figure 4.5. (a) Electronic potential and (b) highest occupied molecular orbital plots for $(Tp^*)MoOX_2$ ($X = F, Cl, Br, I$)..... 109
- Figure 5.1. The definition of the fold angle. 142

- Figure 5.2. The ORTEP drawing of $(Tp^*)MoO(bdtCl_2)$. The atoms are drawn as 50% probability ellipsoids. H-atoms have been made arbitrarily small for clarity 143
- Figure 5.3. Compound $(Tp^*)MoO(bdtCl_2)$ in $P2(1)/c$ space group, orientation along a axis in a unit cell..... 144
- Figure 5.4. The ORTEP drawing of $(Tp^*)MoO(qdt)$. The atoms are drawn as 50% probability ellipsoids. H-atoms have been made arbitrarily small for clarity 145
- Figure 5.5. Top view: the ORTEP drawing of $(Tp^*)MoO(qdt)$. The atoms are drawn as 50% probability ellipsoids. H-atoms have been made arbitrarily small for clarity 145
- Figure 5.6. Compound $(Tp^*)MoO(qdt)$ in $P\bar{1}$ space group, orientation along a axis in a unit cell..... 146
- Figure 5.7. The ORTEP drawing of $(Tp^*)WO(bdt)$. The atoms are drawn as 50% probability ellipsoids. H-atoms have been made arbitrarily small for clarity..... 147
- Figure 5.8. Compound $(Tp^*)WO(bdt)$ in $P2(1)/n$ space group, orientation along a axis in a unit cell..... 148
- Figure 5.9. The ORTEP drawing of $Cp_2Mo(bdt)$. The atoms are drawn as 50% probability ellipsoids. H-atoms have been made arbitrarily small for clarity..... 149
- Figure 5.10. The ORTEP drawing of $Cp_2Mo(bdt)$ after grow command in XP. A dimer of benzenedithiolate can be noticed on the left, cocrystallized with $Cp_2Mo(bdt)$. The atoms are drawn as 50% probability ellipsoids. H-atoms have been made arbitrarily small for clarity. 150
- Figure 5.11. Compound $Cp_2Mo(bdt)$ in $P2(1)/c$ space group, orientation along a axis in a unit cell..... 151
- Figure 6.1. Schematic drawing of $(Tp^*)MoO(S-S)$ (where Tp^* = hydrotris(3,5-dimethylpyrazol-1-yl)borate, bdt = 1,2-benzenedithiolate, $bdtCl_2$ = 3, 6-dichloro-1, 2-benzenedithiolate, qdt = 2,3-dithioquinoxaline, tdt = 3, 4 toluenedithiolate) complexes..... 174
- Figure 6.2. The He I and He II photoelectron spectroscopy of $(Tp^*)MoO(bdt)$. The ionization band 1 corresponds to a metal based ionization and bands 2, 2', 3, 3' correspond to dithiolate based ionizations. 175
- Figure 6.3. The He I and He II photoelectron spectroscopy of $(Tp^*)MoO(bdtCl_2)$. The ionization band 1 corresponds to a metal based ionization and bands 2, 2', 3, 3' correspond to dithiolate based ionizations. 176

- Figure 6.4. The He I and He II photoelectron spectroscopy of (Tp*)MoO(S-S) series of compounds. The ionization band 1 corresponding to a metal based ionization shows a trend consistent with the electron withdrawing property of the coordinated dithiolate. The ionization bands 2, 2', 3, 3' correspond to dithiolate based orbitals. 177
- Figure 6.5. Comparison of the He I photoelectron spectrum of (Tp*)MO(bdt) (where M = Mo and W). 178
- Figure 6.6. The He I and He II photoelectron spectra of (Tp*)WO(tdt)..... 179
- Figure 6.7. Frontier orbitals of (Tp)MoO(bdt). These orbitals have significant metal and dithiolate characters..... 180
- Figure 6.8. Frontier orbitals of (Tp)WO(bdt). These orbitals have significant metal and dithiolate characters..... 181
- Figure 6.9. Fold angle variation against individual orbital contribution to highest occupied molecular orbital (HOMO) and total bonding energy of the molecule. .. 182
- Figure 7.1. Representation of the {(Tp*)Mo(NO)}²⁺ system containing equatorial ene-1,2-dithiolate ligands (S-S) coordinated to the Mo center. Structures of the dithiolate dianions (S-S) are also shown. 217
- Figure 7.2. Orbital interaction diagram in (a) (Tp*)Mo(NO)(SPh)₂ and (b) (Tp*)Mo(NO)(S-S) complexes. 218
- Figure 7.3. The ORTEP drawing of (Tp*)Mo(NO)(bdt), (Tp*)Mo(NO)(tdt), and (Tp*)Mo(NO)(bdtCl₂). The atoms are drawn as 50% probability ellipsoids. H-atoms have been made arbitrarily small for clarity. 219
- Figure 7.4. Compound (Tp*)Mo(NO)(bdtCl₂) in Pnma space group, orientation along c axis in a unit cell..... 220
- Figure 7.5. The distribution of fold angles (θ) of ene-1,2-dithiolates in group VI transition metal-ene-1,2-dithiolate complexes. 221
- Figure 7.6. The orbital splitting diagram for the molybdenum t_{2g} orbitals of the {Mo(NO)}³⁺ and {MoO}³⁺ cores.^{63, 64} 222
- Figure 7.7. Photoelectron spectra of (Tp*)MoO(tdt), (Tp*)MoO(bdt), (Tp*)MoO(bdtCl₂). A broad metal based ionization can be deconvoluted with two Gaussians..... 223

- Figure 7.8. Photoelectron spectra of (Tp*)MoE(tdt), (Tp*)MoE(bdt), (Tp*)MoE(bdtCl₂) (where E = O, NO) pairs. 224
- Figure 7.9. The frontier molecular orbitals of (Tp)Mo(NO)(bdt). Major contributions from individual atomic orbitals are also provided. 225
- Figure 8.1. The active site of chicken liver sulfite oxidase illustrating a pyranopterin dithiolate appended to the Mo center. 252
- Figure 8.2. The bonding interaction of the symmetric combination (S_{π}^{+}) of sulfur out-of-plane orbitals with the metal in-plane *d* orbital upon folding of the dithiolate along the S...S vector indicated by the line. 253
- Figure 8.3. Gas-phase photoelectron spectra of (Tp*)MoO(bdt), Cp₂Mo(bdt), and Cp₂Ti(bdt) with HeI and HeII excitation..... 254
- Figure 8.4. A comparison of the He I gas-phase photoelectron spectra of Cp₂Mo(bdt) and Cp₂Mo(bdtCl₂). 255
- Figure 8.5. A comparison of the He I gas-phase photoelectron spectra of Cp₂Mo(bdt) and Cp₂W(bdt), Cp₂WH₂ and Cp₂W(bdt), and HeI and HeII spectra of Cp₂W(bdt)..... 256
- Figure 8.6. Gas-phase photoelectron spectra of Cp₂Ti(pdt) with HeI and HeII excitation. 257
- Figure 8.7. Calculated three frontier orbitals (HOMO, HOMO-1, and HOMO-2) of (Tp*)MoO(bdt), Cp₂Mo(bdt), Cp₂Ti(bdt) and Cp₂W(bdt). All contours have the same cutoff level (0.05)..... 258
- Figure 9.1. The definition of the fold angle along the S·S vector, shown for the proposed active site of aldehyde.....270
- Figure 9.2. Bioinspired computational models of the active site of MOP.....271
- Figure 9.3. The lowest unoccupied molecular orbital (LUMO) of the oxidized active site of complex 1 (fold angle: 42.6°) that accepts two electrons in the reduction half cycle. 272
- Figure 9.4. The frontier orbitals (highest occupied molecular orbital; HOMO and HOMO-1) of the reduced active site complex 3 (fold angle: 10.4°)..... 273
- Figure A2.1. (a) The molecular orientation of [Mo(IV)(mnt)₂(SPh)₂][PPh₄]₄, (b, c and d) The frontier molecular orbitals of [Mo(IV)(mnt)₂(SPh)₂][PPh₄]₄..... 297

Figure A3.1. The ORTEP drawing of $(\text{Tp}^*)\text{MoO}_2(\text{SCH}_2\text{Ph})$. The atoms are drawn as 50% probability ellipsoids. H-atoms have been made arbitrarily small for clarity.....302

Figure A.4.1. The He I and He II photoelectron spectra of $(\text{Tp}^*)\text{VO}(\text{dtc})$ (where $\text{dtc} = \text{S}_2\text{CN}(\text{CH}_3)_2^-$).....303

ABSTRACT

Coordination by an axial oxo and an equatorial ene-dithiolate group is a salient feature of the active sites of the mononuclear pyranopterin Mo/W enzymes. Discrete mononuclear model complexes encompassing these features are important in understanding the metal-ligand interactions in these active sites. The compounds $(\text{Tp}^*)\text{ME}(\text{S-S})$ ($\text{M} = \text{Mo}, \text{W}$; $\text{E} = \text{O}, \text{NO}$) and $\text{Cp}_2\text{M}(\text{S-S})$ ($\text{M} = \text{Ti}, \text{Mo}, \text{W}$) (where Tp^* is hydrotris(3,5-dimethyl-1-pyrazolyl)borate, Cp is η^5 -cyclopentadienyl, S-S represents a generic ene-1,2-dithiolate ligand for example 1,2-benzenedithiolate and 3,6-dichloro-1,2-benzenedithiolate) provide access to three different electronic configurations of the metal, formally d^1 , d^2 and d^0 , respectively. These compounds also allow the study of two metal, two axial ligand and two equatorial ene-dithiolate perturbations. X-ray crystallography, density functional theory and photoelectron spectroscopy are utilized to understand the metal-sulfur interaction in the above complexes. Subtle differences in the geometry of these compounds are observed, including the metal-dithiolate fold angle which is sensitive to the electronic occupation of the metal in-plane orbital. This orbital is presumably the “host” orbital to the electrons during catalysis. The work in this area has resulted in the development of a dithiolate-folding-effect. This effect relates to the experimental verification of the Lauher and Hoffmann bonding model for the metal-dithiolate interaction in these complexes. This “dithiolate-folding-effect” is proposed to account for the electronic buffering at the metal center. This effect may provide a regulatory mechanism for the metal-sulfur interactions and could be a factor in the

electron transfer reactions that regenerate the active sites of molybdenum and tungsten enzymes. The structure and properties of these compounds are correlated with those of the enzyme active sites.

CHAPTER 1: Introduction

Enzymes are biological catalysts that enhance the rate of a variety of physiologically important reactions. Metalloproteins that perform a catalytic function are called metalloenzymes. The prefix “metallo” explains that these enzymes contain transition metals at their active centers.¹ Metal ions are required in many critical biological processes. Metals ions are also some of the essential nutrients and are becoming increasingly prevalent in diagnostic and therapeutic agents.² Some of the metal ions, formerly thought of as poisons, *e.g.* selenium and molybdenum, are now in the list of essentials elements for life.² Metalloenzymes containing molybdenum are present in all forms of life: archaea, bacteria, fungi, plants, and animals, including humans.^{3,4}

1.1 Bioavailability of molybdenum and tungsten

Molybdenum is the most abundant transition metal in the oceans although its abundance in the Earth’s crust is low. In the oceans, molybdenum and tungsten exists as their water soluble oxides and sulfides, respectively. The average concentration of dianionic molybdate ion, MoO_4^{2-} , in sea water is 10 $\mu\text{g/L}$ compared with about 0.5 $\mu\text{g/L}$ for Zn and 0.1 $\mu\text{g/L}$ for Cu and W.⁴

1.2 The Mo/W enzymes and pyranopterindithiolate cofactor

There are more than fifty pyranopterin enzymes that contain molybdenum or tungsten at their active sites. These enzymes catalyze a variety of oxidation/ reduction reactions in carbon, sulfur and nitrogen metabolism.⁵ Some of these enzymes catalyze an oxygen atom transfer reaction (Table 1.1) and are referred to as “oxotransferases”.⁴

However, this term is not universally accepted. The water molecule is the ultimate source or sink of oxygen atoms and these reactions accompany the transfer of two electrons. These reactions are also coupled to the electron transfer between oxidized/reduced substrates, an Fe-S center, heme, or flavin. These enzymes are further categorized into three classes, sulfite oxidase (SO), xanthine oxidase (XO) and dimethyl sulfoxide (DMSO) reductase.⁶ The name “pyranopterin” or “pyranopterindithiolate” comes from the cofactor common to all of these enzymes. This cofactor was previously referred to as molybdopterin.⁷ The active sites of these enzymes may contain one or two of these cofactors as shown in Figure 1.1. The pyranopterindithiolate (PDT) cofactor contains a pyran ring fused with pterin rings and an ene-1, 2-dithiolate (hereafter referred to as enedithiolate) motif that appends it to the metal centers in the active sites of the above enzymes.⁸

1.3 The sulfite oxidase (SO) and xanthine oxidase (XO) active sites

The sulfite oxidase (SO) and xanthine oxidase (XO) family of enzymes contain only one pyranopterindithiolate (PDT) cofactor.⁶ The SO family of enzymes can be isolated from animal livers, plants and bacteria. Chicken liver SO is a homodimeric protein of 110 kD molecular weight, and has two domains that harbor Mo and heme, respectively.⁹ The chicken liver,⁹ plant¹⁰ and human SO (heme domain only) have been structurally studied using X-ray crystallography. The active site of the chicken liver SO features molybdenum pentacoordinated with two oxygen and three sulfur donor ligands. The metal ion was found in an unusual square pyramidal coordination geometry not

encountered before for molybdenum compounds. One of the two oxygen ligands is an axial-oxo bound at 1.7 Å distance to the metal center and is referred to as a “spectator oxygen” atom. The other oxygen atom on the equatorial plane is at 2.3 Å distance, and is anticipated to be either a water molecule or a hydroxo ligand. Two of the three equatorial sulfur atoms come from the PDT cofactor (at 2.4 Å) and the third ligand is a cysteinyl (Cys 185 at 2.5 Å) residue.⁹

Aldehyde oxidase (MOP) is in the XO family of enzymes and the active site of MOP again features a pentacoordinated molybdenum center ligated by one PDT, two oxygen donor atoms and one sulfur donor atom.¹¹⁻¹³ This sulfur donor atom (sulfido) is most frequently exchanged by oxo during protein purification resulting in a desulfo form of the enzyme which is not catalytically competent. A recent report of the atomic resolution crystal structure of the MOP in desulfo form provides details of the active site.¹¹ The molybdenum atom is covalently coordinated to dithiolate sulfur atoms at 2.41 Å and 2.50 Å, an oxo atom at 1.79 Å, a water or a hydroxo at 2.02 Å in the equatorial plane and an apical oxo ligand at 1.77 Å. Unlike SO, the PDT cofactor in MOP is appended to a cytosinedinucleotide. The X-ray structures of a number of other pyranopterin enzymes are now known, and these structural results raise fundamental questions about the role of the PDT coordination in the overall catalytic cycle of molybdenum enzymes.^{8,12-16}

1.4 Proposed catalytic mechanism for SO and XO

SO catalyzes the oxidation of sulfite to sulfate which is an important terminal reaction in the oxidative degradation of sulfur containing amino acids like cysteine and methionine. A proposed reaction scheme is shown in Figure 1.2.^{6,17-19} The Mo(VI) oxidation state is the resting state of the enzyme with a d^0 electronic configuration of the metal center. It is believed that during catalysis the equatorial oxygen atom is transferred to the substrate with a concomitant two electron reduction of the equatorial metal orbital. Therefore, the metal center receives two electrons and is reduced to Mo(IV), a d^2 electronic configuration. The resting state Mo(VI) is regenerated through Mo(V) intermediate oxidation state.

XO catalyzes carbon-hydrogen bond activation reactions.^{19,20} An example of an enzyme in this family is aldehyde oxidase (MOP) that catalyzes oxidation of aldehyde substrates to their respective carboxylic acids. A proposed reaction scheme for this is shown in Figure 1.3 where Mo(VI), d^0 electronic configuration, is the resting state of the enzyme. The proposed mechanism involves an attack of the hydroxide oxygen atom on the carbonyl carbon of the substrate and a subsequent transfer of the hydride atom to the sulfido sulfur atom coordinated to the metal center.^{12,19,21-23} This reduces the metal center to Mo(IV), d^2 electronic configuration, and the active site is regenerated as product is displaced by a water molecule.

1.5 Bioinorganic modeling of SO and XO

Metal sites in biological systems have been intriguing to chemists. Unfolding their roles and understanding their interactions with the surrounding ligands has not been an easy task. The complicated active site features are often hard to duplicate, but can be broken down into more manageable features to be incorporated into synthetic or computational models. For example, the active site of chicken liver sulfite oxidase discussed above has metal-dithiolate, metal-(di)oxo and metal-thiolate as some of the features that one would like to incorporate into small molecular models of SO active sites. These features shown in Figure 1.4, would provide flexibility of understanding metal-oxo, metal-dithiolate, metal-thiolate or a combination of these in small molecular models. These discrete molecules are amenable to a variety of physical methods IR, NMR, EPR, X-ray diffraction, photoelectron spectroscopy etc. Some advantages of studying these molecules include their structural studies in high (atomic) resolution which is not always possible with proteins. In some cases the reactivity models, *i.e.* models that carry out desired reactions, have been possible to synthesize. However, an apparent disadvantage is that models cannot imitate the real active sites owing to the complexities of the protein environment.

Long before the structures of the SO/XO families of enzymes were known, bioinorganic chemists had already started addressing issues involving metals, ligands and their interactions relevant to the active sites of these enzymes. This work will present synthesis, purification, physical characterization using IR, EPR, NMR, and X-ray diffraction of model compounds. The X-ray crystal structures are a convenient starting

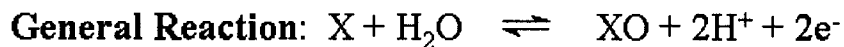
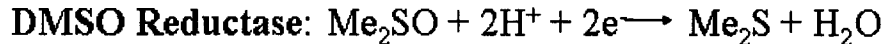
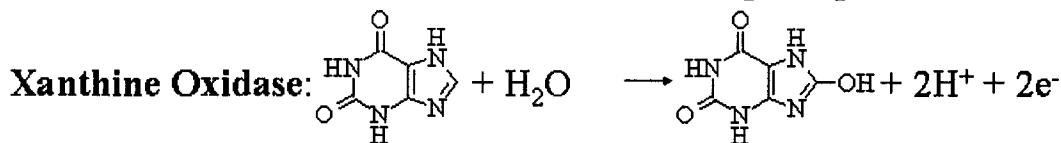
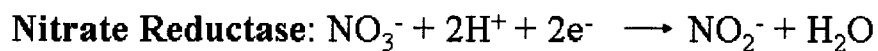
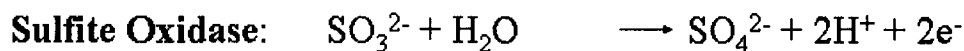
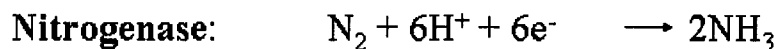
point for the high level density functional theory (DFT) calculations of these or simplified models. DFT calculations provide details of the frontier molecular orbitals including the contributions of the individual atomic orbitals. The use of photoelectron spectroscopy as a powerful technique for discerning important metal-sulfur interactions will be shown here. DFT calculations further help band assignments in photoelectron spectroscopy.

Two types of metal-dithiolate systems, shown in Figure 1.5, will be mainly discussed in this work. First is a scorpionate ligand (Tp*; hydrotris(3, 5-dimethylpyrazol-1-yl)borate) based system and the second is a bent-metallocene (biscyclopentadienyl)-dithiolate system. In the scorpionate ligand systems, two metal atoms (Mo and W), two axial ligations (O and NO) and a series of enedithiolate ligand perturbations can be synthesized. The (Tp*)MO(dithiolate) (where M = Mo, W) system provides access to Mo(V) oxidation state, a d^1 electronic configuration of the metal center. The (Tp*)MoO(dithiolate) system also features an axial oxo ligation *cis* to enedithiolate ligand, reminiscent of the “spectator oxo” ligand in the active site of SO and XO families of enzymes. The enedithiolate system is a 1,2-benzenedithiolate or one of its derivatives. Thus, this model can be studied for combined metal-oxo and metal-enedithiolate interactions. These compounds, being Mo(V) species, are EPR active and are the only known discrete and neutral Mo(V) systems that can also be studied with photoelectron spectroscopy. (Tp*)MoO(dithiolate) compounds are synthesized²⁴ from the (Tp*)MoOCl₂ precursor first reported by Trofimenko in 1971.^{25,26}

Another system studied here is the bent-metallocene $\text{Cp}_2\text{M}(\text{dithiolate})$ (where $\text{M} = \text{Mo, W, Ti}$) system. This system is a simpler system as it contains only the metal-dithiolate features of the above enzyme active sites.²⁷ The $\text{Cp}_2\text{Mo}(\text{dithiolate})$ systems were first synthesized in 1970.^{28,29} They provide access to the Mo(IV) oxidation state of the metal center. Their spectroscopic studies presented in this work will establish them as an ideal system to understand metal-sulfur interactions.

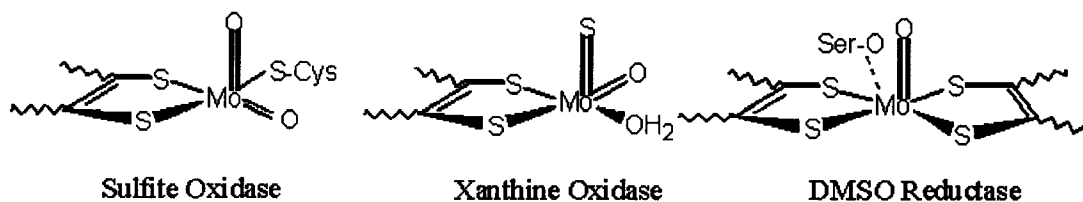
Table 1.1. Some reactions catalyzed by molybdenum containing enzymes. Nitrogenase, although a molybdenum containing enzyme, is not a pyranopterindithiolate containing enzyme. A general reaction scheme for a pyranopterindithiolate containing enzyme is shown.

Some Reactions Catalyzed by Molybdenum-containing Enzymes



Pyranopterin Molybdenum and Tungsten Enzymes

3 Families based on structure/reactivity



X-ray crystallography reveals
a common structural unit:
pyranopterin cofactor

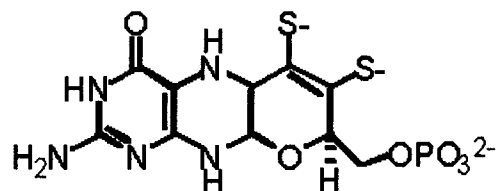


Figure 1.1. Classification of the pyranopterinindithiolate containing enzymes. Also shown is a schematic representation of the pyranopterinindithiolate cofactor.

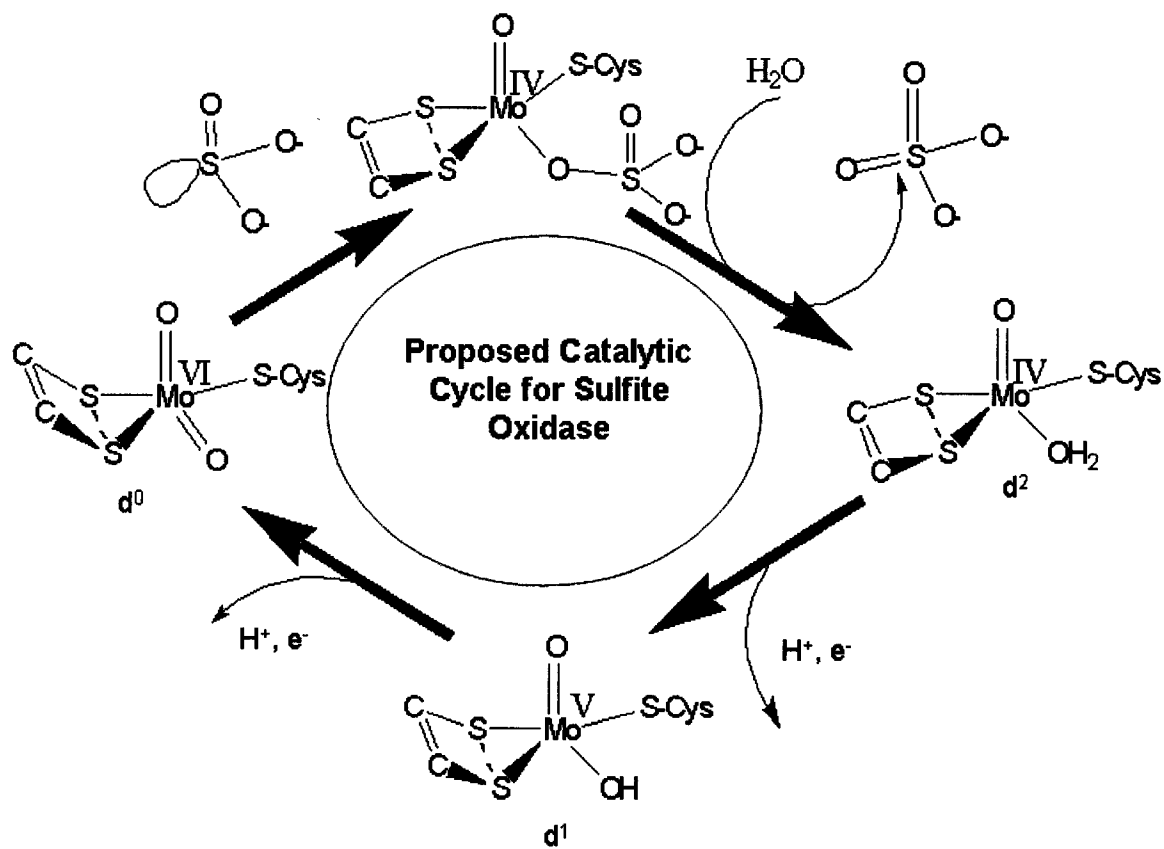


Figure 1.2. The proposed catalytic mechanism for sulfite oxidase. Mo(VI) on left hand side is the resting state of the enzyme. During catalysis the metal center undergoes electronic configurations changes that involve d⁰, d² and d¹ states (the S-S vector is shown as a broken line).

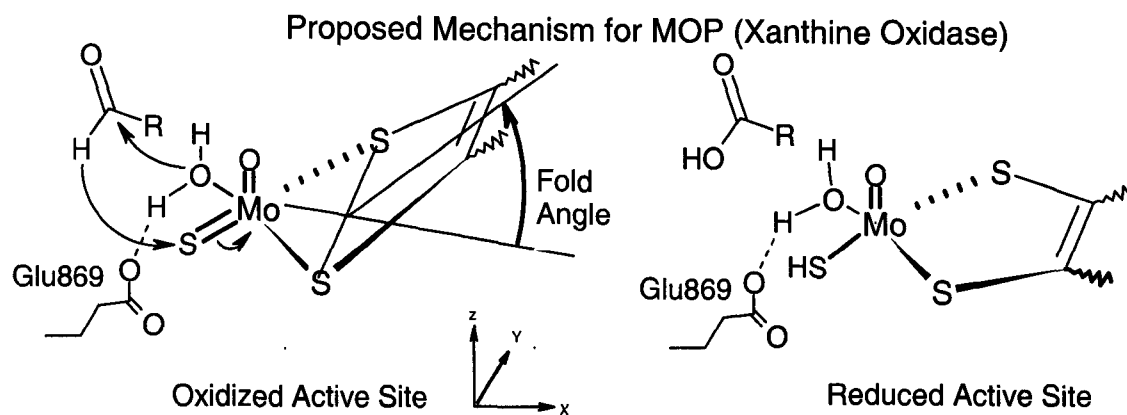


Figure 1.3. The proposed mechanism of aldehyde oxidase (MOP) involves a hydride atom transfer to the terminal sulfido group that reduces the Mo (VI) center to Mo(IV) and is considered to be an important step during catalysis.

Bioinorganic Modeling

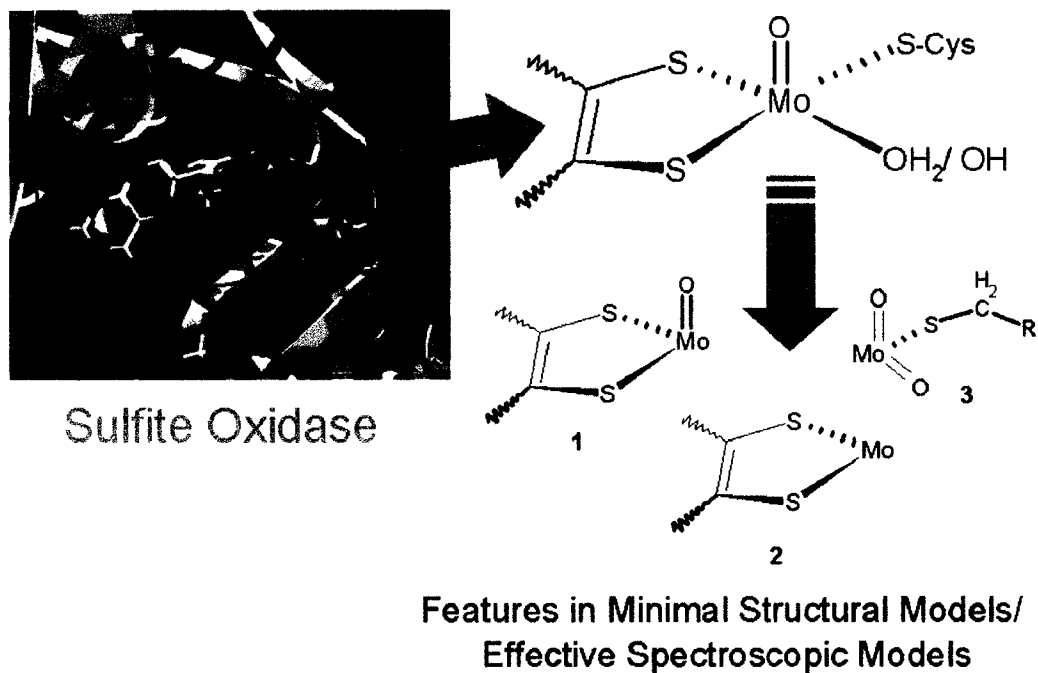
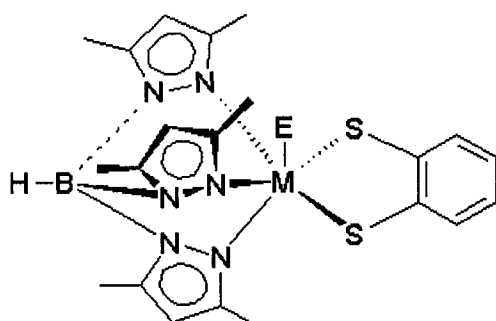
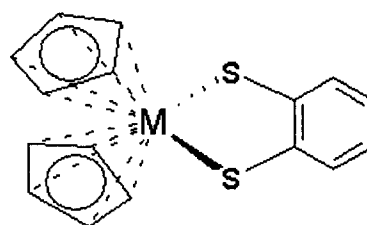


Figure 1.4. Modeling of the active site of sulfite oxidase. Breakdown of the active site into more manageable features that can be incorporated into minimal molecular models.

Active Site Models



$(Tp^*)ME(bdt)$
 $M = Mo, W$
 $E = O \quad M(V) d^1$
 $\quad = NO \quad M(II) d^4$



$Cp_2M(bdt)$
 $M = Mo, W \quad M(IV) d^2$
 $\quad = Ti \quad M(IV) d^0$

Figure 1.5. Active site models that contain one enedithiolate.

1.6 References

1. Garner, D. C.; Banham, R.; Cooper, S. J.; Davies, E. S.; Stewart, L. J. In *Handbook on Metalloproteins*; Bertini, I.; Sigel, A.; Sigel, H., Eds.; Marcel Dekker, Inc.: New York, 2001, pp 1023-1090.
2. Thompson, K. H.; Orvig, C. *Science* **2003**, *300*, 936-939.
3. Kisker, C. *Handbook of Metalloproteins, Volume 2*; Messerschmidt, A., Huber, Ed.; John Wiley & Sons LTD: New York, 2001, pp 1121-1135.
4. Sigel, A.; Sigel, H. *Molybdenum and Tungsten: Their Roles in Biological Processes.*; Metals Ions in Biological Systems; vol. 39; Dekker: New York, 2002.
5. Enemark, J. H.; Cosper, M. M. In *Metal Ions in Biological Systems*; Vol. 39: *Molybdenum and Tungsten. Their Roles in Biological Processes*; Sigel, A.; Sigel, H., Eds.; Marcel Dekker, Inc.: New York, 2002, pp 621-654.
6. Hille, R. *Chem. Rev.* **1996**, *96*, 2757-2816.
7. Rajagopalan, K.; Johnson, J. L. *J. Biol. Chem.* **1992**, *267* (15), 10199-202.
8. Schindelin, H.; Kisker, C.; Rees, D. *JBIC, J. Biol. Inorg. Chem.* **1997**, *2* (6), 773-781.
9. Kisker, C.; Schindelin, H.; Pacheco, A.; Wehbi, W.; Garrett, R. M.; Rajagopalan, K. V.; Enemark, J. H.; Rees, D. C. *Cell* **1997**, *91*, 973-983.
10. Schrader, N.; Fischer, K.; Theis, K.; Mendel, R. R.; Schwarz, G.; Kisker, C. *Structure* **2003**, *11* (10), 1251-1263.

11. Rebelo, J.; Dias, J.; Huber, R.; Moura, J.; Romao, M. *JBIC, J. Biol. Inorg. Chem.* **2001**, *6* (8), 791-800.
12. Huber, R.; Hof, P.; Duarte, R.; Moura, J.; Moura, I.; Liu, M.; LeGall, J.; Hille, R.; Archer, M.; Romao, M. *Proc. Natl. Acad. Sci. USA* **1996**, *93* (17), 8846-51.
13. Romao, M. J.; Archer, M.; Moura, I.; Moura, J. J.; LeGall, J.; Engh, R.; Schneider, M.; Hof, P.; Huber, R. *Science* **1995**, *270*, 1170-6.
14. Boyington, J.; Gladyshev, V.; Khangulov, S.; Stadtman, T.; Sun, P. *Science* **1997**, *275*, 1305-8.
15. Schindelin, H.; Kisker, C.; Hilton, J.; Rajagopalan, K.; Rees, D. *Science* **1996**, *272* (5268), 1615-21.
16. Chan, M.; Mukund, S.; Kletzin, A.; Adams, M.; Rees, D. *Science* **1995**, *267*, 1463-9.
17. Hille, R. *JBIC, J. Biol. Inorg. Chem.* **1996**, *1* (5), OCT, 397.
18. Hille, R. *Essays in Biochemistry, Vol 34, 1999* **1999**, *34*, 125.
19. Hille, R. *Biochim. Biophys. Acta* **1994**, *1184* (2-3), 143-69.
20. Stockert, A. L.; Shinde, S. S.; Anderson, R. F.; Hille, R. *J. Am. Chem. Soc.* **2002**, *124* (49), 14554-14555.
21. Romao, M. J.; Rosch, N.; Huber, R. *JBIC, J. Biol. Inorg. Chem.* **1997**, *2* (6), 782-785.
22. Ilich, P.; Hille, R. *J. Phys. Chem. B* **1999**, *103* (25), 5406-5412.
23. Ilich, P.; Hille, R. *J. Am. Chem. Soc.* **2002**, *124* (24), 6796-6797.
24. Dhawan, I. K.; Enemark, J. H. *Inorg. Chem.* **1996**, *35*, 4873-4882.

25. Trofimenko, S. *Inorg. Chem.* **1971**, *10* (3), 504-7.
26. Swiatoslav Trofimenko. *Scorpionates-The Coordination Chemistry of Polypyrazolylborate Ligands*; Imperial College Press: London, 1999.
27. Joshi, H. K.; Cooney, J. J. A.; Inscore, F. E.; Gruhn, N. E.; Lichtenberger, D. L.; Enemark, J. H. *Proc. Natl. Acad. Sci. USA* **2003**, *100* (7), 3719-3724.
28. Fourmigue, M. *Coord. Chem. Rev.* **1998**, *178-180* (Pt. 1), 823-864.
29. Kutoglu, A.; Köpf, H. *J. Organomet. Chem.* **1970**, *25*, 455-460.

CHAPTER 2: Experimental Section

1.0 Synthesis of Compounds

1.1 Abbreviations

Tp*, hydrotris(3,5-dimethyl-1-pyrazolyl)borate; Cp, η^5 -cyclopentadienyl; bdt, 1,2-benzenedithiolate; qdt, 2,3-dithioquinoxaline; tdt, 3,4-toluenedithiolate; bdtCl₂, 3,6-dichloro-1, 2-benzenedithiolate. (S-S) represents a generic ene-1,2-dithiolate ligand that forms a five membered chelate ring with the Mo atom.

1.2 General

All reactions and manipulations were carried out under an inert atmosphere of argon gas using standard Schlenk techniques, a high-vacuum/gas double line setup, and an inert atmosphere glove bag. The argon was predried by passing the high-purity-grade gas through a series of drying towers. All glassware was dried in an oven at 150°C and Schlenk ware was further purged by repeated evacuation and inert gas flushes prior to use. Tetrahydrofuran (THF) and toluene were distilled from Na/benzophenone; triethylamine was distilled from Na/K amalgam.¹ The prepurified solvents were subsequently transferred and stored under N₂ over fresh drying agents. These solvents were freshly distilled under nitrogen prior to use, thoroughly degassed by repeated freeze-thaw-pump cycles, and transferred to reaction vessels via steel cannulae under a positive pressure of inert gas. Dichloromethane, 1,2-dichloroethane (DCE), cyclohexane, toluene (EM Science, Omnisolv; for the synthesis of Cp₂ based compounds), n-hexane

and n-pentane (Burdick and Jackson) were used as received and deoxygenated by bubbling with argon.

TLC analysis was carried out on silica gel 60 F₂₅₄ plastic sheets (EM Science) and column chromatography was carried out in glass columns with silica gel (Merck, grade 9385, 230-400 mesh, pore diameter 60 Å) as the stationary phase. Mass spectra were recorded on a JEOL HX110 high-resolution sector instrument utilizing fast atom bombardment (FAB) ionization in a matrix of 3-nitrobenzyl alcohol (NBA). IR spectra (4000-400 cm⁻¹) were collected on a Nicolet Avatar ESP 360 FT-IR spectrophotometer in KBr disks or as dichloromethane solutions (between NaCl plates) at room temperature. Electronic absorption spectra of samples dissolved in 1,2-dichloroethane solutions were recorded with a 1-cm pathlength Helma quartz cell equipped with a teflon stopper, on a Cary 300 (250-900nm) spectrophotometer. Solvent background corrections were made in all cases. ¹H-NMR (CDCl₃) spectra were acquired on a Bruker DRX-500 spectrometer operating at a ¹H frequency of 500.13 MHz using a 5 mm Nalorac triple-resonance 3-axis gradient probe. Chemical shifts were referenced to residual CHCl₃ at 7.24 ppm unless otherwise stated.

Details of the preparation of compounds used in this study are described in subsequent chapters. However, a brief description of their syntheses are given here.

1.3 Synthesis of (Tp*)MoOX₂ (X = F, Cl, Br) Complexes

The compound (Tp*)MoOCl₂ was used as a precursor for the synthesis of all [(Tp*)MoO] based compounds used in this work.² The dihalide complexes have been

prepared from the reaction of the corresponding halo acid with $(\text{Tp}^*)\text{MoO}(\text{OMe})_2$ which was prepared from $(\text{Tp}^*)\text{MoOCl}_2$ in a one step reaction described in detail elsewhere.³

1.4 Synthesis of $(\text{Tp}^*)\text{MoO}(\text{S-S})$ Complexes

$(\text{Tp}^*)\text{MoOCl}_2$ compound was also used as a precursor for the preparation of corresponding metal-dithiolate complexes. A solution of $(\text{Tp}^*)\text{MoOCl}_2$ in toluene was deoxygenated thoroughly with argon saturation while being stirred at $\sim 80^\circ\text{C}$. Dithiol ligands were purchased from Aldrich and added in slight excess to this suspension under a positive pressure of argon. Dry degassed Et_3N was added slowly dropwise via a gas tight syringe to this rigorously stirring solution. The mildly refluxing reaction solution was observed to change gradually from an emerald green to a dark red-brown color after 4 hours of stirring. The reaction progress was monitored by TLC analysis. The reaction was stopped upon observing the near disappearance of the green $(\text{Tp}^*)\text{MoOCl}_2$ precursor concomitant with the maximal formation of the red-brown product.

1.5 Synthesis of $(\text{Tp}^*)\text{Mo}(\text{NO})(\text{S-S})$ Complexes

Molybdenum hexacarbonyl ($\text{Mo}(\text{CO})_6$, Aldrich) was dried in vacuum prior to use. Potassium hydrotris(3,5-dimethyl-1-pyrazolyl)borate (KTp^*), the precursor complexes $(\text{Tp}^*)\text{Mo}^{\text{V}}(\text{NO})(\text{CO})_2$ and $(\text{Tp}^*)\text{Mo}^{\text{V}}(\text{NO})\text{I}_2\cdot\text{C}_6\text{H}_5\text{CH}_3$ and the ligands H_2bdt (1,2-benzenedithiol) were prepared according to literature procedures.⁴⁻⁶ The ligand H_2tdt (3,4-toluenedithiolate) and H_2bdtCl_2 (3,6-dichloro-1,2-benzenedithiol) employed in the

syntheses of the $(Tp^*)Mo^V(NO)(S-S)$ compounds were used as received from Aldrich. Details of syntheses are described in Chapter 7.

1.6 Synthesis of $Cp_2M(S-S)$ Complexes

Bis(cyclopentadienyl)metal(IV)dichloride (Cp_2MCl_2 , $M = Mo, W$, Aldrich) was used as a starting material. Ligand exchange reaction with $(S-S)^{2-}$ resulted in the corresponding $Cp_2Mo(S-S)$ complexes. These starting $H_2(S-S)$ ligands can be deprotonated using a base, for example triethylamine or sodium hydroxide. An aqueous organic solvent is required for dissolving the dihalide precursor in the reaction mixture and enhanced yields of the desired product. The details of synthesis are given in Chapter 8 and described in the literature.⁷

2.0 Gas-Phase Photoelectron Spectroscopy

2.1 Data Collection.

Photoelectron spectra were recorded using an instrument that features a 36-cm hemispherical analyzer (McPherson) and custom designed sample cells and detection and control electronics.⁸ The excitation source is a quartz lamp with the ability, depending on operating conditions, to produce HeI (21.21 eV) and HeII (40.8 eV) photons. For the He I and HeII experiments, the ionization energy scale was calibrated using the $^2E_{1/2}$ ionization of methyl iodide (9.538 eV), The argon $^2P_{3/2}$ ionization also was used as an internal calibration lock of the absolute ionization energy to control spectrometer drift within ± 0.001 eV throughout data collection. During HeI and HeII data collection the

instrument resolution, measured using the full-width-at-half-maximum of the argon $^2P_{3/2}$ ionization, was 0.02-0.035 eV. All data are intensity corrected with an experimentally determined instrument analyzer sensitivity function that assumes a linear dependence of analyzer transmission (intensity) to the kinetic energy of the electrons within the energy range of these experiments.

All of the spectra were corrected for the presence of ionizations from other emission lines. These corrections are necessary because discharge sources are not monochromatic. The HeI spectra were corrected for the HeI β line (1.9 eV higher in energy, and 3% the intensity of the HeI α line), the HeII spectra were corrected for the HeII β line (7.568 eV higher in energy, and 12% the intensity of the HeII α line).

All samples sublimed cleanly with no detectable evidence of decomposition products in the gas phase or as a solid residue. If decomposition occurred it has been noted in the experimental description in the respective chapters. The sublimation temperatures are described in Table 2.1 and monitored using a "K" type thermocouple passed through a vacuum feedthrough and attached directly to the ionization cell. The sample of compound H₂bdt (1,2-benzene dithiol) is volatile at room temperature and was run from a glass tube with a Teflon stopcock attached to the instrument via a Swagelock glass to metal connection (Teflon ferrule) and using a needle valve to control the flow of sample into the ionization chamber.

2.2 Data Analysis.

In the figures of the data, the vertical length of each data mark represents the experimental variance of that point.⁹ The valence ionization bands are represented analytically with the best fit of asymmetric Gaussian peaks.⁹ The Gaussians are defined with the position, amplitude, halfwidth for the high binding energy side of the peak, and the halfwidth for the low binding energy side of the peak. The peak positions and halfwidths are reproducible to about ± 0.02 eV ($\approx 3\sigma$ level). The parameters describing an individual ionization are less certain when two or more peaks are close in energy and are overlapping. If the combined band contour does not contain sufficient information for independent determination of the individual peak parameters, the number of peaks and/or independent parameters in the analytical representation are appropriately reduced. These situations are evident in the tables or results, where half-widths for similar peaks are occasionally constrained to be the same.

Confidence limits for the relative integrated peak areas are about 5%, with the primary source of uncertainty being the determination of the baseline subtracted from the area of the peaks. The baseline is caused by electron scattering and taken to be linear over the small energy range of these spectra. The total area under a series of overlapping peaks is known with the same confidence, but the individual peak areas are more uncertain. The fitting procedures used are described in more detail elsewhere.

3.0 X-ray Crystallography

Crystals having approximate dimensions of approximately 0.10 x 0.10 x 0.1 mm were mounted on a glass fiber in a random orientation. The methods of crystallization are reported in Table 2.2. Examination of the crystal on a Bruker SMART 1000 CCD detector X-ray diffractometer at 170(2)K and a power setting of 50 KV, 40 mA showed measurable diffraction to at least $\theta = 30^\circ$. Data were collected on the SMART1000 system using graphite monochromated Mo K_α radiation ($\lambda = 0.71073\text{\AA}$). Initial cell constants and an orientation matrix for integration were determined from reflections obtained in three orthogonal 5° wedges of reciprocal space. The frames were integrated using the Bruker SAINT software package's narrow frame algorithm. The final cell parameters, data collection and refinement details are described later in subsequent chapters. Empirical absorption and decay corrections, wherever required, were applied using the program SADABS and has been described with the structure descriptions. The calculated density in Mo containing compounds was found close to 1.5 g/cm^3 . Systematic absences and intensity statistics indicated the described space groups and were found consistent with refinement.

The structures were solved using SHELXS in the Bruker SHELXTL (Version 5.0) software package. Refinements were performed using SHELXL and illustrations were made using XP. Solution was achieved utilizing direct methods followed by Fourier synthesis. Hydrogen atoms were added at idealized positions, constrained to ride on the atom to which they are bonded and given thermal parameters equal to 1.2 or 1.5 times U_{iso} of that bonded atom. A parameter describing extinction was included. The final

anisotropic full-matrix least squares refinement based on F^2 of all reflections converged described R1, wR2 and goodness-of-fit values. Scattering factors and anomalous dispersion were taken from International Tables Vol C, Tables 4.2.6.8 and 6.1.1.4.^{10,11}

4.0 Theoretical Methods

Geometry optimization, SCF (self-consistent field) and molecular orbital calculations were performed using the ADF (Amsterdam density functional theory calculations) package (release 2000.02). Starting geometries were obtained from crystal structures and are described in respective chapters. Two types of approximations were used. A local density approximation with X_σ functional¹² and a generalized gradient approximation, with the exchange correction of Becke¹³ and the correlation correction of Lee *et. al.*,¹⁴ was used for all density functional calculations. All core levels were treated as frozen orbitals and their details are provided in individual chapters. Also noted are the basis sets, Slater type orbitals and polarization functions for elements. Calculations on the ground-state molecules were performed in the spin-restricted mode. Spin-unrestricted Δ SCF (self-consistent field) calculations were performed on the proposed ion states formed by photoionization by removing one electron from the relevant orbital and comparing the total energy with that of the ground state molecule. A linear correction was applied for comparison of the calculated and the observed energies, *i.e.* the calculated Δ SCF energies and orbital energies were shifted by the difference between experimentally obtained and calculated energies of the HOMO.

Table 2.1. Experimental details of the photoelectron spectroscopic studies.

Molecule	Collection Temp (°C)	Photon Source	Resolution	File Names	Energy Region
(Tp*)MoOCl ₂	186-229	He I	17-26	hkj01.f*	15.7-5.5
				hkj01.c*	12.0-6.45
		He II	18-28	hkj01.x*	20.0-5.0
				hkj01.y*	12.0-6.45
(Tp*)MoOBr ₂	150-216	He I	21-29	hkj02.f*	15.7-5.5
				hkj02.c*	11.5-6.86
		He II	21-30	hkj02.x*	20.0-5.0
				hkj02.y*	11.5-6.86
(Tp*)MoOF ₂	172-229	He I	25-42	hkj03.f*	15.7-5.5
				hkj03.c*	11.5-6.88
		He II	21-33	hkj03.x*	20.0-5.0
				hkj03.y*	11.5-6.87
(Tp*)VO(dtc)	147-229	He I	23-30	hkj04.f*	15.7-5.5
(Tp*)MoO(bdtCl ₂)		He I	19-25	hkj07.f*	15.7-5.5
				hkj07.c*	10.8-6.37
		He II	19-21	hkj07.x*	20.0-5.0
				hkj07.y*	12.0-6.27
(Tp*)MoO(bdt)	170-229	He I	18-25	hkj08.f*	15.7-5.5
				hkj08.c*	12.0-5.9
		He II	16-23	hkj08.x*	20.0-5.0
				hkj08.y*	12.0-5.9
H ₂ bdtCl ₂	23-56	He I	19-23	hkj09.f*	15.7-5.5
				hkj09.c*	12.25-7.62
				hkj09.z*	9.5-8.0
		He II	19-24	hkj09.x*	20.0-5.0
	hkj09.y*			12.25-7.62	
	23-56	He I	30-34	hkj14.f*	15.7-5.5
				hkj14.c*	12.5-7.68
		He II	24-30	hkj14.x*	20.0-5.0
hkj14.y*				12.5-7.68	

Table 2.1 Continued

Molecule	Collection Temp (°C)	Photon Source	Resolution	File Names	Energy Region
(Tp*)WO(bdt)	156-235	He I	22-25	hkj11.f*	15.7-5.5
				hkj11.c*	10.5-6.2
		He II	29-35	hkj18.y*	20.0-5.0
				hkj18.z*	8.5-5.72
				hkj22.x*	20.0-5.0
hkj22.c*	8.00-5.59				
Cp ₂ Mo(bdtCl ₂)	203-229	He I	21-30	hkj16.f*	15.7-5.5
				hkj16.c*	8.5-5.72
		He II		hkj18.y*	20.0-5.0
				hkj18.z*	8.5-5.72
Cp ₂ Ti(bdt)	152-203	He I	21-30	hkj17.f*	15.0-4.8
				hkj17.c*	10.5-6.05
		He II	26-32	hkj23.x*	20.0-5.0
				hkj23.y*	8.5-6.28
Cp ₂ Ti(bdtCl ₂)	171-205	He I	20-24	hkj19.f*	15.7-5.5
				hkj19.c*	10.5-6.24
Cp ₂ Ti(SPh) ₂	155-205	He I	20-25	hkj21.f*	15.7-5.5
				hkj21.c*	10.5-6.24
Cp ₂ Ti(pdt)	190-214	He I	20-25	hkj24.f*	15.7-5.5
				hkj24.c*	8.5-6.3
		He II	17-27	hkj24.y*	20.0-5.0
				hkj24.z*	8.5-6.3
(Tp*)MoOF ₂	172-229	He I	21-33	hkj25.f*	15.7-5.5
				hkj25.c*	11.25-9.76
Cp ₂ W(bdt)	170-200	He I	20-22	hkj26.f*	15.7-5.5
				hkj26.c*	7.75-5.52
		He II	21-26	hkj26.a*	20.0-5.0
				hkj26.z*	7.75-5.52
KTp ^{(CF₃)₂}	86-107	He I	26-30	hkj13.f*	15.7-5.5
				hkj13.c*	12.7-8.25

Table 2.1 Continued

Molecule	Collection Temp (°C)	Photon Source	Resolution	File Names	Energy Region
H ₂ bd	23.6	He I	22-25	hkj10.x*	15.7-5.5
				hkj10.y*	12.25-7.6
		He II	29-35	hkj10.f*	20.0-5.0
				hkj10.c*	12.25-7.6

Table 2.2. Experimental details of the crystallographic studies.

Molecule	Solvent System	Crystallization Method	Data Collection/ Refinement File Name	R1 (%)
(Tp*)Mo(NO)(tdt)*	DCM/ Heptane	Vapor diffusion	hkj00	4.84
(Tp*)Mo(NO)(bdt)*	DCM/ Pentane	Liquid diffusion	hkj01	6.30
(tacn)Mo(CO) ₃	unknown	Liquid diffusion	hkj02	2.26
(Tp*)MoO(qdt)	DCM/ Pentane	Vapor diffusion	hkj03	3.46
[PPh ₄] ₂ [VO(qdt) ₂]	Acetonitrile/ Pentane	Liquid diffusion	hkj04	#
[Et ₃ NH] ₂ [VO(tdt) ₂]	Acetonitrile/ Pentane	Liquid diffusion	hkj05	
[Et ₃ NH] ₂ [VO(bdtCl ₂) ₂]	Acetonitrile/ Pentane	Liquid diffusion	hkj06	
(Tp*)WO(bdt)	Ether/Pentane	Vapor diffusion	hkj07	6.05
(Tp*)Mo(NO)(bdtCl ₂)	DCM/ Pentane	Liquid diffusion	hkj09	5.17
(Tp*)MoO(bdtCl ₂)	DCM/ Pentane	Liquid diffusion	hkj10	4.42
(Tp*)MoOBr ₂	DCM/ Pentane	Vapor diffusion	hkj11	5.67
(Tp*)MoO ₂ (SCH ₂ Ph)	DCM/ Pentane	Vapor diffusion	hkj12	5.55
[Mo(mnt) ₂ (SPh) ₂][PPh ₄] ₂	Acetonitrile/ Isopropyl alcohol	Liquid diffusion	hkj13	4.54
[Mo(mnt) ₂ (SPh)]		Liquid diffusion	hkj14	\$
Cp ₂ Mo(bdt)	Acetonitrile/ Pentane	Liquid diffusion	hkj16	2.91

* The data collection on these crystals was previously done by Dr. Ish K. Dhawan. However, data refinement using new version of software (SHELXTL version 5) was done in this work.

Data collected, but upon refinement, the final structure was unexpected (V-O cluster). This might be due to oxidation of the product.

\$ Data collection of intense twin peaks. During refinement twinning was considered, but no solution was reached.

5.0 References

1. W. Armarego, D. Perrin, *Purification of Laboratory Chemicals, 4th ed.*, Pergamon Press, New York, **1997**, p. 512.
2. Trofimenko, S. *Inorg. Chem.* **1971**, *10* (3), 504-7.
3. Cleland, W. E., Jr.; Barnhart, K. M.; Yamanouchi, K.; Collison, D.; Mabbs, F. E.; Ortega, R. B.; Enemark, J. H. *Inorg. Chem.* **1987**, *26*, 1017-1025.
4. McCleverty, J. A.; Seddon, D.; Bailey, N. A.; Walker, N. J. *J. Chem. Soc., Dalton Trans.* **1976**, *10*, 898-908.
5. Reynolds, S.; Smith, C.; Jones, C.; McCleverty, J. *Inorg. Synth.* **1985**, *23*, 4-9.
6. Giolando, D. M.; Kirschbaum, K. *Synthesis* **1992**, *5*, 451-2.
7. Kutoglu, A.; Köpf, H. *J. Organomet. Chem.* **1970**, *25*, 455-460.
8. Lichtenberger, D. L.; Kellogg, G. E.; Kristofzski, J. G.; Page, D.; Turner, S.; Klinger, G.; Lorenzen, J. *Rev. Sci. Instrum.* **1986**, *57* (9), 2366.
9. Lichtenberger, D. L.; Copenhaver, A. S. *J. Electron Spectrosc. Relat. Phenom.* **1990**, *50* (4), 335-52.
10. Cromer, D. T.; Waber, J. *Int. Tables X-Ray Crystallogr.* **1974**, *4*, 71-147.
11. Cromer, D. T.; Ibers, J. A. *Int. Tables X-Ray Crystallogr.* **1974**, *4*, 148-51.
12. Te Velde, G.; Bickelhaupt, F.; Baerends, E.; Fonseca Guerra, C.; Van Gisbergen, S.; Snijders, J.; Ziegler, T. *J. Comp. Chem.* **2001**, *22* (9), 931-967.
13. Becke, A. D. *Phys. Rev. A.* **1988**, *38*, 3098-3100.
14. Lee, C.; Yang, W.; Parr, R. G. *Phys. Rev. B.* **1988**, *37*, 785.

CHAPTER 3: Electronic Structures of Hydrotris(pyrazol-1-yl)borates and Ene-1,2-dithiolene Ligands

Part of this chapter has been submitted for publication as

Joshi, H. K.; Arvin, M. E.; Durivage, J. C.; Gruhn, N. E.; Carducci, M. D.; Westcott, B. L.; Lichtenberger, D. L.; Enemark, J. H. "Photoelectron Spectra of Potassium Salts of Hydrotris(pyrazol-1-yl)borates: Electronic Structure of the Electron Withdrawing Scorpionates $\text{Tp}^{(\text{CF}_3)_2}$, $\text{Tp}^{*\text{Cl}}$ and Comparison to Tp^* and Tp " Polyhedron, **2003**, in press

1.0 Introduction

The majority of the compounds that are studied in this work contain one or both of these ligand types: (a) hydrotris(pyrazol-1-yl)borates, (b) ene-1,2-dithioleues. These ligands and their electronic structures are discussed in this chapter. Scorpionates based on polypyrazolylborates are a well-known class of ligands with very rich coordination chemistry.¹⁻³ One of the most symmetric (C_{3v}) of these, hydrotris(pyrazol-1-yl)borate (Tp), is a generic tridentate monoanionic ligand (Figure 3.1 a and b). Symmetrically substituted Tp ligands (Figure 3.1 and b) that conserve *pseudo*- C_3 symmetry and coordinate to a metal center in a tridentate fashion are called homoscorpionates. Complexes of the Tp-based ligands are known for most metals in the periodic table. Substitutions at the 3, 4 and 5 positions of the pyrazole in the Tp framework allow both steric and electronic control of metal centers by restricting the number and the positions of vacant coordination sites,⁴⁻⁶ the size or shape of the substrates⁷ and by stabilizing electron rich^{8,9} or electron poor^{6,10} metal centers. One example of such substitution at the 3 and 5 positions of the pyrazole ring is the trifluoromethyl (CF_3) group. The resulting hydrotris(3,5-bis(trifluoromethyl)pyrazol-1-yl)borate ($Tp^{(CF_3)_2}$) ligand is structurally similar to its methylated analogue hydrotris(3,5-dimethylpyrazol-1-yl)borate (Tp^*), and therefore, allows perturbations of ligand electronic effects without significant perturbations in steric factors. Polyfluorinated ligands such as $Tp^{(CF_3)_2}$ commonly improve the volatility and oxidation resistance of their metal complexes.^{11,12} They have very electrophilic metal centers relative to their hydrocarbon analogues (Tp^*).^{11,12}

Another widely accepted family of ligands in organometallic chemistry is the derivatives of the cyclopentadienyl ($\eta^5\text{-C}_5\text{H}_5^-$, Cp) ligands. The Tp and the Cp ligands are both monoanionic and formally six-electron donors, but one notable difference lies in the mode of their ligation to metals. The Cp based ligands involve a π -type interaction with the metal centers whereas the Tp based ligands are primarily σ -donors, with the exception of the recent report of a $\eta^5\text{-Tp}^{\text{CF}_3, \text{CH}_3}$ potassium π -bonding interaction by Gorun *et al.*¹³ Bergman *et al.* have compared the relative electron-donating abilities of Tp and Cp and found a lack of generalization as this ability varies with the identity of the metal, its oxidation state and other ligands of the complex.¹⁴ Pioneering research work in the area of C-H bond activation by Jones and Bergman has compared the differences in related Tp and Cp transition metal complexes.^{15,16} Recent theoretical study of methane activation by $\text{TpRe}(\text{CO})_2$ and $\text{CpRe}(\text{CO})_2$ compounds by Cundari *et al.* reveals that the Tp framework is more stereoelectronically flexible than Cp.¹⁷

Previous photoelectron spectroscopic studies have been reported on the metal complexes of the Cp based ligands and their electronic structure perturbation due to direct halogen (F, Cl) substitutions on the Cp rings.¹⁸ However, the Cp ligands involving CF_3 substitutions are very difficult to synthesize, and their metal adducts are rare in the literature. The analogous $\text{Tp}^{(\text{CF}_3)_2}$ ligands are well known^{11,12} and form stable metal adducts.

Na^+ or K^+ salts of the Tp based ligands are used in almost all ligand transfer reactions for synthesis of the transition metal adducts of these scorpionates. Previous structural characterization and computational work have been applied to these salts.

Reglinski *et al.* have compared the Tp and the trismethimazolyl borate (Tm) ligands by X-ray crystallography and *ab initio* calculations and found a clear difference in behavior on going from hard nitrogen donor atoms in Tp to soft sulfur donor atoms in Tm.¹⁹ The X-ray crystal structures of the Na⁺ or K⁺ salts of several Tp based ligands are known and have provided the starting geometry for our computational studies.

Sterically demanding bulky ligands like the scorpionates discussed here are used to facially coordinate a metal and prevent polynucleation of metal complexes. Several model complexes of these ligands have been used in bioinorganic model chemistry.^{1,10} One of the questions in this ligand chemistry is whether the ligand itself is chemically innocent. For example, the oxo-molybdenum complexes of Tp* ligands have been utilized as minimum molecular models for the pyranopterin molybdenum and tungsten enzymes. In the EPR studies of the paramagnetic molybdenum center in these complexes,^{4,5} very small ¹⁴N superhyperfine interactions were observed from trispyrazole nitrogen atoms. The Tp based ligands are also silent for electronic absorption and MCD spectroscopies²⁰⁻²² and thus allow spectroscopic investigations of both the biologically relevant functional groups/ligands and the metals in the model complexes. A technique capable of assessing the metal and ligand characters of orbitals and studying the electronic structure of small molecules is gas-phase photoelectron spectroscopy using multiple energy ionization sources.²³ Photoelectron spectroscopic studies of the Mo adducts of the homoscorpionate Tp* have been reported earlier by our group^{24,25} and others.²⁶ All of these studies found that the Tp* ligand has a very prominent signature in 8-11 eV region in the photoelectron spectra of these Mo complexes that can allow

electronic structure studies of scorpionate ligands. However, these previous studies were focused on metal-sulfur ionizations that are located at lower ionization energies than Tp* based ionizations, and no attempts were made to explore the origin of the Tp* signatures (referred to as the “forest region” in these earlier studies). A series of photoelectron spectroscopic and computation studies using density functional theory were done to understand metal-halide interactions in (Tp*)MoO(X₂) (X = F, Cl, Cr, I).²⁷ The importance of understanding of the electronic structure of the Tp* is illustrated by photoelectron spectroscopic studies of (Tp*)MoO(qdt) (qdt = quinoxaline dithiolate), where the Tp* based ionizations overshadow the metal and sulfur based ionizations.²⁶ Previous attempts have been made to elucidate the electronic structure of the pyrazole,²⁸ several compounds containing the BH₄⁻ group²⁹ and the parent Tp ligand by photoelectron spectroscopy.^{30,31} Fragala *et al.* utilized a combination of theoretical calculations (CNDO) and photoelectron spectroscopy^{30,31} and found that in the scorpionate-metal adducts, the ionizations of the ligand based molecular orbitals are unaffected by the nature of the central metal.³¹ However, a detailed comparison among homoscorpionates using high-level density functional theory (DFT) and experimental gas-phase photoelectron spectroscopy has not been described. To the best of our knowledge, this report is the first gas-phase photoelectron spectroscopy investigation of the electronic structures of halogen containing scorpionates. The reported experimental and computational findings quantitates the electron withdrawing effect of CF₃ substituent on the Tp and Tp* ligand.

The electronic structures of the potassium salts of the homoscorpionates hydrotris(3,5-dimethylpyrazol-1-yl)borate (Tp^* , **1**), hydrotris(3,5-bis(trifluoromethyl)pyrazol-1-yl)borate ($\text{Tp}^{(\text{CF}_3)_2}$, **2**) are compared using gas-phase photoelectron spectroscopy and density functional theory (DFT). DFT calculations also are reported for the generic scorpionate potassium (hydrotris(pyrazol-1-yl)borate) (KTp). This is the first such experimental probe of the electronic structure of halogen containing scorpionate ligand and subtle differences in the ionizations from the frontier orbitals in the photoelectron spectra of **1** and **2** are observed that give insight into the influence of substituents upon metal-scorpionate bonding. Distinct assignments of the ionizations from the nitrogen σ -donor orbitals (σ_{N}) and σ_{BH} molecular orbitals are possible experimentally by the use of variable (He I and He II) excitation energies. The experimentally observed first ionization energy of **2** is stabilized by ~ 2.0 eV relative to **1** due to the strong electron withdrawing effect of the trifluoromethyl groups. The photoelectron spectroscopic studies of $\text{NaTp}^{(\text{CF}_3)_2}$ further confirm the assignments of ionizations from σ_{N} orbitals for **2** associated with the *a* and *e* sets in C_3 symmetry.

Ene-1, 2-dithiolenes, shown in Figure 3.1 (c), are another class of ligands discussed in this chapter. Transition metal-sulfur complexes containing unsaturated sulfur donor chelating agents, ene-1,2-dithiolenes, are of continuing interest in a full gamut of areas ranging from metal-sulfur interactions to their applications in bioinorganic modeling, material science and catalysis.³² The unusual ability of enedithiolenes to stabilize transition metals in multiple oxidation states have been recognized since these complexes were first investigated.^{32,33} The 1, 2-benzenedithiolenes ligand can be

synthesized from its precursors in a couple of steps.^{34,35} Here an electronic structure study of 1,2-benzenedithiolene (H_2bdt ; **3**) and 3,6-dichloro-1,2-benzenedithiolene (H_2bdtCl_2 ; **4**) has been presented utilizing photoelectron spectroscopy and density functional theory.

2.0 Experimental

2.1 General

All reactions were carried out under an inert atmosphere of argon gas using standard Schlenk techniques and a high-vacuum/gas double line setup. All glassware was dried in an oven at 150°C and Schlenkware was further purged by repeated evacuation and inert gas flushes prior to use. Benzene and toluene were distilled from Na/benzophenone; triethylamine was distilled from Na/K amalgam.³⁶ The prepurified solvents were subsequently transferred and stored under N_2 over fresh drying agents. These solvents were freshly distilled under nitrogen prior to use, thoroughly degassed by repeated freeze-thaw-pump cycles, and transferred to reaction vessels via steel cannulae under a positive pressure of inert gas.

Compounds **1** and **2** were prepared according to the literature procedures.^{2,3,11,12} All of these compounds were purified by Soxhlet extraction and by sublimation as required. Mass spectra were recorded on a JEOL HX110 high-resolution sector instrument utilizing fast atom bombardment (FAB) ionization in a matrix of 3-nitrobenzyl alcohol (NBA). IR spectra ($4000-400\text{ cm}^{-1}$) were collected on a Nicolet Avatar ESP 360 FT-IR spectrophotometer in KBr disks or as dichloromethane solutions (between NaCl plates) at room temperature. Solvent background corrections were made

in all cases. $^1\text{H-NMR}$ (CDCl_3) spectra were acquired on a Bruker DRX-500 spectrometer operating at a ^1H frequency of 500.13 MHz using a 5 mm Nalorac triple-resonance 3-axis gradient probe. Chemical shifts were referenced to residual CHCl_3 at 7.24 ppm.

Compounds **3** and **4** were used as purchased from Aldrich.

2.3 Photoelectron spectroscopy

Photoelectron spectra were recorded using an instrument that features a 36-cm radius, 8-cm gap hemispherical analyzer (McPherson) and custom-designed excitation source, sample cells, and detection and control electronics that have been described in more detail.²⁴ The difference between the argon $^2\text{P}_{3/2}$ ionization at 15.759 eV and the methyl iodide $^2\text{E}_{1/2}$ ionization at 9.538 eV was used to calibrate the ionization energy scale. The argon $^2\text{P}_{3/2}$ ionization also was used as an internal calibration lock of the absolute ionization energy throughout data collection. During data collection the instrument resolution (measured using fwhm of the argon $^2\text{P}_{3/2}$ peak) was 0.020-0.035 eV. All data are intensity corrected with an experimentally determined instrument analyzer sensitivity function.

All samples sublimed cleanly with no detectable evidence of decomposition products in the gas phase or as a solid residue. The potassium and sodium salts of these ligands are hygroscopic and usually crystallize as a dimer with bridging water molecules. Contamination from the water of crystallization was observed in the photoelectron spectrum that disappeared with time due to the evaporation of water. Therefore, upon sublimation only the monomer is likely to be present in the gas phase. The sublimation

temperatures were ($^{\circ}\text{C}$, 10^{-4} Torr, monitored using a "K" type thermocouple passed through a vacuum feedthrough and attached directly to the sample cell) 210° - 225° for compound **1**, 50° - 60° for compound **2**, room temperature (25°) for compounds **3** and **4**.

For the PES data presented in Figures 3.2-3.6, the vertical length of each data mark represents the experimental variance of that point. The valence ionization bands are represented analytically with the best fit of asymmetric Gaussian peaks as described in more detail elsewhere.³⁷ The bands are defined with the position, amplitude, halfwidth for the high binding energy side of the peak, and the halfwidth for the low binding energy side of the peak. The number of peaks used in a fit was based solely on the features of a given band profile. The peak positions and halfwidths are reproducible to about ± 0.02 eV $\sim 3\sigma$). The parameters describing an individual Gaussian peak are less certain when two or more peaks are close in energy and overlap.

2.4 Theoretical Methods

Geometry optimization, SCF (self-consistent field) and molecular orbital calculations were performed using the ADF (Amsterdam density functional theory calculations) package (release 2000.02). Starting geometries were obtained from crystal structures of NaTp¹⁹ and **2**.¹¹ Compound **2** was constructed in SPARTAN. A generalized gradient approximation, with the exchange correction of Becke³⁸ and the correlation correction of Lee *et al.*,³⁹ was used for all density functional calculations. All core levels (up to 2s for K, up to 1s for C, N, B and Na) were treated as frozen orbitals. The calculations employed triple-zeta basis sets with Slater type orbitals and a

polarization function for all elements. Calculations on the ground-state molecules were performed in the spin-restricted mode. Spin-unrestricted Δ SCF (self-consistent field) calculations were performed on the proposed ion states formed by photoionization by removing one electron from the relevant orbital and comparing the total energy with that of the ground state molecule. A linear correction was applied for comparison of the calculated and the observed energies, *i.e.* the calculated Δ SCF energies and orbital energies were shifted by the difference between experimentally obtained and calculated energies of the HOMO.

3.0 Results and Discussions

3.1 Gas-Phase Photoelectron Spectroscopy Studies of Scorpionate Ligands

The gas-phase photoelectron spectra of **1** and **2** recorded with a He I photon source are shown in Figure 3.2. There are several differences between these spectra that result from the changes in substituents on the pyrazole rings. In the ionization energy region greater than ~ 12 eV the main differences between these three spectra are due to the addition or removal of ionizations associated with the C-H σ bonds of the CH₃ substituents, the C-F σ bonds of the CF₃ substituents, or the halogen lone pair ionizations of the CF₃ substituents. For example, the spectrum of **3** contains much intensity in the region of 15-18 eV due to F lone pair ionizations. In general, however, the region of the photoelectron spectra greater than ~ 12 eV gives very little information for these molecules due to the large number of overlapping ionizations present.

The region of the photoelectron spectra with ionization energies below ~12 eV contains the most information that can be used to analyze the electronic differences between these scorpionate ligands. This region of the spectra is shown in more detail in Figure 3.3. The features in this region and our assignments in general agree with those of NaTp and TITp previously reported by Fragala and co-workers.^{30,31} Each of these spectra contain at lowest ionization energy an envelope of ionizations labeled A that is fairly well separated from all other ionizations. The ionizations under bands A can be assigned to the total of six possible linear combinations of the pyrazole π -orbitals, two from each pyrazole ring, that possess one node. In the deconvolutions shown in Figure 3.3 (positions of the Gaussians used in the deconvolutions are listed in Table 3.1), bands A can be modeled with three Gaussians for **1** and **2**. As the substituents are varied the ionizations under band A shift in energy but the spread of the ionizations does not change dramatically, indicating that all the ionizations under band A are approximately shifting by the same amount. If the position of the lowest energy Gaussian that is used to model the band is used as a measure of the shift, the total stabilization of band A from **1** to **2** is 1.98 eV, indicative of a very strong electron withdrawing effect of the trifluoromethyl substituents.

In each of the photoelectron spectra the next group of ionizations that follow band A, and that are labeled bands B and C, are due to the σ_N and σ_{BH} molecular orbitals. According to group theory for scorpionate ligands in C_3 symmetry, the σ_N orbitals transform as e and a sets. The a -symmetry σ_N orbitals have the proper symmetry to overlap with the empty s orbital on K and therefore will be expected to be stabilized

relative to the a -symmetry σ_N orbitals. In Fragala and co-workers previous study on NaTp there were two distinct bands in this energy region, and they assigned the e -symmetry σ_N ionization at lower ionization energy followed by the overlapping a -symmetry σ_N and σ_{BH} ionizations.³⁰ In contrast, the spectra of **1** and **2** reported here all require three Gaussians to model the shape of the ionization envelope in this region.

To aid in the assignment of these ionizations, data were also collected on **1** with a He II excitation source, which will change the relative intensity of ionizations depending upon the atomic character of the molecular orbitals with which they are associated.^{23,40,41} A comparison of the He I and He II spectra of **1** is shown in Figure 3.4. The most distinct difference between the spectra collected with different ionization sources is that the band labeled C decreases in intensity dramatically in the He II spectrum, as would be expected for the σ_{BH} ionization. The assignment of these ionizations of **1** is then that band B is the e -symmetry σ_N ionization, band B' is the a -symmetry σ_N ionization and band C is the σ_{BH} ionization. Some splitting of the e -symmetry σ_N ionizations would be expected if the symmetry is lower than C_3 , but any such splitting is not large enough to be experimentally observed. The σ_N and σ_{BH} ionizations also shift as the substituents on the pyrazole rings are varied. In **2**, band C (σ_{BH}) shifts to higher ionization energy due to the electron withdrawing effect of the trifluoromethyl groups on the pyrazole rings.

Fragala *et al.* have reported changes in the position and the intensity of the σ_N ionizations for unsubstituted MTp as M is changed from Na to Tl.³⁰ They have observed that the a -symmetry σ_N ionization is stabilized in the Tl complex due to the more

covalent interaction of the nitrogen σ -donors orbitals with the softer Tl atom than with the relatively harder Na atom. The ionization of the nitrogen σ -donor orbitals (bands B and B') for Tp* is shifted to higher energy in the photoelectron spectra of molybdenum complexes^{24,25} than for **1**, consistent with a more covalent nature of the interaction with the Mo metal center with the nitrogen σ -donor orbitals as compared to the K⁺ cation. To further evaluate the effect that differences in metals have on the σ -donor abilities of more electron withdrawing scorpionate ligands, a photoelectron spectrum was collected of Na(Tp^{(CF₃)₂) for comparison to K(Tp^{(CF₃)₂). Figure 3.5 shows a stack plot of the close-up spectra of these Na and K adducts of Tp^{(CF₃)₂. A slight shift to higher energy of bands B and B' is observed in Na(Tp^{(CF₃)₂) in comparison to K(Tp^{(CF₃)₂), which is counterintuitive to the expectation that K⁺ complexes should be more covalent than complexes to harder Na⁺. This might be due to the strong electron withdrawing effect of CF₃ in Tp^{(CF₃)₂ resulting in electron deficient nitrogen atoms σ -bonded to the metal. These electron deficient (harder) σ -donor nitrogen atoms can interact better with hard Na⁺ relative to K⁺. The bands A, B and B' are destabilized by 0.1 eV, 0.28 eV and 0.62 eV, respectively, in the photoelectron spectrum of K(Tp^{(CF₃)₂) in comparison to Na(Tp^{(CF₃)₂). A significant destabilization of B' is further evidence of its assignment to a set of symmetric σ -donor nitrogen orbitals, which has the right symmetry to donate electron density into the unfilled symmetric metal *s* orbitals and hence is affected the most by metal substitution.}}}}}}}}

3.3 Computational Results of Scorpionate Ligands

Geometry optimization of NaTp beginning from the reported crystal structure¹⁹

converged without significant changes in the geometry. This ligand geometry was used as a starting point for the geometry optimization of the KTp and **1**. Geometry optimization of **2** started with the crystal structure coordinates.¹¹ A similar pattern of molecular orbitals was calculated for KTp and for compounds **1** and **2**. The results for KTp are generalized and discussed below in detail, with representative molecular orbitals plotted in Figure 3.6. The lowest unoccupied molecular orbital (LUMO), has primarily metal *s* character (Figure 3.6 a), and is well isolated (4.216 eV in KTp) from the filled ligand-based molecular orbitals. The highest occupied and several lower energy molecular orbitals that are closely spaced in energy (HOMO to HOMO-5) are primarily pyrazole- π in character. These orbitals correspond to the ionizations under band A of the photoelectron spectra for **1-2** (Figure 3.2-3.4). The molecular orbital plots for the HOMO and HOMO-1 are shown in Figure 3.6 b and 3.6 c and show that these molecular orbitals primarily consist of the combinations of pyrazole- π orbitals.

Pyrazole- π orbitals are separated by 0.68 eV from the next group of molecular orbitals that comprise mainly the σ -donor nitrogen orbitals of the pyrazole rings. These σ -donor nitrogen orbitals are *e* and *a* symmetry orbitals in the C_3 symmetry. The orbital with the correct symmetry to interact with the metal-*s* orbital (K 4s) is plotted in Figure 3.6 d. A third type of calculated molecular orbital is 0.68 eV more stable than the σ -donor combination of the nitrogen orbitals discussed above. This molecular orbital is σ_{BH} in character (Figure 3.6 e) and corresponds to the ionization occurring under band C in Figures 3.2-3.5 for **1** and **2**.

The computed molecular orbital energies and ΔSCF estimate of calculated

ionization energies for removal of an electron from **1** and **2** are reported in Table 3.1, and plots of the HOMO of each of these molecules are shown in Figure 3.7. The substitution of CF_3 in **2** results in a very strong electron withdrawing effect and stabilizes the pyrazole- π based molecular orbitals (HOMO) by 2.27 eV relative to **1**. This calculated shift compares very well with the corresponding experimentally obtained value of ~ 2.0 eV. The σ_{BH} and σ_{N} (a -symmetry) orbitals for **1** and **2** also are plotted in Figure 3.9 for comparison. The methyl or trifluoromethyl substitutions, for **1** and **2**, at the 3 and 5 positions of pyrazole ring do not significantly change the nature of the σ_{BH} and σ_{N} orbitals.

Finally It is noted that the Mulliken charges at the potassium atom for compounds **1**, KTp, and **2** (0.88, 0.91 and 0.99, respectively) correspond very well to the electron withdrawing properties of the substitutions in these compounds. The Mulliken charge at the metal center in compound **2** (0.99) contrasts with that of 0.88 in **1** and confirms the experimental findings of us and others¹¹ of a very electropositive metal center in the metal adducts of $\text{Tp}^{(\text{CF}_3)_2}$. Thus, the homoscorpionates discussed here offer a variety of possibilities for the modification of the steric and the electronic properties by variations of the substitution at the 3, 4 and 5 positions of the pyrazole rings.

3.4 Photoelectron Spectroscopic and Computational Studies of Ene-1,2-dithiolene Ligands

The He I and He II photoelectron spectra of ene-1,2-dithiolene ligands **3** and **4** are shown in Figure 3.8 in the approximate energy range 8-11.0 eV and their peak positions

are given in Table 3.1. The 1, 2-benzenedithiolene being a prototype aryldithiolene ligand, our discussion of the electronic structure of the dithiolene ligands will start with this ligand. A simplified molecular orbital picture for 1, 2-benzenedithiol is shown in Figure 3.9. The valence orbitals that must be considered here are benzene e_{1g} and symmetric and antisymmetric combinations of sulfur out of plane orbitals (S_{π}^{+} and S_{π}^{-}). The density functional theoretical calculations and photoelectron spectroscopic results done in this work (*cf.* $Cp_2Ti(bdt)$ in Chapter 8) and by others⁴² show that the highest occupied molecular orbital (HOMO) has substantial S_{π}^{+} character and is antibonding in nature between S_{π}^{+} and C_{π}^{+} (out of plane or π orbitals of C=C) of the benzene ring. Thus the S_{π}^{+} orbital is destabilized the most due to an effective overlap from the C_{π}^{+} orbital and is set at an appropriate energy to interact with the transition metal d orbitals. The ionization bands, labeled as 1, 1', 2 and 2', in the photoelectron spectrum can be assigned to the molecular orbitals obtained theoretically and are shown in Figure 3.10. In the He II source, the ionizations assigned to the molecular orbital with sulfur character decrease in intensity. Therefore, all four of these occupied frontier orbitals must decrease in intensity in He II ionization. This intensity change is hard to observe in the absence of an ionization band in this energy range shown in Figure 3.8, that remains unchanged between He I and He II sources. A relative intensity change has been observed in the spectra of **4** and is discussed below.

Similarly, the first four ionization bands, labeled as 1, 1', 2 and 2', in the lower energy region of the photoelectron spectra of **4** (Figure 3.8) are assignable to the symmetric and antisymmetric combinations of sulfur out of plane orbitals (S_{π}^{+} and S_{π}^{-}).

The substitutions of the Cl at 3 and 6 positions of the benzenedithiolene will add some chlorine character to the antisymmetric S_{π}^{-} orbital (HOMO-1 and HOMO-2). No chlorine character is expected for the HOMO and HOMO-3 orbitals that have a nodal plane going through 3 and 6 positions of the 3, 6-dichloro-1,2-benzenedithiolate ligand. A significant decrease in the intensity of band 2' is observed in the He II source that is consistent with the presence of the chlorine character in the corresponding molecular orbital (HOMO-2). A further exploration of the role of "ene" in raising the energy of the S_{π}^{+} orbitals will be presented in Chapter 8, where it will be shown that the energy ordering of S_{π}^{+} and S_{π}^{-} is reversed in the absence of the "ene" functionality.

4.0 Conclusions

The general shape of the low energy ionizations bands A, B, and C in the photoelectron spectra of **1** and **2**, is not greatly effected by the nature of the metal ions as reported here and by others.³¹ However, substitutions at the 3, 4 and 5 positions of the pyrazole ring can shift the ionization energies of the bands significantly, as especially shown by the CF_3 substitutions.

The scorpionates discussed in this work are coordinated to the metal through the nitrogen atoms of the pyrazole rings and this σ -bonding is modulated by electron density at the metal center or *vice versa*. The electronic structure of scorpionate ligands presented here includes distinct assignments of σ_{BH} and σ_N (*a* and *e*-symmetry) orbitals confirmed experimentally for the first time. This will help in understanding the

electronic structure of scorpionate-based transition metal complexes utilized in bioinorganic modeling and organometallic catalysis. The shift in the positions of band B can be an indicator of the extent of σ -bonding of these scorpionate ligands upon coordination with transition metals and will be a topic of discussion in later studies.⁴³ The electronic structure studies of enedithiolate ligands show that they have a symmetric combination of the sulfur out of plane orbitals as their highest occupied molecular orbital.

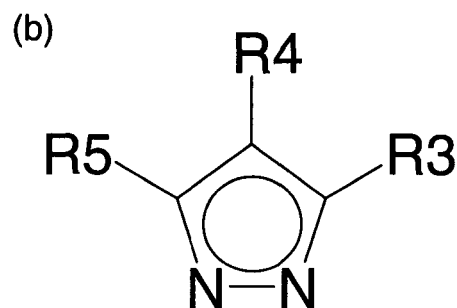
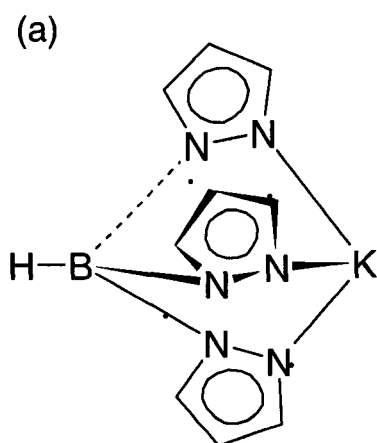
Table 3.1. Experimental ionization energies (I.E.), calculated absolute orbital eigenvalues ($-\epsilon_i$) and calculated Δ SCF first ionization energies of compounds **1-3** and experimental ionization energies for **4** (all values in eV).

Experimental I.E.	Calculated $-\epsilon_i$ (Shifted) ^b	($-\epsilon_i$) HOMO	Δ SCF	Label and Assignment
K(Tp*) (1)				
7.63-8.45 ^a	7.63-8.08	4.66	6.66	Band A, Pyrazole- π
9.51, 9.99	8.93-9.31			Band B, σ N
10.58	9.88			Band C, σ BH
K(Tp^{(CF₃)₂) (2)}				
9.61-10.55 ^a	9.61-10.13	6.93	8.78	Band A, Pyrazole- π
11.26, 11.88	10.66-11.23			Band B and B', σ N
12.44	11.88			Band C, σ BH
H₂bdt (3)				
8.39	8.39	5.39	7.90	$S\pi^+$, $C\pi^+$ antibonding
8.99	8.66			$S\pi^-$, $C\pi^-$ antibonding
9.41	9.80			$S\pi^-$, $C\pi^-$ bonding
10.33	10.14			$S\pi^+$, $C\pi^+$ bonding
H₂bdtCl₂ (4)^c				
Experimental I.E.		Label and Assignment		
8.55		$S\pi^+$ antibonding		
8.86		$S\pi^-$ antibonding		
10.37		$S\pi^-$ bonding		
10.78		$S\pi^+$ bonding		

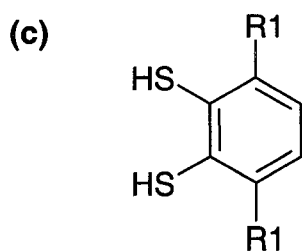
^a Range of experiment I.E. values for Band A are taken from the positions of Gaussians used to deconvolute the data. This does not imply that these values are vertical ionization energies.

^b Eigenvalues were shifted so the HOMO eigenvalue matches the position of the lowest energy Gaussian used to deconvolute the experimental data.

^c Only the experimental values of ionizations and their assignments are presented for **4**.



Tp : R3, R4, R5 = H
 Tp^{CH₃} or Tp* (1) : R3, R5 = CH₃, R4 = H
 Tp^{(CF₃)₂} (2) : R3, R5 = CF₃, R4 = H



H₂bdt (3) : R1, R2 = H
 H₂bdtCl₂ (4) : R1, R2 = Cl

Figure 3.1. (a) A generic tripodal scorpionate ligand hydrotris(pyrazol-1-yl)borate; KTp. (b) Examples of substitutions at the 3 and 4 positions of the pyrazole ring. These substitutions retain the C_3 symmetry of the adducts. (c) A generic aryldithiolate ligand.

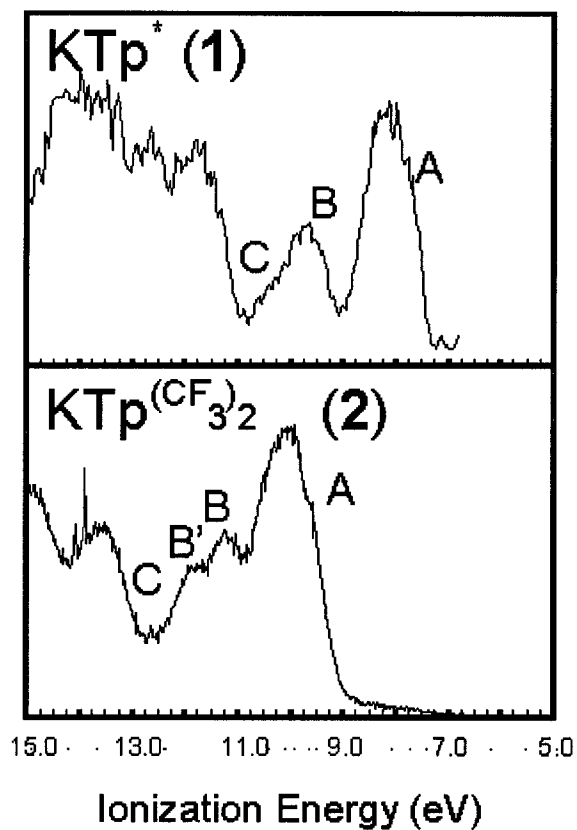


Figure 3.2. The He I full photoelectron spectra of the potassium salts of hydrotris(3,5-dimethylpyrazol-1-yl)borate, Tp^* (1) and hydrotris(3,5-bis(trifluoromethyl)pyrazol-1-yl)borate, $\text{Tp}^{(\text{CF}_3)_2}$ (2). Both of the spectra have three general features labeled as bands A, B and C in the lower energy region. These bands are assigned as A: pyrazole- π ; B, B': σ_{N} of the pyrazole nitrogen orbitals; C: σ_{BH} of the trispyrazole borate ligands.

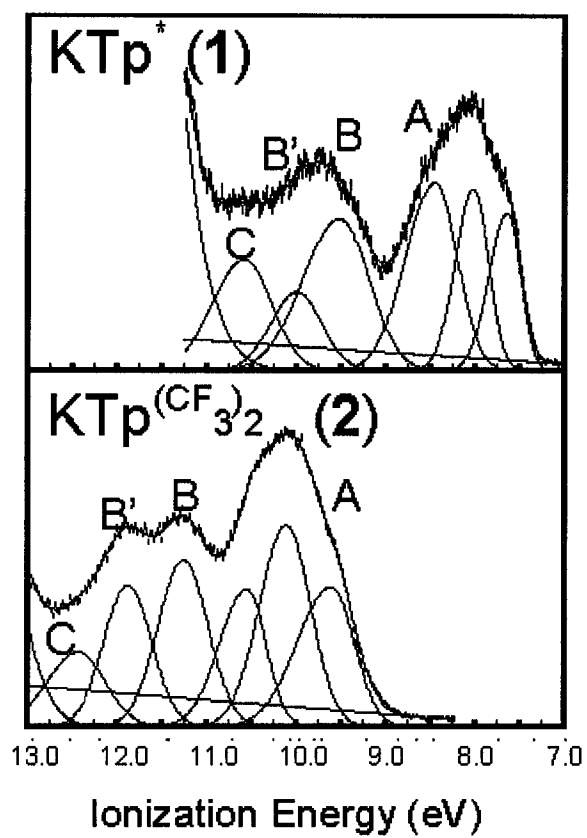


Figure 3.3. The He I close up photoelectron spectra of $\text{KTp}^* (1)$; and $\text{KTp}^{(\text{CF}_3)_2} (2)$. Bands A, B and C are assigned as in Figure 3.2.

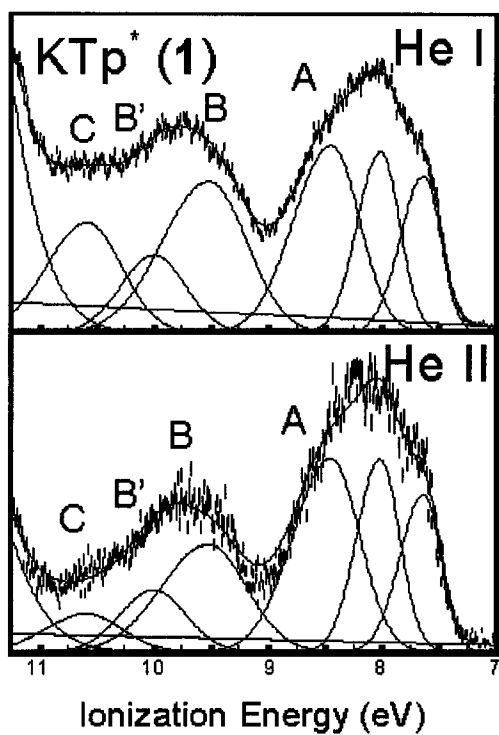


Figure 3.4. The He I and He II close up spectra of KTp*. Ionizations associated with molecular orbitals with hydrogen contributions decrease in relative intensity in the He II source.

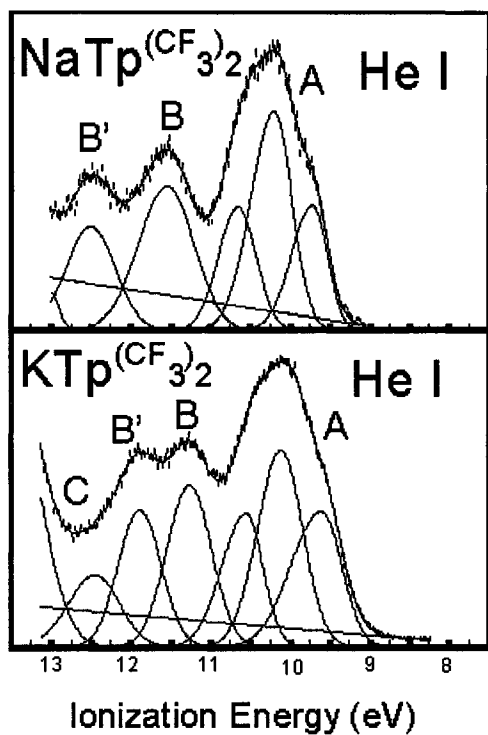


Figure 3.5. He I close-up photoelectron spectra of NaTp(CF₃)₂ (top) and KTp(CF₃)₂ (bottom). The bands are assigned as A: pyrazole- π ; B, B': σ_N (e -symmetric and a symmetric combinations, respectively) of the pyrazole nitrogen orbitals; C: σ_{BH} of the trispyrazole borate ligand.

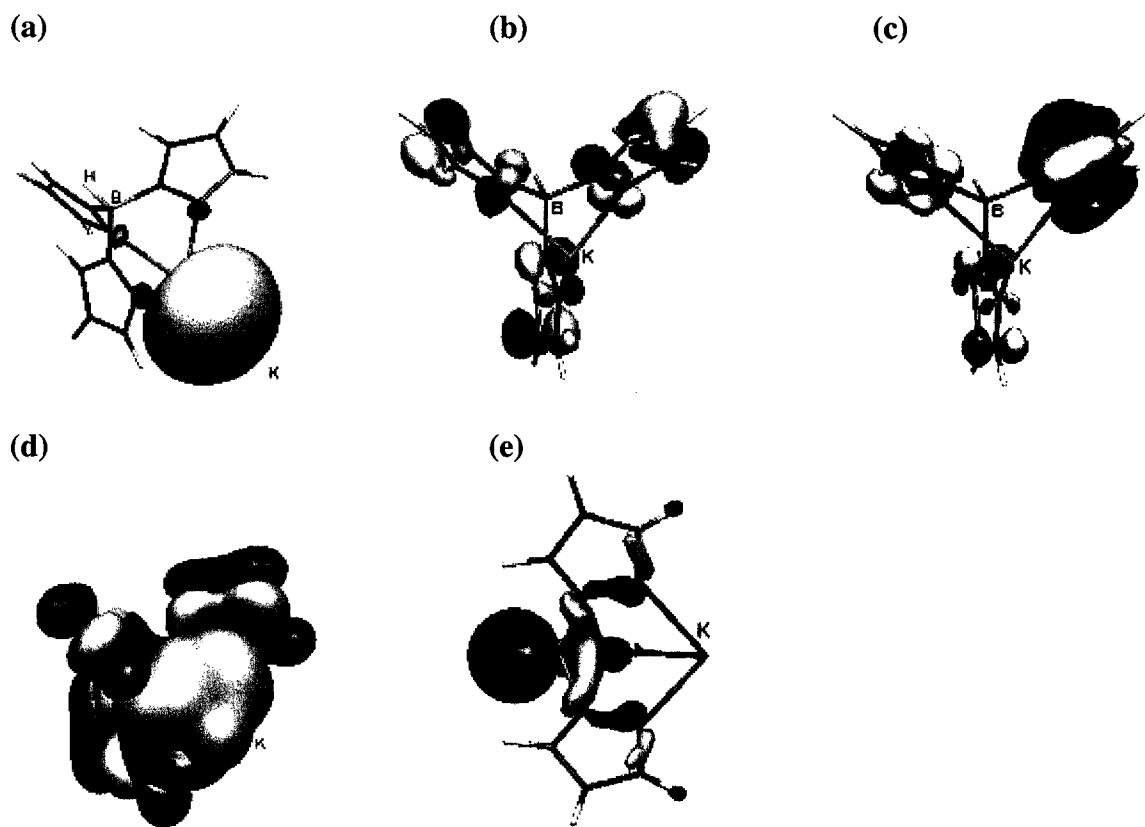


Figure 3.6. Molecular orbital plots (at 0.05 cutoff levels unless stated) of KTp. (a) Lowest occupied molecular orbital (LUMO) is primarily metal in character (at 0.03 cutoff levels). (b) The highest occupied molecular orbital (HOMO) is primarily pyrazole- π in character. (c) HOMO-1 is again pyrazole- π in character. (d) An example of the pyrazole σ -donor (σ_N) molecular orbital (at 0.008 cutoff levels). (e) The hydrotris(pyrazol-1-yl)borate σ_{BH} molecular orbital.

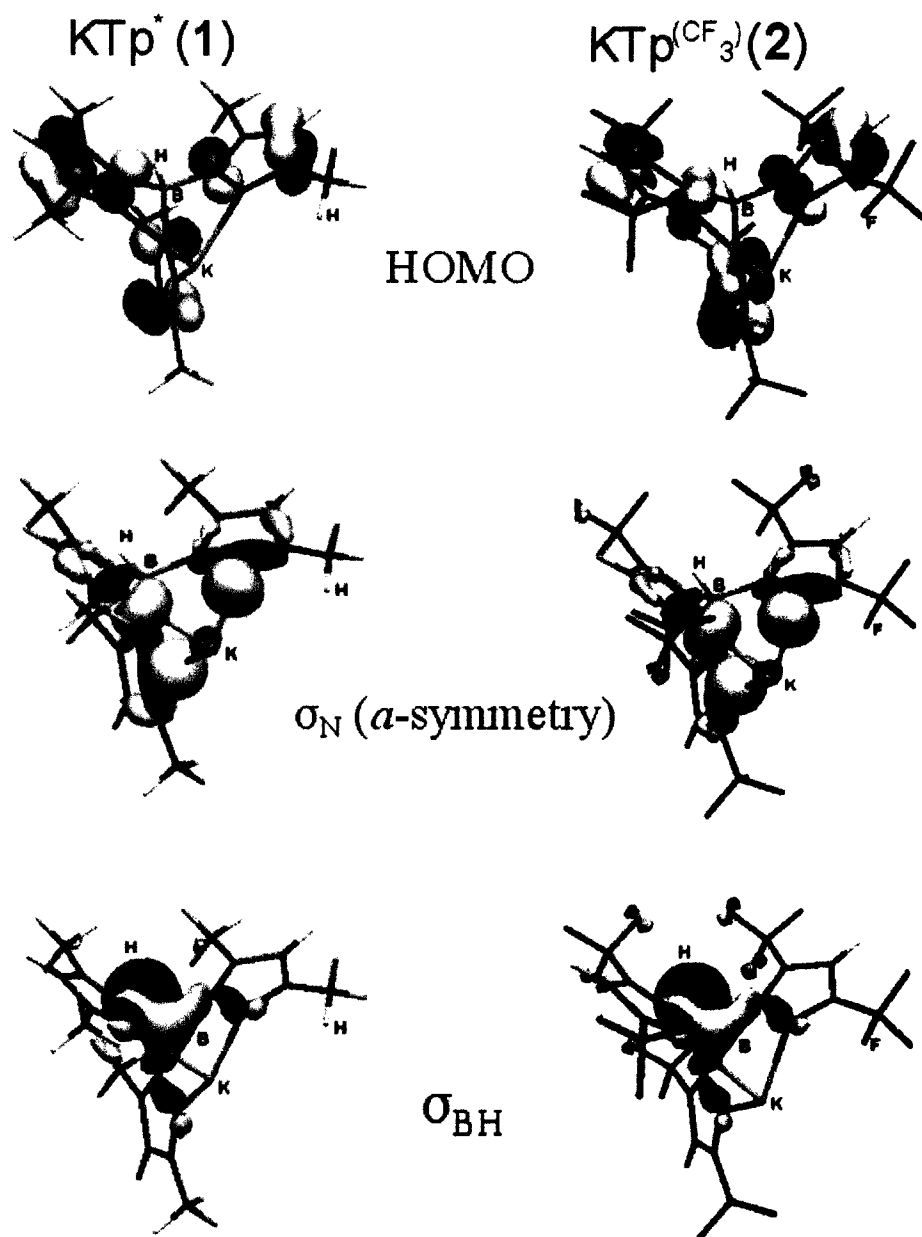


Figure 3.7. Comparison of the highest occupied molecular orbitals (HOMO), σ_N (α -symmetric) and σ_{BH} orbitals of compounds 1-3 (at 0.05 cutoff levels).

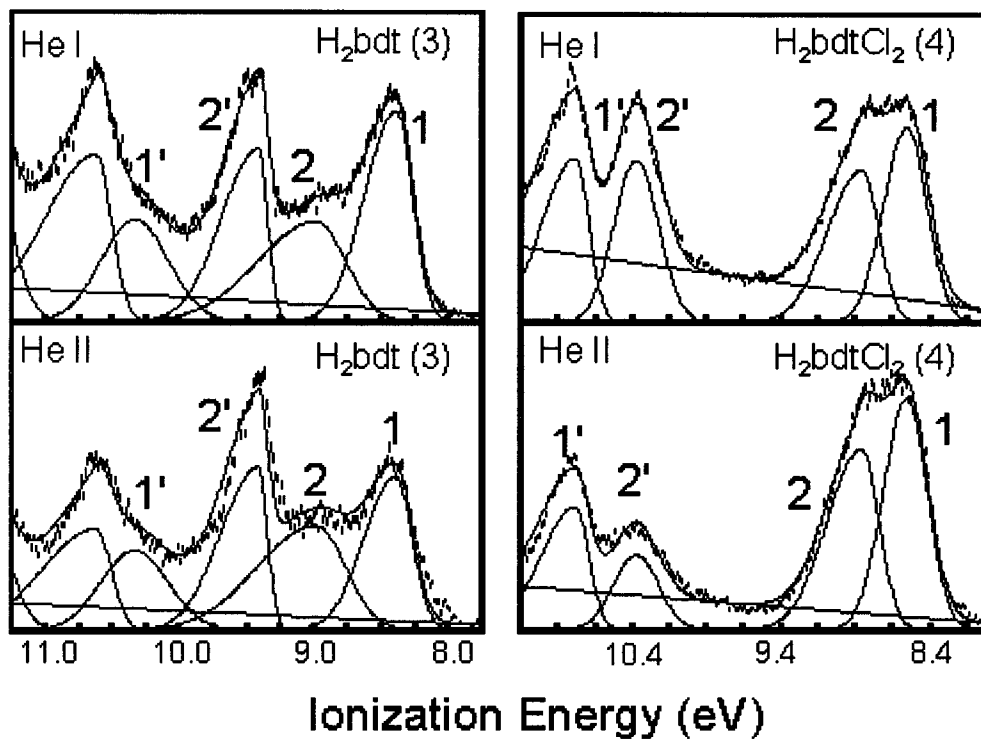


Figure 3.8. The He I full photoelectron spectra of 1, 2-benzenedithiolate (H_2bdt ; **3**) and 3, 6-dichlorobenzene-1, 2-dithiolate (H_2bdtCl_2 ; **4**). Both of the spectra have four first ionizations labeled as bands 1, 2, 2', 1' in the lower energy region. These bands are assigned as 1, 1': bonding and antibonding orbitals of S_{π^+} ; 2, 2': bonding and antibonding orbitals of S_{π^-} (where S_{π^+} and S_{π^-} = symmetric and antisymmetric combinations of dithiolate out of plane orbitals)

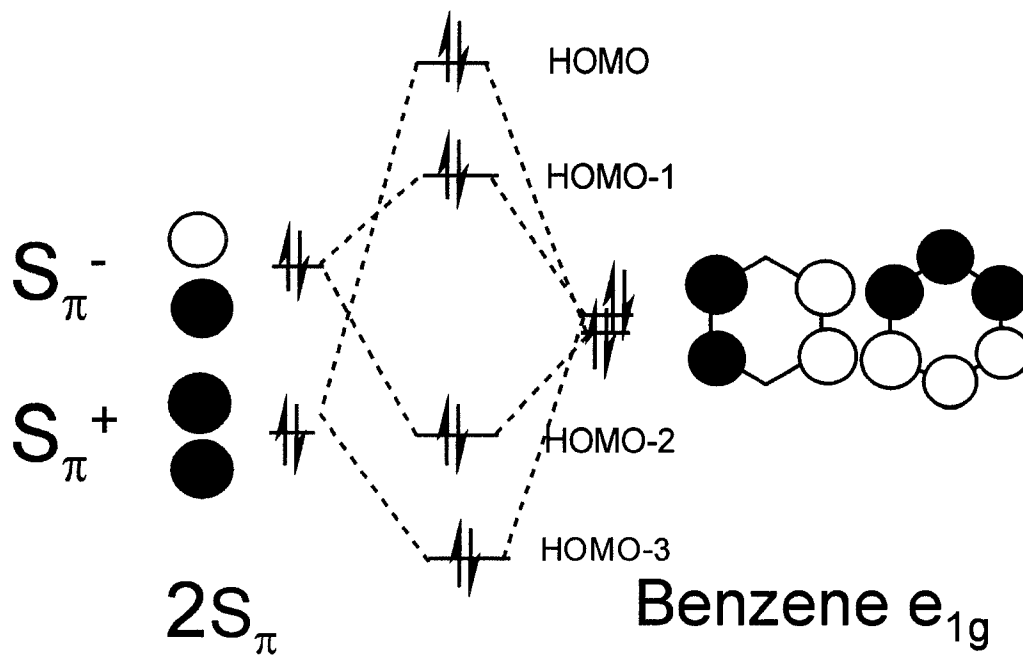


Figure 3.9. The molecular orbital diagram of 1, 2-benzenedithiol. The S_{π}^{+} orbital is raised in energy due to an effective overlap from C=C π -orbital of benzene.

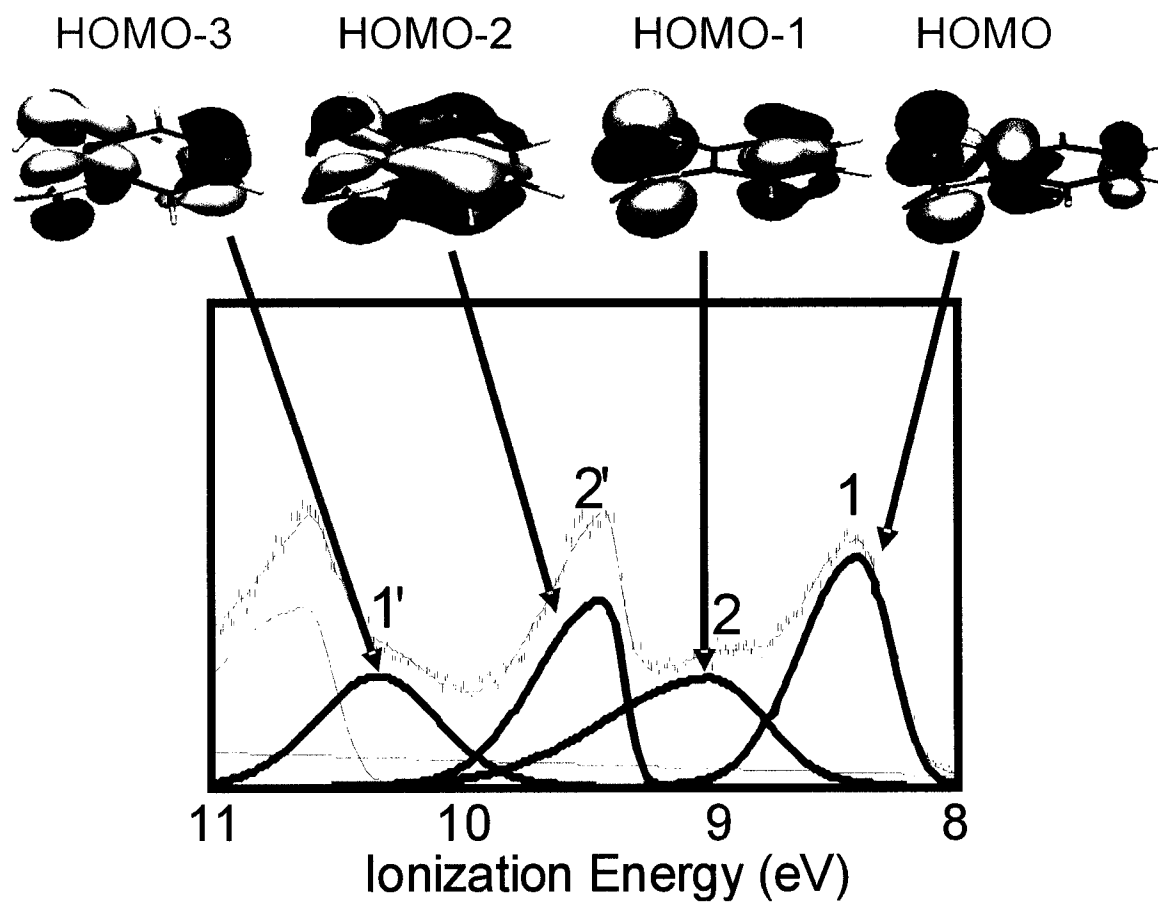


Figure 3.10. The one-to-one correlation of first four ionization bands with theoretically calculated frontier molecular orbitals of 1, 2-benzenedithiol. Bands 1, 1', 2, 2' have been assigned as described in Figure 3.8.

5.0 References

1. Swiatoslav Trofimenko. *Scorpionates-The Coordination Chemistry of Polypyrazolylborate Ligands*; Imperial College Press: London, 1999.
2. Trofimenko, S. *J. Am. Chem. Soc.* **1967**, *89* (13), 3170-7.
3. Trofimenko, S. *J. Am. Chem. Soc.* **1967**, *89* (24), 6288-94.
4. Dhawan, I. K.; Pacheco, A.; Enemark, J. H. *J. Am. Chem. Soc.* **1994**, *116*, 7911-7912.
5. Dhawan, I. K.; Enemark, J. H. *Inorg. Chem.* **1996**, *35*, 4873-4882.
6. Inscore, F. E.; Rubie, N.; Joshi, H. K.; Kirk, M. L.; Enemark, J. H. *manuscript submitted to Inorg. Chem.*
7. Trofimenko, S. *Abstracts of Papers, 225th ACS National Meeting, New Orleans, LA, United States, March 23-27, 2003* **2003**, INOR-008.
8. Joshi, H. K.; Inscore, F. E.; Schirilin, J. T.; Dhawan, I. K.; Carducci, M. D.; Bill, T. G.; Enemark, J. H. *Inorg. Chim. Acta* **2002**, *337*, 275-286.
9. Schirilin, J. T.; Inscore, F. E.; Joshi, H. K.; Dhawan, I. K.; Enemark, J. H. *Abstracts of Papers - American Chemical Society* **2001**, *221st*, INOR-505.
10. Joshi, H. K.; Cooney, J. J. A.; Inscore, F. E.; Gruhn, N. E.; Lichtenberger, D. L.; Enemark, J. H. *Proc. Natl. Acad. Sci. USA* **2003**, *100* (7), 3719-3724.
11. Dias, H. R.; Jin, W.; Kim, H. J.; Lu, H. L. *Inorg. Chem.* **1996**, *35* (8), 2317-28.
12. Dias, H. R.; Kim, H. J. *Organometallics* **1996**, *15* (25), 5374-5379.
13. Hu, Z.; Gorun, S. M. *Inorg. Chem.* **2001**, *40* (4), 667-671.

14. Tellers, D. M.; Skoog, S. J.; Bergman, R. G.; Gunnoe, T. B.; Harman, W. D. *Organometallics* **2000**, *19* (13), 2428-2432.
15. Jones, W. D.; Feher, F. J. *J. Am. Chem. Soc.* **1982**, *104* (15), 4240-2.
16. Te Velde, G.; Bickelhaupt, F.; Baerends, E.; Fonseca Guerra, C.; Van Gisbergen, S.; Snijders, J.; Ziegler, T. *J. Comp. Chem.* **2001**, *22* (9), 931-967.
17. Bergman, R. G.; Cundari, T. R.; Gillespie, A. M.; Gunnoe, T. B.; Harman, W. D.; Klinckman, T. R.; Temple, M. D.; White, D. P. *Organometallics* **2003**, *22* (11), 2331-2337.
18. Lichtenberger, D. L.; Elkadi, Y.; Gruhn, N. E.; Hughes, R. P.; Curnow, O. J.; Zheng, X. *Organometallics* **1997**, *16* (24), 5209-5217.
19. Reglinski, J.; Garner, M.; Cassidy, I. D.; Slavin, P. A.; Spicer, M. D.; Armstrong, D. R. *J. Chem. Soc., Dalton Trans.* **1999**, *13*, 2119-2126.
20. Inscore, F. E.; McNaughton, R.; Westcott, B.; Helton, M. E.; Jones, R.; Dhawan, I. K.; Enemark, J. H.; Kirk, M. L. *Inorg. Chem.* **1999**, *38*, 1401-1410.
21. Carducci, M. D.; Brown, C.; Solomon, E. I.; Enemark, J. H. *J. Am. Chem. Soc.* **1994**, *116*, 11856-11868.
22. McMaster, J.; Carducci, M. D.; Yang, Y.-S.; Solomon, E. I.; Enemark, J. H. *Inorg. Chem.* **2001**, *40*, 687-702.
23. Green, J. C. *Acc. Chem. Res.* **1994**, *27* (5), 131-7.
24. Westcott, B. L.; Gruhn, N. E.; Enemark, J. H. *J. Am. Chem. Soc.* **1998**, *120*, 3382-3386.

25. Joshi, H. K.; Inscore, F. E.; Schirlin, J. T.; Dhawan, I. K.; Carducci, M. D.; Bill, T. G.; Enemark, J. H. *Inorg. Chim. Acta* **2002**, 337, 275-286.
26. Helton, M. E.; Gruhn, N. E.; McNaughton, R. L.; Kirk, M. L. *Inorg. Chem.* **2000**, 39 (11), 2273-2278.
27. Joshi, H. K.; Gruhn, N. E.; Lichtenberger, D. L.; Enemark, J. H. *manuscript in preparation*.
28. Craddock, S.; Findlay, R.; Palmer, M. *Tetrahedron* **1973**, 29 (14), 2173-81.
29. Downs, A. J.; Egdell, R. G.; Orchard, A. F.; Thomas, P. D. *J. Chem. Soc., Dalton Trans.* **1978**, 12, 1755-61.
30. Bruno, G.; Ciliberto, E.; Fragala, I.; Granozzi, G. *Inorg. Chimi. Acat.* **1981**, 48 (1), 61-4.
31. Bruno, G.; Centineo, G.; Ciliberto, E.; Di Bella, S.; Fragala, I. *Inorg. Chem.* **1984**, 23 (13), 1832-6.
32. McCleverty, J. *Prog. Inorg. Chem.* **1968**, 10, 49-221.
33. Eisenberg, R. *Prog. Inorg. Chem.* **1970**, 12, 295-369.
34. Ferretti, A. *Org. Synth.* **1962**, 42, 54-6.
35. Giolando, D. M.; Kirschbaum, K. *Synthesis* **1992**, 5, 451-2.
36. W. Armarego, D. Perrin, *Purification of Laboratory Chemicals, 4th ed.*, Pergamon Press, New York, **1997**, p. 512.
37. Lichtenberger, D. L.; Copenhaver, A. S. *J. Electron Spectrosc. Relat. Phenom.* **1990**, 50 (4), 335-52.
38. Becke, A. D. *Phys. Rev. A.* **1988**, 38, 3098-3100.

39. Lee, C.; Yang, W.; Parr, R. G. *Phys. Rev. B.* **1988**, *37*, 785.
40. Yeh, J.; Lindau, I. *At. Data Nucl. Data Tables* **1985**, *32* (1), 1-155.
41. Glass, R. S.; Gruhn, N. E.; Lichtenberger, D. L.; Lorance, E.; Pollard, J. R.; Birringer, M.; Block, E.; DeOrazio, R.; He, C.; Shan, Z.; Zhang, X. *J. Am. Chem. Soc.* **2000**, *122* (21), 5065-5074.
42. Guimon, C.; Pfister-Guillouzo, G.; Meunier, P.; Gautheron, B.; Tainturier, G.; Pouly, S. *J. Organomet. Chem.* **1985**, *284* (3), 299-312.
43. Joshi, H. K.; Inscore, F. E.; Gruhn N. E.; Enemark, J. H. *manuscript in preparation.*

CHAPTER 4: Experimental and Theoretical Evaluation of Metal- Halide Interactions in (Tp*)MoOX₂ Compounds (X = F, Cl, Br, I) by Gas-Phase Photoelectron Spectroscopy and Density Functional Theory; Molecular Structure of (Tp*)MoOBr₂

1.0 Introduction

Transition metal halides are the basic building blocks of inorganic compounds that impact our daily lives as these compounds are some of the most common catalysts used in industry.¹ Variation in the halide ligand can retain the nature of the system, but can fine tune both the reactivity and selectivity of these catalysts for a given transformation.¹ Study of metal-halide (M-X) interactions has been an integral part of the extensively studied electronic structure and bonding in these compounds. The comparisons of the σ -donor and the π -donor abilities of different halides to metals is one of the most interesting research questions addressed in these studies. Substantial literature precedent^{2,3} is available, based on IR spectroscopic data,⁴⁻⁶ electrochemical potentials,⁷ chemical reactivity,^{4,5,8} and theoretical calculations,^{4,9,10} for suggesting that among the halides, it is the fluoride ligand that appears to be the most efficient electron pair donor towards the metal. The nature of this interaction remains highly controversial, however, Holland et al.^{11,12} have come up with a different theory based on Drago's E-C bonding schemes,¹ where M-X bonding is primarily explained in terms of electrostatic (E) and covalent (C) contributions. In some late transition metal compounds destabilizing π interactions were not considered to be the dominant effect in M-X bonding.^{11,12}

Photoelectron spectroscopy and theoretical calculations have been used to study metal-halide interactions in the carbonyl adducts of Mn, Re, Fe, Cr, W. For example the

electronic structure and bonding studies of $M(\text{CO})_5\text{X}$ ($M = \text{Mn, Re}$ and $\text{X} = \text{Cl, Br, I}$, and/or H) type compounds by Fenske, DeKock, Hall, and Lichtenberger,¹³⁻¹⁵ etc. One of the frontier orbitals, the highest occupied molecular orbital (HOMO), in these compounds is primarily both metal- d and halogen- π in character. Green et al. have reported photoelectron spectroscopic studies of $\text{V}(\eta^5\text{-C}_5\text{H}_5)_2\text{X}$ ($\text{X} = \text{Cl, Br, I}$) in He I and He II ionization sources and found evidence for weak but significant π interactions between metal d and halogen p orbitals in these compounds.¹⁶ Lichtenberger et al. have also reported gas-phase valence photoelectron spectroscopic studies of $\text{CpRe}(\text{NO})(\text{L})\text{X}$ ($\text{Cp} = \eta^5\text{-C}_5\text{H}_5$ and $\eta^5\text{-C}_5(\text{CH}_3)_5$; $\text{L} = \text{CO, P}(\text{C}_6\text{H}_5)_3$; $\text{X} = \text{Cl, Br, I}$) and found extensive metal-halogen mixing in the ionizations and very delocalized electronic structure throughout the metal-ligand system.¹⁵ They reported increasing halogen character of the $\text{M-X } \pi^*$ orbitals in going from the chloride to the iodide compound, however, the first three ionizations remain mostly metal throughout. This is in contrast to the previously studied $\text{Re}(\text{CO})_5\text{X}$ compounds,¹⁴ where the first ionization shifted from predominantly metal to predominantly halogen in proceeding from $\text{X} = \text{Cl}$ to $\text{X} = \text{I}$. Detailed electronic structure studies of titanocene, zirconocene and hafnocene halides suggest that iodine behaves as both a strong σ - and π -donor.¹⁷

Similar studies have also been reported on the dihalide compounds of the type $\text{M}(\text{CO})_4\text{X}_2$. For example Levenson et al. reported the photoelectron spectroscopy of $\text{Fe}(\text{CO})_4\text{X}_2$ ($\text{X} = \text{Br, I}$) and found that ionizations from d orbitals appear at higher energy than those for $\text{Mn}(\text{CO})_5\text{X}$ compounds.¹⁸ The valence orbitals of $\text{M}(\text{CO})_4\text{X}_2$ transition metal derivatives are well known.¹⁹ Similar examples of the electronic structure studies

exist for metals of group VI. Morris-Sherwood et al. have reported photoelectron spectroscopy and molecular orbital calculations on $(\eta^5\text{-C}_5\text{H}_5)\text{M}(\text{NO})_2\text{X}$ ($\text{M} = \text{Cr}, \text{W}$ and $\text{X} = \text{Cl}, \text{Br}, \text{I}$).²⁰ They compared the ionization energies of metal-halogen σ bonds and suggested that W-X bonds are stronger than Cr-X bonds, which is consistent with the relative metal-chloride bond lengths from X-ray data. A density functional study of open shell cyclopentadienyl-molybdenum(II) compounds by Cacelli et al. comparing Mo-X ($\text{X} = \text{F}, \text{Cl}, \text{Br}, \text{I}$) π bonding found that the π -stabilizing ability decreases in the order $\text{F} > \text{Cl}, \text{Br}, \text{I} > \text{H}$.²¹

The experimental and theoretical studies as a function of halogen atoms on the well known $(\text{Tp}^*)\text{MoOX}_2$ ($\text{X} = \text{F}$ (**1**), Cl (**2**), Br (**3**), I (**4**)) series of compounds (Figure 4.1(a)) for studying their electronic structure and bonding, has been carried out.²² These compounds are of additional interest because the axial ligation of an oxo group to the biologically relevant Mo center is reminiscent of the spectator oxygen atom bound to molybdenum in pyranopterin dithiolate enzymes.²³ The metal-oxo interactions of group VI metals (Mo, W) has been previously studied using photoelectron spectroscopy of $\text{Mo}(\eta^5\text{-C}_5\text{H}_4\text{Me})_2\text{O}$, $[\text{W}(\eta^5\text{-C}_5\text{H}_4\text{Me})_2\text{O}]$ and $[\text{W}(\eta^5\text{-C}_5\text{Me}_5)_2\text{O}]$ compounds,²⁴ but compounds 1-3 possess a formally Mo(V) center with apical oxo and equatorial monoanionic halide ligands. The presence of this special axial geometry of the $\text{Mo}\equiv\text{O}$ unit, and the formal oxidation state Mo(V) of the metal center have lead to the studies of these compounds (**1-3**) as first generation spectroscopic models of molybdenum enzymes by a variety of physical methods, including electron paramagnetic resonance (EPR).²⁵ The related Mo(V) compounds, $(\text{Tp}^*)\text{MoO}(\text{alkoxide})_2$ and $(\text{Tp}^*)\text{MoO}(\text{dithiolate})$, have

been studied using photoelectron spectroscopy and metal based ionizations are clearly observed at lower ionization energies.²⁶⁻³¹ These compounds are stabilized in the Mo(V) oxidation state in a pseudo-octahedral geometry where the scorpionate ligand (Tp*) facially coordinates the metal. The photoelectron spectra of these compounds have a prominent, but now well understood signature of ionizations occurring from Tp*.³²⁻³⁴ In the photoelectron spectroscopy of K(Tp*), the ionizations starting from the lowest energy region were assigned to pyrazole- π based orbitals followed by σ_N , and σ_{BH} .³⁴

The changes in the nature of the pyranopterindithiolates due to hydrogen bonding³⁵ and dithiolate folding³⁰ can change in the electronic properties of the dithiolate sulfur atoms and might play a role in modulating the effective nuclear charge (Z' eff) on the metal center during the course of catalysis and/or determining differences among the various pyranopterin Mo enzymes. Metal-sulfur covalency has been an interesting area of research in this regard. The purpose of this study is to use gas-phase photoelectron spectroscopy to understand the metal-halide covalency in oxo-Mo(V) centers. This study is also an essential benchmark for understanding the electronic structure of oxomolybdenum-dithiolate based small molecular models for the pyranopterindithiolate-containing enzyme active sites. In contrast to remote ligand substitution in (Tp*)MoO(dithiolate) compounds,^{29,31,36-38} the (Tp*)MoOX₂ system provides flexibility of ligand substitutions as different halide ligands (X) are easily substituted, allowing the study of the influence of halogens on the metal-halide interactions. The differences in the polarizabilities and electronegativities of the halogens can lead to appreciable changes in Z' eff of the metal center. This series of (Tp*)MoOX₂ compounds provides an

opportunity to investigate the effects of combining a given set of σ -donors (N from pyrazole rings), with both σ -donor and π -donor halides and contains an invariant monooxomolybdenum core. There is a little previous literature on gas-phase photoelectron spectroscopy studies of metal-fluoride interactions. To our knowledge, this study is the first direct investigation of metal-fluoride interactions using photoelectron spectroscopy.

A very strong interaction between molybdenum and the axial oxo ligand results in the splitting of the t_{2g} orbitals (d_{xy} and d_{xz} , d_{yz}).^{28,36,38-42} If one considers the Mo \equiv O bond parallel to the molecular z axis, then the d_{xz} and d_{yz} orbitals will be destabilized due to the strong σ and π -donor oxo ligand. As a result metal in-plane orbital (d_{xy} in xy plane) is the most stabilized valence metal d orbital. A simplified molecular orbital scheme for the orbitals in the xy plane of (Tp*)MoOX₂ molecule is shown in Figure 4.1(b). The orbitals in this plane that must be considered are metal in-plane (d_{xy} or $d_{x^2-y^2}$) and combinations of halogen in plane orbitals (p_x and p_y). A general expression for bonding and antibonding molecular orbital is $\pi = c_1 d_{xy} + c_2 \pi_s$, where d_{xy} represents a metal orbital, π_s is a symmetric combination of halogen in-plane p -orbitals and c_1 and c_2 are two constants. The magnitudes of constants c_1 and c_2 will determine the contributions of the fragment orbitals to these interactions and hence the extent of mixing in each of the metal - halide interactions in this plane. The electronegativity of the halogen atom stabilizes all the molecular orbitals, while the overlap between the metal and halogen orbitals leads to the destabilization of the antibonding molecular orbitals and hence a trend opposite to the one predicted on the basis of the electronegativity. In some cases it has been observed that the overlap effect is sufficiently large that the first ionization energies are

significantly destabilized. This later phenomenon, known as the inverse halogen effect,⁴³⁻⁴⁸ has recently been observed on Cp*Fe(dppe)X series (X = F, Cl, Br, I) and studied employing thermodynamics, NMR and Mössbauer spectroscopy, structural and theoretical approaches.⁴⁹ A similar theory has been proposed²⁸ for oxo-Mo monodithiolate compounds where a pseudo σ -bonding interaction that effectively couples the Mo d_{xy} redox orbitals into the sulfur in-plane orbitals of the coordinated dithiolate has been suggested. This pseudo σ interaction is present in compounds **1-4**, and might aid in understanding of this common electronic structure theme of oxo-Mo dithiolate centers in enzymes.^{28,30,50} The antibonding orbital discussed above for (Tp*)MoOX₂ system is partially occupied and will be referred to as the HOMO (highest occupied molecular orbital).

2.0 Experimental and Theoretical Section

2.1 Abbreviations

Tp*, hydrotris(3,5-dimethylpyrazol-1-yl)borate; Tp, hydrotris(pyrazol-1-yl)borate.

2.2 Synthesis

Potassium hydrotris(3,5-dimethylpyrazol-1-yl)borate (KTp*) and the compounds **1-4** were prepared and characterized according to the literature precedent.^{22,51}

2.3 X-Ray Crystal Structure Determination

A yellow plate of C₁₅H₂₂BBr₂MoN₆O (**3**) was mounted on a glass fiber for structure determination using a Bruker SMART 1000 CCD detector X-ray diffractometer. Key

parameters for the structure determination are summarized in Table 4.1. Empirical absorption and decay corrections were applied using the program SADABS. The structure was solved by direct methods using SHELXS in the Bruker SHELXTL (Version 5.0) software package. Refinements were performed using the freely available SHELXL and illustrations were made using XP. Hydrogen atoms were added at idealized positions, constrained to ride on the atom to which they are bonded and given thermal parameters equal to 1.2 or 1.5 times U_{iso} of that bonded atom. A parameter describing extinction was included. Scattering Factors and anomalous dispersion were taken from International Tables Vol C Tables 4.2.6.8 and 6.1.1.4.^{52,53}

2.4 Photoelectron Spectroscopy

Photoelectron spectra were recorded using an instrument that features a 36-cm, 8 cm gap hemispherical analyzer (McPherson) and custom designed sample cells and detection and control electronics. The instrument and data collection and manipulation procedures have been described in detail elsewhere.^{30,34} During data collection the instrument resolution (measured using the full-width-at-half-maximum of the argon 2P_{3/2} peak) was 0.020-0.030 eV.

The sublimation temperatures (5°C, at 10^{-4} torr) were: 198°C for **1**, 193°C for **2**, and 169°C for **3** (monitored using a "K" type thermocouple passed through a vacuum feed through and attached directly to the sample cell). Valence region spectra of all the compounds investigated are shown in Figures 4.3 and 4.4. The mass spectra recorded at temperatures used in the collection of the spectra confirmed that the parent ion is present.

The spectra are represented analytically with the best fit of asymmetric Gaussians.⁵⁴ Each Gaussian is defined with the position, amplitude, halfwidth for the high binding energy side, and the halfwidth for the low binding energy side. The peak positions and halfwidths are reproducible to about 0.02 eV (3σ level). The parameters describing an individual ionization peak are less certain when two or more peaks are close in energy and overlap. The number of peaks used in a spectral deconvolution was based solely on the features of a given band profile. The deconvolution procedures are described in more detail elsewhere.⁵⁴

2.5 Computational details

Density functional theory (DFT) calculations were carried out using the Amsterdam density functional (ADF) program (ADF version 2000.01).⁵⁵⁻⁵⁷ The hydrotris(3,5 dimethylpyrazol-1-yl) borate ligand (Tp*) was truncated to the hydrotris(pyrazol-1-yl) borate ligand (Tp) to simplify the computational efforts. The functional xalpha was used to generate the atoms as well as for molecular calculations. A double- ζ Slater-type orbital (STO) basis set was used for H, C, B, N, F, Cl, Br and a triple- ζ with polarization (IV) basis sets were used for Mo and I. Atoms were used with frozen cores up to the 1s level for F, C, B, N, O; to the 2p level for Cl; to the 3p level for Br; to the 4p level for I and to either the 3d or 4p level for Mo. Both of the frozen cores for Mo produced similar results and results for 3d are presented. Full geometry optimizations (assuming C_1 symmetry) were carried out on each compound using the above approach. Calculations on the ground-state molecules were performed in the spin-restricted mode. Spin-restricted, SCF (self-consistent field) calculations were performed

on the proposed ion states formed by photoionization by removing one electron from the relevant orbital and comparing the total energy with that of the ground state molecule. The ionizations energies were also calculated by taking the difference of SCF (self-consistent field) energies of the spin unrestricted neutral ground state and the molecular ion state. Molecular visualization software Molekel was used for generating the pictures shown in Figure 4.5.⁵⁸

3.0 Results

3.1 X-ray Crystal Structure of (Tp*)MoOBr₂

The X-ray crystal structure for **3** is reported in this work (Figure 4.2). The average Mo-O and Mo-X bond lengths in **3** (1.640 Å, 2.335 Å) is 0.054 Å and 0.401 Å smaller than **4** (1.694 Å, 2.736 Å). The terminal oxo group exerts a strong trans effect⁵⁹ lengthening the Mo-N31 distance by 0.163 Å in **3** and 0.207 Å in **4**. The average Mo-N bond lengths of nitrogen donors cis to the oxo ligand are similar in **3** (2.167 Å) and **4** (2.150 Å). The X-M-X angle in **3** (95.1Å) is 0.5 Å larger than **4** (94.6Å).

The rotational disorder in **3** can be rationalized by the site occupancy factor analysis. This analysis in the crystal structure of **3** reveals that there is 80.62 % oxygen and 19.38 % bromine at site 1, 9.69 % oxygen and 90.30 % bromine at site 2 and site 3, thus approximately 20% of molecules of **3** had crystallized in a different orientation (rotated along a three fold axis) than the rest of them.

Two X-Ray crystal structures of **2** (CSD REFCODE: BEBCOA,⁶⁰ DOXJAB⁶¹) have also been reported with disorders. These disorders are thermodynamically favored

as a pseudo C_{3v} symmetry is imposed on the system because of the Tp* ligand and this compound crystallizes randomly in such a fashion that halide and oxygen atoms might be switched, giving rise to disordered structures. The molecular structure of **1** is not yet determined.

3.2 Gas-Phase Photoelectron Spectroscopy: Valence Ionizations

The general attributes and band assignments of the valence photoelectron spectroscopy of (Tp*)MoOX₂ shown in Figures 4.3 and 4.4 will be provided here. Plots of the He I photoelectron spectra of compounds **1-3** in the energy range 6.5 to 11.5 eV are shown in Figure 4.3 and reported in Table 4.2. In general, the region of the photoelectron spectra greater than 11.5 eV contains overlapping ionizations and provides very little information for these molecules. The lowest energy band (Band A) can be assigned to a partially occupied metal based orbital (Mo d¹) based on the reported photoelectron spectroscopic studies of similar species; Tp*Mo(E)(OR)₂ and Tp*Mo(E)(S-S) (E = O, S, NO).²⁶⁻³⁰

He I photoelectron spectroscopy of KTp* reported and assigned recently by us and others shows the pyrazole- π based bands in the region 7 to 11 eV.³²⁻³⁴ The higher formal oxidation state of the metal center in these compounds (Mo(V)), and therefore, the higher charge potential, will shift the Tp* based ionizations to higher energy than in KTp*. A comparison of the photoelectron spectra of KTp* and **1-3** shown in Figure 4.3 indicates that the ionizations (Band B) from the pyrazole- π based orbitals shift by approximately ~1 eV in **1-3**. The σ_N and σ_{BH} of the ligand, the former being a bonding orbital to metal (Mo(V)), will be stabilized more than ~1 eV and will be outside the

spectral range shown in Figure 4.3. Therefore, in Figures 4.3 and 4.4, the ionizations between 8-10 eV (Band B) for **1-3** are mostly pyrazole π based and other higher energy ionizations can be either halogen or oxygen based. Fluorine, being a highly electron withdrawing element, has its lone pair ionizations stabilized at around 17 eV in HF and other fluoro-organic compounds.⁶² Therefore, in **1**, the fluorine lone pair ionizations will be outside the spectral window shown in Figure 4.3. This suggests that the ionization band C at 10.51 ± 0.02 eV which does not change in intensity in the He II source can be assigned to the $\pi(\text{Mo}\equiv\text{O})$ based molecular orbital. A similar ionization feature is present at 10.63 ± 0.02 eV in **2** and 10.58 ± 0.02 eV in **3** that remains unchanged in intensity in He II and is consistent with ionization from a $\pi(\text{Mo}\equiv\text{O})$ based orbital. The ionization bands X_1 - X_3 in **2** and X_1 , X_2 in **3** decrease in intensity in He II photon source (Figure 4.4). The decrease in intensity of these bands indicates substantial halogen character in the associated molecular orbitals, and therefore, these bands can be assigned to halogen based orbitals, as described in Table 4.2.

3.4 Computational Results

Due to the absence of good molecular structures, the DFT calculations were used to optimize the geometry for all the structures (**1-4**) under study. The calculated bond lengths (presented in Appendix A1) are close to the available experimental data. The calculated ionization energies are reported in Table 4.2. The DFT calculations were performed to obtain the contributions from individual atomic orbital to the HOMO (Table 4.2). According to the calculations **1** has 19.26% fluorine character, **2** has 28.12 %

chlorine character, **3** has 32.28 % bromine character and **4** has 37.78% iodine character. Plots of the electronic potential and the HOMO for **1-4** are shown in Figure 4.5.

4.0 Discussion

The general shape of the spectral profile is comparable in compounds **1-3**. The lowest energy ionization band is similar to the previously reported photoelectron spectra of (Tp*)MoO(alkoxide)₂ and (Tp*)MoO(dithiolate) compounds²⁶⁻³⁰ and has been assigned to a metal based molecular orbital. The ionization energies corresponding to this band in **1-3** are not strikingly different despite significant differences in the electronegativities of the coordinated halides.

According to theoretical calculations on atomic subshell photoionization cross sections done by Lindau et al.,⁶³ bands with fluorine character will grow and bands with chlorine and bromine character will decrease in intensity as the ionization source is changed from He I to He II. The experimental verification of these relative changes in the intensity of the ionizations between He I and He II sources have been previously reported for halogen containing molecules.^{62,64} A shoulder to pyrazole based ionizations observed at 7.63 eV for KTp*, and at about 8.2 eV for **1-3**, primarily contains contributions from carbon and nitrogen atoms that do not change significantly with He II ionization source. A comparison of the peak areas, given in Table 4.3, reveals that in compound **1** the first band increases 38% with respect to second band, implying significant F character in the ionization of the HOMO. For compound **2**, the first band decreases 50% with respect to the second band, implying significant Cl character in the

ionization of the HOMO. Meaningful percent change calculations cannot be made for compound **3**, as the second band is not well resolved.

The first ionizations energies in the photoelectron spectroscopy of compounds $\text{Tp}^*\text{MoO}(\text{S-S})$ series (where (S-S) represents a generic ene-1,2-dithiolate ligand that forms a five membered chelate ring with the Mo atom) are 6.95 eV for $\text{Tp}^*\text{MoO}(\text{tdt})$, 7.04 eV for $\text{Tp}^*\text{MoO}(\text{bdt})$, 7.26 eV for $\text{Tp}^*\text{MoO}(\text{bdtCl}_2)$ and 7.72 eV for $\text{Tp}^*\text{MoO}(\text{qdt})$ (where bdt, 1,2-benzenedithiolate; qdt, 2,3-dithioquinoxaline; tdt, 3,4-toluenedithiolate; bdtCl_2 , 3,6-dichloro-1, 2-benzenedithiolate).^{29,36,65} Comparing these values to those for **1-3** suggests that halides are more electron withdrawing than tdt, bdt and bdtCl_2 . However, the qdt ligand is more electron withdrawing than the halogens or the other ene-dithiolate ligands.

The calculated ionization energies for **1-4** reported in Table 4.2 reveal similar trends to those obtained experimentally by photoelectron spectroscopy. This trend neither follows the electronegativity trend nor the inverse halogen effect. As we go down the halogen series, the calculated percent metal character in the HOMO decreases and the percent halogen character increases and follows a trend (Figure 4.5 (b)) similar to that measured by EPR hyperfine splitting studies.^{22,25,66,67} The polarizability of electron rich halogen *p* orbitals increases as we go down the halogen group. The pseudo σ -bonding is most prominent in the case of $\text{X} = \text{I}$, as there is more electron density between halogen atoms due to the diffuseness of halogen *p* orbitals. The halogen character of the HOMO in **1** is the least among all the compounds suggesting that fluoride ligand is very compact

and more like a point charge, and that electrostatic interactions might be important for explaining its ionization energies.

Electronic potentials for **1-4**, plotted in Figure 4.5 (a) show that electron density is mostly delocalized in the pyrazole ring. These plots give a very good comparison of electronic potential at oxygen and halogen atoms in these molecules. There is relatively more negative electronic potential at the halogen atom for **1** compared to **2**, **3** and **4** consistent with their electronegativities. As we proceed from F to I in the halogen series the electronic potential at the oxygen atom increases at the expense of its decrease on halogen atoms. Thus, this interplay between halogen and the axial oxo atom leaves a similar charge potential at the formally Mo(V) metal center in **1-4**, and therefore, results in similar energy of the first ionization in their photoelectron spectra.

The (Tp*)MoOX₂ system contains a formally Mo(V) metal center with one unpaired electron in a predominately metal based molecular orbital (HOMO). Previously reported EPR^{22,25,66,67} studies in this series (X= F, Cl, Br) show a very high metal character in the HOMO (> 80 %), whereas significant halogen character was calculated by DFT methods.

The ionization band present at 10.51 eV in **1**, 10.63 eV in **2** and 10.58 eV in **3** is of similar shape and equal in area and does not appreciably change in intensity between He I and He II sources. This band cannot be a σ_{BH} based ionization because the σ_{BH} based ionization in K(Tp*) significantly decreases in He II ionization source.³⁴ Also, as mentioned earlier the σ_{N} and σ_{BH} based ionizations are outside this spectral range. Therefore, this feature is assigned to an oxomolybdenum (Mo≡O) based orbital. The IR

$\nu_{\text{Mo=O}}$ stretching vibrations previously reported for these species at 964 cm^{-1} for **1**; 962 cm^{-1} for **2**; and 961 cm^{-1} for **3** do not change significantly with the electronegativity of the coordinated halides.²² The presence of an invariant oxomolybdenum band C in the photoelectron spectra of **1-3** and similar IR $\nu_{\text{Mo=O}}$ stretching vibrations suggest the presence of an electronically isolated $\text{Mo}\equiv\text{O}$ diatomic unit in compounds **1-3** that dominates the electronic structures of these compounds and related mimics of molybdenum and tungsten based pyranopterindithiolate enzymes.^{28,38-42} The ionizations corresponding to $\pi(\text{Mo}\equiv\text{O})$ in the previous photoelectron spectroscopic study²⁴ of $\text{Mo}(\eta^5\text{-C}_5\text{H}_4\text{Me})_2\text{O}$, $[\text{W}(\eta^5\text{-C}_5\text{H}_4\text{Me})_2\text{O}]$ and $[\text{W}(\eta^5\text{-C}_5\text{Me}_5)_2\text{O}]$ compounds are at 10.67 eV, 10.65 eV and 9.84 eV, respectively, and their similar ionization energies with those for **1-3** further support our assignments of Band C.

5.0 Conclusions

Theoretically obtained first ionization energies have similar trend as obtained experimentally by photoelectron spectroscopy and EPR for **1-3**. The presence of a $\pi(\text{Mo}\equiv\text{O})$ band at similar energies in the photoelectron spectra of **1-3** suggests an electronically isolated $\text{Mo}\equiv\text{O}$ diatomic core. A strong molybdenum and axial oxo interaction dominates the electronic structure of these and similar other species. The DFT calculations show that the metal-halide covalency increases in these compounds as we go down the halogen group due to the increased number of electrons leading to more diffusion of the electron cloud along the halogen-metal bond. The compound **4** has the most covalent metal-halogen interaction. Significant differences in the metal-ligand

covalency are observed between coordination of molybdenum with the first row element (F; **1**) and other elements (Cl; **2**, Br; **3**, I; **4**) in the halogen group resulting in highly covalent bonds in **2-4**. This could suggest that relatively softer second row element sulfur has been selected in the biological systems for enhanced covalent interaction with metal to relatively harder first row element oxygen in the pyranopterindithiolate cofactor.

Table 4.1. Crystal data and structure refinement for (Tp*)MoOBr₂ (**3**)

Empirical formula	C ₁₅ H ₂₂ B Br ₂ Mo N ₆ O
Formula weight	568.96
Temperature	100(2) K
Wavelength	0.71073 Å
Crystal system	Monoclinic
Space group	P2(1)/c
Unit cell dimensions	a = 9.006(1) Å α = 90° b = 15.937(2) Å β = 105.287(3)° c = 14.250(2) Å γ = 90°
Volume	1972.8(5) Å ³
Z	4
Density (calculated)	1.916 Mg/m ³
Absorption coefficient	4.733 mm ³
F(000)	1116
Crystal size	0.30 x 0.15 x 0.01 mm ³
Theta range for utilized data	1.96 to 26.40°
Limiting Indices	-11 ≤ h ≤ 11, -19 ≤ k ≤ 19, -17 ≤ l ≤ 17
Reflections utilized	20671
Independent reflections	4033 [R(int) = 0.1336]
Completeness to theta = 26.40°	99.9 %
Absorption correction Integration	SADABS
Max. and min. transmission	0.8238 and 0.3513
Refinement method	Full-matrix least-squares on F ²
Data / restraints / parameters	4033 / 6 / 246
Goodness-of-fit on F ²	1.122
Final R indices [I > 2σ(I)]	R1 = 0.0567, wR2 = 0.1545
R indices (all data)	R1 = 0.0945, wR2 = 0.1718
Largest diff. peak and hole	0.995 and -1.636 e.Å ⁻³
RMS difference density	0.180e.Å ⁻³

Table 4.2. Experimental ionization energies (I.E.), calculated absolute orbital eigenvalues ($-\epsilon_i$) and calculated Δ SCF first ionization energies of compounds 1-3 (all values in eV).

Experimental I.E. (eV)	Calculated $-\epsilon_i$ (Shifted) ^b	($-\epsilon_i$) HOMO % Metal/ % Halide Character in HOMO	Δ SCF (eV)	Label and Assignment
K(Tp*)				
7.63-8.45 ^a	7.63-8.08	4.66	6.66	Band B, Pyrazole- π
9.51, 9.99	8.93-9.31			σ N
10.58	9.88			σ BH
(Tp*)MoOF₂ (1)				
7.63 ^a	7.63	3.95 72.23/ 18.12	6.80	Band A
8.40-9.30	9.85-10.64			Band B, Pyrazole- π
10.51	10.91, 11.22			Band C, π (Mo=O)
(Tp*)MoOCl₂ (2)				
7.68 ^a	7.68	4.38 66.75/ 26.28	6.94	Band A
8.37-9.33	9.5, 10.0- 10.30			Band B, Pyrazole- π
9.80	9.4			X ₁ : Cl in-plane
10.63	10.80			Band C, π (Mo=O)
10.91, 11.22	9.53, 9.80			X ₂ , X ₃ : Cl out-of-plane
(Tp*)MoOBr₂ (3)				
7.55 ^a	7.55	4.30 61.94/ 30.22	6.76	Band A
8.31-9.28	9.44-10.13			Band B, Pyrazole- π
10.13	8.91			X ₁ : Br in-plane
10.58	10.90			Band C, π (Mo=O)
10.89	9.10, 9.37			X ₂ : Br out-of-plane

^a Range of experiment I.E. values for Band A are taken from the positions of Gaussians used to deconvolute the data. This does not imply that these values are vertical ionization energies.

^b Eigenvalues were shifted so the HOMO eigenvalue matches the position of the lowest energy Gaussian used to deconvolute the experimental data.

Table 4.3. Ionization energies and areas of Gaussian fits.

Molecule	First Ionization Energies (eV)	Areas of Gaussians				Relative Areas HeII/HeI
		HeI		HeII		
		Peak 1	Peak 2	Peak 1	Peak 2	
(Tp*)MoOF ₂ (1)	7.63	0.17	1.00	0.20	1.00	18%
(Tp*)MoOCl ₂ (2)	7.68	0.38	1.00	0.19	1.00	50%
(Tp*)MoOBr ₂ (3)	7.54	1.13	1.00	0.18	1.00	38.5%

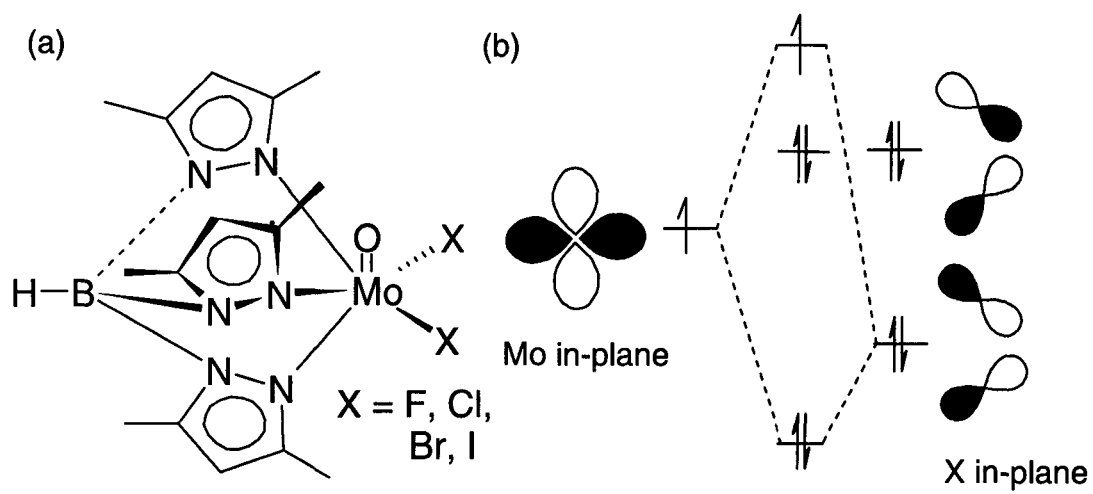


Figure 4.1. (a) Systematic representation of $(\text{Tp}^*)\text{MoOX}_2$ ($\text{X} = \text{F}, \text{Cl}, \text{Br}, \text{I}$). (b) Simplified molecular orbital scheme for orbitals in the xy plane showing metal and halide interaction.

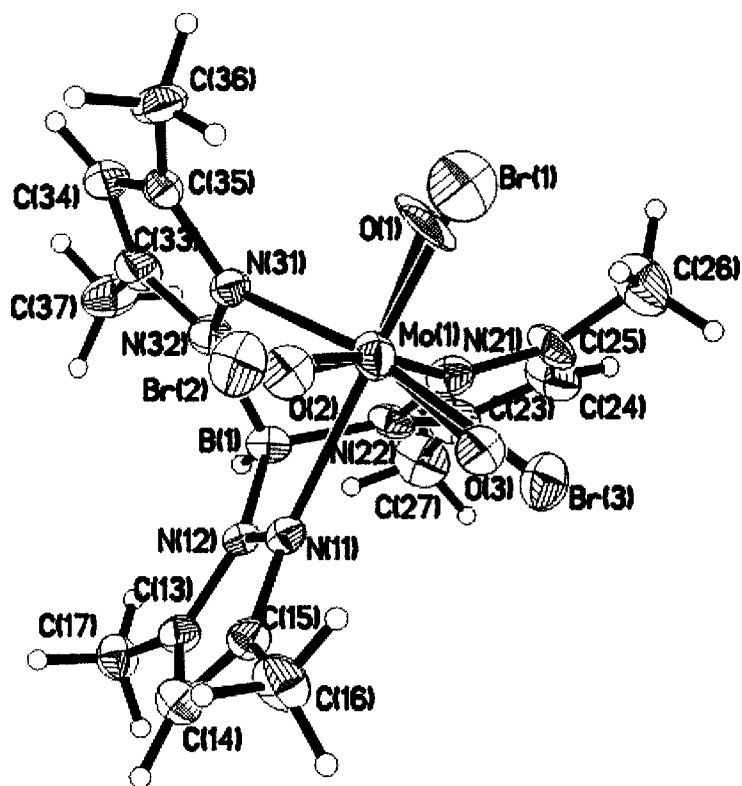


Figure 4.2. ORTEP representation of (Tp*)MoOBr₂ (3) at 50% probability level. Hydrogen atoms are made arbitrarily small for comparison. A rotational disorder can be viewed along the pseudo three fold axis.

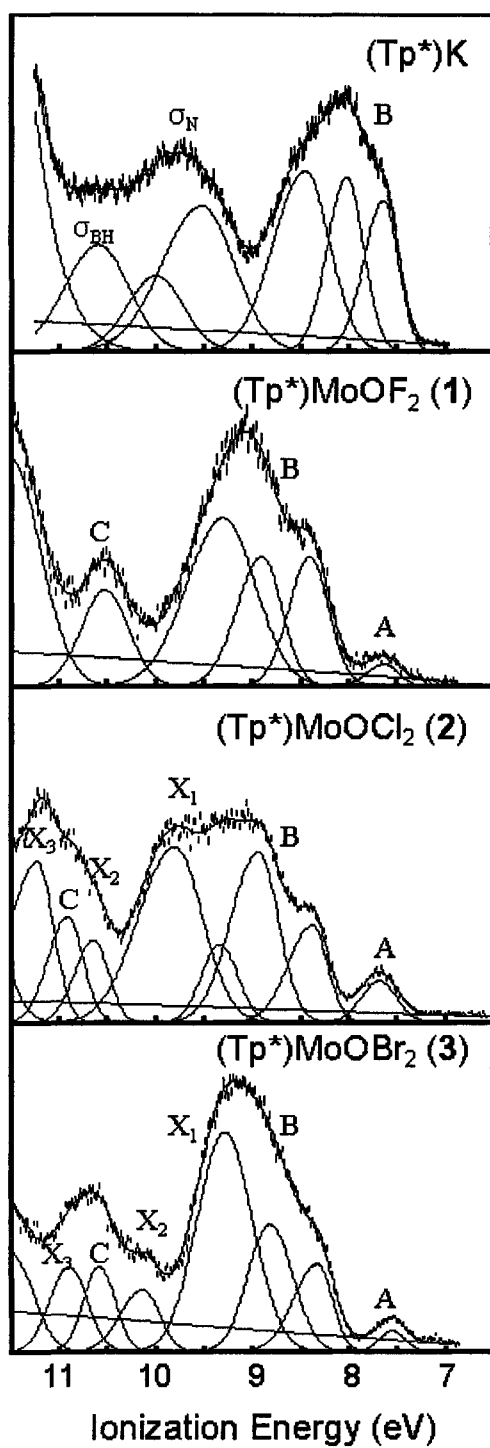


Figure 4.3. The stack plot of the He I photoelectron spectra of (Tp*)K, (Tp*)MoOF₂ (1), (Tp*)MoOCl₂ (2) and (Tp*)MoOBr₂ (3)

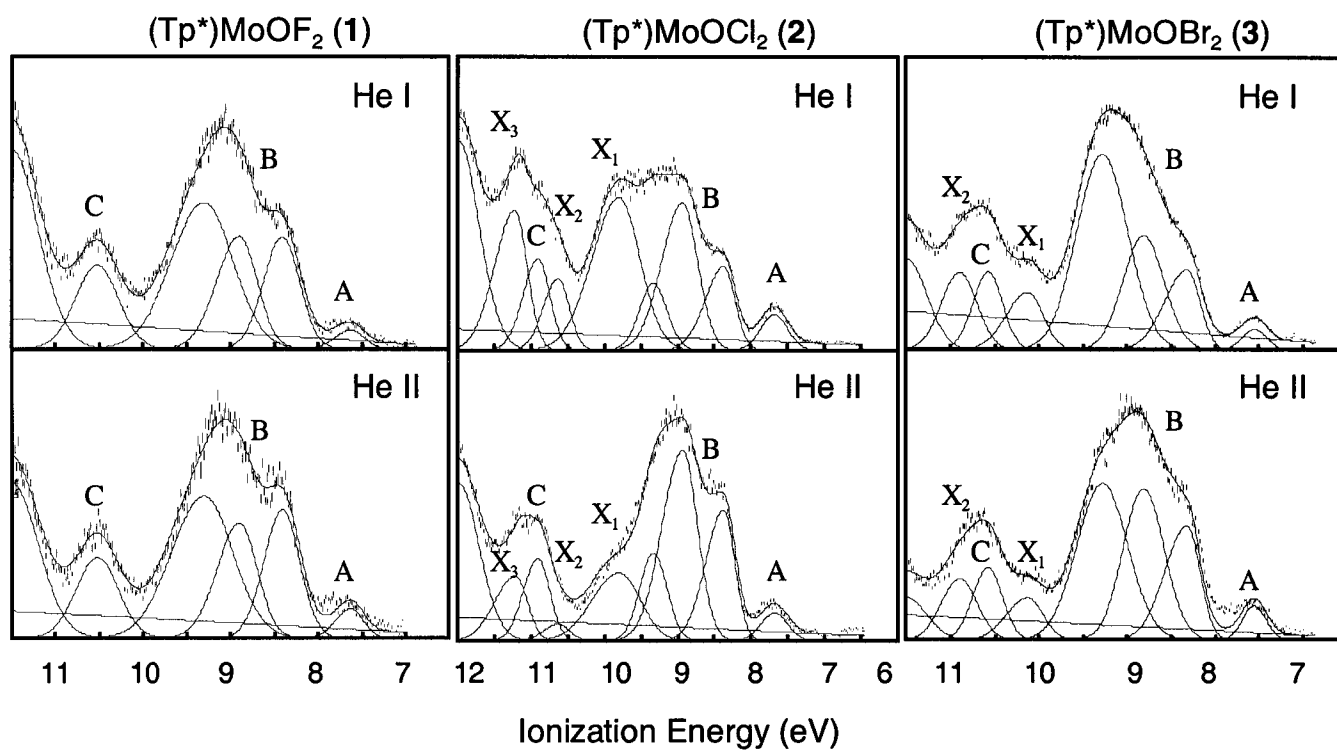


Figure 4.4. The He I and He II photoelectron spectra of (Tp*)MoOF₂ (1), (Tp*)MoOCl₂ (2) and (Tp*)MoOBr₂ (3)

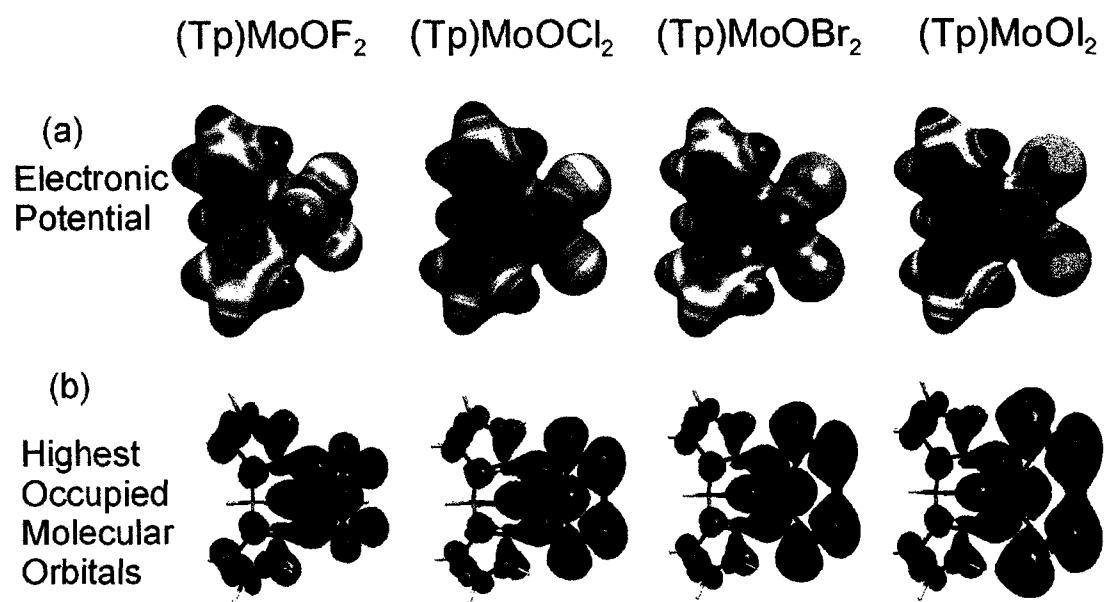


Figure 4.5. (a) Electronic potential and (b) highest occupied molecular orbital plots for (Tp*)MoOX₂ (X = F, Cl, Br, I).

6.0 References

1. Fagnou, K.; Lautens, M. *Angew. Chem., Int. Ed.* **2002**, *41* (1), 26-47.
2. Caulton, K. G. *New J. Chem.* **1994**, *18* (1), 25-41.
3. Doherty, N. M.; Hoffmann, N. W. *Chem. Rev.* **1991**, *91* (4), 553-73.
4. Poulton, J. T.; Sigalas, M. P.; Folting, K.; Streib, W. E.; Eisenstein, O.; Caulton, K. G. *Inorg. Chem.* **1994**, *33* (7), 1476-85.
5. Huang, D.; Caulton, K. G. *J. Am. Chem. Soc.* **1997**, *119* (13), 3185-3186.
6. Vaska, L.; Peone, J. J. *J. Chem. Soc. D.* **1971**, *9*, 418-19.
7. Schiavon, G.; Zecchin, S.; Pilloni, G.; Martell, M. *J. Inorg. Nucl. Chem.* **1977**, *39* (1), 115-7.
8. Darensbourg, D. J.; Klausmeyer, K. K.; Reibenspies, J. H. *Inorg. Chem.* **1995**, *34* (20), 4933-4.
9. Johnson, T. J.; Folting, K.; Streib, W. E.; Martin, J. D.; Huffman, J. C.; Jackson, S. A.; Eisenstein, O.; Caulton, K. G. *Inorg. Chem.* **1995**, *34* (2), 488-99.
10. Abu-Hasanayn, F.; Goldman, A. S.; Krogh-Jespersen, K. *Inorg. Chem.* **1994**, *33* (22), 5122-30.
11. Holland, P. L.; Andersen, R. A.; Bergman, R. G.; Huang, J.; Nolan, S. P. *J. Am. Chem. Soc.* **1997**, *119* (52), 12800-12814.
12. Holland, P. L.; Andersen, R. A.; Bergman, R. G. *Comments on Inorganic Chemistry* **1999**, *21* (1-3), 115-129.
13. Fenske, R. F.; DeKock, R. L. *Inorg. Chem.* **1970**, *9* (5), 1053-60.

14. Hall, M. B. *J. Am. Chem. Soc.* **1975**, *97* (8), 2057-65.
15. Lichtenberger, D. L.; Rai-Chaudhuri, A.; Seidel, M. J.; Gladysz, J. A.; Agbossou, S. K.; Igau, A.; Winter, C. H. *Organometallics* **1991**, *10* (5), 1355-64.
16. Green, J. C.; Payne, M. P.; Teuben, J. *Organometallics* **1983**, *2* (2), 203-10.
17. King, W. A.; Bella, S. D.; Gulino, A.; Lanza, G.; Fragala, I. L.; Stern, C. L.; Marks, T. J. *J. Am. Chem. Soc.* **1999**, *121* (2), 355-366.
18. Levenson, R. A.; Cihonski, J. L.; Milazzo, P.; Ceasar, G. P. *Inorg. Chem.* **1975**, *14* (10), 2578-9.
19. Elian, M.; Hoffmann, R. *Inorg. Chem.* **1975**, *14* (5), 1058-76.
20. Morris-Sherwood, B. J.; Kolthammer, B. W.; Hall, M. B. *Inorg. Chem.* **1981**, *20* (9), 2771-6.
21. Cacelli, I.; Poli, R.; Quadrelli, E. A.; Rizzo, A.; Smith, K. M. *Inorg. Chem.* **2000**, *39* (3), 517-524.
22. Nipales, N. S.; Westmoreland, T. D. *Inorg. Chem.* **1995**, *34* (13), 3374-7.
23. Enemark, J. H.; Cosper, M. M. In *Metal Ions in Biological Systems*; Vol. 39: *Molybdenum and Tungsten. Their Roles in Biological Processes*; Sigel, A.; Sigel, H., Eds.; Marcel Dekker, Inc.: New York, 2002, pp 621-654.
24. Bridgeman, A. J.; Davis, L.; Dixon, S. J.; Green, J. C.; Wright, I. N. *J. Chem. Soc., Dalton Trans.* **1995**, *6*, 1023-7.
25. Nipales, N. S.; Westmoreland, T. D. *Inorg. Chem.* **1997**, *36* (5), 756-757.
26. Chang, C. S. J.; Rai-Chaudhuri, A.; Lichtenberger, D. L.; Enemark, J. H. *Polyhedron* **1990**, *9*, 1965-1973.

27. Westcott, B. L.; Gruhn, N. E.; Enemark, J. H. *J. Am. Chem. Soc.* **1998**, *120*, 3382-3386.
28. Inscore, F. E.; McNaughton, R.; Westcott, B.; Helton, M. E.; Jones, R.; Dhawan, I. K.; Enemark, J. H.; Kirk, M. L. *Inorg. Chem.* **1999**, *38*, 1401-1410.
29. Helton, M. E.; Gruhn, N. E.; McNaughton, R. L.; Kirk, M. L. *Inorg. Chem.* **2000**, *39* (11), 2273-2278.
30. Joshi, H. K.; Cooney, J. J. A.; Inscore, F. E.; Gruhn, N. E.; Lichtenberger, D. L.; Enemark, J. H. *Proc. Natl. Acad. Sci. USA* **2003**, *100* (7), 3719-3724.
31. Joshi, H. K.; Inscore, F. E.; Schirlin, J. T.; Dhawan, I. K.; Carducci, M. D.; Bill, T. G.; Enemark, J. H. *Inorg. Chim. Acta* **2002**, *337*, 275-286.
32. Bruno, G.; Ciliberto, E.; Fragala, I.; Granozzi, G. *Inorg. Chim. Acta* **1981**, *48* (1), 61-4.
33. Bruno, G.; Centineo, G.; Ciliberto, E.; Di Bella, S.; Fragala, I. *Inorg. Chem.* **1984**, *23* (13), 1832-6.
34. Joshi, H. K.; Arvin, M. A.; Durivage, J. C.; Gruhn, N. E.; Carducci, M. D.; Westcott, B. L.; Lichtenberger, D. L.; Enemark, J. H. *Polyhedron* **2003**.
35. Kisker, C.; Schindelin, H.; Pacheco, A.; Wehbi, W.; Garrett, R. M.; Rajagopalan, K. V.; Enemark, J. H.; Rees, D. C. *Cell* **1997**, *91*, 973-983.
36. Inscore, F. E.; Joshi, H. K.; McElhaney, A. E.; Enemark, J. H. *Inorg. Chim. Acta* **2002**, *331*, 246-256.
37. Westcott, B. L.; Enemark, J. H. *Inorg. Chem.* **1997**, *36* (23), 5404-5405.

38. Joshi, H. K.; Inscore, F. E.; Gruhn N. E.; Enemark, J. H. *manuscript in preparation*.
39. Carducci, M. D.; Brown, C.; Solomon, E. I.; Enemark, J. H. *J. Am. Chem. Soc.* **1994**, *116*, 11856-11868.
40. McMaster, J.; Carducci, M. D.; Yang, Y.-S.; Solomon, E. I.; Enemark, J. H. *Inorg. Chem.* **2001**, *40*, 687-702.
41. McNaughton, R. L.; Tipton, A. A.; Rubie, N. D.; Conry, R. R.; Kirk, M. L. *Inorg. Chem.* **2000**, *39* (25), 5697-5706.
42. Helton, M. E.; Pacheco, A.; McMaster, J.; Enemark, J. H.; Kirk, M. L. *J. Inorg. Biochem.* **2000**, *80* (3-4), 227-233.
43. Zietlow, T. C.; Hopkins, M. D.; Gray, H. B. *J. Am. Chem. Soc.* **1986**, *108* (26), 8266-7.
44. Hascall, T.; Rabinovich, D.; Murphy, V. J.; Beachy, M. D.; Friesner, R. A.; Parkin, G. *J. Am. Chem. Soc.* **1999**, *121* (49), 11402-11417.
45. Krueger, S. T.; Owens, B. E.; Poli, R. *Inorg. Chem.* **1990**, *29* (10), 2001-6.
46. Aston, G. M.; Badriya, S.; Farley, R. D.; Grime, R. W.; Ledger, S. J.; Mabbs, F. E.; McInnes, E. J.; Morris, H. W.; Ricalton, A.; Rowlands, C. C.; Wagner, K.; Whiteley, M. W. *J. Chem. Soc., Dalton Trans.* **1999**, *24*, 4379-4388.
47. Bartlett, I. M.; Carlton, S.; Connelly, N. G.; Harding, D. J.; Hayward, O. D.; Orpen, A. G.; Ray, C. D.; Rieger, P. H. *Chem. Comm.* **1999**, *23*, 2403-2404.
48. Krueger, S. T.; Poli, R.; Rheingold, A. L.; Staley, D. L. *Inorg. Chem.* **1989**, *28* (26), 4599-607.

49. Tilsted, M.; Fjeldahl, I.; Hamon, J. R.; Hamon, P.; Toupet, L.; Saillard, J. Y.; Costuas, K.; Haynes, A. *J. Am. Chem. Soc.* **2001**, *123* (41), 9984-10000.
50. McNaughton, R. L.; Helton, M. E.; Rubie, N. D.; Kirk, M. L. *Inorg. Chem.* **2000**, *39* (20), 4386-4387.
51. Saleh, A. A.; Pleune, B.; Fettingner, J. C.; Poli, R. *Polyhedron* **1997**, *16* (8), 1391-1397.
52. Cromer, D. T.; Waber, J. *Int. Tables X-Ray Crystallogr.* **1974**, *4*, 71-147.
53. Cromer, D. T.; Ibers, J. A. *Int. Tables X-Ray Crystallogr.* **1974**, *4*, 148-51.
54. Lichtenberger, D. L.; Copenhaver, A. S. *J. Electron Spectrosc. Relat. Phenom.* **1990**, *50* (4), 335-52.
55. Baerends, E. J.; Ellis, D. E.; Ros, P. *Chem. Phys.* **1973**, *2*, 41-51.
56. te Velde, G.; Baerends, E. J. *J. Comput. Phys.* **1992**, *99* (1), 84-98.
57. Te Velde, G.; Bickelhaupt, F.; Baerends, E.; Fonseca Guerra, C.; Van Gisbergen, S.; Snijders, J.; Ziegler, T. *J. Comp. Chem.* **2001**, *22* (9), 931-967.
58. Portmann, S.; Luthi, H. P. *Chimia* **2000**, *54* (12), 766-769.
59. pi donor ligands, f. e. o., exert a very strong trans effect lengthening the bond trans to them..
60. Ferguson, G.; Kaitner, B.; Lalor, F. J.; Roberts, G. *J. Chem. Res., Synop.* **1982**, *1*, 6-7.
61. Lincoln, S.; Koch, S. A. *Inorg. Chem.* **1986**, *25* (10), 1594-602.
62. Briggs, D. *Handbook of X-Ray and Ultraviolet Photoelectron Spectroscopy.*; Briggs, D., Ed.: Publisher: (Heyden, London, Engl.), 1977, p 399 pp.

63. Yeh, J.; Lindau, I. *At. Data Nucl. Data Tables* **1985**, *32* (1), 1-155.
64. Lichtenberger, D. L.; Elkadi, Y.; Gruhn, N. E.; Hughes, R. P.; Curnow, O. J.; Zheng, X. *Organometallics* **1997**, *16* (24), 5209-5217.
65. Westcott, B.; Gruhn, N.; Enemark, J. *J. Am. Chem. Soc.* **1998**, *120* (14), APR 15, 3382-3386.
66. Cleland, W. E., Jr.; Barnhart, K. M.; Yamanouchi, K.; Collison, D.; Mabbs, F. E.; Ortega, R. B.; Enemark, J. H. *Inorg. Chem.* **1987**, *26*, 1017-1025.
67. Chang, C. S. J.; Enemark, J. H. *Inorg. Chem.* **1991**, *30*, 683-688.

CHAPTER 5: Structural Studies of Active Site Models: Metal Dithiolates with and without a Terminal Oxo Ligand

A portion of this chapter has been published as

Inscore, F. E.; Joshi, H. K.; McElhaney, A.; Enemark, J. H. "Remote ligand substituent effects on the properties of oxo-Mo(V) centers with a single ene-1,2-dithiolate ligand"

Inorg. Chim. Acta **2002**, 331, 246-256.

1.0 Introduction

The X-ray crystal structure of small molecular models of metalloproteins is intriguing as one can often get high resolution structures without involving the complex experimentation and cumbersome data refinement that has to be undergone in macromolecular crystallography. Small molecular crystallography can often be conducted at in-house facilities and refinement yields a very high resolution solution, providing fine details of the molecular structures.

This chapter reports some atomic resolution structures that contain one enedithiolate ligand coordinated to either Mo or W. The effect of variation of substituents on the benzene ring of the enedithiolate ligand, and variation of metal from Mo to W will be discussed. Finally, a correlation between the geometric and the electronic structures will be attempted.

There are a number of structures of oxo-Mo(V) complexes reported that contain the $[(Tp^*)MoO]^{2+}$ core.¹⁻⁸ However, only a few structures of oxometal complexes of group VI that contain one enedithiolate ligand have been reported.^{2,3,9,10} Until recently, the crystal structure of $(Tp^*)MoO(bdt)$ (**1**) reported in 1994 was the only representative structure of this family.^{2,3}

The structures of $(Tp^*)MoO(bdtCl_2)$ (**2**) and $(Tp^*)MoO(qdt)$ (**3**) and their tungsten analogue $(Tp^*)WO(bdt)$ (**4**) are reported here. A comparison and contrast among the structural parameters of the family of oxometal-enedithiolate compounds **1-4** and a metal-enedithiolate compound $Cp_2Mo(bdt)$ (**5**) are also presented. These

mononuclear six-coordinate monooxo-Mo(V) monodithiolene complexes (**1**, **2**, and **3**), in addition to the bis-thiolate $(\text{Tp}^*)\text{MoO}(\text{SPh})_2$ are, to the best of our knowledge, the only known species of the $[(\text{Tp}^*)\text{MoO}(\text{S}_2)]$ system type that have been structurally characterized by single-crystal X-ray diffraction.

2.0 X-Ray Crystal Structure Determinations

The crystals for structural characterization were obtained from either vapor or liquid diffusion. A burgundy plate of $(\text{Tp}^*)\text{MoO}(\text{bdtCl}_2)$ (**2**) was obtained by slow vapor diffusion of hexane into a dichloromethane solution at room temperature. Suitable crystals of the $(\text{Tp}^*)\text{MoO}(\text{qdt})$ (**3**) complex were obtained as dark-red blocks by slow vapor diffusion of pentane into a dichloromethane solution at room temperature. A green plate of $(\text{Tp}^*)\text{WO}(\text{bdt})$ (**4**) was obtained by slow vapor diffusion of pentane into ether, and a brown needle of $\text{Cp}_2\text{Mo}(\text{bdt})$ (**5**) was obtained from liquid diffusion of pentane into an acetonitrile solution of **5**. The experimental details for the X-ray crystallographic study of **2-5** are summarized in Tables 5.1, 5.3, 5.6 and 5.8, respectively, and the key intermolecular bond lengths and angles are summarized in Tables 5.2, 5.4, 5.5, 5.7, and 5.9. Each crystal mounted on a glass fiber (in a glass capillary) one at a time in a random orientation, and examined on a Bruker SMART 1000 CCD detector X-ray diffractometer at 170(2) K and a power setting of 50 kV (40 mA). The structural data presented here is shown with empirical absorption and decay corrections using the program SADABS wherever required, as specified in Tables 5.1, 5.3, 5.6 and 5.8. The structure was solved by direct methods using SHELXS in the Bruker SHELXTL (Version 5.0) software

package. Refinements were performed using SHELXL and illustrations were made using XP. Hydrogen atoms were added at idealized positions, constrained to ride on the atom to which they are bonded and given thermal parameters equal to 1.2 or 1.5 times U_{iso} of that atom. Scattering factors and anomalous dispersion were taken from International Tables Vol C, Tables 4.2.6.8 and 6.1.1.4.^{11,12} Selected crystallographic data and molecular structural parameters are listed in Tables 5.1, 5.3, 5.6 and 5.8, respectively. The crystals of **3** contain one half molecule solvent (hexane) of crystallization per asymmetric unit. The large values of thermal displacement parameters of the carbon atoms of the hexane of crystallization can be attributed to the partial loss of solvent molecules during the time interval between crystal isolation and low temperature data collection. The ORTEP diagram of **2-5** are shown in 50% probability level and their crystal packing diagram are shown in Figures 5.2-5.11.

3.0 X-ray Structure Analysis

3.1 Structure of $(\text{Tp}^*)\text{MoO}(\text{bdtCl}_2) \cdot 1/2(\text{C}_6\text{H}_{14})$

The structure of $(\text{Tp}^*)\text{MoO}(\text{bdtCl}_2)$ (**2**), determined by single-crystal X-ray diffraction, is shown in Figures 5.2 and 5.3. Table 5.2 presents selected interatomic distances and bond angles. The molecule exhibits a distorted pseudo-octahedral coordination geometry, where the Mo atom is ligated by a terminal oxo atom, two sulfur donor atoms of the bdtCl_2 ligand and three nitrogen atoms of the tridentate facially coordinated Tp^* ligand. No symmetry is imposed on **2** by its space group, but the effective symmetry is C_s . The terminal oxo ligand and the two sulfur donor atoms of the

ene-1,2-dithiolate chelate ligand (bdtCl₂) are constrained to be mutually *cis* to each other by the *fac* stereochemistry imposed by the tridentate Tp* ligand. This is the second such structurally characterized six-coordinate oxo-Mo(V) complex that contains a single ene-1,2-dithiolate ligand *cis* to the terminal oxo group. The structure of (Tp*)MoO(bdt)^{2,2} has been previously reported.

The structural parameters of the [(Tp*)MoO]²⁺ core in (Tp*)MoO(bdtCl₂) agree with those found for other oxo-Mo(V) complexes.¹⁻⁸ The observed Mo≡O distance (1.679(3) Å) is similar to that of (Tp*)MoO(bdt) (1.678(4) Å),^{2,3} (Tp*)MoO(qdt) (1.6865(18) Å), and (Tp*)MoO(SPh)₂ (1.676(4) Å).¹ The terminal axial oxo ligand, as expected, exerts a strong *trans* influence, lengthening the Mo-N31 distance (2.391(3) Å) by 0.214 Å relative to Mo-N21 (2.177(2) Å) and 0.225 Å relative to Mo-N11 (2.166(3) Å). This effect is slightly greater than that observed in the (Tp*)MoO(bdt) complex where the Mo-N31 bond was found to be 2.372(4) Å.² The average Mo-S distance (2.3744(12) Å) in (Tp*)MoO(bdtCl₂) is indistinguishable from that observed in (Tp*)MoO(bdt) (2.373(2) Å). These Mo≡O and Mo-S bond length comparisons for (Tp*)MoO(bdtCl₂) and (Tp*)MoO(bdt), clearly show that these structural parameters are not significantly perturbed by remote ligand substituent effects. The bond angles about the six-coordinate Mo atom deviate significantly from that of octahedral geometry, as illustrated by O-Mo-S1 = 101.81(10)° and O-Mo-S2 = 100.99(10)°. The average O-Mo-S angle of 101.40° is slightly greater than that reported for (Tp*)MoO(bdt) (100.95°).² The molybdenum atom is displaced ~0.258 Å above the mean N₂S₂ equatorial plane in the direction of the apical oxo ligand. This is smaller than observed for (Tp*)MoO(bdt)

at 0.264 Å.² The S-Mo-S chelate bite angle of 84.38(4)° is tighter by 0.74° relative to the corresponding angle (85.12(6)°) in (Tp*)MoO(bdt).² The S--S nonbonded contact distance was calculated to be 3.190 Å; this is only 0.021 Å smaller than that observed for (Tp*)MoO(bdt) (3.211 Å).

The most significant differences between the structures of (Tp*)MoO(bdtCl₂) (**3**) and (Tp*)MoO(bdt) (**1**) is the angle (δ) formed between the ene-1,2-dithiolate (S-C=C-S) least squares plane and the S-Mo-S plane along the line of intersection containing the S---S atoms. This angle in (**2**) is 173.1°, and thus the S-C=C-S plane is folded up towards the terminal oxo group by $\theta = 180^\circ - \delta = 6.9^\circ$. The fold angle (θ) is defined as an acute angle between metal-sulfur and sulfur-carbon planes within the metallacycle (see Figure 5.1). The (bdtCl₂) ring structure itself is essentially planar. The fold angle for (Tp*)MoO(bdt) is considerably greater with $\theta = 21.3(1)^\circ$.² This deformation in (Tp*)MoO(bdt) has been previously attributed to a steric interaction between the C36 methyl group of the trans N31 pyrazolyl ring and the C1 and C2 atoms of the chelate ring.³ The C36---C1 and C36---C2 non-bonded contact distances in (Tp*)MoO(bdt) are 3.58 and 3.57 Å, respectively, and significantly greater than the corresponding distances of 3.375 and 3.345 Å in (Tp*)MoO(bdtCl₂). The estimated van der Waals contact between a methyl group and an aromatic ring is 3.72 Å. Thus, non-bonded contacts in (Tp*)MoO(bdtCl₂) would seemingly favor a larger fold angle, as was observed in (Tp*)MoO(bdt). The packing of the molecules in the unit cell for each of these systems was also examined, and it was determined for **2** that the C36 methyl groups from neighboring molecules were well separated from the C1 and C2 atoms (greater than 8 Å). The packing diagram

showed that the closest Cl---Cl distance between neighboring molecules was 3.920 Å, greater than the van der Waals contact of 3.60 Å for chlorines. The results for the packing diagram analysis suggests that non-bonded intermolecular contacts are not the cause of the observed fold angle deviation. The origin and contributions to this fold angle in (Tp*)MoO(bdt), (Tp*)MoO(bdtCl₂), and (Tp*)MoO(qdt) has been investigated through DFT calculations and is discussed in Chapter 6. Comparison of the bond distances within the S-C=C-S chelate rings of **1** and **2** shows that the C1-C2 distance of **1** of 1.395(8) Å and the distance in **2** of 1.406(5) Å are similar. The average S-C distances of 1.760(6) in **1** and 1.751(4) Å in **2** are also not significantly different from one another.

3.2 Structure of (Tp*)MoO(qdt) (**3**)

The structure of (Tp*)MoO(qdt) (**3**), determined by single-crystal X-ray diffraction, is presented in Figure 5.4. The perspective view (Fig. 5) illustrates the general atomic numbering scheme used for defining the molecular structural parameters of **3** and other related [(Tp*)MoO(S₂)] complexes. Table 5.4 presents selected interatomic distances and bond angles for (Tp*)MoO(qdt) (**3**). Table 5.5 provides the corresponding mean geometric structural parameters of (Tp*)MoO(bdt) (**1**) and (Tp*)MoO(bdtCl₂) (**2**) for comparative purposes. The molecular structure of **3** (Fig. 4, 5 and Table 5.3) revealed the distorted six-coordinate geometry, which is defined by one terminal axial oxygen, two equatorial dithiolate sulfurs, and three pyrazolyl ring nitrogens. No symmetry is crystallographically imposed on the (Tp*)MoO(qdt) complex by the *P* $\bar{1}$ space group; however, the effective point symmetry of the molybdenum center is *C*₅. The terminal oxo ligand and the two sulfur donor atoms of the ene-1,2-dithiolate

chelate ligand (qdt) are constrained to be mutually *cis* to each other by the *fac* stereochemistry imposed by the tridentate (Tp*)⁻ ligand. The bond angles about the six-coordinate Mo atom deviate from that of octahedral geometry. This is evident by the three nonlinear *trans* angles, and as illustrated by the obtuse O-Mo-S1 = 99.82(7)° and O-Mo-S2 = 99.75(7)° *cis* angles. The O-Mo-S and O-Mo-N *cis* angles are found to be greater than 90° in all of the structurally characterized (Tp*)MoO(S₂) complexes, as anticipated. The angular distortions of the equatorial ligand donor atoms *cis* to a terminal oxo has been rationalized in terms of minimizing nonbonded repulsions between the filled p(π) orbitals of the donor atoms coordinated to Mo and the π-electron density in the short Mo≡O bond. The rigid geometric constraints and bonding properties of the (Tp*)⁻ ligand minimize the *cis* angular distortions involving the pyrazolyl ring nitrogens coordinated to Mo. These distortions result in the characteristic square pyramidal geometry for five-coordinate oxo-Mo(V) systems containing two to four sulfur donors, and are clearly greater than those in the six-coordinate (Tp*)MoO(S₂) complexes. This is evident from the larger O-Mo-S angles (~108°) and a greater displacement of Mo from the least-squares basal plane (~0.5 – 0.8 Å) in the five-coordinate complexes. The structural parameters of the [(Tp*)MoO]²⁺ core are not unusual and are in agreement with those found for other related structurally characterized oxo-Mo(V) complexes.¹⁻⁸ The observed Mo≡O distance (1.686(2) Å) in **3** is not significantly different from that of (Tp*)MoO(bdt) (1.678(4) Å),^{2,3} (Tp*)MoO(bdtCl₂) (1.679(3) Å) or (Tp*)MoO(SPh)₂ (1.676(4) Å). The terminal oxo ligand, as expected, exerts a *trans* influence, lengthening the Mo-N31 distance (2.348(2) Å) by 0.177 Å relative to Mo-N21 (2.171(2) Å) and 0.164

Å relative to Mo-N11 (2.184(2) Å). The Mo-N31 distance (2.372(4) Å) observed in (Tp*)MoO(bdt) is somewhat longer than in **3**. The average Mo-S distance (2.388 Å) in (Tp*)MoO(qdt) is lengthened (~0.015 Å (7σ)) compared to that observed in (Tp*)MoO(bdt) (2.373(2) Å). The mean O-Mo-S angle in **3** (99.8°) is slightly smaller than in **1** (100.9°) or **2** (101.4°) (see Table 5.4). The O-Mo-N *cis* angles in each of these complexes are observed to decrease slightly relative to an increase in the mean O-Mo-S angle, which tilts the N₂S₂ least squares-plane towards the ± z axes (projected along the Mo≡O bond vector), respectively. The *trans* O-Mo-N31 angle is distorted the least in **3**, which possesses the smallest mean O-Mo-S angle within this series of compounds. These angular deviations within the equatorial N₂S₂ planes of **3**, **2**, and **1** appear to be invariant as reflected by the nearly constant dihedral angle ($\theta_d \approx 162^\circ$) measured between the midpoint of the MoS₂ and MoN₂ planes in these six-coordinate systems. The result of these distortions in the *cis* angles (O-Mo-L_{eq} > 90°) is that the molybdenum atom in **3** is displaced ~0.258 Å above the N₂S₂ least-squares plane in the direction of the axial oxo ligand. This perpendicular displacement is slightly less than that observed for (Tp*)MoO(bdt) (0.264 Å). The S-Mo-S angle is 85.14(2)°, and nearly identical to that observed for (Tp*)MoO(bdt) (85.12(6)°). However, due to the elongated Mo-S bond lengths in **3**, the measured S---S non-bonded contact distance (3.231 Å) is slightly greater than that observed for (Tp*)MoO(bdt) (3.210 Å). This metric parameter is somewhat smaller than the estimated van der Waals contact of 3.7 Å and the nominal non-bonded S---S contact of 3.4 Å in the (Tp*)MoO(SPh)₂ complex (Mo-S_{avg} = 2.382 Å, S-Mo-S = 90.98°), which underscores the unique geometric constraints imposed by the ene-1,2-

dithiolate chelate ring coordinated to Mo in **1-3**. The other mean non-bonded contact distances in (Tp*)MoO(qdt) involving the atoms defining the inner coordination sphere about Mo are also slightly less than their estimated van der Waals contacts, as was the case for **1** and **2**.

The qdt ligand in **3** is approximately planar but folded up toward the terminal oxo ligand (Figure 5.4 and 5.5). The fold angle measured with respect to the midpoint of each of the planes is 29.5° in **3**. This is somewhat greater than the $21.3(1)^\circ$ fold angle measured for (Tp*)MoO(bdt). This deformation has been previously attributed to a steric (non-bonded) interaction between the C36 methyl group of the *trans* N31 pyrazolyl ring and the chelate ring C1 and C2 atoms of (Tp*)MoO(bdt). The C36---C1 and C36---C2 contact distances of 3.57 and 3.58 Å, respectively, in **1** are less than the estimated van der Waals contact of 3.72 Å between a methyl group and an aromatic ring. However, the C36---C1 and C36---C2 contact distances of 3.797 and 3.752 Å in **3** are substantially larger than those reported for **1** and **2**. A crystal packing analysis of **3** revealed no additional interactions with neighboring molecules (Figure 5.6). The C36---C1 and C36---C2 contact distances illustrate an interesting point regarding the symmetry of the molecule. The O-Mo-N31 angle is 169.2° , and the C36---C1 and C36---C2 distances are indistinguishable in (Tp*)MoO(bdt). A similar O-Mo-N31 angle is observed in (Tp*)MoO(qdt) (169.85°), but the C36---C1 and C36---C2 contact distances differ by 0.045 Å. These data are consistent with the N31 pyrazolyl ring deviating slightly from the mirror plane (see Figure 5.4; where C36 is canted towards C2) implying a lower

symmetry (C_1) for this compound (**3**). However, the difference in non-bonded contacts is sufficiently small that the effective point symmetry of **3** is still treated as C_5 .

The metric parameters of the MoS_2C_2 chelate ring are also of particular interest. Both complexes (**1** and **3**) have nearly identical S-C bond lengths of 1.76 Å that are within the normal range reported for oxo-Mo(V) ene-1,2-dithiolate systems.¹⁻⁸ However, the C1-C2 distance of 1.444(4) Å for **3** is larger than the corresponding bond length of 1.395(8) Å in **1** (Table 5.5). The dimensions of the qdt ligand in **3** are similar to those which have been reported for $[\text{Mo}(\text{qdt})_3]^{2-/1-}$, $[\text{Ni}(\text{qdt})_2]^{2-}$ and $[\text{Cu}(\text{qdt})_2]^{2-/1-}$.¹³⁻¹⁵ Therefore, the longer C1-C2 bond length observed in $(\text{Tp}^*)\text{MoO}(\text{qdt})$ relative to $(\text{Tp}^*)\text{MoO}(\text{bdt})$ appears to be a structural feature characteristic of transition metal complexes possessing the qdt ligand, which reflects the electron-withdrawing properties of the heterocyclic nitrogen atoms of the pyrazine ring that is fused directly to the ene-1,2-dithiolate chelate. The ene-1,2-dithiolate chelate ring fragment in these $(\text{Tp}^*)\text{MoO}(\text{dithiolate})$ complexes also exhibits a significant structural variation with respect to the Mo-S-C angle (Table 5.5). The mean Mo-S-C angle of 102.0° in **3** is smaller than that measured for **1** (103.8°) and **2** (107.0°).

The results of the X-ray crystallographic studies of $(\text{Tp}^*)\text{MoO}(\text{qdt})$ (**3**) and those reported previously for $(\text{Tp}^*)\text{MoO}(\text{bdt})$ (**1**) and $(\text{Tp}^*)\text{MoO}(\text{bdtCl}_2)$ (**2**) are important for understanding remote, and second coordination sphere ligand effects on the geometric and electronic structures of oxo-Mo mono-ene-1,2-dithiolate systems. The key feature obtained from comparing the molecular parameters of $(\text{Tp}^*)\text{MoO}(\text{qdt})$ (**3**) and $(\text{Tp}^*)\text{MoO}(\text{bdt})$ (**1**) is that the coordinate geometries are very similar, suggesting that

remote effects resulting from substitution on the benzene ring of the ene-1,2-dithiolate ligand do not induce significant structural changes involving the inner coordination about the molybdenum atom. These results are consistent with structures of oxo-Mo-ene-1,2-dithiolates obtained by X-ray and EXAFS that show no appreciable differences in the Mo-S bond distance.¹⁶⁻²⁰ However, as these remote effects involve EXAFS indiscernible changes, their contributions to the overall geometric structure in the protein active sites during catalytic turnover can only be elucidated directly by high-resolution X-ray crystallography as it becomes available. This is important, as the molecular structures of **3**, **2** and **1** have revealed that remote ligand effects do induce substantial changes in the second coordination sphere, which is evident by perturbations to the fold (θ) and Mo-S-C angles of the ene-1,2-dithiolate chelate. These outer-sphere structural variations may play an important role in fine tuning the electronic properties of oxomolybdenum dithiolates. Therefore, it remains to be determined whether the electronic structure differences observed between these complexes are due exclusively to the electron donating capabilities of the dithiolate ligand S donor atoms, as suggested by the relatively invariant inner coordination sphere metric parameters, or are also a consequence of second coordination sphere effects resulting in structural variations which affect the orientation of those orbitals involved in Mo-S interactions. These electronic and geometric structure correlations will be discussed in Chapters 6, 7 and 8.

3.3 Structure of (Tp*)WO(bdt) (4)

To the best of our knowledge, the X-ray crystal structure of (Tp*)WO(bdt) (4) reported here represents the first mononuclear six-coordinate monooxo-W(V) monoenedithiolate complex that has been structurally characterized by single-crystal X-ray diffraction. This structural characterization is of additional interest for the metal effects on the structural parameters upon substitution of a second row transition metal by a third row transition metal. Similar to its molybdenum analogue (1), the six-coordinate W center is facially coordinated by a hydrotris(3, 5-dimethylpyrazol-1-yl) ligand and a benzenedithiolate that is *cis* to the oxo ligand. The W≡O bond is 1.684(8) Å and compares to the observed Mo≡O distances of 1.678(4) Å in 1, 1.679(3) Å in 2, 1.686(2) Å in 3 and 1.676(4) Å in (Tp*)MoO(SPh)₂. The terminal oxo ligand, as expected, exerts a *trans* influence, lengthening the W-N31 distance (2.369(10) Å) by 0.189 Å relative to W-N21 (2.180(12) Å) and 0.183 Å relative to Mo-N11 (2.186(9) Å) that compares with the average *trans* effect of 0.194 Å in 1. The average Wo-S distance of 2.377 compares with Mo-S distance 2.373 Å in 1. The mean O-W-S angle of 100.8° in 4 is larger than O-Mo-S angle in 3 (99.8°) but slightly smaller than in 1 (100.9°) or 2 (101.4°). These angular deviations within the equatorial N₂S₂ planes of 1-4 appear to be invariant as reflected by the nearly constant dihedral angle ($\theta_d \approx 162^\circ$) measured between the midpoint of the MS₂ and MN₂ (where M = Mo or W) planes in these six-coordinate systems. The result of these distortions in the *cis* angles (O-W-L_{eq} > 90°) is that the tungsten atom in 4 is shifted 0.232 Å above the N₂S₂ least-squares plane in the direction of the apical oxo

ligand and this shift is slightly smaller than that observed for **1** (Tp*)MoO(bdt) (0.264 Å). The S-W-S angle of 85.73(12)° is larger than that observed for (Tp*)MoO(bdt) (85.12(6)°). The key bond lengths and angles for **4** are given in Table 5.7 and an ORTEP drawing of the molecule and its crystal packing is shown in Figures 5.7 and 5.8. The bdt ligand in **4** is folded up toward the terminal oxo ligand by an angle of 20.6° and compares with the 21.3(1)° fold angle measured for (Tp*)MoO(bdt) complex and is smaller than that of 29.5° in (Tp*)MoO(qdt) (**3**).

3.4 Structure of Cp₂Mo(bdt) (**5**)

The crystal structure of Cp₂Mo(bdt) has been reported previously²¹ but its coordinates are not available in the Cambridge Structural Database. The crystal structure was determined again in this work and utilized as a starting point for the density functional calculation reported in Chapter 7.

The crystal data, structure refinement parameters and key bond lengths and angles are given in Tables 5.8 and 5.9. The ORTEP diagram is shown in Figures 5.9 and 5.10. The molecules of Cp₂Mo(bdt) co-crystallize (see Figure 5.10) with a dimer of benzenedithiolate (C₆H₄S₂)₂, the source of which is not known. This dimer might have formed upon oxidation of the compound on the silica gel column during purification. However, this impurity did not affect the quality of the crystal, the diffraction data or the refinement. This crystal and the structure refinement turned out to be the best one of all of the structures reported in this work. The final R1 value is very small (2.9 %) and Goodness of fit (1.066) is very close to 1.00 for an ideal refinement. A crystal packing diagram for **5** is shown in Figure 5.11. The Mo-S bond lengths of 2.4355(6) Å and 2.4416(6) Å are larger than those observed for (Tp*)MoO(bdt) (**1**) and their average of 2.4386(6) Å contrasts with the average Mo-S bond lengths of 2.373(2) in **1**, 2.374(12) in **2**, and 2.388(7) in **3**. The lengthening of the Mo-S bond in Cp₂Mo(bdt) (**5**) might be due to the effective reduction of the metal center, that has an electronic configuration of 4d² in **5** compared to 4d¹ in **1-3**. S-Mo-S angle of 82.04(2) is smaller than that observed for

1-4 ($85.12(6)^\circ$ in **1** (Tp^*) $\text{MoO}(\text{bdt})$ and $85.73(12)^\circ$ in **4** ($(\text{Tp}^*)\text{WO}(\text{bdt})$)). The cyclopentadienyl rings are bent at an angle of 46.1° .

The fold angles of the metal-dithiolate are 5.9° and 8.2° in the two crystallographically distinct but chemically equivalent molecules.

4.0 Geometric and Electronic Structural Correlation:

The most significant structural perturbation observed within the (Tp^*) $\text{MoO}(\text{S-S})$ system is the fold angle (θ , Figure 5.1), which exhibits considerable variation among the (Tp^*) $\text{ME}(\text{S-S})$ and $\text{Cp}_2\text{Mo}(\text{bdt})$ complexes that have been investigated. For the (Tp^*) $\text{MoO}(\text{S-S})$ compounds the fold angle varies between $6.9 - 29.5^\circ$. The fold angle of **2** (6.9°) is substantially smaller than that of **1** (21.3°) and **3** (29.5°). Investigation of the crystal packing forces and electronic contributions to the fold angle in **1-4** has been done to assess the role that the fold angle may play in controlling the electronic structure and reactivity of Mo ene-1,2-dithiolate systems. Previous electronic studies and available crystal structures on various Mo(V)/ Mo(IV) dithiolene complexes such as [$\text{Cp}_2\text{Mo}(\text{S-S})$] $^+$,²²⁻²⁵ [$\text{MoO}(\text{S-S})_2$] $^-$,^{16,17,26} and [$\text{Mo}(\text{S-S})_3$] $^-$ ²⁷ revealed that the fold angle generally decreased upon reduction of the Mo center. This distortion appears to be electronic in origin. In a recent anionic and neutral photoelectron spectroscopic and computational study of $\text{Cp}_2\text{M}(\text{bdt})$ ($\text{M} = \text{Mo}, \text{Ti}$), [$\text{MoO}(\text{bdt})_2$] $^-$ and related compounds it was proposed that the fold angle was electronic in origin and appears to persist in the gas phase.^{10,28,29} The observed variances in fold angle as a function of the metal, axial substitution, and

electron donor properties of the dithiolate ligand in (Tp*)MoO(dithiolate) compounds seems electronic in origin. However, the fold angle observed in **1**, **2**, and **3** does not appear to follow the trends in the electron donor properties of the dithiolate ligand implied by the measured solution reduction potentials.³⁰ It is proposed that this structural distortion may fine tune the electronic structure and properties of the oxo-Mo(V) dithiolate systems, and also may play a regulatory role in the pyranopterin Mo and W enzymes during catalysis. The postulated role of this fold angle in conjunction with the obtuse O-M-S angles (oxo-gate hypothesis, orbital overlap model)³¹ would be to control the orientation (overlap) of the ene-1,2-dithiolate S p(π) donor orbitals with the Mo 4d_{xy} redox orbital and concomitantly with the unoccupied metal acceptor orbitals (d_{xz,yz}, d_{x²-y²}, and d_{z²}).

The compounds **1-5** provide access to two electronic configurations d¹ and d² of the metal center and the fold angles of the dithiolate range from 6.9° to 29.5° for the d¹ and 5.9° and 8.2° for d². The structure of Cp₂Mo(bdt) (**5**) (d²) reveals presence of a planar dithiolate. Structural studies of compounds with no electrons in the metal in-plane (metal orbital(s) in the metal-sulfur plane) orbital, are reported and discussed in Chapter 7. A large fold angle has been observed in these cases. Thus, the fold angle of the dithiolate, which is a geometric parameter, is closely related to the electronic occupation of the metal in-plane orbital. This folding could possibly play a role in modulating redox potentials by controlling the Mo effective nuclear charge via S σ and S π charge donation into the unfilled Mo acceptor d-orbitals.

Table 5.1. Crystal data and structure refinement parameters for (Tp*)MoO(bdtCl₂) (**2**).

Empirical formula	C ₂₁ H ₂₄ BCl ₂ MoN ₆ OS ₂ ·1/2C ₆ H ₁₄	
Formula weight	618.23	
Temperature	173(2) K	
Wavelength	0.71073 Å	
Crystal system	Monoclinic	
Space group	P2(1)/c	
Unit cell dimensions	a = 7.963(3) Å	α = 90°.
	b = 26.272(11) Å	β = 105.352(7)°.
	c = 14.016(6) Å	γ = 90°.
Volume	2828(2) Å ³	
Z	4	
Density (calculated)	1.553 Mg/m ³	
Absorption coefficient	0.83 mm ⁻¹	
F(000)	1252	
Crystal size	0.25 x 0.10 x 0.03 mm ³	
Theta range for utilized data	1.69 to 27.78°.	
Limiting Indices	-10 ≤ h ≤ 9, -34 ≤ k ≤ 34, -18 ≤ l ≤ 17	
Reflections utilized	30776	
Independent reflections	6266 [R(int) = 0.0539]	
Completeness to theta = 27.78°	93.7 %	
Absorption correction	None	
Max. and min. transmission	0.9757 and 0.8203	
Refinement method	Full-matrix least-squares on F ²	
Data / restraints / parameters	6266 / 0 / 340	
Goodness-of-fit on F ²	1.040	
Final R indices [I>2sigma(I)]	R1 = 0.0442, wR2 = 0.1005	
R indices (all data)	R1 = 0.0764, wR2 = 0.1147	
Largest diff. peak and hole	0.636 and -0.432 e.Å ⁻³	
RMS difference density	0.098e.Å ⁻³	

Table 5.2. Important bond lengths [Å] and angles [°] for (Tp*)MoO(bdtCl₂) (2).

Mo(1)-O(1)	1.679(3)	N(11)-Mo(1)-N(21)	86.17(11)
Mo(1)-N(11)	2.166(3)	O(1)-Mo(1)-S(2)	100.99(10)
Mo(1)-N(21)	2.177(3)	N(11)-Mo(1)-S(2)	94.92(8)
Mo(1)-S(2)	2.3683(12)	N(21)-Mo(1)-S(2)	167.05(8)
Mo(1)-S(1)	2.3805(12)	O(1)-Mo(1)-S(1)	101.81(10)
Mo(1)-N(31)	2.391(3)	N(11)-Mo(1)-S(1)	166.47(8)
S(2)-C(2)	1.750(4)	N(21)-Mo(1)-S(1)	91.54(8)
S(1)-C(1)	1.753(4)	S(2)-Mo(1)-S(1)	84.38(4)
C(2)-C(1)	1.406(5)	O(1)-Mo(1)-N(31)	166.79(11)
O(1)-Mo(1)-N(11)	91.60(12)	N(11)-Mo(1)-N(31)	78.40(11)
O(1)-Mo(1)-N(21)	91.87(12)	S---S bite distance:	3.190 Å
		Mo distance from N ₂ S ₂ plane:	0.258 Å

Table 5.3. Crystal data and structure refinement parameters for (Tp*)MoO(qdt) (3).

Empirical formula	C ₂₃ H ₂₆ BMoN ₈ OS ₂	
Formula weight	601.39	
Temperature	170(2) K	
Wavelength	0.71073 Å	
Crystal system	Triclinic	
Space group	<i>P</i> $\bar{1}$	
Unit cell dimensions	a = 9.8424(7) Å b = 11.2323(8) Å c = 11.9408(8) Å	$\alpha = 92.7560(10)^\circ$ $\beta = 98.9530(10)^\circ$ $\gamma = 104.1680(10)^\circ$
Volume	1259.21(15) Å ³	
Z	2	
Density (calculated)	1.586 Mg/m ³	
Absorption coefficient	0.721 mm ⁻¹	
F(000)	614	
Crystal size	0.15 x 0.10 x 0.10 mm ³	
Theta range for utilized data	1.73 to 29.57°.	
Limiting Indices	-13 ≤ h ≤ 13, -15 ≤ k ≤ 15, -16 ≤ l ≤ 16	
Reflections utilized	16848	
Independent reflections	6424 [R(int) = 0.0309]	
Completeness to theta = 29.57°	90.9 %	
Absorption correction	Empirical	
Max. and min. transmission	1.00 and 0.934873	
Refinement method	Full-matrix least-squares on F ²	
Data / restraints / parameters	6424 / 0 / 331	
Goodness-of-fit on F ²	1.071	
Final R indices [I > 2σ(I)]	R1 = 0.0346, wR2 = 0.0850	
R indices (all data)	R1 = 0.0490, wR2 = 0.0925	
Largest diff. peak and hole	1.626 and -0.349 e.Å ⁻³	
RMS difference density	0.098 e.Å ⁻³	

Table 5.4. Important bond lengths [Å] and angles [°] for (Tp*)MoO(qdt) (3).

Mo(1)-O(1)	1.686(2)
Mo(1)-N(11)	2.171(2)
Mo(1)-N(21)	2.184(2)
Mo(1)-N(31)	2.348(2)
Mo(1)-S(1)	2.3824(7)
Mo(1)-S(2)	2.3938(7)
S(2)-C(2)	1.761(3)
S(1)-C(1)	1.760(3)
C(2)-C(1)	1.444(4)
O(1)-Mo(1)-N(11)	93.49(9)
O(1)-Mo(1)-N(21)	93.00(8)
N(11)-Mo(1)-N(21)	86.30(8)
O(1)-Mo(1)-N(31)	169.85(8)
N(11)-Mo(1)-N(31)	79.68(8)
N(21)-Mo(1)-N(31)	79.16(7)
(S1)-Mo(1)-N(31)	87.13(6)
(S2)-Mo(1)-N(31)	88.13(5)
O(1)-Mo(1)-S(1)	99.82(7)
N(11)-Mo(1)-S(1)	166.68(6)
N(21)-Mo(1)-S(1)	93.06(6)
O(1)-Mo(1)-S(2)	99.75(7)
N(11)-Mo(1)-S(2)	92.55(6)
N(21)-Mo(1)-S(2)	167.25(6)
S(1)-Mo(1)-S(2)	85.14(2)
C(1)-S(1)-Mo(1)	101.69(9)
C(2)-S(2)-Mo(1)	102.38(9)
C(1)-C(2)-S(2)	120.3(2)
C(2)-C(1)-S(1)	120.5(2)
S---S bite distance:	3.231
Mo distance from N ₂ S ₂ plane:	0.258
Fold Angle (θ)	29.5
θ _a (MoS ₂ ∠ MoN ₂)	162.2

Table 5.5. Important mean bond lengths [Å] and angles [°] for (Tp*)MoO(qdt) (**3**), (Tp*)MoO(bdt) (**1**) and (Tp*)MoO(bdtCl₂) (**2**).^a

	(3)	(2)	(1) ^b
Mo(1)-O(1)	1.686(2)	1.679(3)	1.678(4)
Mo(1)-N(eq)	2.177(2)	2.171(3)	2.178(5)
Mo(1)-N(31)	2.348(2)	2.391(3)	2.372(4)
Mo(1)-S(eq)	2.388(7)	2.374(12)	2.373(2)
S-C	1.761(3)	1.751(4)	1.760(6)
C(2)-C(1)	1.444(4)	1.406(5)	1.395(8)
O(1)-Mo(1)-N(eq)	93.25(9)	91.73(12)	92.35(2)
N(11)-Mo(1)-N(21)	86.30(8)	86.17(11)	85.5(2)
O(1)-Mo(1)-N(31)	169.85(8)	166.79(11)	169.2(2)
N(eq)-Mo(1)-N(31)	79.42(8)	78.70(11)	79.8(2)
S(eq)-Mo(1)-N(31)	87.63(6)	88.32(8)	86.95(1)
O(1)-Mo(1)-S(eq)	99.79(7)	101.40(10)	100.95(2)
N(11)-Mo(1)-S(1)	166.68(6)	166.47(8)	167.3(1)
N(21)-Mo(1)-S(1)	93.06(6)	91.54(8)	93.7(1)
N(11)-Mo(1)-S(2)	92.55(6)	94.92(8)	92.6(1)
N(21)-Mo(1)-S(2)	167.25(6)	167.05(8)	166.1(1)
S(1)-Mo(1)-S(2)	85.14(2)	84.38(4)	85.12(6)
Mo-S(eq)-C	102.0	107.0	103.8
S(eq)-C(1)-C(2)	120.4	120.6	121.0
S---S bite distance:	3.231	3.190	3.210
Mo distance from N ₂ S ₂ plane:	0.258	0.258	0.264
Fold Angle (θ)	29.5	6.9	21.3
θ _d (MoS ₂ ∠ MoN ₂)	162.2	162.2	161.2

^a eq refers to averaged equatorial ligand parameters. ^b Parameters taken from reference.²

Table 5.6. Crystal data and structure refinement for (Tp*)WO(bdt) (4).

Empirical formula	$C_{21}H_{26}BN_6O_2S_2W$	
Formula weight	637.26	
Temperature	173(2) K	
Wavelength	0.71073 Å	
Crystal system	Monoclinic	
Space group	P2(1)/n	
Unit cell dimensions	a = 10.7433(11) Å	$\alpha = 90^\circ$.
	b = 14.5586(15) Å	$\beta = 100.430(2)^\circ$.
	c = 15.6532(16) Å	$\gamma = 90^\circ$.
Volume	2407.8(4) Å ³	
Z	4	
Density (calculated)	1.758 Mg/m ³	
Absorption coefficient	4.997 mm ⁻¹	
F(000)	1252	
Crystal size	0.10 x 0.10 x 0.02 mm ³	
Theta range for utilized data	1.93 to 27.33°.	
Limiting Indices	-13 ≤ h ≤ 13, -17 ≤ k ≤ 17, -19 ≤ l ≤ 19	
Reflections utilized	24586	
Independent reflections	5031 [R(int) = 0.1224]	
Completeness to theta = 27.33°	92.4 %	
Absorption correction	None	
Max. and min. transmission	0.9067 and 0.6349	
Refinement method	Full-matrix least-squares on F ²	
Data / restraints / parameters	5031 / 0 / 295	
Goodness-of-fit on F ²	0.986	
Final R indices [I > 2σ(I)]	R ₁ = 0.0605, wR ₂ = 0.1360	
R indices (all data)	R ₁ = 0.1421, wR ₂ = 0.1782	
Largest diff. peak and hole	1.701 and -1.810 e.Å ⁻³	
RMS difference density	0.229 e.Å ⁻³	

Table 5.7. Important bond lengths [Å] and angles [°] for (Tp*)WO(bdt) (**3**).

C(2)-C(1)	1.424(19)
W(1)-O(1)	1.684(8)
W(1)-N(21)	2.180(12)
W(1)-N(11)	2.186(9)
W(1)-S(2)	2.365(4)
W(1)-N(31)	2.369(10)
W(1)-S(1)	2.389(3)
S(1)-C(1)	1.791(15)
S(2)-C(2)	1.748(14)
O(1)-W(1)-N(21)	91.6(4)
O(1)-W(1)-N(11)	93.8(4)
N(21)-W(1)-N(11)	84.9(4)
O(1)-W(1)-S(2)	101.4(3)
N(21)-W(1)-S(2)	166.9(3)
N(11)-W(1)-S(2)	93.6(3)
O(1)-W(1)-N(31)	168.9(4)
S(2)-W(1)-S(1)	85.73(12)
N(31)-W(1)-S(1)	86.8(2)
S(2)-W(1)-N(31)	87.5(3)
O(1)-W(1)-S(1)	100.2(3)
C(1)-S(1)-W(1)	103.5(5)
C(2)-S(2)-W(1)	104.5(5)
C(3)-C(2)-S(2)	120.8(11)
C(1)-C(2)-S(2)	121.7(11)

Table 5.8. Crystal data and structure refinement for Cp₂Mo(bdt) (**5**).

Empirical formula	C ₇₆ H ₆₄ Mo ₄ S ₁₂	
Formula weight	1745.75	
Temperature	170(2) K	
Wavelength	0.71073 Å	
Crystal system	Monoclinic	
Space group	P2(1)/c	
Unit cell dimensions	a = 12.4247(9) Å	α = 90°.
	b = 20.1645(15) Å	β = 109.474(2)°.
	c = 14.1781(11) Å	γ = 90°.
Volume	3348.9(4) Å ³	
Z	2	
Density (calculated)	1.731 Mg/m ³	
Absorption coefficient	1.152 mm ⁻¹	
F(000)	1760	
Crystal size	.3 x .3 x .5 mm ³	
Theta range for utilized data	1.74 to 27.52°.	
Limiting Indices	-16 ≤ h ≤ 16, -26 ≤ k ≤ 26, -18 ≤ l ≤ 18	
Reflections utilized	40594	
Independent reflections	7704 [R(int) = 0.0401]	
Completeness to theta = 27.52°	99.9 %	
Absorption correction	Empirical	
Refinement method	Full-matrix least-squares on F ²	
Data / restraints / parameters	7704 / 0 / 415	
Goodness-of-fit on F ²	1.066	
Final R indices [I > 2σ(I)]	R1 = 0.0291, wR2 = 0.0656	
R indices (all data)	R1 = 0.0396, wR2 = 0.0692	
Largest diff. peak and hole	0.952 and -0.335 e.Å ⁻³	
RMS difference density	0.093 e.Å ⁻³	

Table 5.9. Important bond lengths [Å] and angles [°] for Cp₂Mo(bdt) (**5**).

Mo(1)-S(11)	2.4355(6)
Mo(1)-S(12)	2.4416(6)
S(11)-C(11)	1.759(2)
S(12)-C(12)	1.763(2)
C(12)-C(11)	1.397(3)
S(11)-Mo(1)-S(12)	82.04(2)
C(11)-S(11)-Mo(1)	108.10(8)
C(12)-S(12)-Mo(1)	107.39(8)

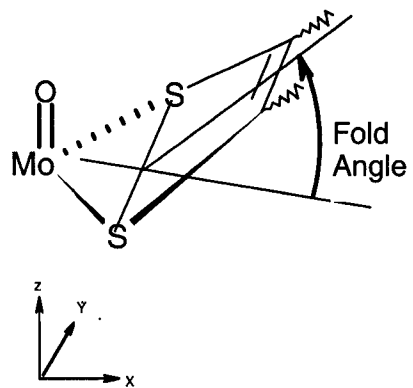


Figure 5.1. The definition of the fold angle.

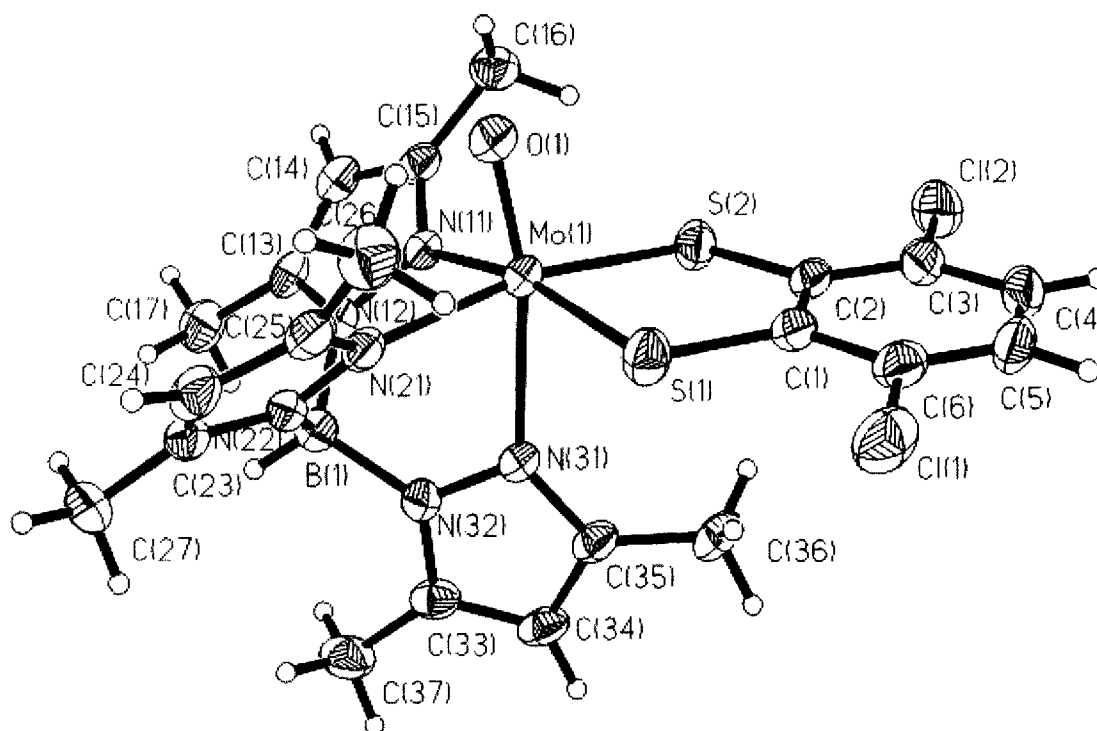


Figure 5.2. The ORTEP drawing of (Tp*)MoO(bdtCl₂) (2). The atoms are drawn as 50% probability ellipsoids. H-atoms have been made arbitrarily small for clarity

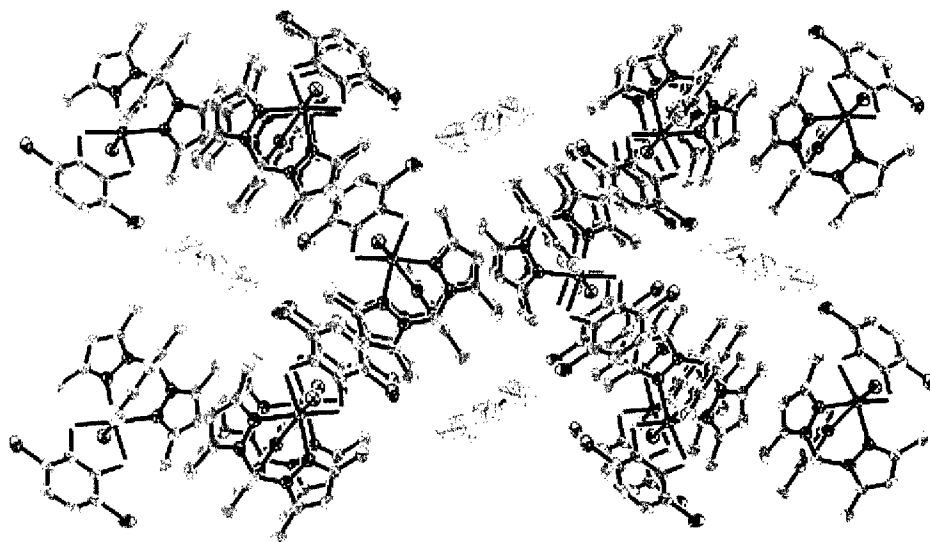


Figure 5.3. Compound $(\text{Tp}^*)\text{MoO}(\text{bdtCl}_2)$ (**2**) in $P2(1)/c$ space group, orientation along a axis in a unit cell.

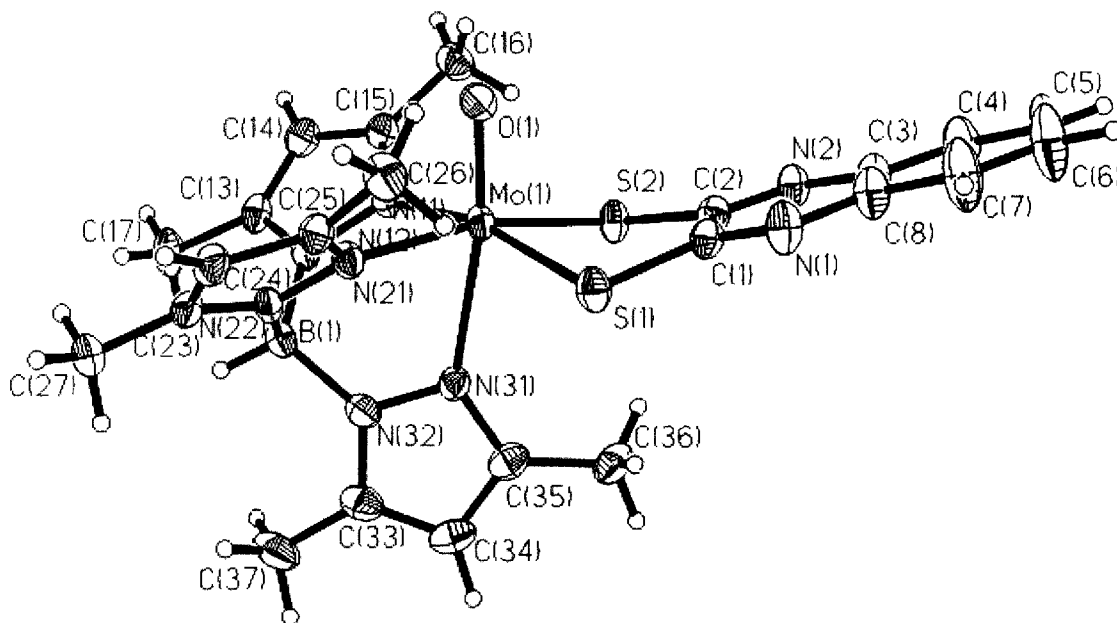


Figure 5.4. The ORTEP drawing of $(\text{Tp}^*)\text{MoO}(\text{qdt})$ (**3**). The atoms are drawn as 50% probability ellipsoids. H-atoms have been made arbitrarily small for clarity

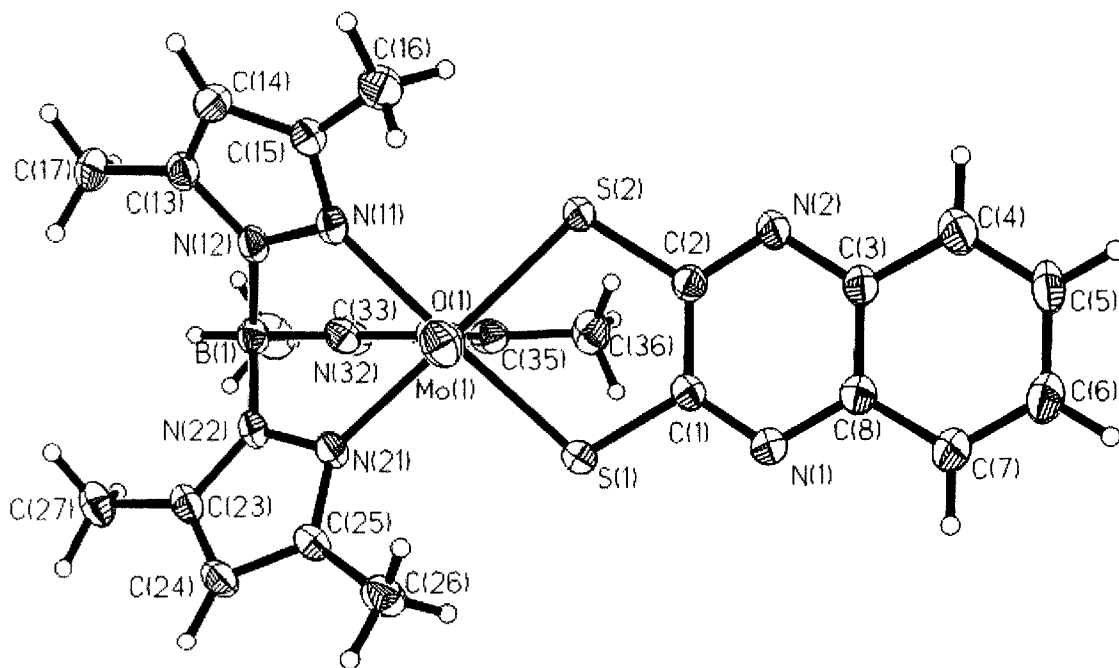


Figure 5.5. Top view: the ORTEP drawing of $(\text{Tp}^*)\text{MoO}(\text{qdt})$ (**3**). The atoms are drawn as 50% probability ellipsoids. H-atoms have been made arbitrarily small for clarity

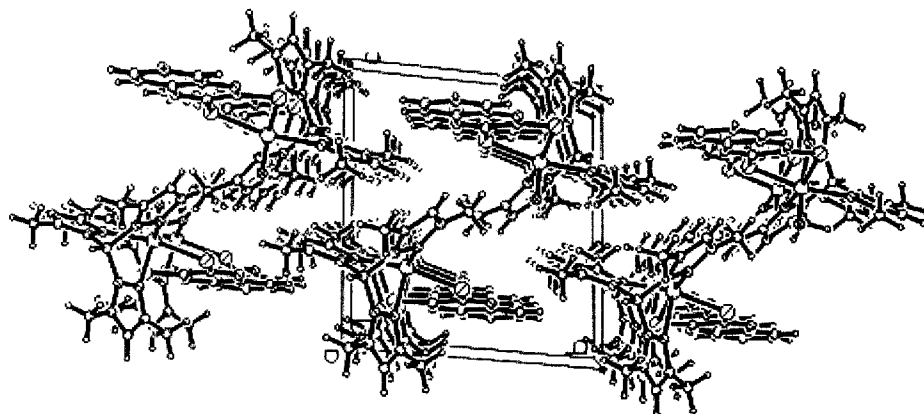


Figure 5.6. Compound (Tp*)MoO(qdt) (2) in $P\bar{1}$ space group, orientation along a axis in a unit cell.

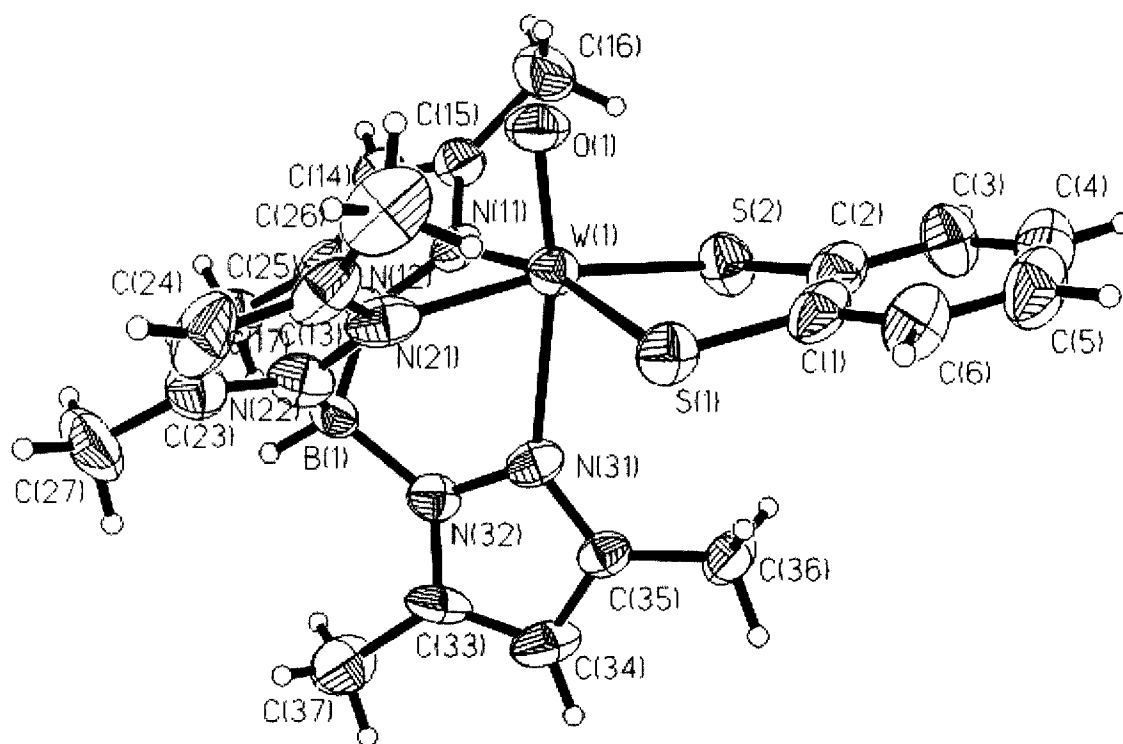


Figure 5.7. The ORTEP drawing of $(\text{Tp}^*)\text{WO}(\text{bdt})$ (**4**). The atoms are drawn as 50% probability ellipsoids. H-atoms have been made arbitrarily small for clarity.

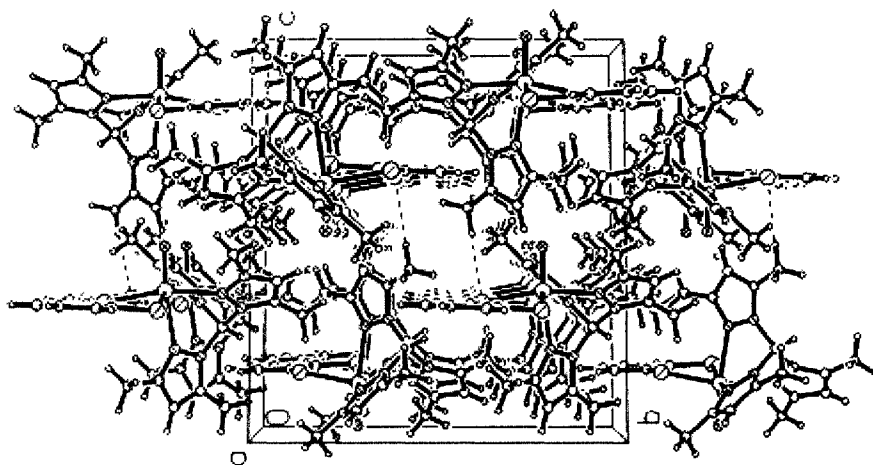


Figure 5.8. Compound (Tp*)WO(bdt) (4) in P2(1)/n space group, orientation along a axis in a unit cell.

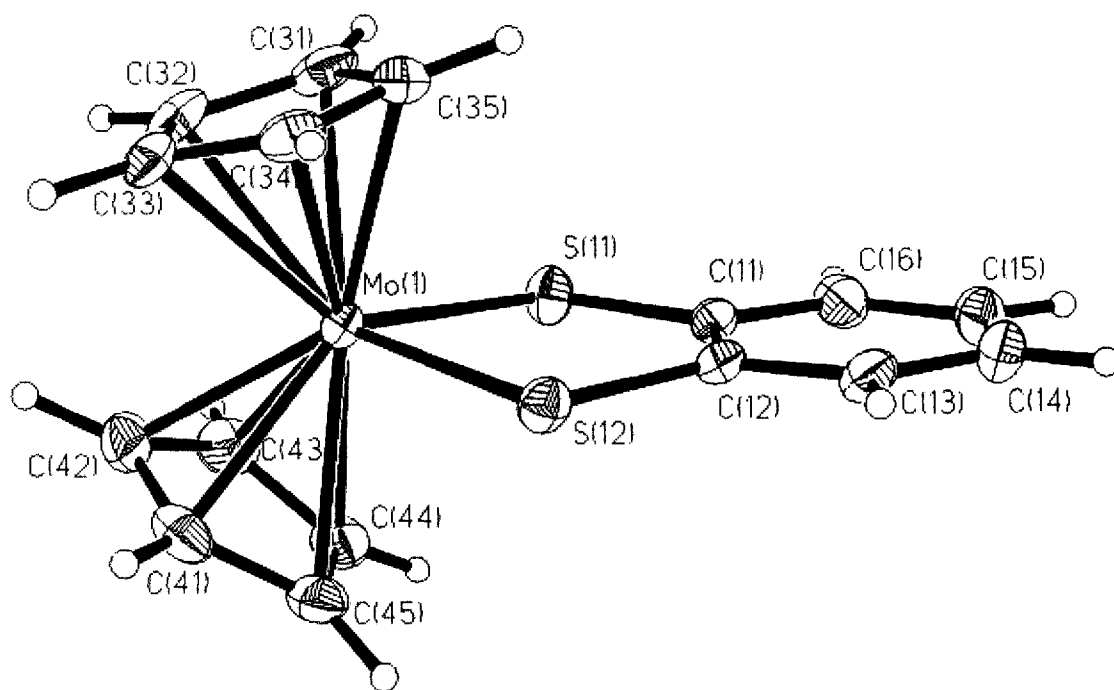


Figure 5.9. The ORTEP drawing of Cp₂Mo(bdt) (**5**). The atoms are drawn as 50% probability ellipsoids. H-atoms have been made arbitrarily small for clarity.

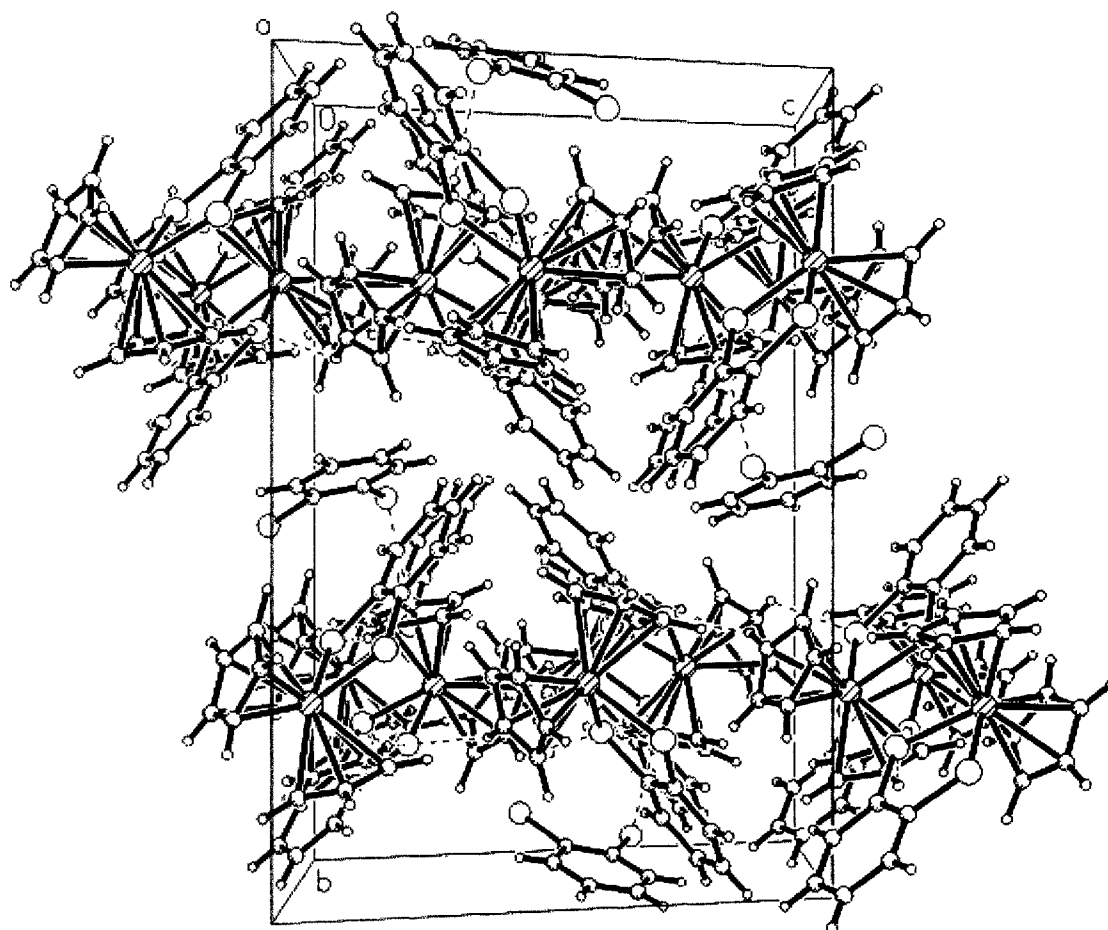


Figure 5.11. Compound Cp₂Mo(bdt) (5) in P2(1)/c space group, orientation along a axis in a unit cell.

5.0 References

1. Cleland, W. E., Jr.; Barnhart, K. M.; Yamanouchi, K.; Collison, D.; Mabbs, F. E.; Ortega, R. B.; Enemark, J. H. *Inorg. Chem.* **1987**, *26*, 1017-1025.
2. Dhawan, I. K.; Pacheco, A.; Enemark, J. H. *J. Am. Chem. Soc.* **1994**, *116*, 7911-7912.
3. Dhawan, I. K.; Enemark, J. H. *Inorg. Chem.* **1996**, *35*, 4873-4882.
4. Chang, C. S. J.; Pecci, T. J.; Carducci, M. D.; Enemark, J. H. *Acta Crystallogr.* **1992**, *C48*, 1096-1097.
5. Basu, P.; Bruck, M. A.; Li, Z.; Dhawan, I. K.; Enemark, J. H. *Inorg. Chem.* **1995**, *34*, 405-407.
6. Chang, C. S. J.; Pecci, T. J.; Carducci, M. D.; Enemark, J. H. *Inorg. Chem.* **1993**, *32*, 4106-4110.
7. Roberts, S. A.; Ortega, R. B.; Zolg, L. M.; Cleland, W. E., Jr.; Enemark, J. H. *Acta Crystallogr., Sect. C: Crystallogr. Struct. Commun.* **1987**, *C43*, 51-53.
8. Kipke, C. A.; Cleland, W. E., Jr.; Roberts, S. A.; Enemark, J. H. *Acta Crystallogr.* **1988**, *C45*, 870-872.
9. Inscore, F. E.; Joshi, H. K.; McElhaney, A. E.; Enemark, J. H. *Inorg. Chim. Acta* **2002**, *331*, 246-256.
10. Joshi, H. K.; Inscore, F. E.; Schirlin, J. T.; Dhawan, I. K.; Carducci, M. D.; Bill, T. G.; Enemark, J. H. *Inorg. Chim. Acta* **2002**, *337*, 275-286.
11. Cromer, D. T.; Waber, J. *Int. Tables X-Ray Crystallogr.* **1974**, *4*, 71-147.
12. Cromer, D. T.; Ibers, J. A. *Int. Tables X-Ray Crystallogr.* **1974**, *4*, 148-51.

13. Boyde, S.; Garner, C. D.; Enemark, J. H.; Bruck, M. A.; Kristofzski, J. G. *J. Am. Chem. Soc., Dalton Trans.* **1987**, 2267-2271.
14. Pignedoli, A.; Peyronel, G.; Antolini, L. *Acta Crystallogr., Sect. B: Struct. Crystallogr. Cryst. Chem.* **1974**, B30, Pt. 9, 2181-5.
15. Boyde, S.; Garner, C. D.; Clegg, W. *J. Chem. Soc., Dalton Trans.* **1987**, 5, 1083-7.
16. Boyde, S.; Ellis, S. R.; Garner, C. D.; Clegg, W. *J. Chem. Soc., Chem. Commun.* **1986**, 20, 1541-3.
17. Lim, B.; Donahue, J.; Holm, R. *Inorg. Chem.* **2000**, 39 (2), 263-73.
18. Lim, B.; Willer, M.; Miao, M.; Holm, R. *J. Am. Chem. Soc.* **2001**, 123 (34), 8343-9.
19. Musgrave, K. B.; Donahue, J. P.; Lorber, C.; Holm, R.; Hedman, B.; Hodgson, K. *O. J. Am. Chem. Soc.* **1999**, 121 (44), 10297-10307.
20. Musgrave, K. B.; Lim, B. S.; Sung, K. M.; Holm, R.; Hedman, B.; Hodgson, K. *O. Inorg. Chem.* **2000**, 39 (23), 5238-5247.
21. Kutoglu, A.; Köpf, H. *J. Organomet. Chem.* **1970**, 25, 455-460.
22. Fourmigue, M. *Coord. Chem. Rev.* **1998**, 178-180 (Pt. 1), 823-864.
23. Fourmigue, M.; Domercq, B.; Jourdain, I. V.; Molinie, P.; Guyon, F.; Amaudrut, J. *Chem. Eur. J.* **1998**, 4 (9), 1714-1723.
24. Clerac, R.; Fourmigue, M.; Gaultier, J.; Barrans, Y.; Albouy, P.; Coulon, C. *European Physical Journal B: Condensed Matter Physics* **1999**, 9 (3), 431-443.
25. Domercq, B.; Coulon, C.; Fourmigue, M. *Inorg. Chem.* **2001**, 40 (2), 371-378.

26. Donahue, J. P.; Goldsmith, C. R.; Nadiminti, U.; Holm, R. *J. Am. Chem. Soc.* **1998**, *120* (49), 12869-12881.
27. Cervilla, A.; Llopis, E.; Marco, D.; Perez, F. *Inorg. Chem.* **2001**, *40* (25), 6525-8.
28. Wang, X.-B.; Inscore, F. E.; Yang, X.; Cooney, J. J. A.; Enemark, J. H.; Wang, L.-S. *J. Am. Chem. Soc.* **2002**, *124*, 10182-10191.
29. Joshi, H. K.; Cooney, J. J. A.; Inscore, F. E.; Gruhn, N. E.; Lichtenberger, D. L.; Enemark, J. H. *Proc. Natl. Acad. Sci. USA* **2003**, *100* (7), 3719-3724.
30. McElhaney, A. E.; Inscore, F. E.; Schirilin, J. T.; Enemark, J. H. *Inorg. Chim. Acta* **2002**, *341*, 85-90.
31. Inscore, F. E.; McNaughton, R.; Westcott, B.; Helton, M. E.; Jones, R.; Dhawan, I. K.; Enemark, J. H.; Kirk, M. L. *Inorg. Chem.* **1999**, *38*, 1401-1410.

CHAPTER 6: Electronic Structure Comparison to Ionization Potential of Oxo-Mo/W Ene-1, 2-dithiolate Compounds: Experimental and Theoretical Evaluation of the Second Coordination Effects

1.0 Introduction

Pyranopterindithiolate Mo and W enzymes are ubiquitous in nature. These enzymes are categorized into three families based on their structure and reactivity, (i) sulfite oxidase (SO), (ii) xanthine oxidase (XO) and (iii) dimethylsulfoxide (DMSO) reductase.^{1,2} They catalyze a variety of oxidation/reduction and oxygen atom transfer reactions in carbon, nitrogen and sulfur metabolism.¹ The oxygen atom transfer reactions are also accompanied by a transfer of two electrons. The versatile chemistry including ability to switch between multiple oxidation states and their bioavailability designate the transition metals Mo and W suitable for enzymatic reactions.

The X-ray crystal structures and EXAFS studies of sulfite oxidase from chicken liver^{3,4} and plant,⁵ *Arabidopsis thaliana*, reveal presence of an unusual square pyramidal coordination geometry of Mo center with a pyranopterindithiolate *cis* to an axial oxo ligand. The chicken liver and plant sulfite oxidase represent the only known structurally characterized enzymes in the SO family, where the 3 D structures of Mo containing domain is known. However, a number of enzymes have been structurally characterized in the XO family including a recent atomic resolution crystal structure of aldehyde oxidase (MOP) at 1.28 Å from *Desulfovibrio gigas*. These structures highlight the presence of a single Mo=O (bond lengths of 1.7 Å⁴ and 1.77 Å⁵) in an axial position. The mononuclear W-containing enzymes aldehyde ferredoxin oxidoreductase (AOR), formaldehyde ferredoxin oxidoreductase (FOR) from the hyperthermophilic archaeon *Pyrococcus furiosus* (Pf), and formate dehydrogenase (W-FDH) from *Desulfovibrio gigas* are some examples of structurally characterized pyranopterin W enzymes.⁶⁻⁹ The

crystallographic results for these enzymes have established that two pyranopterin dithiolate ligands are coordinated to W in a distorted square pyramidal arrangement. A selenium atom (as a Se-cysteine) is coordinated to the W site in W-FDH.^{6,7} The results from a W-XAS study of dithionite-reduced active samples of Pf AOR reported the presence of a single W≡O (1.75Å), four or five W-S (2.40Å), and one possible W-O/N (1.97Å) interaction(s).¹⁰ While no details of the active site were reported in the X-ray crystallography studies, the W-XAS, EPR, spectroscopic and chemical data appears to be in good agreement with the crystallographically determined structure with respect to the type and number of ligands coordinated to W.¹¹⁻¹⁷ The structural data for Pf AOR can be interpreted in the context of a monooxo-W(VI) active site (desoxo-W(IV) site), or that a single terminal oxo ligand may be present throughout the catalytic cycle of Pf AOR as observed in the xanthine oxidase family of Mo containing enzymes.

A structural role for the pyranopterindithioate cofactor has begun to emerge with the recent report of a number of the enzyme crystal structures; however a functional role has not been established yet. This cofactor is postulated to modulate the effective nuclear charge and hence the chemical potential of the metal center. Some of these issues can be addressed through studies of the discrete molecules containing essential features of the active sites. The metal coordination to the pyranopterindithiolate can be mimicked up to the second coordination sphere by metal-enedithiolate adducts. An unusual ability of dithiolate ligands to stabilize the multiple oxidation states of the metal center was realized when these compounds were first reported.¹⁸

The spectroscopic,¹⁹⁻²⁶ electrochemical,²⁷⁻³⁰ and oxo atom transfer reactivity,^{28,31-38} properties of oxo-M, oxo-M dithiolene and M-dithiolene complexes (M= Mo, W) are of considerable importance for developing insight into the origin of Mo vs W selectivity at the active sites of the pyranopterin-dithiolate Mo and W enzymes. Some very interesting trends of chemically reversible redox couples measured for a wide range of mononuclear Mo and W complexes are present.^{27,29,30} The half-wave potentials are found to be not only dependent upon the nature of the central metal ion but also on the nature of the ligand donor atoms and remote ligand substituents for the same metal. The reduction potentials of Mo and W complexes possessing identical donor ligand sets, without exception, follow the order $E_{\text{Mo}} > E_{\text{W}}$.²⁷ The more positive reduction potentials for the Mo complexes is indicative of their greater ability to be reduced relative to their equivalent W counterparts. The more positive reduction potentials of Mo redox couples than their W analogues ($E_{\text{Mo}} > E_{\text{W}}$) might be due to the inherent difference between valence ionization energies of 4d and 5d shells. The Mo and W complexes of M-hexachloride (0.68 V) and M-trisdithiolate type have considerable (0.04 ~ 0.20 V) separation of reduction potentials.^{29,30} Oxo-M (V/IV) complexes possessing ene-1,2-dithiolate ligands such as bdt and mnt (maleonitrile dithiolate) are of the symmetric dithiolate type. In the $[\text{MO}(\text{bdt})_2]^{-1/2}$ couple for example, the M(V) oxidation state is well defined by EPR spectroscopy and as a consequence, the bidentate sulfur donor chelate ligand coordinated to the +5 and +4 metal ion centers is reasonably formulated as a dithiolate dianion with a formal oxidation state of 2-.²⁷ Within this formulation, the oxidation states of the metal and redox innocent dithiolate ligand are both well defined.

The decreased potential difference in complexes of $[\text{MO}(\text{L})_4]^{-1/2}$ type containing sulfur donor ligands relative to those possessing halide donors ($\text{L} = \text{Cl}$) has been attributed to bond covalency as in the $[\text{MO}(\text{SPh})_4]^{-1/2}$ and $[\text{MO}(\text{SR})_4]^{-1/2}$ type compounds,²³ and their redox potential difference ($E_{\text{Mo}^0} - E_{\text{W}} = 0.28 \text{ V}$) is approximately the same as that in $[\text{MO}(\text{bdt})_2]^{-1/2}$. The decreased potential difference discussed by Holm and co-workers,²⁷ is presumably a direct consequence of the covalency of the Mo-S and W-S bonds that leads to considerable delocalization of the electronic charge and thus diffusing the effect of the metal. The $[\text{MO}(\text{mnt})_2]^{-1/2}$ couples exhibit a potential difference of $\sim 0.17 \text{ V}$. The smallest potential differences (0.04 V) are found between the highly oxidized Mo and W $[\text{M}(\text{tfd})_3]^{0/-1; -1/2}$ complexes (where $\text{tfd}^{2-} = 1,2\text{-bis}(\text{trifluoromethyl})\text{ethylene-1,2-dithiolate}$) in which the metal and noninnocent ligand oxidation states are not certain as a result of electron delocalization. Similar metal-dependent trends in reduction potentials have been observed within an analogous series of asymmetric ene-1,2-dithiolate complexes, $[\text{MO}(\text{dithiolene})_2]^{-1/2}$ (where dithiolene = $-\text{SC}(\text{H})\text{C}(\text{R})\text{S}-$; $\text{R} = \text{phenyl}$, pyridin-2-yl, pyridin-3-yl, pyridin-4-yl, quinoxalin-2-yl), which exhibited W(V)-W(IV) couples $\sim 0.225 \text{ V}$ more negative than the corresponding Mo(V)-Mo(IV) system.^{25,26} The potential differences ($E_{\text{Mo}^0} - E_{\text{W}} \sim 0.225 - 0.240 \text{ V}$) appears to be invariant regardless of the nature of the substituent R group and is only slightly smaller to that reported between the symmetric ene-1,2-dithiolate $[\text{MO}(\text{bdt})_2]^{-1/2}$ complexes. However, examination of the individual W(V)-W(IV) couples (and of the Mo analogs as well) clearly showed that the nature of the remote substituents strongly influence the magnitude of the reduction potentials. The M(V)/M(IV) reduction potentials become less negative (harder to

oxidize) as the net electron withdrawing nature of the R group increases (e.g. R: Ph (W, -0.705 V; Mo, -0.480 V); quinoxaline-2-yl (W, -0.520 V; Mo, -0.280 V)). It is significant that the potential shift as a function of these two R groups is ~ 0.200 V for both the W and Mo series. Such differences in redox potentials may be important with respect to one metal ion being preferred over the other metal for a specific biological role. In this context, Holm and co-workers have shown that the relative strength of Mo \equiv O and W \equiv O bonds appear to facilitate faster oxygen atom transfer for Mo vs. W, which may add selectivity (reactivity differences) based on reduction potentials.²⁷

The scorpionate ligand stabilized group VI metal compounds (Tp*)Mo(bdt) (1), (Tp*)Mo(bdtCl₂) (2), (Tp*)Mo(qdt) (3), (Tp*)Mo(tdt) (4), (Tp*)W(bdt) (5), (Tp*)W(tdt) (6) (where Tp* = hydrotris(3,5-dimethylpyrazol-1-yl)borate, bdt = 1,2-benzenedithiolate, bdtCl₂ = 3, 6-dichloro-1, 2-benzenedithiolate, qdt = 2,3-dithioquinoxaline, tdt = 3, 4-toluenedithiolate) have been studied as minimum molecular models of the M(V) oxidation state that contain a M \equiv O group *cis* to an enedithiolate relevant to the active sites of pyranopterindithiolate enzymes. A combination of electronic absorption, magnetic circular dichroism, and resonance Raman spectroscopies was utilized by Inscore and Kirk *et al.* to probe the excited state electronic structure of LWO(bdt) and LWO(tdt).³⁹

The solution redox potential studies of (Tp*)MO(S-S) found a strong dependence of electrochemical potential on nature of the remote substituents on the benzene ring of the dithiolate ligand.⁴⁰ However, the heterogeneous electron transfer rates were insensitive to the variation of metal (M = Mo or W) or remote ligand substitution.⁴⁰ The

reduction potential difference of Mo/W couple in (Tp*)MO(tdt) complexes is 0.38 V, and again the Mo complex was found easier to be reduced.⁴⁰

The previous photoelectron spectroscopic studies on (Tp*)MoO(diolato) complexes⁴¹ indicate that the lowest ionization is a metal based ionization. In these complexes, the diolato ligand is part of metallocycle and it was shown that increase in the size of the cycle by modification in dialato ligand lowers the ionization energy of the HOMO. The ionization region 8.00 -11.00 eV contains overlapping ionizations for these complexes and has been assigned to the pyrazole- π based molecular orbitals. This study was followed by a comparative photoelectron spectroscopic studies of (Tp*)MoE(OEt)₂ and (Tp*)MoE(tdt) (where E = O, S, NO) that found that the changes in the oxidation states of the metal and the π -effects of strongly bound axial ligands are essentially neutralized by the coordinated enedithiolate ligand and resulted in the proposal of an “electronic-buffering effect” of the dithiolate coordination.⁴² The dithiolate based ionization were identified in another follow-up study on (Tp*)MoO(qdt) complex.⁴³ The Cp₂M(dithiolate) compounds have been recently utilized to study metal-dithiolate interactions.⁴⁴ The reports of the experimental evidence of a “dithiolate-folding-effect” for these have provided a mechanism for the buffering of electron density at the metal center that can be instrumental in stabilizing multiple oxidation states of the metal center.⁴⁴ Similarly, interactions of the metal and oxo ligation have been studied utilizing X-ray crystal structural and MCD, rR and electronic spectroscopies.⁴⁵ An “oxo-gate hypothesis” emphasizing the strong metal-oxo interactions dominating the electronic structure of related compounds was proposed.⁴⁵ According to this hypothesis a strong σ

and π -donor oxo ligand destabilizes the metal out of plane orbitals (d_{xz} , d_{yz}). Thus the metal in plane orbital (d_{xy}) is well isolated from the rest of the metal d orbitals and is poised in an appropriate orientation to couple the metal into a pseudo- σ pathway for electron transfer regeneration of the active site.

Here, the electronic structure studies are reported, utilizing a combination of photoelectron spectroscopy and density functional theory, of prototype $(Tp^*)MO(bdt)$ ($M = Mo, W$) and their other known derivatives. This is the first photoelectron spectroscopic study of scorpionate tungsten complexes, and their comparison to analogous molybdenum complexes provides a systematic mean for the study of change in metal. Density functional theoretical calculations have been performed to gain further insight into electronic structures.

2.0 Experimental Section

2.1 Abbreviations

Tp^* , hydrotris(3,5-dimethyl-1-pyrazolyl)borate; bdt, 1,2-benzenedithiolate; qdt, 2,3-dithioquinoxaline; tdt, 3,4-toluenedithiolate; $bdtCl_2$, 3,6-dichloro-1, 2-benzenedithiolate. (S-S) represents a generic ene-1,2-dithiolate ligand that forms a five membered chelate ring with the Mo atom.

2.2 Synthesis and characterization

Reactions and operations required for preparing the compounds were performed under strict anaerobic conditions obtained by blanketing synthetic manipulations with pre-purified argon gas and by utilizing standard Schlenk techniques, a high-vacuum/gas double line manifold, and an inert atmospheric glove bag. Glassware was oven-dried at 150°C and repeatedly flushed with inert gas prior to use. The employed organic solvents were purified following standard procedures, distilled under nitrogen gas, degassed by freeze-thaw-pump cycles, and transferred to reaction vessels under inert gas via steel cannulae techniques.

Reagents used in synthetic procedures were generally used as received. The following reagents (Aldrich) were dried and/or distilled in vacuo and stored under nitrogen gas prior to use: H₂bdt (1,2-benzenedithiol), H₂tdt (3,4-toluenedithiol), and H₂bdtCl₂ (3,6-dichloro-1,2-benzenedithiol). Potassium hydrotris(3,5-dimethyl-1-pyrazolyl)borate (KTp*)⁴⁶ and the precursor complexes (Tp*)MoOCl₂,⁴⁶ and (Tp*)WOI₂³⁹ were prepared according to the literature. The compounds (Tp*)MoO(bdt),^{47,48} (Tp*)MoO(tdt),⁴⁹ and (Tp*)MoO(bdtCl₂)⁵⁰ were synthesized as previously described. The synthesis, isolation, purification, and characterization of (Tp*)WO(bdt) and (Tp*)WO(tdt) involved procedures developed by Young and co-workers.^{39,51}

Reaction progress was monitored and product purity was confirmed by thin-layer chromatography (silica gel 60 F₂₅₄ plastic sheets, EM Science). All of the dithiolate compounds were purified under argon by column chromatography (silica gel, 230-400

mesh) prior to spectroscopic and electrochemical characterization as previously discussed in the literature.⁴⁷⁻⁵⁰ Multiple physical methods were utilized in the characterization of the compounds. Electronic absorption spectra of samples solvated in 1,2-dichloroethane were collected on a modified Cary 14 (with OLIS interface, 250-2600 nm) spectrophotometer. Infrared (IR) spectra ($4000\text{-}400\text{ cm}^{-1}$) were acquired in KBr disks or as dichloromethane solutions (between NaCl plates) on a Nicolet Avatar ESP 360 FT-IR spectrophotometer. Mass spectra were recorded on a JEOL HX110 high-resolution sector instrument utilizing fast atom bombardment (FAB) ionization in a matrix of 3-nitrobenzyl alcohol (NBA). Electronic paramagnetic resonance (EPR) spectra of fluid solutions (298 K) or of frozen glasses (77 K) in dry degassed toluene were acquired at X-band frequency ($\sim 9.1\text{ GHz}$) with a Bruker ESP 300 spectrometer for these complexes containing a $\{(\text{Tp}^*)\text{Mo}\}^{2+}$ (formally d^1) center. The results of these spectroscopic studies were consistent with previous data and confirmed the purity of the samples for photoelectron spectroscopic studies.⁴⁷⁻⁵⁰

2.3 Theoretical

Geometry optimization, SCF (self-consistent field) and molecular orbital calculations were performed using the ADF (Amsterdam density functional theory calculations) package (release 2000.02). Starting geometries were obtained from crystal structures of **1**,^{52,53} **2**⁵⁴ and **3**⁵⁵ and **5**. A generalized gradient approximation, with the exchange correction of Becke⁵⁶ and the correlation correction of Lee *et. al.*,⁵⁷ was used for all density functional calculations. All core levels (up to 3d for Mo, 4d for W and 1s for C, N, B and O) were treated as frozen orbitals. The calculations employed triple-zeta

basis sets with Slater type orbitals and a polarization function for all elements. Calculations on the ground-state molecules were performed in the spin-restricted mode. Spin-unrestricted Δ SCF (self-consistent field) calculations were performed on the proposed ion states formed by photoionization by removing one electron from the relevant orbital and comparing the total energy with that of the ground state molecule. A linear correction was applied for comparison of the calculated and the observed energies, *i.e.* the calculated Δ SCF energies and orbital energies were shifted by the difference between experimentally obtained and calculated energies of the HOMO.

3.0 Results

3.1 Gas-Phase Photoelectron Spectroscopy

3.1.1 (Tp*)MoO(S-S) Compounds: Remote Ligand Substitution Effect

The gas-phase photoelectron spectra for compounds **1-4** are shown in Figures 6.2-6.4 and will be discussed in this section. The general shape of ionizations is similar to that previously reported for (Tp*)MoO(S-S) (S-S = tdt and qdt) compounds shown in Figure 6.4. The lower ionization potential, band 1, observed in compounds **1-4** and shown in Figure 6.1-6.3 can be assigned to a metal based ionization. A stack plot of photoelectron spectra of compounds **1-4** shown in Figure 6.4 reveals that the ionization potential of band 1 follows the electron withdrawing trend of remote substitution on the benzene ring of the enedithiolate ligand. The ionization bands 2, 2', 3, 3' are proposed to be symmetric and antisymmetric combinations of in-plane and out of plane dithiolate p orbital based ionizations and further details on them will be provided in the computational section. Photoelectron spectroscopic experiments utilizing He II ionization source, Figure 6.1 and 6.3, were done on compounds **1** and **2**. A careful examination of band intensities for **1** and **2** shows that band 3 increases in intensity in He II source suggesting that the dithiolate orbital associated with this ionization has mixing with metal orbitals. Further ionizations between 8.5 ± 0.02 to 10 ± 0.02 eV are from pyrazole- π based orbitals.

3.1.2 (Tp*)MO(bdt) (M = Mo (1) , W (5)) Compounds: Metal Effect

The He I photoelectron spectra of compounds **1** and **5** stacked in Figure 6.5 are remarkably similar. Band 1 in photoelectron spectra of **5** observed at 7.04 ± 0.02 eV is assigned to tungsten based molecular orbital similar to its Mo counterpart. This tungsten based ionizations occurs at 6.90 ± 0.02 eV for compound **6** and compares with that at 6.95 ± 0.02 eV for analogous molybdenum complex (**3**). For **5** and **6**, bands 2, 2', 3, 3' are assigned to dithiolate sulfur based ionizations similar to their Mo counterparts.

An ionization at around 10.5 eV has been identified as $\pi(\text{Mo}\equiv\text{O})$ in the photoelectron spectroscopic studies of (Tp*)MoOX₂ (where X = F, Cl, Br).⁵⁸ A similar ionization band is observed in the spectra of **1** and **6** where data have been collected near the ionization potential of this band. This ionization band at 10.42 ± 0.02 eV for **1**, 10.25 ± 0.02 eV for **4**, 10.32 ± 0.02 eV for **5** and 10.17 ± 0.02 eV for **6** is assigned to $\pi(\text{M}\equiv\text{O})$ (M = Mo or W) based ionization in these compounds.

In Figure 6.2 and 6.3, band 2 and 2' change in intensities in the He II source. However, in Figures 6.2, 6.3 and 6.6, an increase in the intensity of band 3 in He II ionization for compounds **1**, **2** and **6** is observed. These intensity changes will be further addressed in the discussion section.

3.1.3 Computational Study

DFT calculations were used to optimize the geometry of prototype compounds **1** and **5** and their derivatives (**2**, **4**) starting from their crystal structures. The calculated geometries are reasonably close to the available crystal structure geometries (< 2%

deviations). The calculated ionizations energies are reported in Table 6.1. The DFT calculations were performed to obtain the contributions from individual atomic orbital to the frontier orbitals shown in Figures 6.7 and 6.8 and Table 6.1. For the study of the effect of the variation in the fold angle on electronic structure of these compounds, a computational model (Tp)MoO(edt) (where edt = ethene-1, 2-dithiolate) was constructed and results are plotted in Figure 6.9.

4.0 Discussion

4.1 Gas-phase Photoelectron Spectroscopy

The series of compounds, **1-4**, have remote substitutions on their aromatic rings. These substitutions have a varying electron withdrawing property that manifests in the first ionization potentials for these compounds. Compound **4** corresponds to the most electron withdrawing heterocyclic dithiolate and has the highest ionization potential of all the {(Tp*)MO} (M = Mo, W) core compounds studied by photoelectron spectroscopy to date. These compounds are arranged in Figure 6.4 from top to bottom according to increasing electron withdrawing property of the coordinated dithiolate.

In Figures 6.2, 6.3 and 6.6, increase in the intensity of band 3 in He II ionization for **1**, **2** and **6** is interesting and shows mixing of associated dithiolate orbital with metal orbital. In the photoelectron spectroscopic studies of Cp₂M(bdt) compounds, the two lower energy ionization were experimentally identified as dithiolate sulfur out of plane orbitals (symmetric and antisymmetric combinations). The intensities of dithiolate based ionizations observed for **1-6** are lower than those in Cp₂M(bdt) compounds. The intensity changes of metal and dithiolate based ionizations cannot be quantified

effectively due to the overlapping nature of ionizations and their lower intensities. Some conclusions can be drawn, for example, in Figures 6.2 and 6.3, ionizations 2 and 2' are lower in intensity in the He II source, which is suggestive of their assignment to sulfur-based orbitals. Comparison of these photoelectron spectra to those of KTp^* ,⁵⁹ and $(\text{Tp}^*)\text{MoX}_2$ (where X = F, Cl, Br) suggests the presence of some additional ionization features that appear as an additional shoulder (near 8.25 eV for **1**) to pyrazole- π based ionizations. The deconvolution of this feature as bands 3 and 3' may be due to dithiolate in-plane orbitals. Ionization band 3 increases in intensity in He II ionization in **1**, **2** and **6**, which is suggestive of its assignment to a symmetric combination of sulfur in-plane p orbitals that has right symmetry to mix with a metal in-plane orbital.

The ionization energy of the metal based orbital (first ionization) occurs at 7.04 ± 0.02 eV for both **1** and **5** that contain 1,2-benzenedithiolate, and at 6.95 ± 0.02 eV and 6.90 ± 0.02 eV for both **4** and **6**, respectively, that contain 3,4-toluenedithiolate. It is also interesting to note that in the $\text{Cp}_2\text{Mo}(\text{bdt})$ compound, the ionization energy of the metal-in plane orbital, which is HOMO-1, is observed at 7.04 ± 0.02 eV.⁴⁴ Therefore, irrespective of the other spectator ligands, and different formal oxidation states of the metal, the ionization energy of the metal in-plane orbital seems to be stabilized by the type of enedithiolate.

4.2 Computational Study

The calculated eigenvalues, -4.35 and -4.32, for the HOMO for compounds **1** and **5**, respectively, are very close and add to the experimental finding of similar first ionization energies of these two compounds. The plots of frontier molecular orbitals with

individual atomic orbital contributions are shown in Figure 6.7 and 6.8 for the Mo/W prototype compounds **1** and **5**. The highest occupied molecular orbitals (HOMO) are predominantly metal in-plane. This is consistent with the photoelectron spectroscopic assignments discussed earlier and their EPR studies that show a characteristic EPR signal corresponding to the paramagnetic Mo center. However, the contributions of dithiolate out of plane p orbitals (S_{op}^+) are present in the HOMO, and shows that the metallocycle helps raise the energy of the S_{op}^+ orbitals for mixing with metal based orbitals. This out of plane ligand orbital is not observed in the HOMO of the dihalide complexes of type $(Tp^*)MoOX_2$, discussed previously, due to the absence of any such a metallocycle.

The calculated HOMO-1 orbital is predominantly a S_{op}^+ type orbital and is lower in energy than metal based orbital (HOMO) which is in contrast to $Cp_2Mo(bdt)$ system, where the reverse energy order has been observed. However, in both systems dithiolate out-of-plane orbitals are present as frontier orbitals. The molecular orbital plots for the HOMO-1 also manifest the presence of out of plane carbon- π orbitals of the enedithiolate that raise the energy of S_{op}^+ orbitals for interaction with metal orbitals.

The HOMO-2 is an antisymmetric combination of dithiolate orbitals (S_{op}^-) and the following orbitals are either pyrazole- π based or symmetric or antisymmetric combinations of the dithiolate sulfur in plane orbitals (S_{ip}^+ , S_{ip}^-). A one to one assignment of experimentally obtained ionizations to calculated molecular orbitals is not possible due to very similar computed eigen values of these orbitals. However, the presence of a pseudo-sigma interaction in the frontier orbital (HOMO-8) is encouraging.

This orbital has the appropriate symmetry to mix with the metal in-plane orbital as noted earlier and has been referred to as a pseudo- σ interaction of metal and dithiolate.⁶⁰

The frontier orbitals of the Mo and W prototype compounds **1** and **5** are remarkably similar and show that the substitution of a third row transition metal tungsten for molybdenum does not significantly change the electronic structure of these model compounds.

The results of the theoretical study of variation in the fold angle vs. total bonding energy and atomic contributions to the HOMO of (Tp)MoO(edt) are plotted in Figure 6.9. A shallow total bonding energy profile is present near the experimentally observed fold angle of 21.3° for **1**, suggesting a very small energy change (less than 1 eV or 23 kcal/mol, for a fold angle variation up to 50° above and below the experimental value of 21.3° for **1**) in this process. As the fold angle is varied, the total metal and sulfur characters remain effectively constant in the HOMO, with the change of sulfur in-plane and out of plane contributions compensating for one another.

5.0 Conclusions

The combined photoelectron spectroscopic and density functional theoretical results presented here support the conclusion that these oxomolybdenum and oxotungsten compounds have considerable metal-sulfur covalency. The assignment of lower energy ionizations to frontier orbitals that contain contributions from dithiolate in-plane or out of plane orbitals has been possible. The results presented here for compounds **1-4** reveal a trend in their first ionization energies which is consistent with the electron withdrawing

properties of the substitution on the benzene ring of the dithiolate ligand. The effectively similar ionization potentials for the metal in-plane orbital in **1**, **5** and $\text{Cp}_2\text{Mo}(\text{bdt})^{44}$ and **4** and **6** indicates that dithiolate can maintain a nearly constant effective nuclear charge on metal center. This property of dithiolate donors have been previously summarized as “electronic buffering effect”⁴² and “dithiolate-folding-effect”⁴⁴ and shown here for transition metals Mo and W relevant to the active site of the pyranopterindithiolate enzymes. The computed total energy involved in the variation of fold angle for a $\text{Mo}(\text{V})$, d^1 system is of the order of 23 kcal/mol which compares with the energy of a few hydrogen bonds and can be provided to the pyranopterindithiolate by movements of the protein backbone or breaking of hydrogen bonds. Finally, it is noted that the metal substitution of Mo by W does not significantly change the electronic structure of the metal-dithiolate compounds investigated here.

Table 6.1. Experimental ionization energies (I.E.), calculated absolute orbital eigenvalues ($-\epsilon_i$) and calculated Δ SCF first ionization energies of compounds 1 and 6 (all values in eV).

Experimental I.E.	Calculated $-\epsilon_i$ (Shifted) ^b	($-\epsilon_i$) HOMO	Δ SCF	Label and Assignment
(Tp*)MoO(bdt) (1)				
7.04	7.04	4.35	6.51	1
7.54, 7.71	7.61, 7.85			2, 2'
8.08, 8.24	8.52, 8.70			3, 3'
8.58-9.26 ^a	8.92-9.25			Pyrazole- π
10.22	9.40			$\pi(\text{Mo}=\text{O})$
(Tp*)WO(bdt) (6)				
7.04	7.04	4.32	6.49	1
7.51, 7.71	7.62, 7.88			2, 2'
8.19, 8.42	8.62, 8.76			3, 3'
8.70-9.81 ^a	8.99-9.67			Pyrazole- π
10.32	10.10			$\pi(\text{W}=\text{O})$

^a Range of experiment I.E. values taken from the positions of Gaussians used to deconvolute the data. This does not imply that these values are vertical ionization energies.

^b Eigenvalues were shifted so the HOMO eigenvalue matches the position of the lowest energy Gaussian used to deconvolute the experimental data.

(Tp*)MO(S-S) =

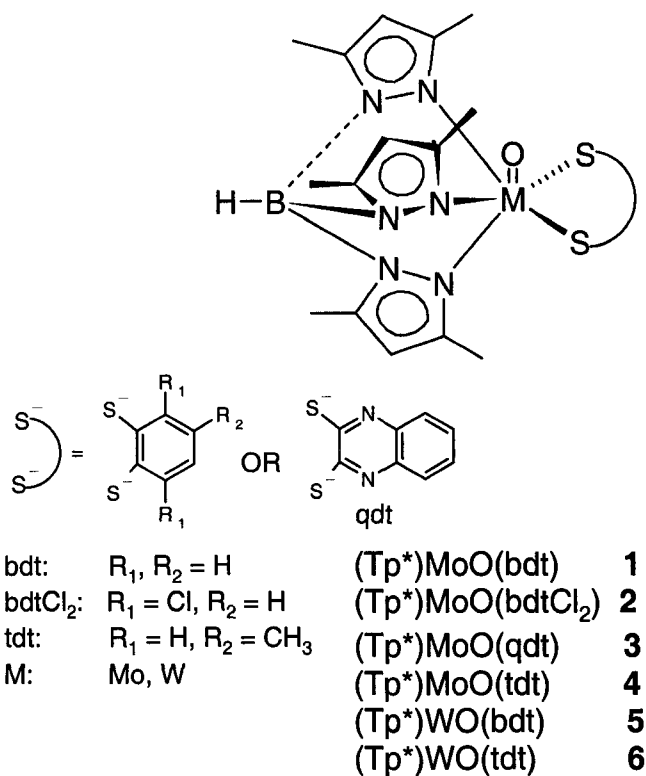


Figure 6.1. Schematic drawing of (Tp*)MoO(S-S) (where Tp* = hydrotris(3,5-dimethylpyrazol-1-yl)borate, bdt = 1,2-benzenedithiolate, bdtCl₂ = 3, 6-dichloro-1, 2-benzenedithiolate, qdt = 2,3-dithioquinoxaline, tdt = 3, 4 toluenedithiolate) complexes.

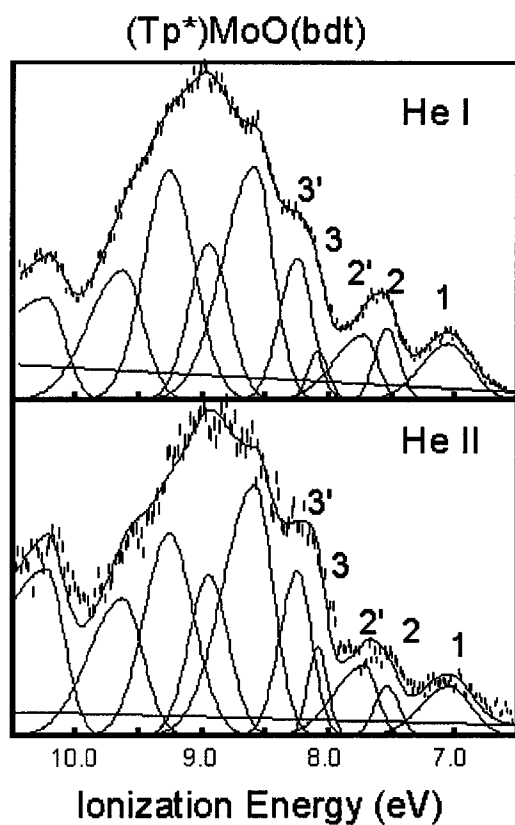


Figure 6.2. The He I and He II photoelectron spectroscopy of (Tp*)MoO(bdt) (**1**). The ionization band 1 corresponds to a metal based ionization and bands 2, 2', 3, 3' correspond to dithiolate based ionizations.

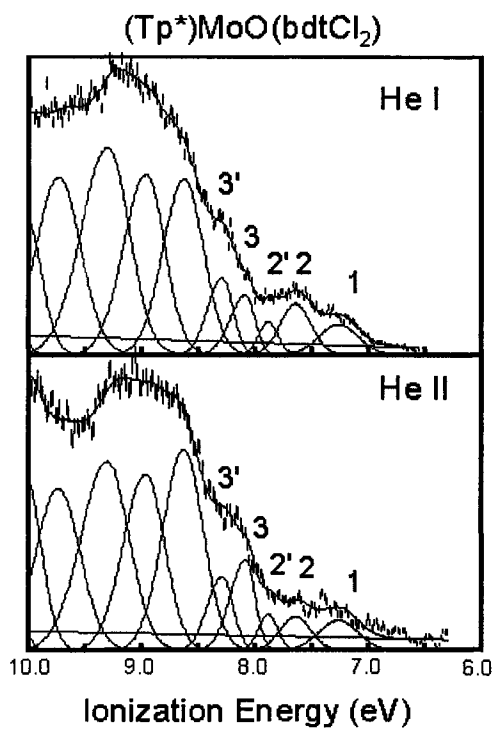


Figure 6.3. The He I and He II photoelectron spectroscopy of $(Tp^*)MoO(bdtCl_2)$ (**2**). The ionization band 1 corresponds to a metal based ionization and bands 2, 2', 3, 3' correspond to dithiolate based ionizations.

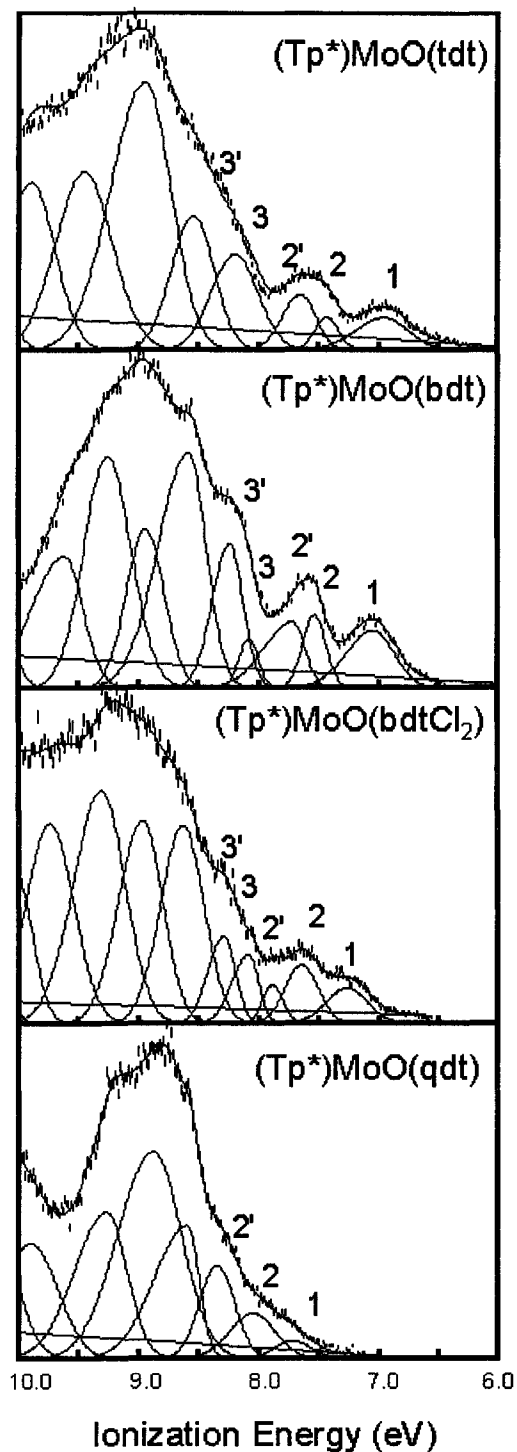


Figure 6.4. The He I and He II photoelectron spectroscopy of $(\text{Tp}^*)\text{MoO}(\text{S-S})$ series of compounds (1-4). The ionization band 1 corresponding to a metal based ionization shows a trend consistent with the electron withdrawing property of the coordinated dithiolate. The ionization bands 2, 2', 3, 3' correspond to dithiolate based orbitals.

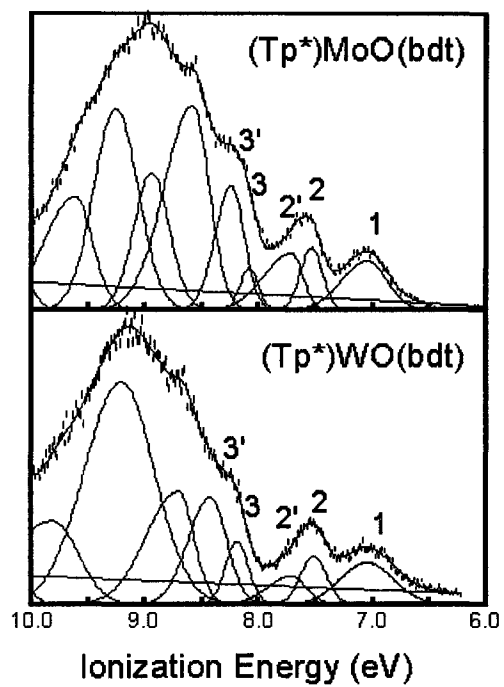


Figure 6.5. Comparison of the He I photoelectron spectrum of $(Tp^*)MO(bdt)$ (where $M = Mo$ and W).

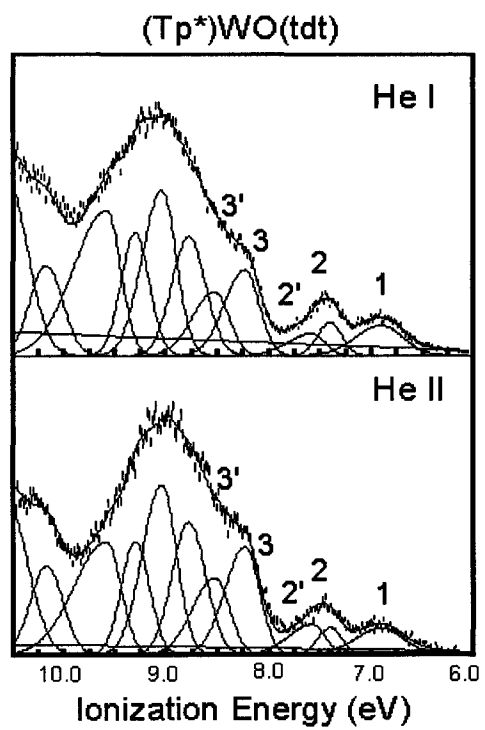


Figure 6.6. The He I and He II photoelectron spectra of (Tp*)WO(tdt).

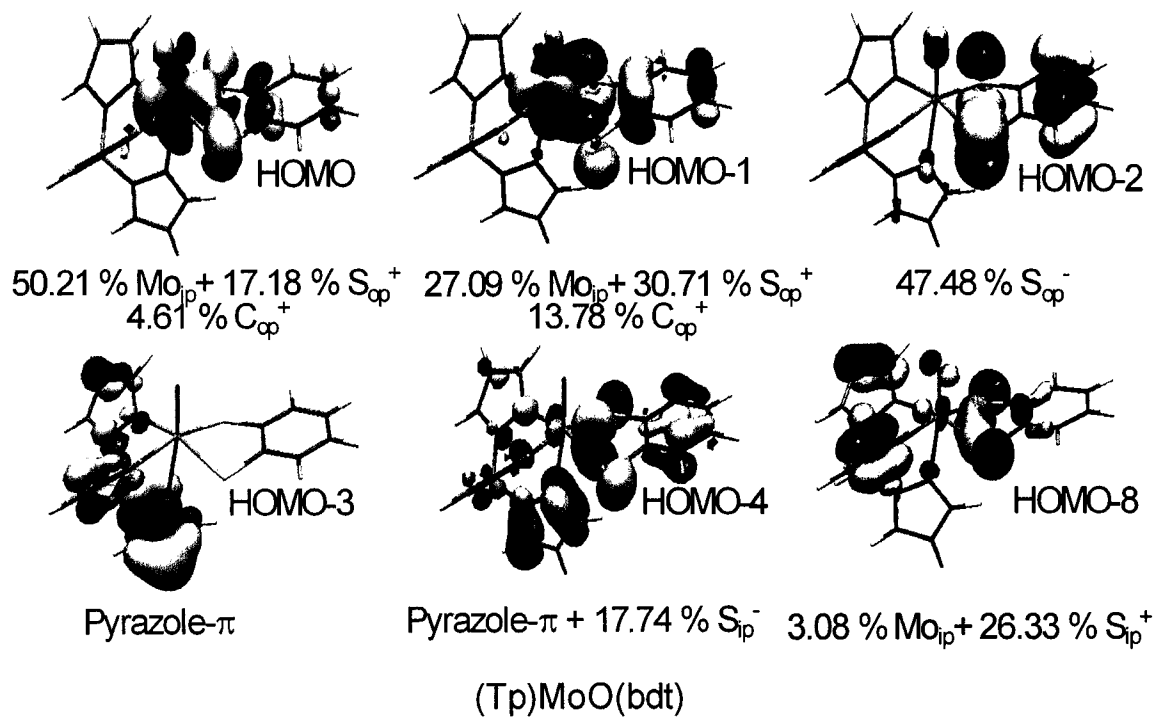


Figure 6.7. Frontier orbitals of (Tp)MoO(bdt) (1). These orbitals have significant metal and dithiolate characters.

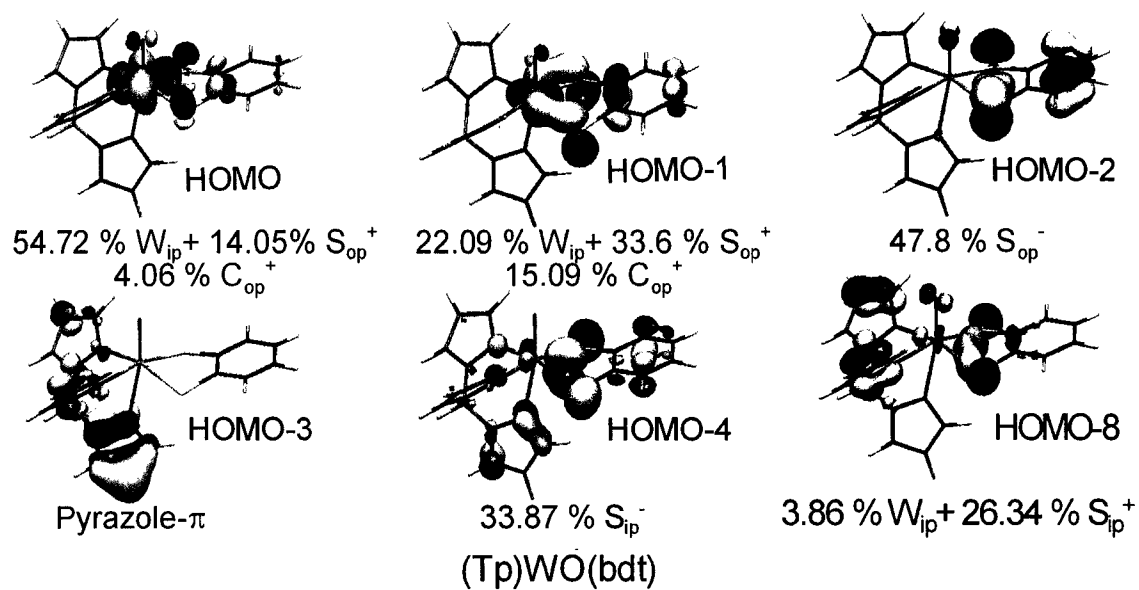


Figure 6.8. Frontier orbitals of (Tp)WO(bdt) (5). These orbitals have significant metal and dithiolate characters.

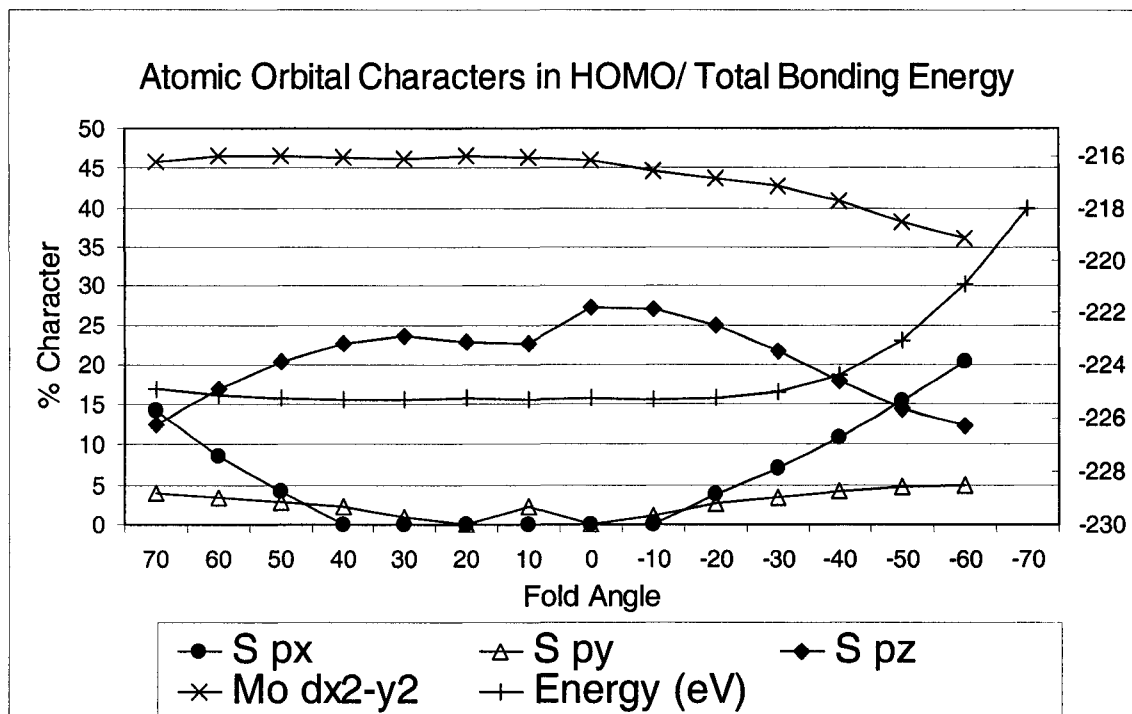


Figure 6.9. Fold angle variation against individual orbital contribution to highest occupied molecular orbital (HOMO) and total bonding energy of the molecule.

6.0 References

1. Sigel, A.; Sigel, H. *Molybdenum and Tungsten: Their Roles in Biological Processes.*; Metals Ions in Biological Systems; vol. 39; Dekker: New York, 2002.
2. Hille, R. *Chem. Rev.* **1996**, *96*, 2757-2816.
3. George, G. N.; Pickering, I. J.; Kisker, C. *Inorg. Chem.* **1999**, *38* (10), 2539-2540.
4. Kisker, C.; Schindelin, H.; Pacheco, A.; Wehbi, W.; Garrett, R. M.; Rajagopalan, K. V.; Enemark, J. H.; Rees, D. C. *Cell* **1997**, *91*, 973-983.
5. Schrader, N.; Fischer, K.; Theis, K.; Mendel, R. R.; Schwarz, G.; Kisker, C. *Structure* **2003**, *11* (10), 1251-1263.
6. Raaijmakers, H.; Teixeira, S.; Dias, J. M.; Almendra, M. J.; Brondino, C. D.; Moura, I.; Moura, J. J.; Romao, M. J. *JBIC, J. Biol. Inorg. Chem.* **2001**, *6* (4), 398-404.
7. Raaijmakers, H.; Macieira, S.; Dias, J. M.; Teixeira, S.; Bursakov, S.; Huber, R.; Moura, J. J.; Moura, I.; Romao, M. J. *Structure* **2002**, *10* (9), 1261-1272.
8. Chan, M.; Mukund, S.; Kletzin, A.; Adams, M.; Rees, D. *Science* **1995**, *267* (5203), 1463-9.
9. Hu, Y.; Faham, S.; Roy, R.; Adams, M.; Rees, D. *J. Mol. Biol.* **1999**, *286* (3), 899-914.
10. Johnson, M. K.; Rees, D. C.; Adams, M. W. *Chem. Rev.* **1996**, *96* (7), 2817-2839.
11. Mukund, S.; Adams, M. W. *J. Biol. Chem.* **1991**, *266* (22), 14208-16.
12. George, G. N.; Prince, R. C.; Mukund, S.; Adams, M. W. *J. Am. Chem. Soc.* **1992**, *114* (9), 3521-3.

13. Arendsen, A. F.; de Vocht, M.; Bultink, Y. B.; Hagen, W. R. *JBIC, J. Biol. Inorg. Chem.* **1996**, *1* (4), 292-296.
14. Koehler, B. P.; Mukund, S.; Conover, R. C.; Dhawan, I. K.; Roy, R.; Adams, M. W.; Johnson, M. K. *J. Am. Chem. Soc.* **1996**, *118* (49), 12391-12405.
15. Calzolari, L.; Gorst, C. M.; Bren, K. L.; Zhou, Z. H.; Adams, M. W.; La Mar, G. N. *J. Am. Chem. Soc.* **1997**, *119* (40), 9341-9350.
16. Mukund, S.; Adams, M. W. *J. Biol. Chem.* **1990**, *265* (20), 11508-16.
17. Johnson, J. L.; Rajagopalan, K.; Mukund, S.; Adams, M. W. *J. Biol. Chem.* **1993**, *268* (7), 4848-52.
18. Eisenberg, R. *Prog. Inorg. Chem.* **1970**, *12*, 295-369.
19. Levason, W.; McAuliffe, C.; McCullough, F. J. *Inorg. Chem.* **1977**, *16* (11), 2911-16.
20. Sabel, D. M.; Gewirth, A. A. *Inorg. Chem.* **1994**, *33* (1), 148-56.
21. Collison, D. *J. Chem. Soc., Dalton Trans.* **1990**, *10*, 2999-3006.
22. Winkler, J. R.; Gray, H. B. *Comments on Inorg. Chem.* **1981**, *1* (4), 257-63.
23. Ellis, S. R.; Collison, D.; Garner, C. D.; Clegg, W. *J. Chem. Soc., Chem. Commun.* **1986**, *19*, 1483-5.
24. Das, S. K.; Biswas, D.; Maiti, R.; Sarkar, S. *J. Am. Chem. Soc.* **1996**, *118* (6), 1387-97.
25. Davies, E. S.; Aston, G. M.; Beddoes, R. L.; Collison, D.; Dinsmore, A.; Docrat, A.; Joule, J. A.; Wilson, C. R.; Garner, C. D. *J. Chem. Soc., Dalton Trans.* **1998**, *21*, 3647-3656.

26. Davies, E. S.; Beddoes, R. L.; Collison, D.; Dinsmore, A.; Docrat, A.; Joule, J. A.; Wilson, C. R.; Garner, C. D. *J. Chem. Soc., Dalton Trans.* **1997**, 21, 3985-3996.
27. Tucci, G. C.; Donahue, J. P.; Holm, R. *Inorg. Chem.* **1998**, 37 (7), 1602-1608.
28. Donahue, J. P.; Lorber, C.; Nordlander, E.; Holm, R. *J. Am. Chem. Soc.* **1998**, 120 (13), 3259-3260.
29. Moock, K. H.; Rock, M. H. *J. Chem. Soc., Dalton Trans.* **1993**, 16, 2459-63.
30. Falaras, P.; Mitsopoulou, C. A.; Argyropoulos, D.; Lyris, E.; Psaroudakis, N.; Vrachnou, E.; Katakis, D. *Inorg. Chem.* **1995**, 34 (18), 4536-42.
31. Goddard, C. A.; Holm, R. *Inorg. Chem.* **1999**, 38 (23), 5389-5398.
32. Lorber, C.; Donahue, J. P.; Goddard, C. A.; Nordlander, E.; Holm, R. *J. Am. Chem. Soc.* **1998**, 120 (32), 8102-8112.
33. Donahue, J. P.; Goldsmith, C. R.; Nadiminti, U.; Holm, R. *J. Am. Chem. Soc.* **1998**, 120 (49), 12869-12881.
34. Pietsch, M. A.; Hall, M. B. *Inorg. Chem.* **1996**, 35 (5), 1273-8.
35. Dutta, S. K.; McConville, D. B.; Youngs, W. J.; Chaudhury, M. *Inorg. Chem.* **1997**, 36 (12), 2517-2522.
36. Rappe, A. K.; Goddard, W. A. *J. Am. Chem. Soc.* **1982**, 104 (12), 3287-94.
37. Luo, L.; Lanza, G.; Fragala, I. L.; Stern, C. L.; Marks, T. J. *J. Am. Chem. Soc.* **1998**, 120 (13), 3111-3122.
38. Young, C. G.; Wedd, A. G. *Chem. Comm.* **1997**, 14, 1251-1257.
39. Inscore, F. E.; Hill, J.; Young, C. G.; Kirk, M. L. *manuscript in preparation.*

40. McElhaney, A. E.; Inscore, F. E.; Schirilin, J. T.; Enemark, J. H. *Inorg. Chim. Acta* **2002**, *341*, 85-90.
41. Chang, C. S. J.; Rai-Chaudhuri, A.; Lichtenberger, D. L.; Enemark, J. H. *Polyhedron* **1990**, *9*, 1965-1973.
42. Westcott, B.; Gruhn, N.; Enemark, J. *J. Am. Chem. Soc.* **1998**, *120* (14), APR 15, 3382-3386.
43. Helton, M. E.; Gruhn, N. E.; McNaughton, R. L.; Kirk, M. L. *Inorg. Chem.* **2000**, *39* (11), 2273-2278.
44. Joshi, H. K.; Cooney, J. J. A.; Inscore, F. E.; Gruhn, N. E.; Lichtenberger, D. L.; Enemark, J. H. *Proc. Natl. Acad. Sci. USA* **2003**, *100* (7), 3719-3724.
45. McNaughton, R. L.; Helton, M. E.; Rubie, N. D.; Kirk, M. L. *Inorg. Chem.* **2000**, *39* (20), 4386-4387.
46. Cleland, W. E., Jr.; Barnhart, K. M.; Yamanouchi, K.; Collison, D.; Mabbs, F. E.; Ortega, R. B.; Enemark, J. H. *Inorg. Chem.* **1987**, *26*, 1017-1025.
47. Dhawan, I. K.; Pacheco, A.; Enemark, J. H. *J. Am. Chem. Soc.* **1994**, *116*, 7911-7912.
48. Dhawan, I. K.; Enemark, J. H. *Inorg. Chem.* **1996**, *35*, 4873-4882.
49. Olson, G. M.; Schultz, F. A. *Inorg. Chim. Acta* **1994**, *225*, 1-7.
50. Inscore, F. E.; Joshi, H. K.; McElhaney, A. E.; Enemark, J. H. *Inorg. Chim. Acta* **2002**, *331*, 246-256.
51. Young, C. G., email communication.

52. Dhawan, I. K.; Pacheco, A.; Enemark, J. H. *J. Am. Chem. Soc.* **1994**, *116* (17), 7911-12.
53. Dhawan, I. K.; Enemark, J. H. *Inorg. Chem.* **1996**, *35* (17), 4873-4882.
54. Inscore, F. E.; Joshi, H. K.; McElhaney, A.; Enemark, J. H. *Inorg. Chim. Acta* **2002**, *331*, 246-256.
55. Inscore, F. E.; Rubie, N.; Joshi, H. K.; Kirk, M. L.; Enemark, J. H. *manuscript submitted to Inorg. Chem.*
56. Becke, A. D. *Phys. Rev. A.* **1988**, *38*, 3098-3100.
57. Lee, C.; Yang, W.; Parr, R. G. *Phys. Rev. B.* **1988**, *37*, 785.
58. Joshi, H. K.; Gruhn, N. E.; Lichtenberger, D. L.; Enemark, J. H. *manuscript in preparation.*
59. Joshi, H. K.; Arvin, M. A.; Durivage, J. C.; Gruhn, N. E.; Carducci, M. D.; Westcott, B. L.; Lichtenberger, D. L.; Enemark, J. H. *Polyhedron* **2003**.
60. Inscore, F. E.; McNaughton, R.; Westcott, B.; Helton, M. E.; Jones, R.; Dhawan, I. K.; Enemark, J. H.; Kirk, M. L. *Inorg. Chem.* **1999**, *38*, 1401-1410.

CHAPTER 7: Six-Coordinate Molybdenum Nitrosyls with a Single Ene-1,2-Dithiolate Ligand

A portion of this chapter has been published as

Joshi, H. K.; Inscore, F. E.; Schirlin, J. K.; Dhawan, I. K.; Carducci, M. D.; Enemark, J.

H. "Six-Coordinate Molybdenum Nitrosyls with a Single Ene-1,2-Dithiolate Ligand"

Inorg. Chim. Acta **2002**, 337, 275-286.

1.0 Introduction

Mononuclear metal-nitrosyl complexes are of continuing interest.^{1,2} Their possible applications include; molecular sensors,³ magnetically-dilute hosts for paramagnetic guests,⁴ non-linear optical⁵ and ferrimagnetic materials.^{6,7} In biology metal-nitrosyls are implicated in the immune system to kill tumor cells,⁸ as a physiological NO carrier,⁹ and as intracellular parasites.¹⁰ The metastable linkage isomers of transition metal nitrosyl complexes have potential technological importance which, in principle, could allow the design of a high capacity storage device.¹¹

In transition metal-nitrosyl complexes there is a significant mixing between the metal d and π^* (NO) orbitals which led to the development of the $\{\text{MNO}\}^n$ formalism for describing mononitrosyl complexes.^{12,13} In this notation n is the total number of electrons contained in the metal d and π^* (NO) orbitals. The title complexes are six-coordinated $\{\text{MNO}\}^4$ species, with the metal center coordinated to a bulky tripodal ligand (Tp^*). The steric interaction of (Tp^*) prevents additional coordination to the metal center, hence, affording stable six-coordinate 16-electron species, which have a formally $4d^4$ electronic configuration (*i.e.* Mo(II)). The $\{\text{MNO}\}^4$ center in $(\text{Tp}^*)\text{Mo}(\text{NO})\text{Cl}_2$ can be reduced by one electron to the corresponding paramagnetic $\{\text{MNO}\}^5$ center, and EPR spectroscopy is consistent with the unpaired electron being localized in a MO that is predominantly Mo $4d_{xy}$.^{3,14,15} McCleverty and Jones and their coworkers have prepared a series of homo- and heterobimetallic complexes in which the redox active $(\text{Tp}^*)\text{Mo}(\text{NO})(\text{X}, \text{Y})$ (where X, Y are mono anions) center is linked to a second redox active metal center through

polyene bridges.^{16,17} These binuclear systems with a reducible $\{\text{MNO}\}^4$ center are of general interest due to their possible application as non-linear optical materials.

The synthesis and molecular structures of the $(\text{Tp}^*)\text{Mo}(\text{NO})(\text{S-S})$ family of compounds (where (Tp^*) is hydrotris(3,5-dimethyl-1-pyrazolyl)borate; (S-S) is an ene-1,2-dithiolate) are reported. The compounds; $(\text{Tp}^*)\text{Mo}(\text{NO})(\text{bdt})$ (**1**), $(\text{Tp}^*)\text{Mo}(\text{NO})(\text{tdt})$ (**2**), and $(\text{Tp}^*)\text{Mo}(\text{NO})(\text{bdtCl}_2)$ (**3**) (bdt, 1,2-benzenedithiolate; tdt, 3,4-toluenedithiolate; bdtCl_2 , 3,6-dichloro-1, 2-benzenedithiolate), are the first such structurally characterized $\{\text{MoNO}\}^4$ compounds that contain a $\{(\text{Tp}^*)\text{Mo}(\text{NO})\}^{2+}$ fragment ligated to an ene-1,2-dithiolate. Numerous metal nitrosyl complexes have been structurally characterized. A Cambridge Crystallographic Database (CSD) search showed 2037 hits of metal-nitrosyl structures, out of which 542 hits were of group VI transition metal-nitrosyl complexes and 292 hits had molybdenum centers.¹⁸ A total of ten structures containing mononuclear 16-electron $\{(\text{Tp}^*)\text{Mo}(\text{NO})(\text{S,S})\}$ cores (where (S,S) = two sulfur donor ligands) including the title complexes, are structurally compared here (Chart 1). The synthesis of compound **2** was first reported by McCleverty and coworkers in 1989.¹⁹ However, this family of compounds has remained essentially unexplored in the intervening years as evident by a recent review of the coordination and organometallic chemistry of metal-NO complexes.¹ Complexes **1-3** (Figure 7.1) are the first structurally characterized Mo-nitrosyl complexes containing a single ene-1,2-dithiolate (S_2C_2) chelate. However, it has long been known that the crystal structures of $\text{LMo}(\text{NO})(\text{SC}_6\text{H}_5)_2$ (where $\text{L} = \eta^5\text{-C}_5\text{H}_5$, Tp^* (**8**)) exhibit unusual ON-Mo-S-C torsion angles (Figure 7.2A) that have been ascribed to $d\pi\text{-}p\pi$ bonding interactions between the thiolate lone pairs, primarily S 3*p* in character,

and the empty Mo $4d_{xy}$ orbitals.^{20,21} Molecular orbital calculations by Hoffmann and coworkers suggested that the sulfur atoms can contribute to the stability of 16-electron systems.^{22,23} Fourmigué *et al.* have shown that the fold angle (θ , Figure 7.2B) is sensitive to the electronic occupation of metal-dithiolate complexes.^{24,25} Here It is shown that the ene-1,2-dithiolate chelate in compounds **1-3**, which have a d_{xy}^0 ground state, exhibit a large fold angle (θ). Similar to $(\text{Tp}^*)\text{Mo}(\text{NO})\text{Cl}_2$, the metal centers in **1-3** can be reduced by one electron to yield the spectroscopically interesting d_{xy}^1 state (formally $(d_{xz}d_{yz})^4 d_{xy}^1$)²⁶⁻²⁸ whose detailed study will be presented elsewhere.²⁹

Compounds **1-3** are of further interest because the active sites of sulfite oxidase and xanthine oxidase have a molybdenum atom coordinated by a single ene-1,2-dithiolate at the active site.^{28,30-32} This pyranopterin-dithiolate unit coordinated to molybdenum is postulated to function as an electron transfer conduit and modulator of the redox potential of the enzyme active site.³³ The electronic structure of these active sites and their relationship to electron transfer is not yet understood; however, the metal-sulfur interaction appears to play an important role.³⁴ The inner coordination-sphere of the small molecular models of the active site seems invariant, even though large differences are observed in the reduction potentials.³⁵⁻³⁷ It has been suggested that modulation of the fold angle (θ) might be pivotal in tuning the properties of these active sites and their models.³⁶

2.0 Experimental Section

2.1 General

All reactions and manipulations were carried out under an inert environment of argon gas using standard Schlenk techniques, a high-vacuum/gas double line setup, and an inert atmosphere glove bag. The argon was predried by passing the high-purity-grade gas through a series of drying towers. All glassware was dried in an oven at 150°C and Schlenk ware was further purged by repeated evacuation and inert gas flushes prior to use. Tetrahydrofuran (THF) and toluene were distilled from Na/benzophenone; triethylamine was distilled from Na/K amalgam.³⁸ The prepurified solvents were subsequently transferred and stored under N₂ over fresh drying agents. These solvents were freshly distilled under nitrogen prior to use, thoroughly degassed by repeated freeze-thaw-pump cycles, and transferred to reaction vessels via steel cannulae under a positive pressure of inert gas. Dichloromethane, 1,2-dichloroethane, cyclohexane, toluene (EM Science, Omnisolv), n-hexane and n-pentane (Burdick and Jackson) were used as received and deoxygenated by bubbling with argon. Molybdenum hexacarbonyl (Mo(CO)₆, Aldrich) was dried in vacuum prior to use. Potassium hydrotris(3,5-dimethyl-1-pyrazolyl)borate (KTp*) and the precursor complexes (Tp*)Mo^V(NO)(CO)₂ and (Tp*)Mo^V(NO)I₂.C₆H₅CH₃ and the ligands H₂bdt (1,2-benzenedithiol) were prepared according to literature procedures.^{39,40} The ligand H₂tdt (4-methyl-1,2-benzenedithiol) and H₂bdtCl₂ (3,6-dichloro-1,2-benzenedithiol) employed in the syntheses of the (Tp*)Mo^V(NO)(S-S) compounds (**2**, **3**) were used as received from Aldrich.

TLC analysis was carried out on silica gel 60 F₂₅₄ plastic sheets (EM Science) and column chromatography was carried out in glass columns with silica gel (Merck, grade 9385, 230-400 mesh, pore diameter 60 Å) as the stationary phase. Mass spectra were recorded on a JEOL HX110 high-resolution sector instrument utilizing fast atom bombardment (FAB) ionization in a matrix of 3-nitrobenzyl alcohol (NBA). IR spectra (4000-400 cm⁻¹) were collected on a Nicolet Avatar ESP 360 FT-IR spectrophotometer in KBr disks or as dichloromethane solutions (between NaCl plates) at room temperature. Electronic absorption spectra of samples dissolved in 1,2-dichloroethane solutions were recorded with a 1-cm pathlength Helma quartz cell equipped with a teflon stopper, on a modified Cary 14 (with OLIS interface, 250-2600 nm) spectrophotometer. Solvent background corrections were made in all cases. ¹H-NMR (CDCl₃) spectra were acquired on a Bruker DRX-500 spectrometer operating at a ¹H frequency of 500.13 MHz using a 5 mm Nalorac triple-resonance 3-axis gradient probe. Chemical shifts were referenced to residual CHCl₃ at 7.24 ppm.

2.2 Synthesis of (Tp*)Mo(NO)(bdt) (1)

In a 100 ml round bottom evacuated Schlenk flask, highly purified (Tp*)Mo(NO)I₂·C₆H₅CH₃ (0.38 g, 0.5 mmol) was added to H₂bdt (0.1 g, 0.7 mmol) in 50 ml of dry, degassed toluene in a 100 ml round bottom Schlenk flask for synthesis of **1**. The mixture was deoxygenated thoroughly with argon saturation while being stirred at ~80° C. Dry, degassed Et₃N (0.4 ml, 2.2 mmol) was added slowly dropwise via a gas tight syringe to this rigorously stirring solution. The solution changed color to greenish and later to deep blue. The reaction mixture was refluxed for 16 hours, and the reaction

progress was monitored by IR spectroscopy (shift of $\nu(\text{NO})$ stretching frequency) and TLC analysis (disappearance of $(\text{Tp}^*)\text{Mo}^{\text{V}}(\text{NO})\text{I}_2$ precursor). Upon completion of the reaction, the blue-green precipitate, primarily $\text{Et}_3\text{N}\cdot\text{HI}$ resulting from the proton abstraction and ligand exchange processes, was removed by filtration from the hot solution under dry argon. The filtrate was cooled to room temperature and evaporated to dryness with a rotary evaporator. The solid dark-purple residue was re-dissolved in toluene, concentrated under vacuum, and layered with n-pentane. The dark-purple powder precipitate was collected by filtration and washed with n-pentane until the filtrate was clear. The powder was then dissolved in dichloromethane, filtered to remove any insoluble materials, and evaporated to dryness in vacuum. The solid was pumped on for several hours to assure dryness and the complete removal of excess triethylamine. The solid material was re-dissolved in dichloromethane, concentrated, and loaded on a silica gel chromatographic column under a positive pressure of argon. A dark-purple fraction (band #1) eluted off the column using dichloromethane: cyclohexane (1:3) as the eluant. Band #1 was further purified by a second silica gel column using dichloromethane: cyclohexane (1:1) as the eluant. The purity of compound was confirmed by TLC analysis. The dark-purple solution, which was deemed pure by TLC was evaporated to dryness in vacuum, re-dissolved in dichloromethane, and layered with n-pentane to yield a dark -purple crystalline material. This material was filtered, washed with pentane and then dried in vacuum. The product was characterized by IR, UV/VIS and mass spectroscopy. Slow vapor diffusion of n-pentane into a saturated dichloromethane solution of **1** afforded diffraction quality crystals. *Characterization:* HRMS $\{\text{M} + \text{H}\}^+$

peak gives $m/z = 565.0798$ (calculated, 565.0792) and corresponds to the formula $\{^{12}\text{C}_{21}\text{H}_{27}\text{N}_7^{11}\text{B}^{32}\text{S}_2^{35}\text{O}^{98}\text{Mo}\}$, IR data (KBr) $\nu(\text{B-H}) = 2551 \text{ cm}^{-1}$, $\nu(\text{NO}) 1670 \text{ cm}^{-1}$, UV-vis data $\lambda(\text{nm})(E(\text{cm}^{-1}); \epsilon(\text{M}^{-1}\text{cm}^{-1}))$: 732(13661; 1576), 579(17271; 4527), 370(27027; 3154), 326(30675; 3645), 292(34247; 5898), $^1\text{H-NMR}$ (500MHz, CD_2Cl_2 , 298 K): $\delta(\text{ppm})$ 8.057, 7.274 (2H, dd, $^3J_{\text{HH}} = 4.5\text{Hz}$, 3.0 Hz; 2H, dd, $^3J_{\text{HH}} = 4.5\text{Hz}$, 3.0 Hz), 5.992, 5.623 (2H, s; 1H, s), 2.485, 2.404, 2.308 (7H, s; 4H, s; 7H, s).

2.3 Synthesis of $(\text{Tp}^*)\text{Mo}(\text{NO})(\text{tdt})$ (2)

The preparation of $(\text{Tp}^*)\text{MoNO}(\text{tdt})$ (2) followed from published procedures.¹⁹ A mixture of $(\text{Tp}^*)\text{Mo}(\text{NO})\text{I}_2 \cdot \text{C}_6\text{H}_5\text{CH}_3$ (0.9 g, 1.2 mmol) and H_2tdt (0.33 g, 2.1 mmol) were refluxed for 16 hours instead of 24 hours as given in the literature.¹⁹ Slight modifications were also made in the work up procedures to obtain the pure compound suitable for growing X-ray diffraction quality crystals. In our work-up procedure the reaction mixture was evaporated to dryness under reduced pressure and the solid obtained was dissolved in a 1:3 CH_2Cl_2 :cyclohexane mixture and subjected to column chromatography. The product is contained in a deep blue band that is well separated from other side products, which do not separate well when eluted with CH_2Cl_2 as in the original preparation.¹⁹ Further purification was achieved by a second column chromatography step using 1:1 CH_2Cl_2 : cyclohexane as the eluant. Slow diffusion of heptane into a CH_2Cl_2 solution of 2 yielded X-ray diffraction quality crystals. Compound 2 show similar spectroscopic features to those reported in the literature.¹⁹

2.4 Synthesis of (Tp*)Mo(NO)(bdtCl₂) (3)

All the synthetic steps were similar to those described for **1**, except for the stoichiometric ratio of the reagents. Highly purified (Tp*)Mo(NO)I₂·C₆H₅CH₃ (677 mg, 1.00 mmol) was added to a solution of H₂bdtCl₂ (220 mg, 1.1 mmol) in 50 ml of dry, degassed toluene in a 100 ml round-bottom Schlenk flask. Characterization: HRMS {M + H}⁺ peak that gives m/z = 633.0035 (calculated, 633.0002) and corresponds to the formula {¹²C₂₁H₂₅N₇¹¹B³²S₂³⁵Cl₂O⁹⁸Mo} for **3**, IR (KBr) ν(B-H) = ν(B-H) = 2548 cm⁻¹; ν(NO) 1674 cm⁻¹, UV-vis data λ(nm)(E(cm⁻¹); ε(M⁻¹cm⁻¹)): 739(13531; 1583), 573(17452; 6476), 372(26882; 3734), 330(30303; 5186), 294(34013, 8477). ¹H-NMR (500MHz, CD₂Cl₂, 298 K): δ(ppm) 7.369 (1H, s), 6.017, 5.629 (2H, s; 1H, s), 2.502, 2.415, 2.287 (7H, s; 4H, s; 7H, s).

2.5 X-Ray Crystal Structure Determinations:

Crystal Structures of 1 and 2: Crystals of **1** and **2** were mounted on glass fibers for structure determination using an Enraf-Nonius CAD4 diffractometer. Crystal data and details of structure determinations are given in Table 7.1. The structures were determined by direct methods and refined on F² by full-matrix least squares with anisotropic parameters for the non-hydrogen atoms. Scattering factors were taken from Cromer and Waber,⁴¹ anomalous dispersion effects were included for all non-hydrogen atoms with the values of Δf' and Δf'' taken from Cromer,⁴² and the structure was solved by direct methods using SHELXS in the Bruker SHELXTL (Version 5.0) software

package. Hydrogen atoms were placed in calculated positions with isotropic displacement parameters.

Crystal Structure of 3: A dark-purple cuboid of **3** was mounted on a glass fiber for structure determination using a Bruker SMART 1000 CCD detector X-ray diffractometer. Key parameters for the structure determination are also summarized in Table 7.1. Empirical absorption and decay corrections were applied using the program SADABS. The structure was solved by direct methods using SHELXS in the Bruker SHELXTL (Version 5.0) software package. Refinements were performed on F^2 by full-matrix least squares with anisotropic displacement parameters for all the non hydrogen atoms (using SHELXL and illustrations were made using XP). Hydrogen atoms were added at idealized positions, constrained to ride on the atom to which they are bonded and given thermal parameters equal to 1.2 or 1.5 times U_{iso} of that bonded atom. Scattering factors and anomalous dispersion were taken from International Tables Vol C, Tables 4.2.6.8 and 6.1.1.4.^{41,42}

2.6 Photoelectron Spectroscopy:

He I gas-phase photoelectron spectra were collected on an instrument with a 36-cm radius hemispherical analyzer (8 cm gap, McPherson) and custom designed sample cells, excitation sources, and detection and control electronics.^{43,44} The excitation source was a quartz lamp with the ability to produce HeI photons (21.21 eV). The ionization energy scale for the HeI experiments was calibrated by using the $^2E_{1/2}$ ionization of methyl iodide (9.538 eV), with the argon $^2P_{3/2}$ ionization (15.759 eV) used as an internal calibration lock during the experiment. During data collection the instrument resolution

(measured using the FWHM of the argon $^2P_{3/2}$ ionization peak) was 0.022 – 0.025 eV.

All data were intensity corrected with an experimentally determined instrument analyzer sensitivity function. The He I spectra were corrected for the presence of ionizations from other lines (He I β line, 1.9 eV higher in energy and 3% the intensity of the He I α line).

All samples sublimed cleanly with no detectable evidence of decomposition products in the gas phase or as a solid residue. The sublimation temperatures were monitored using a “K” type thermocouple passed through a vacuum feed and attached directly to the aluminum ionization sample cell. The sublimation temperatures (in °C, 10^{-4} Torr) were as follows: (Tp*)Mo(NO)(bdt), 209-218°; (Tp*)Mo(NO)(tdt), 220-229°; (Tp*)Mo(NO)(bdtCl₂), 218-230°.

2.7 Theoretical

Geometry optimization, SCF (self-consistent field) and molecular orbital calculations were performed using the ADF (Amsterdam density functional theory calculations) package (release 2000.02). Starting geometries were obtained from crystal structures of **1**, **2**, and **8**. A generalized gradient approximation, with the exchange correction of Becke⁴⁵ and the correlation correction of Lee *et. al.*,⁴⁶ was used for all density functional calculations. All core levels (up to 3d for Mo and 1s for C, N, B and O) were treated as frozen orbitals. The calculations employed triple-zeta basis sets with Slater type orbitals and a polarization function for all elements. Calculations on the ground-state molecules were performed in the spin-restricted mode. Spin-unrestricted SCF (self-consistent field) calculations were performed on the proposed ion states formed

by photoionization by removing one electron from the relevant orbital and comparing the total energy with that of the ground state molecule. A linear correction was applied for comparison of the calculated and the observed energies, *i.e.* the calculated SCF energies and orbital energies were shifted by the difference between experimentally obtained and calculated energies of the HOMO.

3.0 Results and Discussion:

3.1 Synthesis and Physical Properties of Tp*Mo(NO)(S-S) Compounds:

The identities of the reaction products were confirmed by their high resolution mass spectra. The reaction products **1**, **2**, **3** are soluble in dichloromethane, 1, 2-dichloroethane, toluene and benzene. Scheme 1 shows several different routes to the synthesis of Tp*Mo(NO)(S-S) complexes. The Tp*Mo(NO)X₂ precursors (X = Cl, Br, I) are well known; however, partial halogenation of the pyrazole ring at C-4 position has been observed in the preparation of Tp*Mo(NO)Cl₂ and Tp*Mo(NO)Br₂ precursors.⁴⁷ In addition, use of the precursor Tp*Mo(NO)Cl₂ can lead to the formation of unexpected products, including disulfide formation during the synthesis of Tp*Mo(NO)((SCH₂)₂C₆H₄).⁴⁸ The Tp*Mo(NO)I₂·C₆H₅CH₃ precursor has been primarily used for the synthesis of Tp*Mo(NO)(S-S) complexes in this work because it is relatively easy to prepare from Tp*Mo(NO)(CO)₂ and the iodide ligand seems to be a very good leaving group in the subsequent substitution reactions.⁴⁷

The solid-state IR spectra in KBr exhibited bands characteristic of the (Tp*) ligand ($\nu(\text{B-H}) = 2551 \text{ cm}^{-1}$ for **1**, 2550 cm^{-1} for **2** and 2548 cm^{-1} for **3**). This $\nu(\text{B-H})$ is similar to that observed in the range of 2543 to 2549 cm^{-1} for the related chelate complexes (including **5**, **6**).⁴⁸ The solution IR spectra of the (Tp*)Mo(NO)(S-S) complexes in dichloromethane showed no significant frequency shifts or additional bands, indicating that the solid phase and solution structures are similar. The purity of the products was also confirmed by the absence of $\nu(\text{CO})$ and the shift in the $\nu(\text{NO})$ stretching vibrations of the precursor complexes (Tp*)Mo(NO)(CO)₂ ($\nu(\text{CO}) = 1906 \text{ cm}^{-1}$, $\nu(\text{NO}) = 1655 \text{ cm}^{-1}$) and (Tp*)Mo(NO)I₂ ($\nu(\text{NO}) = 1700 \text{ cm}^{-1}$) which also served as a diagnostic tool for monitoring the progress of the reaction.

The values of $\nu(\text{NO})$ range from 1674 cm^{-1} for **3** to 1660 cm^{-1} for **2** and decrease slightly with increasing electron withdrawing properties of the substituents on the benzene rings of the coordinated ene-dithiolates. The reduction potential ($E_{1/2}$) of -723 mV for **3**, -896 mV for **2**, and -862 mV for **1** also follows the trend **3** > **1** > **2**.⁴⁹ McCleverty and coworkers have earlier proposed a correlation between $E_{1/2}$ and $\nu(\text{NO})$.⁵⁰ Our results also show that the more electron withdrawing the ene-dithiolate the higher is the $\nu(\text{NO})$ stretch. Thus $\nu(\text{NO})$ is a sensitive indicator of the perturbation of electron density on the Mo center by the remote substitution on the ene-dithiolate ligand.

The diamagnetic {MoNO}⁴ complexes have been probed using ¹H-NMR.^{1,19,39,40,47,51-53} The 1-D NMR data and the X-ray structures show that complexes **1-3** have effective C_s symmetry with two of the three pyrazolyl rings being magnetically equivalent. The ¹H-NMR spectrum shows pyrazolyl methyl groups in the (Tp*)-ligand

as singlets of relative area 7:4:7 at $\delta(\text{ppm})$ 2.308, 2.404, 2.485 in **1** and $\delta(\text{ppm})$ 2.287, 2.415, 2.502 in **3**. The pyrazolyl 4-H signals appeared as two signals of relative area 1:2 at $\delta(\text{ppm})$ 5.623, 5.992 for **1** and $\delta(\text{ppm})$ 5.629, 6.017 for **3**. These are in the typical range of CH_3 ($\delta(\text{ppm})$ 1.5 to 3.0) and pyrazolyl 4-H ($\delta(\text{ppm})$ 5.0 to 6.5) shifts for other $(\text{Tp}^*)\text{Mo}(\text{NO})(\text{S},\text{S})$ complexes.⁵¹ The aryl protons of the bdt^{2-} ligand in **1** resonate as two doublets of doublets (4.5 Hz, 3.0 Hz) at $\delta(\text{ppm})$ 7.274 and 8.057 and those protons of the bdtCl_2^{2-} ligand in **3** resonate as one singlet at $\delta(\text{ppm})$ 7.369.

3.2 Molecular Structure Analysis of $(\text{Tp}^*)\text{Mo}(\text{NO})(\text{S}-\text{S})$ compounds:

The structures of compounds **1-3**, determined by single-crystal X-ray diffraction, are shown in Figure 7.3. Tables 7.2 and 7.3 show key geometric features of the coordination environment of the Mo atom. Compounds **1-3** are the first structurally characterized six-coordinate $\{\text{MoNO}\}^4$ complexes that contain a single ene-1,2-dithiolate ligand *cis* to the terminal nitrosyl group. Enemark *et al.* have previously reported the structures and properties of the corresponding oxo analogues, $(\text{Tp}^*)\text{MoO}(\text{S}-\text{S})$.^{4,35,54,55} Compounds **1**, **2** and **3** crystallize in three different space groups $P2_1/c$, $P2_1/n$ and $Pnma$, respectively. No symmetry is imposed on **1** and **2** by their space groups, but C_s symmetry is imposed on **3** by the space group $Pnma$ (Figure 7.4). In the crystals of **3**, the atoms N1, O1, Mo1, B1, H1A, N31, N32, C33, C34, H34A, C35, C36, H36A, C37, H37A lie on a mirror plane. In these complexes the terminal nitrosyl ligand and the two sulfur atoms of the ene-dithiolate are constrained to be mutually *cis* to each other by the *fac* stereochemistry imposed by the tridentate Tp^* ligand. Thus molecules of compounds **1** and **2** also have effective C_s symmetry. All three molecules exhibit a distorted pseudo-

octahedral coordination geometry, in which the Mo atom is ligated by a nitrogen atom from the nitrosyl ligand, two sulfur donor atoms of the (S-S) ligands and three nitrogen donor atoms of the tridentate facially coordinated (Tp*) ligand. The maximum angular deviations from ideal octahedral geometry within the N₂S₂ planes of the compounds are: 5.96° in **1** (N(21)-Mo(1)-S(2)); 5.52° in **2** (N(11)-Mo(1)-S(1)); and 4.08° in **3** (N(21)-Mo(1)-S(2), N(11)-Mo(1)-S(1)). The mean deviation of 4.00° in **1**, 3.45° in **2** and 3.38° in **3** is consistent with deviations observed in other structures based on {(Tp*)Mo(NO)}²⁺ fragment.^{21,48,52,53,56,57} The N-Mo-N angles between the nitrogen atoms of (Tp*) ligand are always less than 90°.

Seven other structurally characterized complexes with {(Tp*)Mo(NO)S₂} cores are available in the CSD database (Chart 1).¹⁸ Of these {MoNO}⁴ complexes, only **1-3** have five-membered ene-1,2-dithiolate chelate rings. The molecular structure of a complex containing similar fragment and an oxygen containing five membered chelate ring (catechol) has been reported earlier, in which boron sequestering resulted in the degradation of the (Tp*) ligand skeleton.⁵¹ Structurally characterized chelate compounds **4**, **5**, and **6** contain nine, seventeen, and twenty-five membered chelate rings, respectively.^{48,56} Compound **7** contains the organometallic chelate ligand 1,1'-dithiaferrocenyl-S,S'.⁵⁷ Compounds **8**, **9** and **10** possess two mono thiolates.^{21,52,53}

The structural parameters (bond lengths and angles) for the {(Tp*)Mo(NO)}²⁺ core reported in Table 7.2 for compounds **1**, **2** and **3** are similar to one another and also agree with those found for compounds **4** through **10** (Chart 1). The observed Mo-N1 distance of 1.818(6) Å in **1** is 0.044 Å (8σ) longer than that of 1.774 (6) Å in complexes **2**

and **3**. All three values are between the largest (1.839 Å in **7**) and the smallest (1.730 Å in **5**). Another structural parameter of interest in metal nitrosyl complexes is the M-N-O angle. This angle is 174.2(6)° in **1**, 175.0(4)° in **2** and 174.5(5)° in **3**. The other Mo-N-O angles in Chart 1 range from 179.026° in **8** to 172.431° in **7**. A nearly linear Mo-N-O unit is expected for a six-coordinate {MoNO}⁴ compound.¹³ The N-O bond distance is 1.113(7) Å in **1**, 1.171(5) Å in **2**, and 1.181(7) Å in **3**, and shows no correlation with $\nu(\text{NO})$.

Additional common structural features in these compounds are the angles between *trans* ligands. The angle involving the nitrosyl nitrogen atom (N1-Mo-N31) is close to 180°, whereas other two *trans* angles (S1-Mo-N11 and S2-Mo-N21) fall in the range 160-166°. Compound **3** shows the strongest *trans* effect from a terminal nitrosyl group of all of the compounds in Table 7.2. Its Mo-N31 distance (2.258(5) Å) is 0.110 Å longer relative to Mo-N11 and Mo-N21 (both 2.148 Å). This *trans* effect due to the strong σ donor and π acceptor properties of the nitrosyl ligand³ is not as pronounced as the *trans* effect in the corresponding oxo-Mo analogue of complex **3** where the strong π donor and σ donor properties of the oxo-ligand lengthen the corresponding Mo-N31 distance (2.391(3) Å) by 0.214 Å relative to Mo-N21 (2.177(2) Å) and 0.225 Å relative to Mo-N11 (2.166(3) Å).³⁵

The Mo-S1 and Mo-S2 distances are 2.374(2) Å and 2.3882(19) Å in **1**, 2.3773(15) Å and 2.4078(15) Å in **2** and 2.3926(12) Å in **3**¹. The average Mo-S bond

¹ The shortest Mo-S distance in mononuclear group VI transition-metal-nitrosyl complexes containing at least two sulfur donor ligands is 2.289 Å in (tris(2-

lengths of 2.3811 Å in **1** and 2.3926 Å in **3** compares to 2.376 Å and 2.374 Å in the corresponding oxo-Mo analogues. Thus a slight Mo-S bond lengthening is observed in nitrosyl-Mo family in the chelate complexes which is opposite of the trend observed in non chelated complexes. A bond reduction is observed from an average value of 2.382 Å in (Tp*)MoO(SPh)₂ to 2.357 Å in (Tp*)Mo(NO)(SPh)₂ (**8**). It is interesting to note that the Mo-S distance of 2.375 Å and 2.357 Å in complex **7** does not significantly vary from those in **1** through **3** despite the significant change in the nature of the sulfur donor ligand (1,1'-dithiaferrocenyl-S,S') in **7**.⁵⁷ Table 7.2 shows that there are no significant changes observed in M-S distances between chelate rings and non chelated ligands, however, significant differences are observed in bond angles of S atoms with axial ligands (N1-Mo-S1 or S2). Bond angles N1-Mo-X (X = centroid of S1 and S2) of 86.14(10) Å in **1**, 87.26(14) Å in **2**, and 87.63(13) Å in **3** are the most acute in all of the structurally characterized mononuclear group VI transition metal-nitrosyl complexes containing at least two sulfur donor ligands².

The dihedral angle (ϕ_d) (Table 7.2) between the planes Mo1-N11-N21 and Mo1-S1-S2 groups the ene-1,2-dithiolate compounds **1-3** distinct ($\phi_d > 174^\circ$) from the other complexes in Chart1. The value of $\phi_d = 175^\circ$ for **1** and 174.7° for **3** is significantly larger than 161.9° and 162.2° in corresponding oxo-Mo complexes. This is due to the longer Mo-NO bond (1.818(6) Å in **1** and 1.774(6) Å in **3**) whereas a lone pair interaction

thioethyl)amine-N,S,S',S'')-nitrosyl-molybdenum⁵⁸ and the longest is 2.639 Å in (2,3:8,9-dibenzo-1,4,7,10-tetrathiadecane-S,S',S'',S''')-nitrosyl-diphenyl(methyl)phosphineiminato-molybdenum(III).⁵⁹

² This angle has the largest value of 161.862 Å in (1,2-bis(2-mercaptophenylthio)ethane)-nitroso-trimethylphosphine-molybdenum(II) complex.⁶⁰

of strongly bonded terminal oxo atom (Mo-O = 1.678(4) Å in (Tp*)MoO(bdt) and 1.679(3) Å in (Tp*)MoO(bdtCl₂)) draws the Mo atom out of N₂S₂ (N11-N21-S1-S2) plane. This is also indicated by relatively smaller Mo distances from N₂S₂ plane (Table 7.3) in the reported complexes (0.069 Å in **1** and 0.063 Å in **3**) compared to their oxo analogues (0.264 Å and 0.258 Å respectively).^{4,35,36,54,55}

The ene-1,2-dithiolate fragment does not show significant structural differences with remote substitution as indicated by the average S-C bond length of 1.742 Å in **1**, 1.743 Å in **2** and 1.743 Å in **3** and the C=C bond length of 1.406 Å in **1**, 1.413 Å in **2** and 1.431 Å in **3**. The most significant structural difference between (Tp*)MoE(S-S) systems (where E = NO, O) is the angle (δ) formed between the ene-1,2-dithiolate (S-C=C-S) least squares plane and the S-Mo-S plane along the line of intersection containing the S---S atoms (see Figure 7.2B). This angle in **1** is 137.9°, and thus the S-C=C-S plane is folded up toward the terminal nitrosyl group by $\theta = 180^\circ - \delta = 42.1^\circ$. This fold angle is 41.1° in **2**, and 44.4° in **3** and thus increases slightly with respect to the electron withdrawing nature of the remote substituent on ene-dithiolate. The fold angle is in contrast to what is observed in the oxo-Mo systems where it ranges from 6.9° in (Tp*)MoO(bdtCl₂) to 29.5° in (Tp*)MoO(qdt).^{4,35,36,54,55} The (bdt) ring structure itself is essentially planar in all of the complexes. As mentioned earlier, compounds **1-3** have large fold angles notwithstanding their acute ON-Mo-S angles, which are ~ 14° smaller than the O-Mo-S angles in the analogous oxo-Mo compounds.^{4,35,54,55}

In summary, the molecular structures of **1**, **2** and **3** show that remote substituents on ene-1,2-dithiolate ligand do not significantly alter the structural parameters of the

inner coordination sphere of the Mo center. However, a change of axial ligand (E) from oxo to nitrosyl induces significant changes in the fold angle and the E-Mo-X angle (X = centroid of S1, S2). The large fold angle in nitrosyl-Mo complexes despite their smaller E-Mo-X angle is intriguing. A CSD search for the transition metal complexes containing an ene-1,2-dithiolate chelate showed a range (0-52°) of fold angles.¹⁸ A majority of these complexes have planar ($\theta = 0.0^\circ$) ene-1,2-dithiolate rings but some of them are folded by as much as 52°.^{3, 18, 62} The fold angle range in the structures of group VI transition metal ene-dithiolene complexes is 0 to 44.4° (Figure 7.5) with the largest value of fold angle observed in the complexes **1-3** reported here.

The geometric structure perturbations in terms of the fold angle has implications with respect to the significant differences between the electronic structures of (Tp*)MoE(S-S) (E = NO, O). In these compounds the strong covalent bonding of {MNO}⁴ group leads to an energetically isolated LUMO which is a nonbonding metal *d* orbital (*d_{xy}*) (Figure 7.6). The short Mo-O bond in (Tp*)MoO(S-S) complexes, on the other hand, dominates the splitting of *t_{2g}* orbitals (strong σ and π donor oxo-ligand).^{63, 64} The electronic configuration of the oxo-Mo(V) systems is (*d_{xy}*)¹(*d_{xz}* *d_{yz}*)⁰ and the nitrosyl-Mo(II) is (*d_{xz}* *d_{yz}*)⁴(*d_{xy}*)⁰. The *d_{xy}*-*p* overlap in LMo(NO)(SC₆H₅)₂ (where L = η^5 -C₆H₅, Tp*(**8**)), {MNO}⁴ complexes with filled *d_{xz}* and *d_{yz}* orbitals, is maximized by a ON-Mo-S-C torsion angle near 0 and 180° (Figure 7.2A).^{20, 21} The torsion angle ON-Mo-S-C in the above two LMo(NO)(SC₆H₅)₂ compounds are 12 and -174° in the former and -16 and -

³ The most folded ene-1,2-dithiolate ring has been observed in the disordered structure of a uranium complex where $\theta = 76.21^\circ$.⁶¹

168° in the latter and indicate that the electronic structure of L has little influence on the overall stereochemistry of the complex.^{20,21}

It is believed that the fold angle in compounds **1-3** has an electronic origin that may be attributed to the interaction of sulfur lone pairs (Sp_z or S_π or S_{op} orbitals) with the metal d-orbitals. The folding of the ene-1,2-dithiolate minimizes the interaction of the filled Sp_z orbitals with the filled metal d_{xz} and d_{yz} orbitals and favors the bonding interaction between the Sp_z orbitals and the empty metal d_{xy} orbital (Figure 7.2B). It has been observed that the electronic occupation of d_{xy} orbital has significant effect on the fold angle. The complexes with $(d_{xy})^0$ electronic configuration have the most folded ene-1,2-dithiolate (**1-3**: $\theta = 41.1$ to 44.4°) in related group VI complexes. It is postulated that the fold angle should decrease as the complexes **1-3** are reduced to $(d_{xy})^1$ and the ene-dithiolate should become close to planar ($\theta \approx 0^\circ$) on further reduction to $(d_{xy})^2$. The metallocene-dithiolene complexes show a fold angle (θ) close to 0° in the 18 electron d^2 complexes; upon oxidation this angle increases to $\theta = 45-50^\circ$ in the 16 electron d^0 complexes.^{24,25,62,65,66} The electronic origin of the fold angles in compound **1-3** is a current active research area in our laboratory.^{29,37}

3.3 Photoelectron Spectroscopy

A stack plot of He I gas phase valence photoelectron spectra (PES) of **1**, **2** and **3** in the region 5.00 eV to 15.00 eV is displayed in Figure 7.7. The region from 8.50 eV to 15 eV is primarily due to the ligand ionizations (Tp*, benzene ring, nitrosyl group). The broad Tp* ionization centered about 9 eV is also observed in analogous compounds with

terminal oxo and sulfido groups.^{43,67} In compound **3**, the chlorine lone pair based ionization appearing at 10.76 (0.02) eV is easily assigned based on its reduced intensity in the He II excitation source (spectrum not shown). The ionizations appearing at lower energy than 8.50 eV, assigned to the sulfur and the molybdenum based molecular orbitals, are broader in the nitrosyl complexes (**1**, **2** and **3**) than their oxo-Mo analogues.⁴³ The first ionization energies of 6.95 (0.02) eV for **2**, 6.97(0.02) eV for **1**, and 7.06 (0.02) eV for **3** (Table 7.4) suggest that electron withdrawing substituents on the ene-1,2-dithiolate stabilize the HOMO. However, this effect is less than that observed for the oxo-Mo counterparts, where the energy range is 0.8 eV.³⁷ The first band can be fitted with two symmetric Gaussians, 1 and 1', associated with the metal out of the plane orbitals (d_{xz} and d_{yz}). Bands 2, 2' and 3, 3' are assigned to dithiolate sulfur based orbitals (symmetric and antisymmetric combinations of out of plane (S_{op}^+ , S_{op}^-) and in-plane sulfur p orbitals (S_{ip}^+ , S_{ip}^-), respectively) and are further discussed in detail in the computational section. A stack plot of the photoelectron spectra of pairs of (Tp*)MoE(tdt), (Tp*)MoE(bdt) and (Tp*)MoE(bdtCl₂) (where E = O, NO) is shown in Figure 7.8. The differences in the ionization energies of the HOMO in these pairs are 0.05, 0.13 and 0.26, respectively. These values show that the more electron withdrawing is the substituent on the benzene rings of the enedithiolate ligand, the more separated are the first ionizations in these pairs. This implies that the electron withdrawing groups make the enedithiolate ligand less effective of an electronic buffer due to the withdrawal of the electron density from sulfur atoms.

3.4 Computational Study

The results of DFT calculations are reported in Table 7.4 and Figure 7.9. The individual contributions of the major contributor atomic orbitals to six frontier orbitals are also provided in Figure 7.9. As discussed earlier, the lowest unoccupied molecular orbital (LUMO) is predominantly a metal in-plane orbital (d_{xy}). The highest occupied molecular orbital (HOMO) and HOMO-2 are predominantly metal out of plane orbitals (d_{xz} and d_{yz}). The HOMO-1 orbital that would be proposed to be predominantly a dithiolate out of plane (S_{op}^+ or S_{π}^+) orbital has significant metal in-plane characters mixed in. The S_{op}^+ orbital has the right symmetry and energy to mix with the metal in-plane orbital. Thus, the HOMO-1 supports the hypothesis of dithiolate folding as a stabilizing interaction of filled sulfur p orbitals with the empty metal orbital. The HOMO-3 and HOMO-4 are antisymmetric combinations of the dithiolate out of plane and in-plane molecular orbitals.

4.0 Conclusions

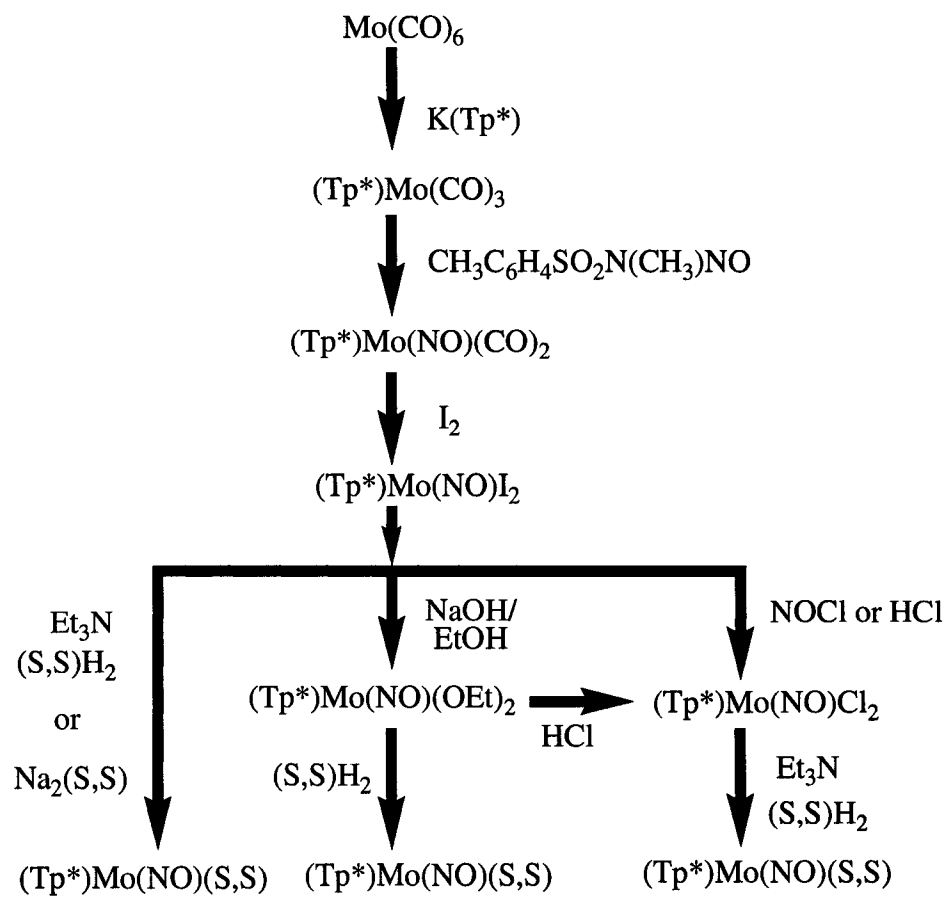
The synthesis, structural and physical characterization of three $(Tp^*)Mo(NO)(S-S)$ compounds have provided an opportunity to investigate the geometric and electronic structure differences of $(Tp^*)MoE(S-S)$ (where $E = O, NO$) systems as a function of axial ligation and remote substituent effects on the ene-1,2-dithiolate ligand. The most significant structural difference is the large fold angle of ene-1,2-dithiolate along S—S axis in the nitrosyl-Mo compounds.

Photoelectron spectroscopy and density functional theoretical studies provide insight into the electronic structures of these molybdenum nitrosyls and supports the hypothesis of folding of the dithiolate ligand. This folding of the dithiolate ligands in compounds **1-3** minimizes the filled-filled interaction of out of plane metal and sulfur orbitals. The frontier orbitals have significant contributions from dithiolate out of plane and in-plane molecular orbitals and support the assignment of ionizations in the photoelectron spectroscopic studies. Thus, there is sufficient evidence to support the electronic origin of the geometric perturbations of dithiolate folding. This angular perturbation (fold angle) is sensitive to the electronic occupation of metal in-plane (equatorial) orbital.

It has been postulated earlier that the variation in the fold angle of pyranopterin-ene-1,2-dithiolate may control the electronic structure of the Mo center of enzymes and could play a regulatory role in their catalysis.³⁵ The reduction potential of these (Tp*)Mo(NO)(S-S) compounds is sensitive to peripheral substitution of the ligand, whereas the first ionization energy is not. This diversity is due to the different orbitals involved in each of these processes and supports the electronic structure origin behind the fold angles in Mo-nitrosyls containing an ene-1,2-dithiolate.

Chart 1. Classification, $\nu(\text{NO})$ (IR, KBr), and Abbreviations of $(\text{Tp}^*)\text{Mo}(\text{NO})(\text{S,S})$ Compounds ((Tp^*): hydrotris(3,5-dimethyl-1-pyrazolyl)borate).

(S,S)	Compound No.	$\nu(\text{NO})$ (cm^{-1})	References
bdt	1	1670	this work
tdt	2	1660	[19], this work
bd tCl_2	3	1674	this work
$\text{S}(\text{CH}_2)_2\text{CONH}(\text{CH}_2)_2\text{S}$	4	1667	[53]
$(1,4\text{-}(\text{SCH}_2)_2\text{C}_6\text{H}_4)_2$	5	1653	[48]
$(1,4\text{-}(\text{SCH}_2)_2\text{C}_6\text{H}_4)_3$	6	1644	[48]
$(\text{Fe}(\eta^5\text{-C}_5\text{H}_4\text{S})_2)$	7	1634	[57]
$(\text{SC}_6\text{H}_5)_2$	8	1682	[21,52]
$(\text{SCH}_2\text{CONHCH}_3)_2$	9	1672	[53]
$(\text{SC}_2\text{H}_4\text{CONHCH}_3)_2$	10	1662	[53]
(bd t)	1,2-benzenedithiolate		
(td t)	3,4-toluenedithiolate		
(bd tCl_2)	3,6-dichloro-1, 2-benzenedithiolate		



Scheme 1. General synthetic routes to the $(\text{Tp}^*)\text{Mo(NO)(S,S)}$ compounds.^{19, 39, 40, 47, 51}

Table 7.1. Crystal data and structure refinement for complexes 1, 2 and 3

Identification code	1	2	3
Empirical formula	C ₂₁ H ₂₆ BMoN ₇ OS ₂	C ₂₂ H ₂₈ BMoN ₇ OS ₂	C ₂₁ H ₂₄ BCl ₂ MoN ₇ OS ₂
Formula weight	563.36	577.38	632.25
Temperature	298(2) K	298(2) K	173(2) K
Wavelength	0.71073 Å	0.71073 Å	0.71073 Å
Crystal system	Monoclinic	Monoclinic	Orthorhombic
Space group	P2 ₁ /c	P2 ₁ /n	Pnma
Unit cell dimensions	$a = 11.115(2)$ Å, $b = 13.667(3)$ Å, $c = 16.410(3)$ Å, $\alpha, \gamma = 90^\circ, \beta = 98.36(3)^\circ$	$a = 15.579(3)$ Å, $b = 9.942(2)$ Å, $c = 16.527(3)$ Å, $\alpha, \gamma = 90^\circ, \beta = 95.79(3)^\circ$	$a = 17.9879(9)$ Å, $b = 13.2277(7)$ Å, $c = 11.2505(6)$ Å, $\alpha, \beta, \gamma = 90^\circ$
Volume	2466.4(8) Å ³	2546.7(9) Å ³	2676.9(2) Å ³
Z	4	4	4
Density (calculated)	1.517 Mg/m ³	1.475 Mg/m ³	1.534 Mg/m ³
Absorption coefficient	0.729 mm ⁻¹	0.707 mm ⁻¹	0.872 mm ⁻¹
F(000)	1152	1160	1252
Crystal size	0.23 x 0.13 x 0.03 mm ³	0.17 x 0.12 x 0.08 mm ³	0.40 x 0.10 x 0.10 mm ³
Theta range for utilized data	1.85 to 24.97°	1.71 to 24.97°	2.14 to 27.29°
Limiting Indices	0 ≤ h ≤ 13, 0 ≤ k ≤ 16, -19 ≤ l ≤ 19	0 ≤ h ≤ 18, 0 ≤ k ≤ 11, -19 ≤ l ≤ 19	-23 ≤ h ≤ 23, -16 ≤ k ≤ 16, -14 ≤ l ≤ 14
Reflections utilized	4328	4468	26517
Independent reflections	4328 [R(int) = 0.0000]	4468 [R(int) = 0.0000]	3004 [R(int) = 0.0741]
Completeness to theta = 24.97°	100.0 %	100.0 %	95.5 %
Absorption correction	None	None	Empirical
Max. and min. transmission	0.9784 and 0.8502	0.9456 and 0.8893	0.9179 and 0.7219
Refinement method	Full-matrix least-squares on F ²	Full-matrix least-squares on F ²	Full-matrix least-squares on F ²
Data / restraints / parameters	4328 / 0 / 289	4468 / 0 / 314	3004 / 0 / 177
Goodness-of-fit on F	1.043	1.051	1.069
Final R indices [I > 2σ(I)]	R1 = 0.0630, wR2 = 0.1218	R1 = 0.0484, wR2 = 0.1092	R1 = 0.0517, wR2 = 0.1202
R indices (all data)	R1 = 0.1507, wR2 = 0.1454	R1 = 0.0922, wR2 = 0.1222	R1 = 0.0921, wR2 = 0.1457
Largest diff. peak and hole	0.855 and -0.550 e.Å ⁻³	0.631 and -0.327 e.Å ⁻³	0.595 and -0.521 e.Å ⁻³
RMS difference density	0.106 e.Å ⁻³	0.077 e.Å ⁻³	0.127 e.Å ⁻³

Table 7.2. Comparison of key bond lengths (Å) and parameters for compounds with {(Tp*)Mo(NO)S₂} core (trans effects are in Å and angles in °).

Comps	Mo-N1	Mo-N1-O1	Mo-N11	Mo-N21	Mo-N31	Mo-S1	Mo-S2	S1-Mo-S2	N1-Mo-X	ΔT	Φ _d
1	1.818(6)	174.2(6)	2.181(6)	2.164(5)	2.260(6)	2.374(2)	2.3882(19)	84.17(8)	86.14(10)	0.088	175.0
2	1.774(4)	175.0(4)	2.187(4)	2.161(4)	2.257(4)	2.3773(15)	2.4078(15)	83.79(5)	87.26(14)	0.080	174.4
3	1.774(6)	174.5(5)	2.148(3)	2.148(3)	2.258(5)	2.3926(12)	2.3926(12)	83.96(6)	87.63(13)	0.110	174.7
4	1.767	175.939	2.230	2.234	2.249	2.342	2.352	105.171	96.547	0.017	164.2
5	1.730	175.509	2.237	2.231	2.256	2.366	2.340	102.612	95.691	0.022	166.6
6	1.759	176.764	2.238	2.234	2.260	2.345	2.339	102.248	94.462	0.024	166.0
7	1.839	172.431	2.202	2.197	2.263	2.375	2.357	90.278	98.165	0.064	167.5
8	1.765	179.026	2.215	2.205	2.244	2.345	2.368	102.957	90.950	0.034	172.7
9	1.763	176.904	2.223	2.219	2.242	2.347	2.349	102.820	95.638	0.020	165.0
10	1.791	177.605	2.209	2.222	2.256	2.337	2.345	104.353	95.794	0.041	166.1

ΔT = Trans Effect [(Mo-N31)-(average Mo-N11 and Mo-N21)]

Φ_d = Dihedral angle between planes Mo-N11-N21 and Mo-S1-S2.

Table 7.3. Selected bond lengths (Å), bond angles (°) and torsion angles (°) (esd's in parentheses).

	1	2	3
N(1)-O(1)	1.113(7)	1.171(5)	1.181(7)
S(1)-C(1)	1.758(9)	1.734(6)	1.743(5)
S(2)-C(2)	1.726(8)	1.751(6)	1.743(5)
C(1)-C(2)	1.406(11)	1.413(7)	1.431(10)
N(1)-Mo(1)-S(1)	84.6(2)	87.78(14)	87.63(13)
N(1)-Mo(1)-S(2)	87.67(18)	86.75(14)	87.63(13)
N(1)-Mo(1)-N(21)	97.4(2)	95.06(18)	96.40(16)
N(1)-Mo(1)-N(11)	97.6(2)	97.72(17)	96.40(16)
N(1)-Mo(1)-N(31)	176.7(2)	177.38(17)	178.0(2)
N(21)-Mo(1)-N(11)	81.3(2)	81.59(15)	82.17(19)
N(21)-Mo(1)-N(31)	84.2(2)	84.27(16)	85.07(14)
N(21)-Mo(1)-S(1)	99.35(16)	97.52(12)	96.80(10)
N(21)-Mo(1)-S(2)	174.04(16)	177.80(12)	175.92(10)
N(11)-Mo(1)-N(31)	85.5(2)	84.70(14)	85.07(14)
N(11)-Mo(1)-S(1)	177.65(16)	174.48(11)	175.92(10)
N(11)-Mo(1)-S(2)	94.97(15)	96.94(11)	96.80(10)
N(31)-Mo(1)-S(1)	92.32(15)	89.79(11)	90.92(11)
N(31)-Mo(1)-S(2)	90.83(15)	93.98(11)	90.92(11)
C(1)-C(2)-S(2)	120.1(6)	121.2(4)	120.52(16)
C(2)-C(1)-S(1)	121.6(6)	120.3(4)	120.52(16)
N(1)-Mo(1)-S(1)-C(1)	-52.9(3)	-52.0(2)	-50.5(2)
N(1)-Mo(1)-S(2)-C(2)	49.2(3)	53.5(2)	50.5(2)
N(21)-Mo(1)-S(1)-C(1)	-149.6(3)	-146.8(2)	-146.62(19)
N(21)-Mo(1)-S(2)-C(2)	-162.0(17)	-161(3)	-138.3
N(21)-Mo(1)-N(1)-O(1)	178(100)	125(5)	138.60(10)
N(11)-Mo(1)-S(1)-C(1)	104(4)	132.8(12)	138.3(14)
N(11)-Mo(1)-S(2)-C(2)	146.6(3)	150.9(2)	146.6
N(11)-Mo(1)-N(1)-O(1)	-99(7)	-153(5)	-138.60(10)
N(31)-Mo(1)-S(1)-C(1)	125.9(3)	129.0(2)	128.24(19)
N(31)-Mo(1)-S(2)-C(2)	-127.8(3)	-124.0(2)	-128.2
N(31)-Mo(1)-N(1)-O(1)	59(9)	50(7)	0.000(6)
S(1)-Mo(1)-S(2)-C(2)	-35.5(3)	-34.60(18)	-37.4
S(1)-Mo(1)-N(1)-O(1)	80(7)	28(5)	42.02(3)
S(2)-Mo(1)-N(1)-O(1)	-5(7)	-56(5)	-42.02(3)
S(2)-Mo(1)-S(1)-C(1)	35.3(3)	35.0(2)	37.41(17)
Mo(1)-S(1)-S(2)-C(2)	138.4(3)	138.8(2)	142.6
Mo(1)-S(2)-C(2)-C(1)	29.0(7)	29.7(4)	31.6
Mo(1)-S(1)-C(1)-C(2)	-31.2(7)	-29.5(5)	-31.6
S - - S bite distance:	3.192	3.195	3.201
Mo distance from N ₂ S ₂ plane:	0.069	0.071	0.063
C36 - centroid of C1 and C2:	4.185	4.159	4.198
Fold Angle (θ)	42.0	41.1	44.4
Dihedral Angle	5.0	5.6	5.3
(between planes: Mo1-N11-N21 and Mo1-S1-S2)			

Table 7.4. Ionization energies (± 0.02 eV) of frontier orbitals in HeI gas phase photoelectron spectra for (Tp*)Mo(E)(S-S) systems.

Complexes	Bands	(Tp*)Mo(E)(tdt)	(Tp*)Mo(E)(bdt)	(Tp*)Mo(E)(bdtCl ₂)
E = NO	1	6.90	6.91	7.00
	1'	7.02	7.16	7.29
	2	7.60	7.66	7.70
	2'	7.84	7.87	7.91
	3	8.27	8.19	8.33
	3'	8.43	8.32	8.65
E = O	1	6.95	7.04	7.26
	2	7.43	7.54	7.65
	2'	7.65	7.71	7.89
	3	8.20	8.08	8.08
	3'	8.54	8.24	8.29

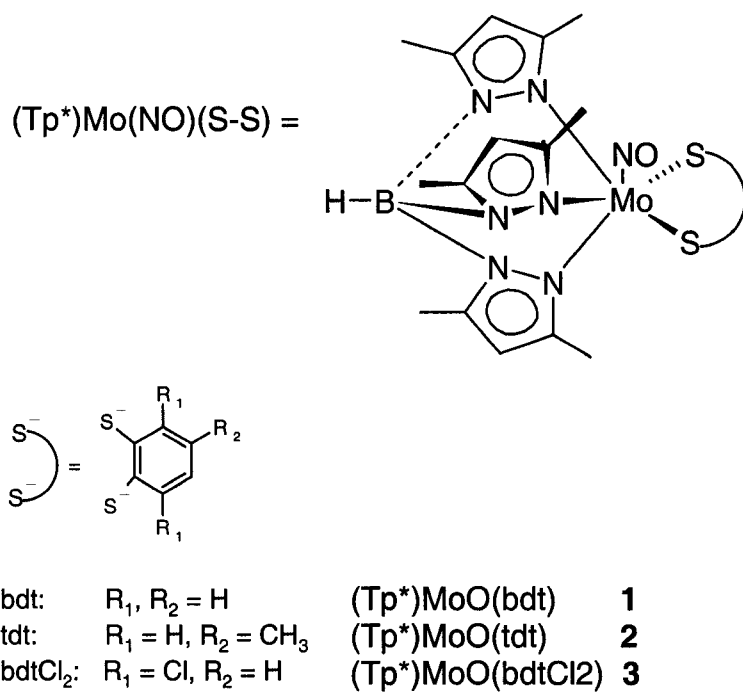


Figure 7.1. Representation of the $\{(\text{Tp}^*)\text{Mo}(\text{NO})\}^{2+}$ system containing equatorial ene-1,2-dithiolate ligands (S-S) coordinated to the Mo center. Structures of the dithiolate dianions (S-S) are also shown.

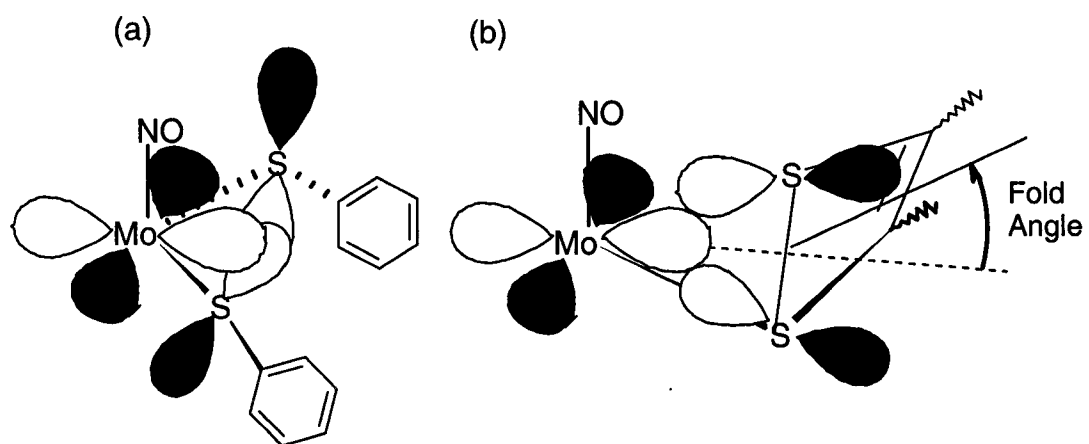


Figure 7.2. Orbital interaction diagram in (a) $(\text{Tp}^*)\text{Mo}(\text{NO})(\text{SPh})_2$ and (b) $(\text{Tp}^*)\text{Mo}(\text{NO})(\text{S-S})$ complexes.

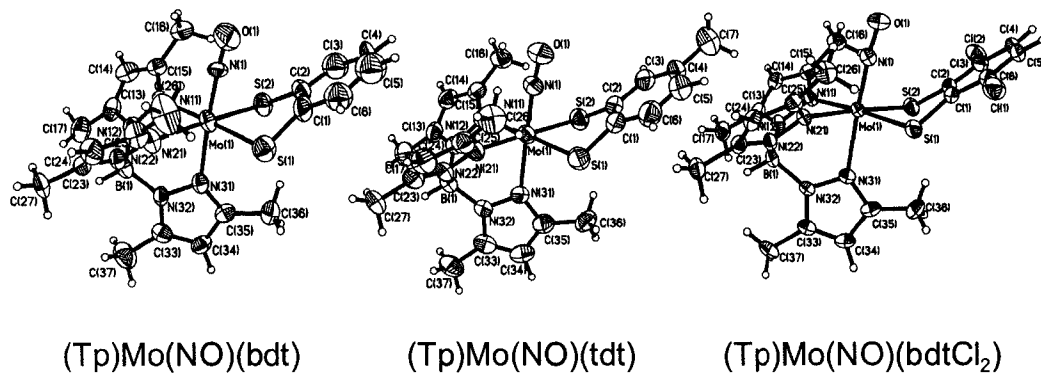


Figure 7.3. The ORTEP drawing of (Tp*)Mo(NO)(bdt) (**1**), (Tp*)Mo(NO)(tdt) (**2**), and (Tp*)Mo(NO)(bdtCl₂) (**3**). The atoms are drawn as 50% probability ellipsoids. H-atoms have been made arbitrarily small for clarity.

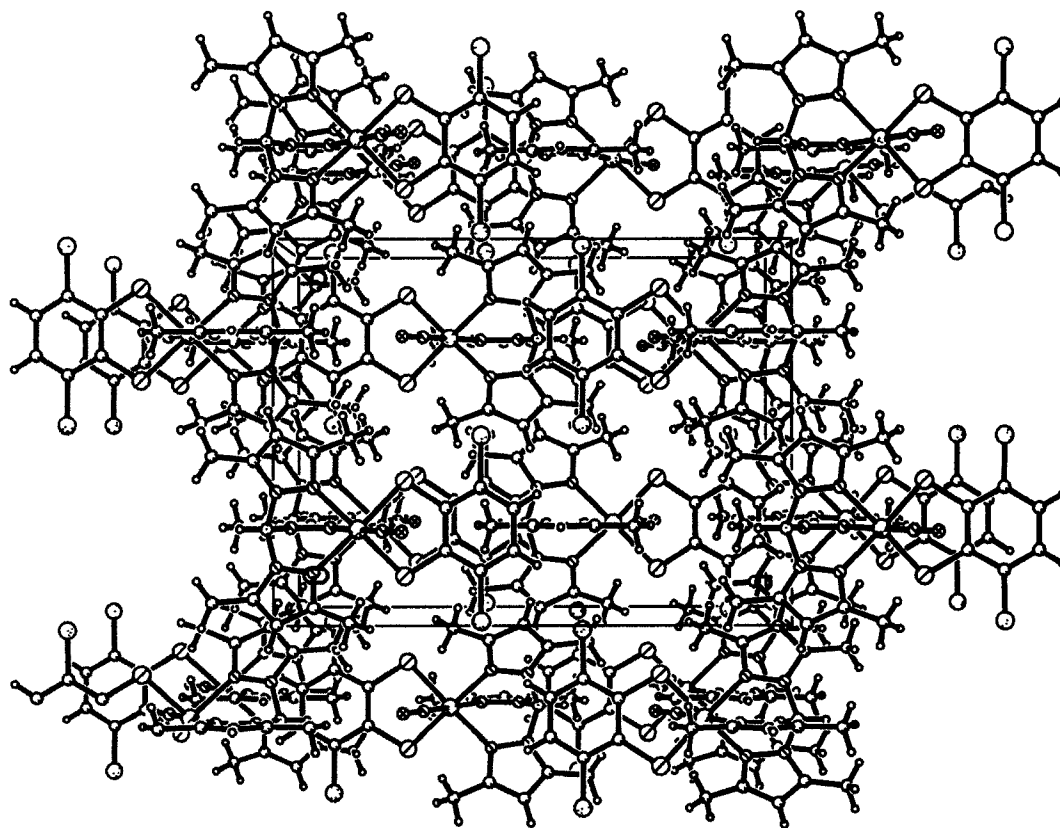


Figure 7.4. Compound $(Tp^*)Mo(NO)(bdtCl_2)$ (3) in $Pnma$ space group, orientation along c axis in a unit cell.

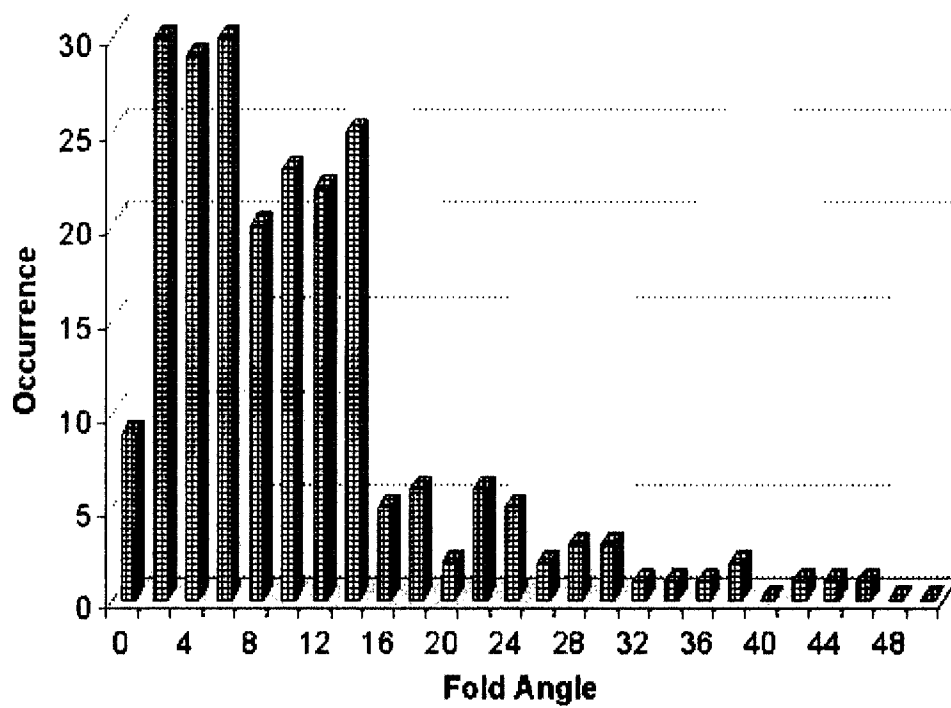


Figure 7.5. The distribution of fold angles (θ) of ene-1,2-dithiolates in group VI transition metal-ene-1,2-dithiolate complexes.

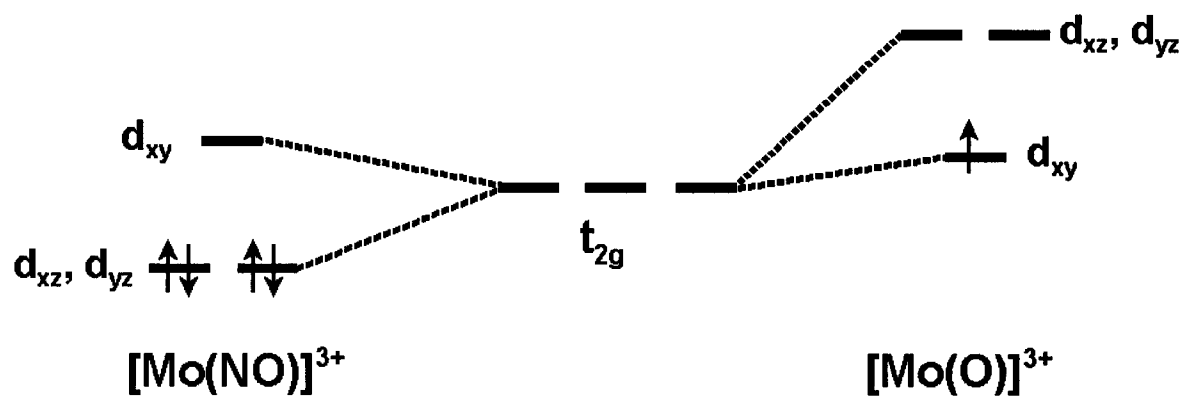


Figure 7.6. The orbital splitting diagram for the molybdenum t_{2g} orbitals of the $\{Mo(NO)\}^{3+}$ and $\{MoO\}^{3+}$ cores.^{63,64}

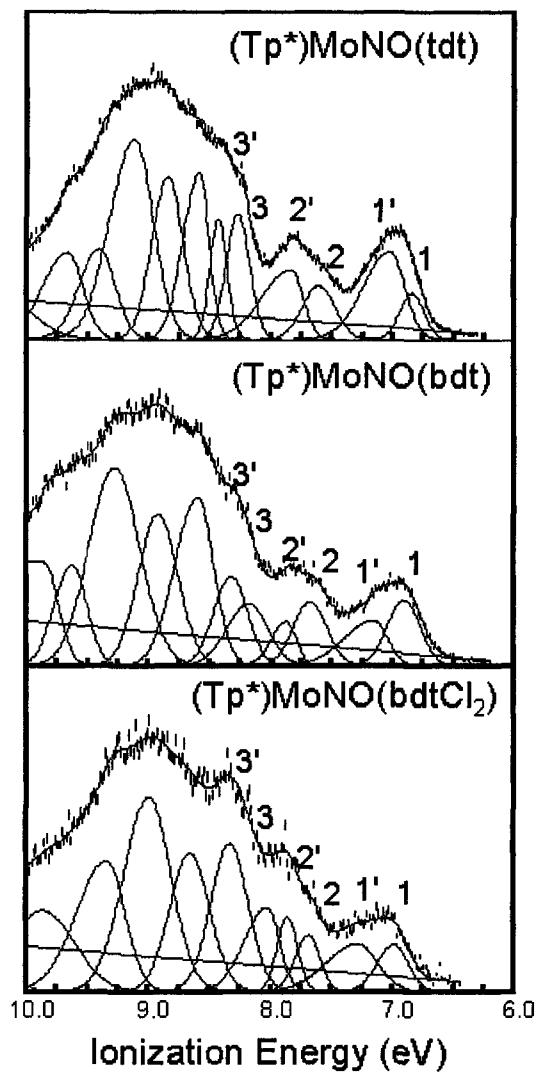


Figure 7.7. Photoelectron spectra of $(Tp^*)MoO(tdt)$ (2), $(Tp^*)MoO(bdt)$ (1), $(Tp^*)MoO(bdtCl_2)$ (2). A broad metal based ionization can be deconvoluted with two Gaussians.

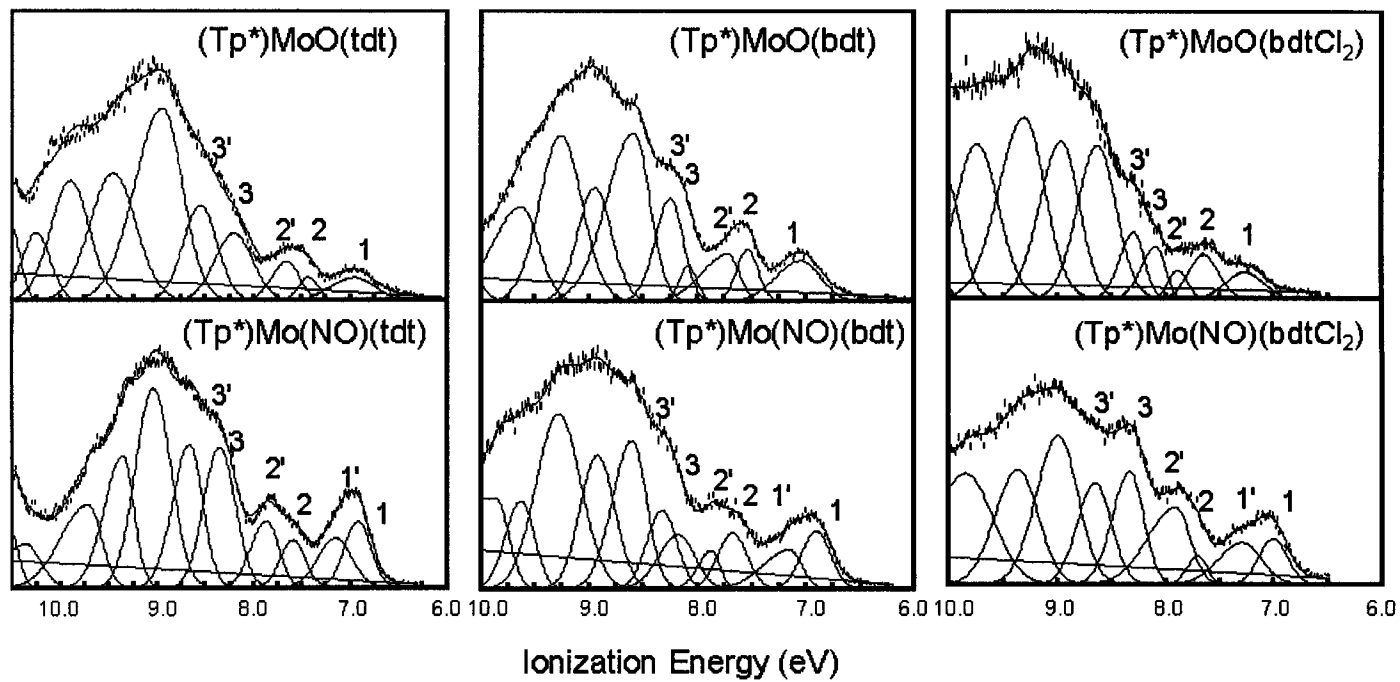


Figure 7.8. Photoelectron spectra of (Tp*)MoE(tdt), (Tp*)MoE(bdt), (Tp*)MoE(bdtCl₂) (where E = O, NO) pairs.

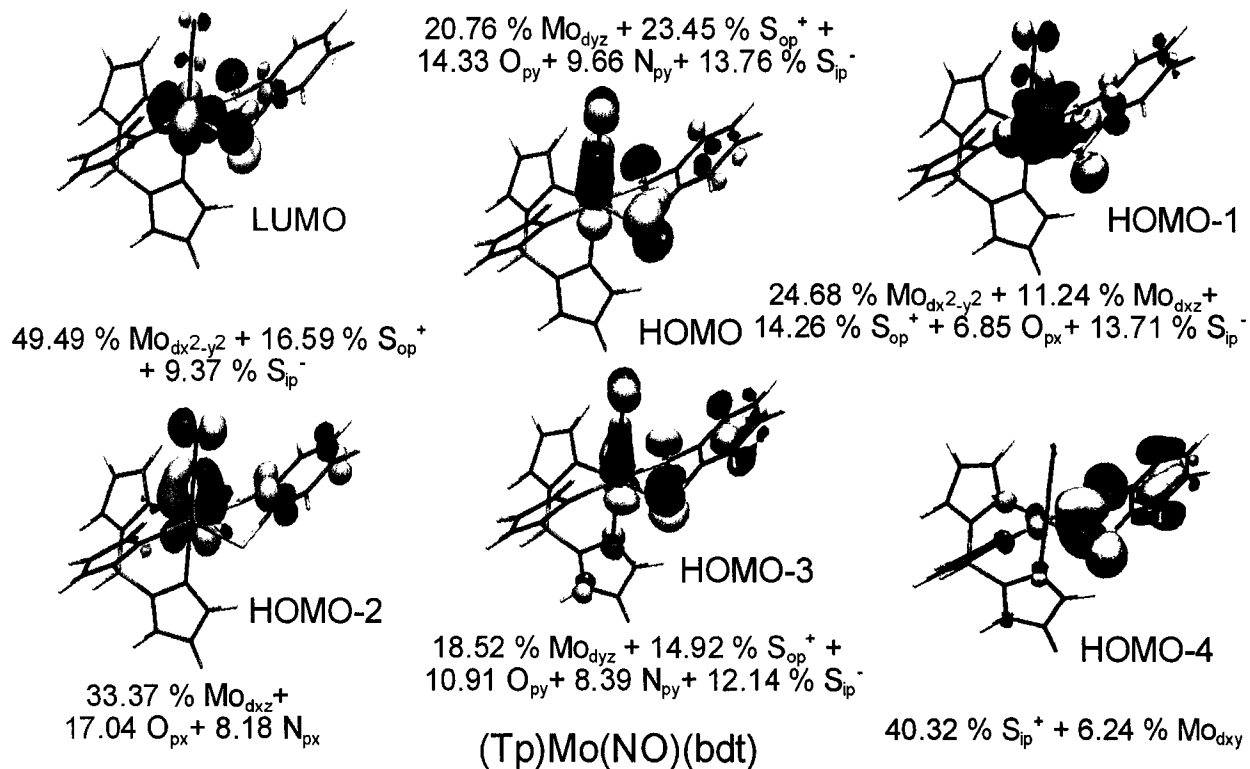


Figure 7.9. The frontier molecular orbitals of (Tp)Mo(NO)(bdt) (1). Major contributions from individual atomic orbitals are also provided.

5.0 References

1. Hayton, T. W.; Legzdins, P.; Sharp, W. B. *Chem. Rev.* **2002**, *102* (4), 935-991.
2. Richter-Addo, G. B.; Legzdins, P. *Metal Nitrosyls*; Oxford University Press: New York, Oxford, 1992.
3. Alobaidi, N.; Salam, S.; Beer, P.; Bush, C.; Hamor, T.; Mcquillan, F.; Jones, C.; Mccleverty, J. *Inorg. Chem.* **1992**, *31* (2), 263.
4. Dhawan, I. K. : Dissertation, The University of Arizona, 1995, p 244 pp.
5. Green, M.; Marder, S.; Thompson, M.; Bandy, J.; Bloor, D.; Kolinsky, P.; Jones, R. *Nature* **1987**, *330*, 6146.
6. Stumpf, H.; Ouahab, L.; Pei, Y.; Grandjean, D.; Kahn, O. *Science* **1993**, *261* 5120.
7. Miller, J.; Epstein, A.; Reiff, W. *Chem. Rev.* **1988**, *88* (1), 201.
8. Yonemura, T.; Okamoto, K.; Ama, T.; Kawaguchi, H.; Yasui, T. *J. Inorg. Biochem.* **1997**, *67* (1-4), 11.
9. Ueno, T.; Suzuki, Y.; Fujii, S.; Vanin, A.; Yoshimura, T. *Biochem. Pharmacol.* **2002**, *63* (3), 485.
10. Karupiah, G.; Xie, Q.; Buller, R.; Nathan, C.; Duarte, C.; MacMicking, J. *Science* **1993**, *261*, 1445-8.
11. Coppens, P.; Novozhilova, I.; Kovalevsky, A. *Chem. Rev.* **2002**, *102* (4), 861-883.
12. Enemark, J. H.; Feltham, R. D. *Coord. Chem. Rev.* **1974**, *13*, 339-406.

13. Westcott, B. L.; Enemark, J. H. In *Inorganic Electronic Structure and Spectroscopy; Volume II: Applications and Case Studies*; Solomon, E. I.; Lever, A. B. P., Eds.: John Wiley and Sons, 1999, pp 403-450.
14. McWhinnie, S.; Jones, C.; Mccleverty, J.; Collison, D.; Mabbs, F. *Polyhedron* **1992**, *11* (20), 2639.
15. McWhinnie, S.; Thomas, J.; Hamor, T.; Jones, C.; McCleverty, J.; Collison, D.; Mabbs, F.; Harding, C.; Yellowlees, L.; Hutchings, M. *Inorg. Chem.* **1996**, *35* (3), 760.
16. Alobaidi, N.; Jones, C.; Mccleverty, J. *Polyhedron* **1989**, *8* (3), 371.
17. Coe, B.; Jones, C.; Mccleverty, J.; Bloor, D.; Kolinsky, P.; Jones, R. *J. Chem. Soc., Chem. Commun.* **1989**, 19, 1485.
18. Cambridge Structural Database; Cambridge University: Cambridge
19. Alobaidi, N.; Jones, C.; Mccleverty, J. *Polyhedron* **1989**, *8* (8), 1033.
20. Ashby, M. T.; Enemark, J. H. *J. Am. Chem. Soc.* **1986**, *108*, 730-733.
21. Roberts, S. A.; Enemark, J. H. *Acta Crystallogr.* **1989**, *C45*, 1292-1294.
22. Kamata, M.; Hirotsu, K.; Higuchi, T.; Tatsumi, K.; Hoffmann, R.; Yoshida, T.; Otsuka, S. *J. Am. Chem. Soc.* **1981**, *103* (19), 5772.
23. Kamata, M.; Yoshida, T.; Otsuka, S.; Hirotsu, K.; Higuchi, T.; Kido, M.; Tatsumi, K.; Hoffmann, R. *Organometallics* **1982**, *1* (1), 227.
24. Avarvari, N.; Faulques, E.; Fourmigue, M. *Inorg. Chem.* **2001**, *40* (11), 2570-2577.
25. Fourmigue, M. *Coord. Chem. Rev.* **1998**, *178-180* (Pt. 1), 823-864.

26. Enemark, J. H.; Raitsimring, A. M.; Astashkin, A. V.; Johnson, J. L.; Rajagopalan, K. V. *J. Inorg. Biochem.* **2001**, *86* (1), 212.
27. Codd, R.; Astashkin, A.; Pacheco, A.; Raitsimring, A.; Enemark, J. *JBIC, J. Biol. Inorg. Chem.* **2002**, *7* (3), 338.
28. Enemark, J. H.; Cosper, M. M. In *Metal Ions in Biological Systems*; Sigel, A.; Sigel, H., Eds.: Marcel Dekker, Inc. New York, 2002, pp 621-653.
29. Inscore, F. E.; Joshi, H. K.; Gruhn, N. E.; Kirk, M. L.; Enemark, J. H. *manuscript in preparation*.
30. Hille, R. *Chem. Rev.* **1996**, *96* (7), 2757.
31. Hille, R. *JBIC, J. Biol. Inorg. Chem.* **1996**, *1* (5), 397.
32. Hille, R. *Essays in Biochemistry, Vol 34*, **1999**, *34*, 125.
33. Inscore, F. E.; McNaughton, R.; Westcott, B.; Helton, M. E.; Jones, R.; Dhawan, I. K.; Enemark, J. H.; Kirk, M. L. *Inorg. Chem.* **1999**, *38*, 1401-1410.
34. Rompel, A.; Cinco, R. M.; Robblee, J. H.; Latimer, M. J.; McFarlane, K. L.; Huang, J.; Walters, M. A.; Yachandra, V. K. *J. Synchr. Radi.* **2001**, *8* (2), 1006-1008.
35. Inscore, F. E.; Joshi, H. K.; McElhaney, A. E.; Enemark, J. H. *Inorg. Chim. Acta* **2002**, *331*, 246-256.
36. Inscore, F. E.; Rubie, N.; Joshi, H. K.; Kirk, M. L.; Enemark, J. H. *manuscript submitted to Inorg. Chem.*
37. Joshi, H. K.; Inscore, F. E.; Gruhn N. E.; Enemark, J. H. *manuscript in preparation*.

38. W. Armarego, D. Perrin, *Purification of Laboratory Chemicals, 4th ed.*, Pergamon Press, New York, **1997**, p. 512.
39. McCleverty, J. A.; Seddon, D.; Bailey, N. A.; Walker, N. J. *J. Chem. Soc., Dalton Trans.* **1976**, 10, 898-908.
40. Reynolds, S.; Smith, C.; Jones, C.; McCleverty, J. *Inorg. Synth.* **1985**, 23, 4-9.
41. Cromer, D. T.; Waber, J. *Int. Tables X-Ray Crystallogr.* **1974**, 4, 71-147.
42. Cromer, D. T.; Ibers, J. A. *Int. Tables X-Ray Crystallogr.* **1974**, 4, 148-51.
43. Westcott, B.; Gruhn, N.; Enemark, J. *J. Am. Chem. Soc.* **1998**, 120 (14), 3382-3386.
44. Lincoln, S.; Koch, S. A. *Inorg. Chem.* **1986**, 25 (10), 1594-602.
45. Becke, A. D. *Phys. Rev. A.* **1988**, 38, 3098-3100.
46. Lee, C.; Yang, W.; Parr, R. G. *Phys. Rev. B.* **1988**, 37, 785.
47. Drane, A. S.; McCleverty, J. A. *Polyhedron* **1983**, 2 (1), 53-7.
48. Hinton, H.; Chen, H.; Hamor, T.; Jones, C.; McQuillan, F.; Tolley, M. *Inorg. Chem.* **1998**, 37 (12), 2933.
49. McElhaney, A. E.; Inscore, F. E.; Schirilin, J. T.; Enemark, J. H. *Inorg. Chim. Acta* **2002**, 341, 85-90.
50. Alobaidi, N.; Chaudhury, M.; Clague, D.; Jones, C.; Pearson, J.; Mccleverty, J.; Salam, S. *J. Chem. Soc., Dalton Trans.* **1987**, 7, 1733.
51. Adams, H.; Bailey, N.; Drane, A.; Mccleverty, J. *Polyhedron* **1983**, 2 (6), 465.
52. Mccleverty, J.; Drane, A.; Bailey, N.; Smith, J. *J. Chem. Soc., Dalton Trans.* **1983**, 1, 91.

53. Huang, J.; Ostrander, R.; Rheingold, A.; Leung, Y.; Walters, M. *J. Am. Chem. Soc.* **1994**, *116* (15), 6769.
54. Dhawan, I. K.; Pacheco, A.; Enemark, J. H. *J. Am. Chem. Soc.* **1994**, *116* (17), 7911-12.
55. Dhawan, I. K.; Enemark, J. H. *Inorg. Chem.* **1996**, *35* (17), 4873-4882.
56. Huang, J.; Ostrander, R.; Rheingold, A.; Walters, M. *Inorg. Chem.* **1995**, *34* (5), 1090.
57. Sidebotham, R.; Beer, P.; Hamor, T.; Jones, C.; Mccleverty, J. *J. Organomet. Chem.* **1989**, *371* (2), C31.
58. Davies, S. C.; Hughes, D. L.; Richards, R. L.; Sanders, J. R. *J. Chem. Soc., Dalton Trans.* **2000**, *5*, 719-725.
59. Sellmann, D.; Keller, J.; Moll, M.; Campana, C.; Haase, M. *Inorg. Chim. Acta* **1988**, *141* (2), 243.
60. Sellmann, D.; Kremitzl, H.; Knoch, F. *Inorg. Chim. Acta* **1994**, *225* (1-2), 163.
61. Arliguie, T.; Fourmigue, M.; Ephritikhine, M. *Organometallics* **2000**, *19* (2), 109-111.
62. Guyon, F.; Lenoir, C.; Fourmigue, M.; Larsen, J.; Amaudrut, J. *Bull. Soc. Chim. Fr.* **1994**, *131* (2), 217-26.
63. Bursten, B. E.; Cayton, R. H. *Organometallics* **1987**, *6* (9), 2004-5.
64. Westcott, B. L.; Enemark, J. H. *Inorg. Chem.* **1997**, *36* (23), 5404-5405.
65. Jourdain, I. V.; Fourmigue, M.; Guyon, F.; Amaudrut, J. *Organometallics* **1999**, *18* (10), 1834-1839.

66. Fourmigue, M.; Lenoir, C.; Coulon, C.; Guyon, F.; Amaudrut, J. *Inorg. Chem.* **1995**, *34* (20), 4979-85.
67. Joshi, H. K.; Cooney, J. J. A.; Inscore, F. E.; Gruhn, N. E.; Lichtenberger, D. L.; Enemark, J. H. *Proc. Natl. Acad. Sci. USA* **2003**, *100* (7), 3719-3724.

CHAPTER 8: Spectroscopic and Computational Investigation of Metal–Dithiolate Fold Angle Effects and the Significance of Unsaturation in the Metallacycle: its Implication to Pyranopterindithiolate Enzymes

A portion of this chapter has been published as

Joshi, H. K.; Cooney, J. J. A.; Inscore, F. E.; Gruhn, N. E.; Lichtenberger, D. L.;

Enemark, J. H. “Investigation of Metal–Dithiolate Fold Angle Effects: Implications for Molybdenum Enzymes” *Proc. Natl. Acad. Sci. USA*, **2003**, 100, 3719-3724.

1.0 Introduction

The bent metallocenes based on cyclopentadienyl ligand and its derivatives were discovered shortly after the discovery of ferrocene. Such bent metallocenes can also contain additional ligands such as dithiolates and have been recently reviewed.¹ The metallocene dithiolates have been very attractive targets for their remarkable optical, electric, magnetic and catalytic properties,^{1,2} and have also been used as models for the active sites of the molybdoenzymes.³

Coordination by the sulfur atoms of one or two ene-1,2-dithiolate (dithiolene) ligands of the novel substituted pyranopterin-dithiolate (“molybdopterin”⁴) is a common structural feature of mononuclear molybdenum-containing enzymes.⁵⁻⁷ These enzymes catalyze a wide range of oxidation/ reduction reactions in carbon, sulfur and nitrogen metabolism. Figure 8.1 shows the structure of sulfite oxidase active site, a representative example^{8,9} of the coordination of the pyranopterin-dithiolate (PDT¹⁰). These structural results raise fundamental questions about the role of the PDT coordination in the overall catalytic cycle of molybdenum enzymes.¹¹ The unusual ability of ene-1,2-dithiolate ligands to stabilize metals in multiple oxidation states has been recognized since the compounds were first investigated.¹² Proposed roles for the PDT ligand include functioning as an electron transfer conduit from the metal to other prosthetic groups¹³ and as a modulator of the oxidation/ reduction potential of the metal site.¹³ During catalysis the metal center is proposed to pass through the M(VI/V/IV) oxidation states, i.e. the Mo d electron count changes from d^0 to d^1 to d^2 . Thus, studies of discrete metal dithiolate

complexes encompassing these and related electron configurations may provide insight concerning metal thiolate bonding and reactivity in enzymes.

Previous structural studies of model molybdenum complexes of the type $(\text{Tp}^*)\text{MoE}(1,2\text{-dithiolate})$ (where E is O or NO, Tp^* is hydrotris(3,5-dimethyl-1-pyrazolyl)borate, and the 1,2-dithiolates are bdt (1,2-benzenedithiolate), bdtCl_2 (3,6-dichloro-1,2-benzenedithiolate) and qdt (2,3-quinoxalinedithiolate)) have shown that the fold angle of the dithiolate metallacycle along the S··S vector (Figure 8.2) varies in a way that is dependent upon the occupation of a d orbital that is in the equatorial plane.¹⁴ For $(\text{Tp}^*)\text{MoO}(\text{bdt})$, which has a formal $4d^1$ electron configuration, the fold angle is 21.3° .^{15,16} However, for $(\text{Tp}^*)\text{Mo}(\text{NO})(\text{bdt})$, the fold angle is 41.1° .¹⁴ Although the metal center of $(\text{Tp}^*)\text{Mo}(\text{NO})(\text{bdt})$ is formally d^4 , the strong π -acceptor character of the NO ligand results in the d orbital in the equatorial plane being empty, whereas for $(\text{Tp}^*)\text{MoO}(\text{bdt})$ this d orbital is half-filled.¹⁴ The larger fold angle for $(\text{Tp}^*)\text{Mo}(\text{NO})(\text{bdt})$ has been ascribed to a stabilizing interaction of the filled p_π orbitals on sulfur with the empty metal orbital in the equatorial plane upon bending,¹⁴ which is illustrated schematically in Figure 8.2. For other reported $(\text{Tp}^*)\text{Mo}(\text{NO})(\text{dithiolate})$ compounds, the fold angle is always $41.1\text{-}44.4^\circ$ and is essentially independent of the electron-donating or electron-withdrawing nature of substituents on the dithiolate ligand.¹⁴ In contrast, for $(\text{Tp}^*)\text{MoO}(\text{dithiolate})$ complexes, the fold angle ranges from 6.9° in $(\text{Tp}^*)\text{MoO}(\text{bdtCl}_2)$ ¹⁷ to 29.5° in $(\text{Tp}^*)\text{MoO}(\text{qdt})$,¹⁸ suggesting a much shallower potential surface for the interaction of the filled sulfur- p_π (S_π) orbitals with the half filled

equatorial metal orbital (metal in-plane or M_{ip}). For comparison, the calculated fold angles for dithiolates in protein structures (Table 8.1) range from 7-30°. ^{8,19-21}

The (Tp*)MoO(dithiolate) compounds have also been investigated by a variety of spectroscopic techniques including EPR, ^{15,16} electronic absorption, resonance Raman and MCD spectroscopies. ^{13,22,23} The general conclusion from these studies is that the singly occupied molecular orbital (SOMO) in these formally d^1 centers has substantial sulfur character. ^{13,22,23} From these studies it was proposed that pseudo-sigma interactions between the in-plane metal orbital and sulfur in-plane lone pairs play an important role in electron transfer reactions that regenerate the active sites of enzymes. ¹³ However, Figure 8.2 suggests that sulfur out-of-plane orbitals could also have a major effect on these processes. To date the role of fold angle upon metal-sulfur interactions has not been quantitatively assessed.

A technique capable of assessing the metal and ligand character of orbitals is gas-phase photoelectron spectroscopy using multiple energy ionization sources. ²⁴ Previously reported photoelectron spectra for (Tp*)MoE(tdt) (where E = O, S, NO and tdt is 3,4-toluenedithiolate) using HeI, HeII and NeI photon sources indicate strong mixing between Mo and S orbitals. ²⁵ Interestingly, the first ionization energy of (Tp*)Mo(NO)(tdt) is nearly identical to that of (Tp*)MoO(tdt), in spite of the difference in axial ligand and total number of metal d electrons. This was called the “electronic buffer effect” of the dithiolate ligand. ²⁵ Subsequent photoelectron spectroscopic studies of other (Tp*)MoE(dithiolate) complexes have shown only small shifts in the first ionization energy with peripheral substitutions on the dithiolate ligand. ^{14,26} Gas phase

photoelectron spectroscopy avoids possible complications of solvent and solid state effects, but a major drawback is that only neutral species are easily studied by this technique, and the (Tp*)MoO(dithiolate) system does not allow access to the important d^0 and d^2 electron configurations of the catalytic cycle. Additional analysis of the molybdenum-dithiolate interaction in the photoelectron spectra of (Tp*)MoO(dithiolate) is also difficult because the broad area of ionizations from the Tp* ligand is not well separated from the region containing Mo-S ionizations.^{14,17,25,27} A third potential complication of interpretation of photoelectron spectra of (Tp*)MoO(dithiolate) complexes is the formation of both singlet and triplet states from ionization of such a d^1 system, although no indication are present that this is a problem.²⁸ Thus, we have further sought a simple system that can provide experimental gas phase photoelectron data for formally d^0 and d^2 metal dithiolate complexes and which is amenable to density functional theory (DFT) calculations with a minimum of simplifying assumptions.

The known bent-metallocene dithiolate compounds ($Cp_2M(dithiolate)$, $M = Ti, Mo$ and Cp is η^5 -cyclopentadienyl) provide access to d^0 (Ti) and d^2 (Mo) electron configurations.^{1,29} A general bonding description of Cp_2MX_2 compounds is well understood,³⁰⁻³² and similar to the (Tp*)MoO(dithiolate) molecules that we have previously studied there is a metal-d orbital in the equatorial plane with respect to the dithiolate ligand that is in this case fully occupied for the d^2 (Mo) electron configuration. Fourmigué and coworkers have extensively studied $Cp_2M(dithiolate)$ and $[CpM(dithiolate)_2]^{-1,0}$ in the context of novel molecular materials.^{1,33,34} They have found that the d^0 compounds, $Cp_2Ti(dithiolate)$, have large fold angles (*e.g.* 46.0° for

$\text{Cp}_2\text{Ti}(\text{bdt})^1$) in the solid state. The barrier to interconversion between the positive and negative extremes of fold angle in solution has been determined by NMR to be 14 kcal mol⁻¹,^{29,33} close to the computed value of 15 kcal mol⁻¹.³⁴ The observed folding for the Ti d⁰ systems could facilitate interaction of the filled S_π orbitals with the empty M_{ip} orbital, similar to the diagram shown in Figure 8.2. In contrast, for the d² metal system, Cp₂Mo(bdt), the fold angle in the solid state is 9.0°. ³⁵ Fourmigué *et al.*³⁶ have found that the oxidation potentials of Cp₂M(dithiolate) compounds are not significantly different for M = Mo and W, suggesting that the HOMO has substantial sulfur character. Pilato *et al.*³ have prepared Cp₂Mo(dithiolate) compounds in which the dithiolate contains an appended pterin group as mimics for pyranopterin dithiolate centers. Molecular orbital calculations and EPR data for [Cp₂Mo(dithiolate)]⁺ cations indicate that the HOMO is significantly ligand based.^{2,3,36-39} A study of (η⁵-tBuC₅H₄)₂Zr(Se₂C₆H₄)⁴⁰ demonstrated that these systems are amenable to gas phase photoelectron spectroscopy. To our knowledge, however, there has been no detailed investigation of the gas phase photoelectron spectra of Cp₂Mo(dithiolate) compounds to experimentally probe the molybdenum and sulfur character in the occupied valence orbitals of these systems to assess whether the valence molecular orbitals are primarily metal, primarily sulfur, or strongly mixed. Here gas-phase photoelectron spectroscopy data for (Tp*)Mo(bdt) (**1**) and Cp₂M(bdt) (M = Mo (**2**), Ti (**3**) and W(**4**)), Cp₂M(bdtCl₂) (M = Mo (**5**), Ti(**6**)) and Cp₂Ti(pdt) (**7**) (where pdt = 1,3- propanedithiolate) is presented. A comparison of photoelectron spectrum of an enedithiolate containing compound **4**, is made with the dihydride containing compound Cp₂WH₂. Wherever noted, the analysis of the

experimental data is aided by DFT calculations on the neutral ground state of the molecules and the ion states formed by photoionization.

2.0 Materials and Methods

2.1 Synthesis of Compounds

Compounds **1-4, 7** were synthesized according to the published procedures. The compounds $(Tp^*)MoO(bdt)$,¹⁵ $Cp_2Mo(bdt)$ ³⁵ and $Cp_2Ti(bdt)$,^{41,42} $Cp_2W(bdt)$ (**4**), $Cp_2Ti(bdtCl_2)$ (**6**),⁴³ $Cp_2Ti(pdt)$ (**7**)⁴⁴ were synthesized under anaerobic conditions using either an inert atmosphere glove bag or standard Schlenk line techniques. The modified synthesis of $Cp_2M(bdt)$ ($M = Mo$ (**2**), W (**4**)) and $Cp_2Mo(bdtCl_2)$ (**5**) involved a 1:3 mixture of water and organic solvent to ensure greater solubility of the precursor (Cp_2MoCl_2) and better yield of the final product. Various physical methods were utilized in the characterization of the compounds. Electronic absorption spectra of samples dissolved in 1,2-dichloroethane were collected on a modified Cary 14 (with OLIS interface, 250-2600 nm) spectrophotometer. Infrared (IR) spectra ($4000-400\text{ cm}^{-1}$) were acquired in KBr disks or as dichloromethane solutions (between NaCl plates) on a Nicolet Avatar ESP 360 FT-IR spectrophotometer. Mass spectra were recorded on a JEOL HX110 high-resolution sector instrument utilizing fast atom bombardment (FAB) ionization in a matrix of 3-nitrobenzyl alcohol (NBA). Electron paramagnetic resonance (EPR) spectra of **1** in fluid solutions (298 K) or frozen glasses (77 K) in dry degassed

toluene were acquired at X-band frequency (~9.1 GHz) with a Bruker ESP 300 spectrometer.

2.2 Photoelectron spectroscopy

Photoelectron spectra were recorded using an instrument that features a 36-cm radius, 8-cm gap hemispherical analyzer (McPherson) and custom-designed excitation source, sample cells, and detection and control electronics that have been described in more detail.²⁵ The difference between the argon $^2P_{3/2}$ ionization at 15.759 eV and the methyl iodide $^2E_{1/2}$ ionization at 9.538 eV was used to calibrate the ionization energy scale. The argon $^2P_{3/2}$ ionization also was used as an internal calibration lock of the absolute ionization energy throughout data collection. During data collection the instrument resolution (measured using fwhm of the argon $^2P_{3/2}$ peak) was 0.020-0.030 eV. All data are intensity corrected with an experimentally determined instrument analyzer sensitivity function.

All samples sublimed cleanly with no detectable evidence of decomposition products in the gas phase or as a solid residue. The sublimation temperatures were ($^{\circ}\text{C}$, 10^{-4} Torr, monitored using a "K" type thermocouple passed through a vacuum feedthrough and attached directly to the sample cell) 195-205 $^{\circ}$ for compound **1**, 190-200 $^{\circ}$ for compound **2**, 175-185 $^{\circ}$ for compound **3** 170-200 $^{\circ}$ for compound **4**, 203-229 $^{\circ}$ for compound **5**, 171-205 $^{\circ}$ for compound **6**, 190-214 $^{\circ}$ for compound **7**.

In the figures the vertical length of each data mark represents the experimental variance of that point. The valence ionization bands are represented analytically with the best fit of asymmetric Gaussian peaks as described in more detail elsewhere.⁴⁵ The bands are defined by the position, amplitude, halfwidth for the high binding energy side of the peak, and the halfwidth for the low binding energy side of the peak. The number of peaks used in a fit was based solely on the features of a given band profile. The peak positions and halfwidths are reproducible to about ± 0.02 eV ($\approx 3\sigma$). The parameters describing an individual Gaussian peak are less certain when two or more peaks are close in energy and overlap.

2.3 Theoretical Methods

The Amsterdam density functional theory package (ADF 2000.01) was used to study the electronic structures of the compounds 1-4.⁴⁶⁻⁴⁸ The program implements numerical integration in Cartesian space⁴⁹ and gradients for geometry optimizations are solved analytically.⁵⁰ Optimized geometries were obtained beginning from the crystal structure geometries and in C_1 symmetry. The 3,5-dimethyl groups on Tp* were replaced by hydrogen atoms to reduce the computational efforts. A generalized gradient approximation, with the exchange correction of Becke⁵¹ and the correlation correction of Lee *et. al.*,⁵² was used for all density functional calculations. All core levels (up to 3d for Mo, up to 1s for C, N, O and S) were treated as frozen orbitals. No core levels for Ti were treated as frozen. The calculations employed triple-zeta basis sets with Slater type orbitals and a polarization function for all elements besides Mo. Calculations on the ground-state molecules were performed in the spin-restricted mode. Spin-unrestricted

Δ SCF calculations were performed on the proposed ion states formed by photoionization by removing one electron from the relevant orbital and comparing the total energy with that of the ground state molecule. A linear correction was applied for comparison of the calculated and the observed energies, *i.e.* the calculated Δ SCF energies and orbital energies were shifted by the difference between experimentally obtained and calculated energies of the HOMO.

3.0 Results and Discussions

3.1 Photoelectron Spectra

The low energy valence region of the gas-phase photoelectron spectra of **1-7** collected with both He I and He II photon sources are presented in Figure 8.3-8.6. This energy region contains the ionizations that correspond to removal of an electron from the first two or three occupied molecular orbitals of these molecules. For the Ti molecule (**3**), the spectra contain two ionizations that correspond to removal of electrons from the symmetric and antisymmetric (bands S_{π}^{+} and S_{π}^{-} , respectively) combinations of sulfur- π orbital (S_{π}) orbitals. For the Mo molecules (**1** and **2**), an additional ionization is observed in this region that corresponds to removal of an electron from the half (**1**) or fully (**2**) occupied equatorial metal d orbital. The specific assignment of the ionizations can be made by comparison of the spectra to those of related molecules and by comparison of the relative ionization intensities as the source energy is varied.²⁵ From previous experimental studies^{24,53} and calculations of atomic photoionization cross-sections,⁵⁴ it is expected that ionizations from orbitals with significant Ti 3d or Mo 4d contributions will

increase in intensity compared to ionizations of primarily S 3p character when data collected with a He II photon source is compared to data collected with a HeI photon source. Mixing of metal and sulfur character in orbitals will result in smaller changes in relative intensities of ionizations being observed.

The lowest energy ionization band (labeled M_{ip} in Figure 8.3) of **1** at 7.04 eV is similar in appearance to the low energy band of related complexes having alkoxide ligands^{27,55} that has been assigned to ionization arising primarily from the half-filled metal-based orbital.^{25,27,55} The two ionizations between 7.25 eV to 8.00 eV can then be assigned to ionizations associated with symmetric (S_{π}^{+}) and antisymmetric (S_{π}^{-}) combinations of S_{π} orbitals based on previous assignment of analogous complexes.^{25,26} More detailed assignment of the S_{π}^{+} and S_{π}^{-} ionizations are not possible due to the significant overlap of these low energy features and the beginning of the Tp^{*} ligand ionizations. The ratio of the areas of the M_{ip} ionization and the sum of the overlapping S_{π}^{+} and S_{π}^{-} ionizations changes very little with change in photon source from He I to He II; the $M_{ip}:(S_{\pi}^{+} + S_{\pi}^{-})$ ratio in He I is 0.66:1.00, that in He II is 0.63:1.00. The observation of only small changes in the relative intensities of the first three bands with ionization source energy was suggested to be evidence of substantial mixing of metal and sulfur character in $(Tp^{*})MoO(tdt)$.²⁵ The photoelectron spectra of the Ti molecule (**3**) show two overlapping ionization bands at 7.18 eV and 7.43 eV that must contain contributions from the S_{π}^{+} and S_{π}^{-} combinations of S_{π} orbitals. The ratio of the areas of the low energy band to the high energy band increases significantly with change in photon source from He I to He II. The ratio in He I is 1.00:1.02; that in He II is 1.00:0.37. This behavior is consistent

with the lower energy peak containing contributions from Ti. Therefore, the lower energy peak is assigned to S_{π}^{+} , which has the proper symmetry to interact with the empty metal orbital upon folding. The higher energy peak in **3** is assigned to the S_{π}^{-} ionization which does not mix significantly with the empty Ti d acceptor orbital (discussed later in detail in the calculations section). The symmetric combination of the sulfur orbitals (S_{π}^{+}) is more destabilized than the antisymmetric combination (S_{π}^{-}) due to the greater interaction with the arene ring π orbital of appropriate symmetry.⁴⁰ This analysis compares well with that of $(\eta^5\text{-}^t\text{BuC}_5\text{H}_4)_2\text{Zr}(\text{Se}_2\text{C}_6\text{H}_4)$,⁴⁰ for which the first band was assigned as a combination of Se_{π}^{+} and Se_{π}^{-} ionizations.

Compound **2** shows three low energy ionizations, one at 6.29 eV and an overlapping pair of peaks at 7.04 eV and 7.24 eV. The He II data for **2** clearly show an increase in the intensity of the middle band, and perhaps a slight decrease in intensity of the highest energy band. These results imply that the middle band (7.04 eV) is mainly metal-based, the lowest energy band (6.29 eV) is primarily S_{π}^{+} with some additional Mo 4d or C 2p character, and the highest energy band (7.24 eV) is S_{π}^{-} . The metal based ionization (M_{ip}) in **1** and **2** stays constant (at 7.04 eV) despite significant perturbations in the first coordination sphere and formal oxidation state of the metal.

3.2 Effect of Metal and Enedithiolate Coordination

Photoelectron spectra of $\text{Cp}_2\text{Mo}(\text{bdtCl}_2)$ (**5**) in He I source is plotted in Figure 8.4. The three lowest energy ionization bands in **2** were assigned to S_{π}^{+} (6.29 eV), M_{ip} (7.04 eV) and S_{π}^{-} (7.24 eV). Similarly, the first three bands in **5** can be assigned to S_{π}^{+} (6.57 eV), M_{ip} (7.29 eV) and S_{π}^{-} (7.49 eV). Therefore, the first three ionizations are shifted to

the higher ionization energies (by an average of 0.26 eV) in compound **5** due to the electron withdrawing chlorine substituents at 3 and 6 positions of the benzene ring of the enedithiolate ligand. Photoelectron spectra for $\text{Cp}_2\text{W}(\text{bdt})$ (**4**), a tungsten analogue of compound **2**, in He I and He II source is plotted in Figure 8.5. Analogous to complex **2**, three lower energy ionizations associated with the frontier orbitals can be assigned to S_π^+ (6.32 eV), M_{ip} (6.90 eV) and S_π^- (7.24 eV) orbitals. The metal based ionization shifts to lower energy which is consistent with change of metal (from Mo to a higher row W). A photoelectron spectra of Cp_2WH_2 ,²⁴ that shows only one ionization feature, at 6.30 eV, associated with the metal based orbital is plotted in Figure 8.5 in region 5.75-7.75 eV and compared with $\text{Cp}_2\text{W}(\text{bdt})$ complex. It is interesting to note that in Cp_2WH_2 , the metal based ionization is shifted to higher ionization potential by 0.60 eV than in compound **4**. The soft sulfur donor atoms of enedithiolate ligand stabilize the energy of the metal based orbital. This shift gives a quantitative idea of shift from hard donor hydrides to relatively soft sulfur donor ligands.

3.3 Significance of Unsaturation (C=C) in the Metallacycle

Chapter 3 discusses the electronic structures of enedithiolate ligands, and in subsequent chapters we have seen how understanding the enedithiolate ligand electronic structure can be a starting point for the understanding of metal-sulfur interactions in metal-dithiolate compounds. It was observed that the frontier orbitals in these compounds have significant contributions from dithiolate sulfur p orbitals. To be specific, the HOMO had significant contributions from symmetric combinations of the dithiolate out of plane orbital (S_π^+). It has been discussed in Chapter 3 that S_π^+ orbitals

are raised in energy due to effective overlap from C_{π}^{+} (symmetric combination of π -orbitals of carbon-carbon double bond. To further understand the role of the C=C double bond in the electronic structures of transition metal-dithiolate complexes, the gas-phase photoelectron spectroscopic studies of the metal complexes with saturated dithiolate ligands was initiated. One such candidate is $Cp_2Ti(pdt)$ (**7**) with a saturated 1, 3-propanedithiolate ligand. The He I and He II photoelectron spectra for **7** are shown in Figure 8.6. Similar to other Ti complexes, **3** and **6**, this is also a d^0 system and two ionizations associated with the dithiolate sulfur orbitals are observed at 7.08 eV and 7.68 eV ionization potential. In the He II ionization source the ionization band at 7.68 eV increases in intensity signifying mixing with the metal orbital. This is a reverse trend than that observed for compound **3**. This suggests that the second band (at 7.68 eV) in **7** can be associated with a S_{π}^{+} like orbital (in this unsaturated complex orientation of S_{π} orbitals might be different from other enedithiolate complexes) that has the right symmetry to mix with the metal based orbital. The other ionization can, therefore, be assigned to a S_{π}^{-} combination. Thus, the absence of C=C switches the order of S_{π}^{+} and S_{π}^{-} orbitals in this complex. This experimental evidence provides an explanation for the role of C=C in enedithiolate, which is to raise the energy of the S_{π}^{+} orbitals.

3.4 Computational Results

The electronic structures of **1-3** were calculated using C_1 symmetry and geometry optimization. The geometry optimized structures compare well with the reported structures determined from X-ray crystallography. As a result of geometry optimization, the dithiolate fold angle changes from the crystallographic fold angle of 21.3° ¹⁵ to 31.0°

in **1**, 9.0° ³⁵ to 4.8° in **2** and 46.0° ⁵⁶ to 41.6° in **3**. The C-S bond length decreases and the dithiolene C-C bond length increases with change from the Mo (**2**) to Ti (**3**) complex, demonstrating that the nature of the metal affects the dithiolene unit. These changes are comparable to those seen for $\text{Cp}_2\text{Mo}(\text{dmit})$ upon oxidation to form $[\text{Cp}_2\text{Mo}(\text{dmit})][\text{AsF}_6]$.³⁴ The bond length differences in the ligand are assigned to the ligand adopting a more dithioketonic character with increase in metal oxidation state.

Density functional theory (DFT) calculations provide additional insight into the metal-dithiolate interactions and indicate that upon dithiolate folding the mixing of metal d and sulfur p_{π} orbitals can be favored by their energy and symmetry match. The ionization energies and general character of the valence orbitals observed for molecules **1-3** by photoelectron spectroscopy match those calculated by the ΔSCF method and by comparison of orbital energies, see Table 8.2. Contour plots of the orbitals for $(\text{Tp}^*)\text{MoO}(\text{dithiolate})$ and $\text{Cp}_2\text{M}(\text{dithiolate})$ that correspond to the ionizations evaluated by photoelectron spectroscopy are shown in Figure 8.7. The highest occupied molecular (HOMO) orbital in **1** is primarily a metal in-plane orbital, whereas it is primarily a sulfur out-of-plane orbital in **2** and **3**. The HOMO-1 orbital for **2** is a metal in-plane orbital. As mentioned earlier, the metal based ionization has similar energy for **1** and **2**. Thus, the dithiolate appears to buffer the electron density at the metal center by affecting the overlap of S_{π} orbitals with the metal center and thereby overcoming the striking differences of σ donor atoms (N and O) in **1** and π donor Cp ligands in **2**. Folding of the ene-dithiolate can influence this overlap of S_{π} (out-of-plane) and metal in-plane orbitals. The symmetric S_{π}^+ orbital has the right symmetry and energy to match the metal in-plane

orbital upon folding of the dithiolate unit, and the mixing of the out-of-plane S_{π}^{+} orbitals and metal in-plane orbital upon folding is shown experimentally by the intensity changes observed in the He I and He II spectra of **2** and **3** (Figure 8.3).

4.0 Conclusions

The gas phase photoelectron spectra of $Cp_2M(bdt)$, $M = Ti$ (**3**) and Mo (**2**), obtained with He I and He II photon sources clearly show that under favorable conditions the ionizations from primarily metal based orbitals and primarily S_{π} -based orbitals can be experimentally distinguished from one another. In addition, an unambiguous demonstration that the symmetric S_{π}^{+} orbital, which can interact with the in-plane metal orbital upon bending, is more easily ionized than the antisymmetric S_{π}^{-} orbital has been made. This successful analysis and assignment of the low energy ionizations of compounds **2** and **3** provides the framework for investigation and direct assignment of the S_{π} and metal-based ionizations in other metal dithiolate systems that may be more strongly mixed than **2** and **3** or that may have less favorable separation of their M-S region from the ionizations of other ligands. It is interesting to note that in the case of **3** the dithiolate ligand can be thought of as a six-electron donor, two electrons from each of the thiolate σ -orbitals and two from the S_{π}^{+} orbital. Hence, by folding the dithiolate ligand may stabilize **3** as an 18-electron complex. This folding effect is in contrast to the nitrosyl group where the transformation from linear to bent coordination transfers a pair of electrons from the metal to a localized orbital on the ligand.⁵⁷

The variation in the fold angle of the dithiolate ligand reflects the electron occupation in the equatorial in-plane metal orbital, as has been noted previously.¹⁴ Folding of the dithiolate ligand enables the S_{π} electron density to modulate the electron density in the equatorial plane of the metal, and thus folding can play a very significant role in the metal-sulfur anisotropic bonding interaction. This “dithiolate-folding-effect” may be important in stabilizing the multiple oxidation states that result from the electron transfer or equatorial oxygen atom transfer (OAT) in pyranopterin Mo/W enzymes (*e.g.* in sulfite oxidase and xanthine oxidase). For example, reduction of the metal in-plane orbital due to the release of an equatorial oxygen atom during OAT should make the dithiolene unit of PDT more planar compared to the fully oxidized enzyme. In this regard, It is noted that the calculated dithiolate fold angles for the two chemically equivalent, but crystallographically distinct, molybdenum centers in sulfite oxidase (Figure 8.1) of 6.6 and 7.0° (Table 8.1) are smaller than that for the oxidized center of aldehyde oxidoreductase (16.6°), whose oxidized structure has been determined to high resolution (1.28 Å).¹⁹ The exact oxidation state of sulfite oxidase in the crystal structure is not known, but there is evidence for photoreduction of the molybdenum center in the synchrotron beam during data collection..^{8,58} The fold angle studies on model systems support the view that the reported structure of sulfite oxidase⁸ is of a reduced form of the enzyme. Dithiolate folding can also modify the electropositive nature of the metal center by varying the overlap of sulfur lone pairs with the metal in-plane orbital. The S_{π} orbitals of dithiolate can therefore serve as an essential instrument for the buffering of electron density at the metal center by either involving themselves in strong mixing with an empty

metal orbital, as shown here for the d^0 Ti complex (**3**), or by localization of electron density on the S_π orbitals in the presence of a filled metal orbital, as shown here for the d^2 Mo complex (**2**). The “ene” nature of the dithiolate appears to be essential for raising the energy of the S_π^+ orbitals for interaction with the metal in-plane orbital. The substitution of Mo in **2** by W in **4** results in the shift of the metal based ionization to lower ionization energy.

Dithiolate folding may also provide a mechanism for the sulfur- π orbitals of the PDT ligand to act as an effective electron transfer pathway from the in-plane orbitals on the metal center to other redox partners via the pyranopterin. For molybdenum and tungsten enzymes the energies involved in substrate binding, docking with electron transfer partners, and dynamic motions of the protein skeleton, may modulate the dithiolate fold angle and, consequently, the electron distribution, overall reduction potential and reactivity of the metal center.

Table 8.1. Metal-dithiolate Fold Angles in Representative Mo Enzymes.

Enzyme (resolution)	Fold Angle (°)
Sulfite Oxidase (1.9 Å)	6.6 and 7.0
Aldehyde Oxidoreductase (MOP) (oxidized) (1.28 Å)	16.6
Xanthine Dehydrogenase (2.1 Å)	20.1 and 14.3
Dimethyl Sulfoxide Reductase (oxidized) (1.3 Å)	18.2 and 33.1

Table 8.2. Experimental and calculated Δ SCF and orbital ionization energies (eV) for the ionizations from sulfur antisymmetric (S_{π^-}), sulfur symmetric (S_{π^+}) and metal in-plane (M_{ip}) orbitals of **1-4**.

compound	(Tp*)MoO(bdt) (1)			Cp ₂ Mo(bdt), (2)			Cp ₂ Ti(bdt) (3)			Cp ₂ W(bdt) (4)		
	PES (assignment)	Δ SCF ^a	orbital energy ^a	PES (assignment)	Δ SCF	orbital energy	PES (assignment)	Δ SCF	orbital energy	PES (assignment)	Δ SCF	orbital energy
1 st ionization	7.04 (M_{ip})	7.04 (6.51)	7.04 (4.35)	6.29 (S_{π^+})	6.29 (6.46)	6.29 (3.96)	7.18 (S_{π^+})	7.18 (6.67)	7.18 (4.58)	6.32 (S_{π^+})	6.32 (6.08)	6.32 (4.00)
2 nd ionization	7.54 (S_{π^+})	S 7.49 T 7.20	7.60	7.04 (M_{ip})	6.75	6.58	7.43 (S_{π^-})	7.37	7.36	6.90 (M_{ip})	7.33	6.59
3 rd ionization	7.71 (S_{π^-})	S 7.53 T 7.47 ^b	7.85	7.24 (S_{π^-})	6.94	6.93	-	-	-	7.24 (S_{π^-})	6.95	6.94
onset of further ionizations	8.23	Did not converge	8.52	8.32	8.07	7.99	8.19	8.12	8.16		8.08	8.01

PES: experimental vertical ionization; Orbital energy: negative of the orbital eigenvalue; S: Singlet; T: Triplet. Δ SCF ionization energies and orbital energies have been shifted so that first Δ SCF ionization energy and highest occupied orbital energy agree with the experimental first ionization energy. Values in parenthesis are unshifted values of the HOMO/SOMO for Δ SCF, and the negative of the orbital eigenvalue of the HOMO/SOMO for orbital energy. ^a The methyl groups of the Tp* ligand were replaced with H atoms to simplify calculations. ^b SCF converged to 3 decimal places.

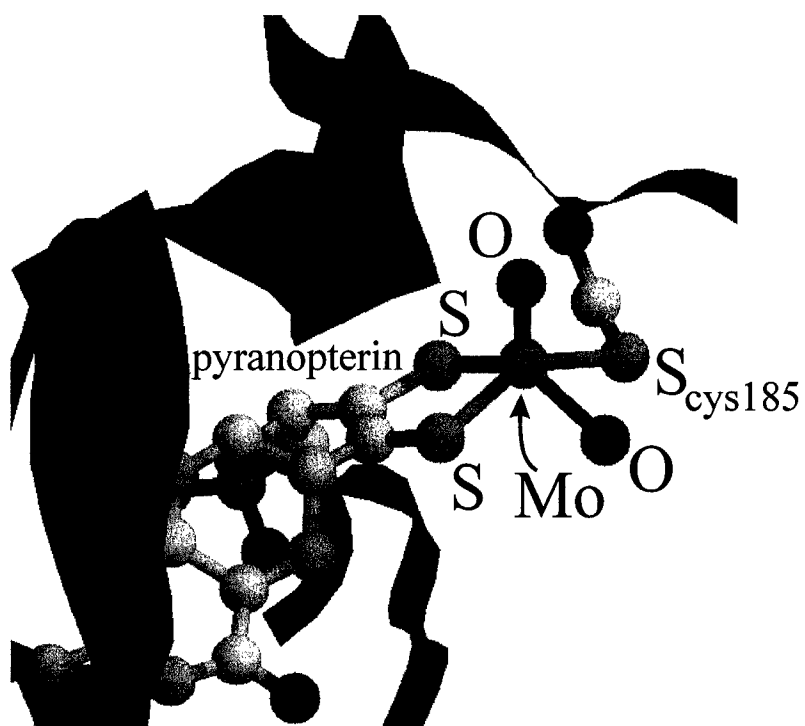


Figure 8.1. The active site of chicken liver sulfite oxidase illustrating a pyranopterin dithiolate appended to the Mo center.

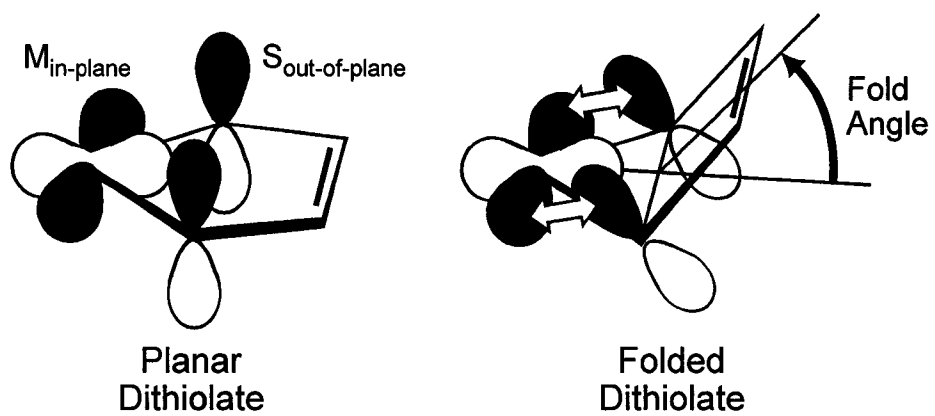


Figure 8.2. The bonding interaction of the symmetric combination (S_{π}^+) of sulfur out-of-plane orbitals with the metal in-plane d orbital upon folding of the dithiolate along the S...S vector indicated by the line.

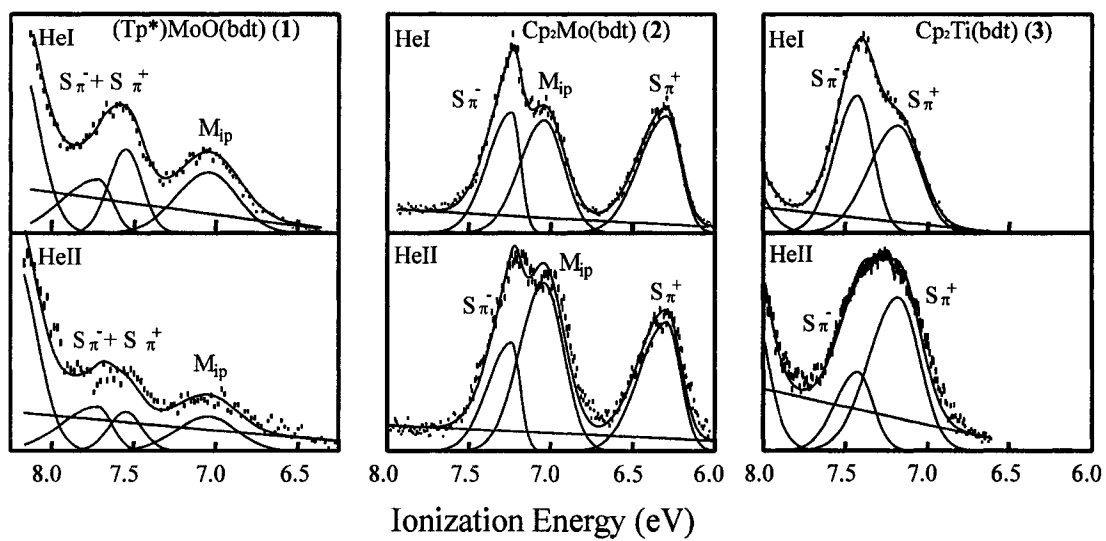


Figure 8.3. Gas-phase photoelectron spectra of $(Tp^*)MoO(bdt)$ (1), $Cp_2Mo(bdt)$ (2), and $Cp_2Ti(bdt)$ (3) with He I and He II excitation.

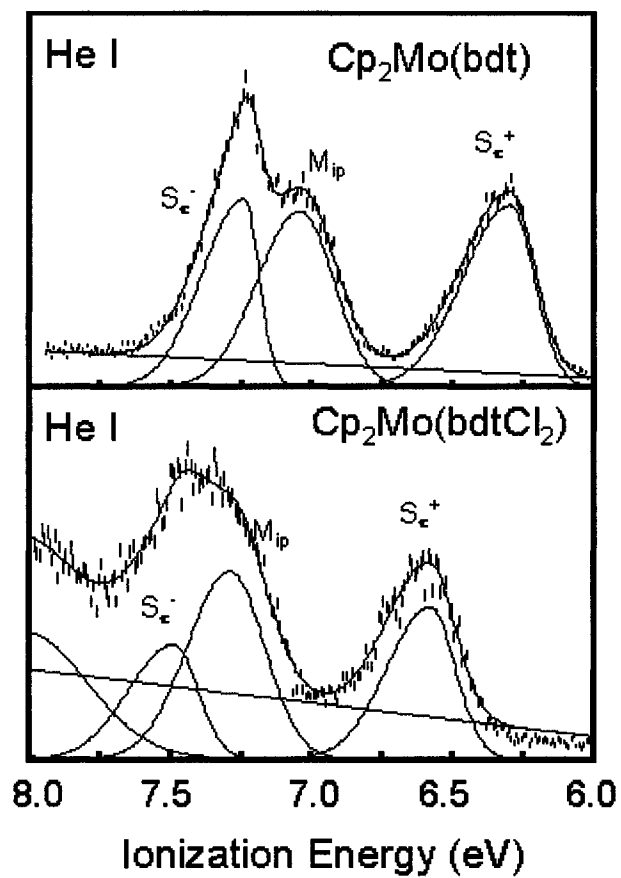


Figure 8.4. A comparison of the He I gas-phase photoelectron spectra of Cp₂Mo(bdt) (2) and Cp₂Mo(bdtCl₂) (5).

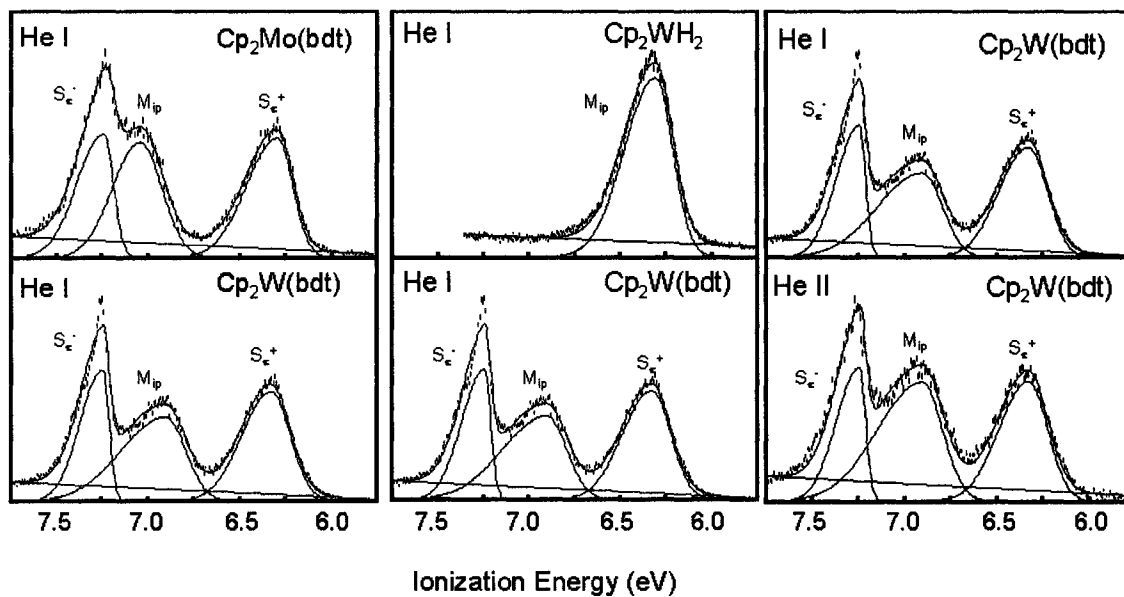


Figure 8.5. A comparison of the He I gas-phase photoelectron spectra of Cp₂Mo(bdt) (2) and Cp₂W(bdt) (4), Cp₂WH₂ and Cp₂W(bdt) (4), and He I and He II spectra of Cp₂W(bdt) (4).

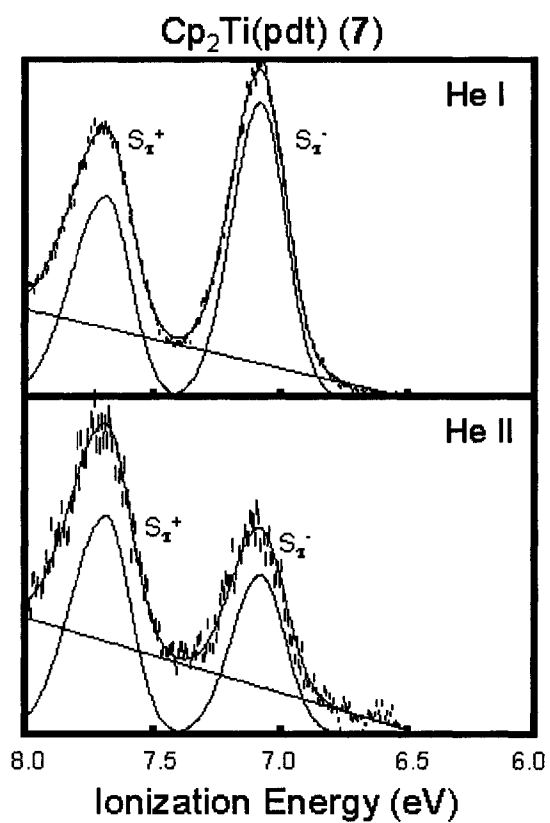


Figure 8.6. Gas-phase photoelectron spectra of Cp₂Ti(pdt) (7) with He I and He II excitation.

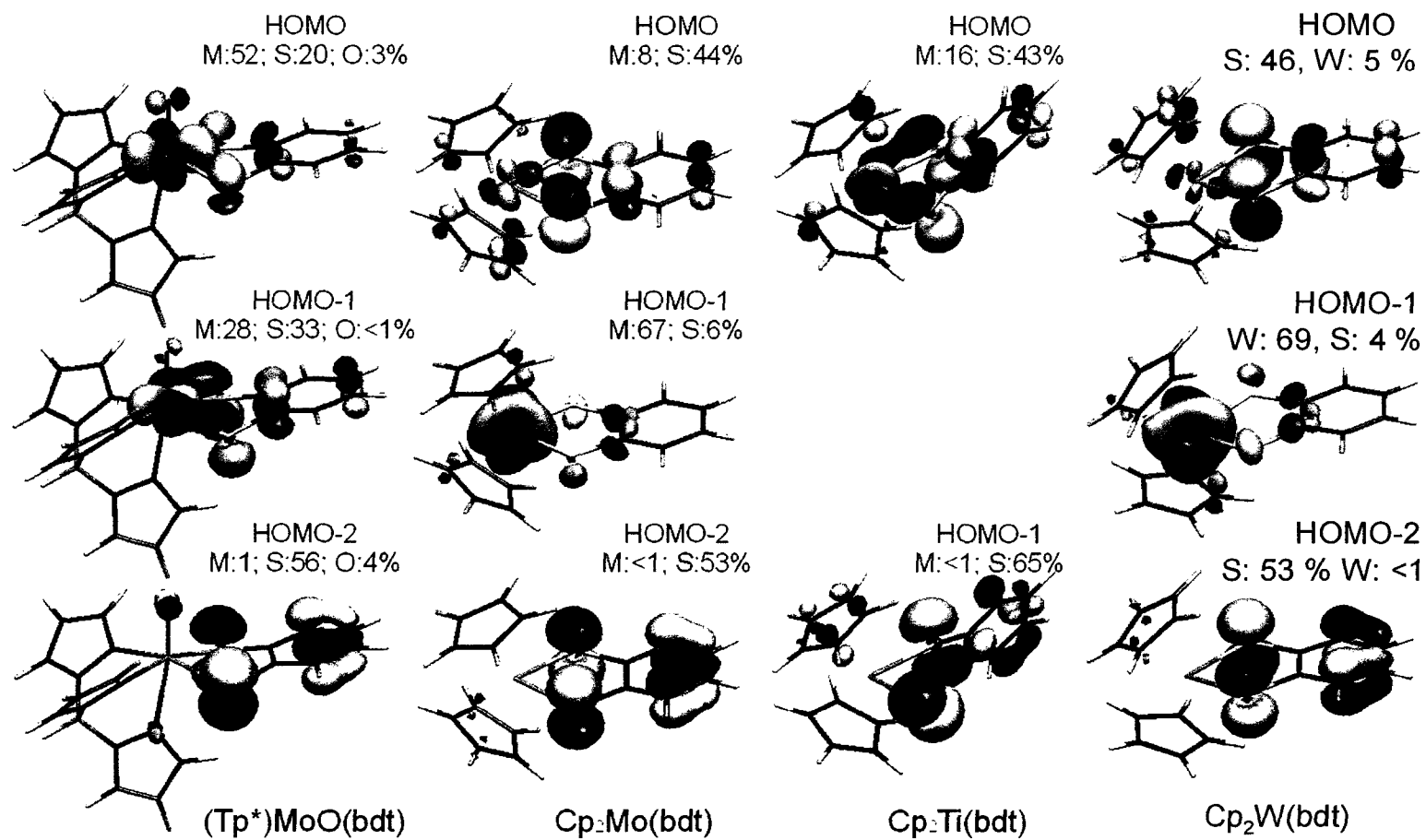


Figure 8.7. Calculated three frontier orbitals (HOMO, HOMO-1, and HOMO-2) of (Tp*)MoO(bdt) (1), Cp₂Mo(bdt) (2), Cp₂Ti(bdt) (3) and Cp₂W(bdt) (4). All contours have the same cutoff level (0.05).

5.0 References

1. Fourmigue, M. *Coord. Chem. Rev.* **1998**, *178-180* (Pt. 1), 823-864.
2. Domercq, B.; Coulon, C.; Feneyrou, P.; Dentan, V.; Robin, P.; Fourmigue, M. *Advanced Functional Materials* **2002**, *12* (5), 359-366.
3. Pilato, R. S.; Eriksen, K.; Greaney, M.; Gea, Y.; Taylor, E.; Goswami, S.; Kilpatrick, L.; Spiro, T.; Rheingold, A.; Stiefel, E. I. *ACS Symposium Series* **1993**, *535* (Molybdenum Enzymes, Cofactors, and Model Systems), 83-97.
4. Rajagopalan, K.; Johnson, J. L. *J. Biol. Chem.* **1992**, *267* (15), 10199-202.
5. Hille, R. *Chem. Rev.* **1996**, *96*, 2757-2816.
6. Stockert, A. L.; Shinde, S. S.; Anderson, R. F.; Hille, R. *J. Am. Chem. Soc.* **2002**, *124* (49), 14554-14555.
7. Garner, D. C.; Banham, R.; Cooper, S. J.; Davies, E. S.; Stewart, L. J. In *Handbook on Metalloproteins*; Bertini, I.; Sigel, A.; Sigel, H., Eds.; Marcel Dekker, Inc.: New York, 2001, pp 1023-1090.
8. Kisker, C.; Schindelin, H.; Pacheco, A.; Wehbi, W.; Garrett, R. M.; Rajagopalan, K. V.; Enemark, J. H.; Rees, D. C. *Cell* **1997**, *91*, 973-983.
9. Kisker, C. *Handbook of Metalloproteins, Volume 2*; Messerschmidt, A., Huber, Ed.; John Wiley & Sons LTD: New York, 2001, pp 1121-1135.
10. Enemark, J. H.; Cosper, M. M. In *Metal Ions in Biological Systems*; Vol. 39: *Molybdenum and Tungsten. Their Roles in Biological Processes*; Sigel, A.; Sigel, H., Eds.; Marcel Dekker, Inc.: New York, 2002, pp 621-654.

11. Schindelin, H.; Kisker, C.; Rees, D. *JBIC, J. Biol. Inorg. Chem.* **1997**, 2 (6), 773-781.
12. Eisenberg, R. *Prog. Inorg. Chem.* **1970**, 12, 295-369.
13. Inscore, F. E.; McNaughton, R.; Westcott, B.; Helton, M. E.; Jones, R.; Dhawan, I. K.; Enemark, J. H.; Kirk, M. L. *Inorg. Chem.* **1999**, 38, 1401-1410.
14. Joshi, H. K.; Inscore, F. E.; Schirlin, J. T.; Dhawan, I. K.; Carducci, M. D.; Bill, T. G.; Enemark, J. H. *Inorg. Chim. Acta* **2002**, 337, 275-286.
15. Dhawan, I. K.; Pacheco, A.; Enemark, J. H. *J. Am. Chem. Soc.* **1994**, 116, 7911-7912.
16. Dhawan, I. K.; Enemark, J. H. *Inorg. Chem.* **1996**, 35, 4873-4882.
17. Inscore, F. E.; Joshi, H. K.; McElhaney, A.; Enemark, J. H. *Inorg. Chim. Acta* **2002**, 331, 246-256.
18. Inscore, F. E.; Rubie, N.; Joshi, H. K.; Kirk, M. L.; Enemark, J. H. *manuscript submitted to Inorg. Chem.*
19. Rebelo, J.; Dias, J.; Huber, R.; Moura, J.; Romao, M. *JBIC, J. Biol. Inorg. Chem.* **2001**, 6 (8), 791-800.
20. Enroth, C.; Eger, B. T.; Okamoto, K.; Nishino, T.; Nishino, T.; Pai, E. F. *Proc. Natl. Acad. Sci. USA* **2000**, 97 (20), 10723-10728.
21. Li, H. K.; Temple, C.; Rajagopalan, K.; Schindelin, H. *J. Am. Chem. Soc.* **2000**, 122 (32), 7673-7680.
22. Carducci, M. D.; Brown, C.; Solomon, E. I.; Enemark, J. H. *J. Am. Chem. Soc.* **1994**, 116, 11856-11868.

23. McMaster, J.; Carducci, M. D.; Yang, Y.-S.; Solomon, E. I.; Enemark, J. H. *Inorg. Chem.* **2001**, *40*, 687-702.
24. Green, J. C. *Acc. Chem. Res.* **1994**, *27* (5), 131-7.
25. Westcott, B. L.; Gruhn, N. E.; Enemark, J. H. *J. Am. Chem. Soc.* **1998**, *120*, 3382-3386.
26. Helton, M. E.; Gruhn, N. E.; McNaughton, R. L.; Kirk, M. L. *Inorg. Chem.* **2000**, *39* (11), 2273-2278.
27. Westcott B. L.; Enemark, J. H. *Inorg. Chem.* **1997**, *36*, 5404-5405.
28. Wang, X.-B.; Inscore, F. E.; Yang, X.; Cooney, J. J. A.; Enemark, J. H.; Wang, L.-S. *J. Am. Chem. Soc.* **2002**, *124*, 10182-10191.
29. Guyon, F.; Lenoir, C.; Fourmigué, M.; Larsen, J.; Amaudrut, J. *Bull. Soc. Chim. Fr.* **1994**, *131*, 217-226.
30. Lauher, J. W.; Hoffmann, R. *J. Am. Chem. Soc.* **1976**, *98* (7), 1729-1742.
31. Green, J. C. *Struct. Bonding (Berlin)* **1981**, *43*, 37-112.
32. Green, J. C. *Chem. Soc. Rev.* **1998**, *27* (4), 263-272.
33. Guyon, F.; Fourmigue, M.; Audebert, P.; Amaudrut, J. *Inorg. Chim. Acta* **1995**, *239* (1-2), 117-24.
34. Domercq, B.; Coulon, C.; Fourmigué, M. *Inorg. Chem.* **2001**, *40*, 371-378.
35. Kutoglu, A.; Köpf, H. *J. Organomet. Chem.* **1970**, *25*, 455-460.
36. Fourmigue, M.; Domercq, B.; Jourdain, I. V.; Molinie, P.; Guyon, F.; Amaudrut, J. *Chem. Eur. J.* **1998**, *4* (9), 1714-1723.

37. Fourmigue, M.; Lenoir, C.; Coulon, C.; Guyon, F.; Amaudrut, J. *Inorg. Chem.* **1995**, *34* (20), 4979-85.
38. Kaiwar, S. P.; Hsu, J. K.; Vodacek, A.; Yap, G.; Liable-Sands, L. M.; Rheingold, A. L.; Pilato, R. S. *Inorg. Chem.* **1997**, *36* (11), 2406-2412.
39. Fomitchev, D. V.; Lim, B. S.; Holm, R. *Inorg. Chem.* **2001**, *40* (4), 645-654.
40. Guimon, C.; Pfister-Guillouzo, G.; Meunier, P.; Gautheron, B.; Tainturier, G.; Pouly, S. *J. Organomet. Chem.* **1985**, *284* (3), 299-312.
41. Klapötke, T.; Köpf, H. *Z. Anorg. Allg. Chem.* **1988**, *558*, 217-222.
42. Lowe, N. D.; Garner, C. D. *J. Chem. Soc. Dalton Trans.* **1993**, 2197-2207.
43. Cooney, J. J. A.; Joshi, H. K.; Gruhn, N. E.; Enemark, J. H. *manuscript in preparation*.
44. Shaver, A.; McCall, J. M. *Organometallics* **1984**, *3* (12), 1823-1829.
45. Lichtenberger, D. L.; Copenhaver, A. S. *J. Electron Spectrosc. Relat. Phenom.* **1990**, *50* (4), 335-52.
46. Baerends, E. J.; Ellis, D. E.; Ros, P. *Chem. Phys.* **1973**, *2*, 41-51.
47. Fonseca Guerra, C.; Snijders, J. G.; te Velde, G.; Baerends, E. J. *Theor. Chem. Acc.* **1998**, *99*, 391-399.
48. Te Velde, G.; Bickelhaupt, F.; Baerends, E.; Fonseca Guerra, C.; Van Gisbergen, S.; Snijders, J.; Ziegler, T. *J. Comp. Chem.* **2001**, *22* (9), 931-967.
49. te Velde, G.; Baerends, E. J. *J. Comput. Phys.* **1992**, *99* (1), 84-98.
50. Versluis, L.; Ziegler, T. *J. Chem. Phys.* **1988**, *88*, 322-329.
51. Becke, A. D. *Phys. Rev. A.* **1988**, *38*, 3098-3100.

52. Lee, C.; Yang, W.; Parr, R. G. *Phys. Rev. B.* **1988**, *37*, 785.
53. Glass, R. S.; Gruhn, N. E.; Lichtenberger, D. L.; Lorance, E.; Pollard, J. R.; Birringer, M.; Block, E.; DeOrazio, R.; He, C.; Shan, Z.; Zhang, X. *J. Am. Chem. Soc.* **2000**, *122* (21), 5065-5074.
54. Yeh, J.; Lindau, I. *At. Data Nucl. Data Tables* **1985**, *32* (1), 1-155.
55. Chang, C. S. J.; Rai-Chaudhuri, A.; Lichtenberger, D. L.; Enemark, J. H. *Polyhedron* **1990**, *9*, 1965-1973.
56. Kutoglu, A. *Z. Anorg. Allg. Chem.* **1972**, *390*, 195-209.
57. Enemark, J. H.; Feltham, R. D. *Coord. Chem. Rev.* **1974**, *13*, 339-406.
58. George, G. N.; Pickering, I. J.; Kisker, C. *Inorg. Chem.* **1999**, *38* (10), 2539-2540.

**CHAPTER 9: Geometrical Control of the Active Site
Electronic Structure of Pyranopterin Enzymes by Metal-
Sulfur Interactions: Aldehyde Oxidase (MOP)**

1.0 Introduction

Pyranopterindithiolate (molybdopterin¹) is a unique cofactor found in the active sites of more than 50 enzymes containing molybdenum or tungsten.² The structure of this cofactor and its coordination to metals is well known from recent crystal structures of several enzymes.³ However, its functional role remains to be established. It is postulated to modulate the redox potential of the metal center and to act as an electron transfer pathway for the regeneration of the metal center.^{4,5} The active sites of the sulfite oxidase (SO) and xanthine oxidase (XO) families of enzymes have one sulfur atom of the pyranopterindithiolate cofactor in an equatorial position and *trans* to their respective catalytically labile oxygen donor ligands. It has been proposed that this geometry facilitates formal oxygen atom transfer in these enzymes via a kinetic *trans* effect.⁶

For discrete complexes, the “fold angle” of the five-membered dithiolate chelate ring (Figure 9.1) depends upon the electron configuration of the metal center.^{5,7} It has been proposed that dynamic variations in protein structure during catalysis can change the fold angle and thereby modulate the charge distribution and reactivity of the active site.^{5,8} Such a “dithiolate-folding-effect” is difficult to establish experimentally because of the lack of atomic resolution protein structures for both oxidized and reduced forms of SO and XO families of enzymes. For XO enzymes, an additional complication is the instability of Mo centers containing both terminal oxo and sulfido groups.⁹ Thus, protein purification often produces the inactive desulfo form of these enzymes. The recent report of the high resolution (1.28 Å) crystal structure of aldehyde oxidase (MOP),¹⁰ a member of the XO family, in the desulfo oxidized state, provides a starting geometry for the

electronic structure calculations on the active site presented here. These calculations assess the possible relationships among fold angle changes, catalytic reactivity and electron transfer regeneration of *mono* ene-dithiolate active sites.

Geometry optimization and electronic structure calculations at the DFT level of theory¹¹ on model complexes, **1-3** (Figure 9.2),¹² derived from the X-ray crystal structure of MOP have been performed.¹⁰ The calculations indicate that the frontier orbitals (Figures 9.3 and 9.4) have significant contributions from both metal in-plane (M_{ip}) and symmetric (S_{π}^{+}) and antisymmetric (S_{π}^{-}) combinations of the dithiolate sulfur out-of-plane p -orbitals.¹³ This is the first instance that contributions from a dithiolate S_{π}^{+} orbital to the frontier orbitals of a model complex with a geometry like that of an enzyme active site have been demonstrated.

The reaction mechanism of the XO family of enzymes has been studied in detail.¹⁴⁻¹⁶ The proposed mechanism involves a hydride atom transfer to the terminal sulfido group that reduces the Mo (VI) center to Mo(IV).¹⁶⁻¹⁹ Previous theoretical studies of the reductive half-reaction catalyzed by the XO family of enzymes^{14,19} provide a framework for the geometrical structure changes but no orbital correlation was made at that time. The Mo(VI) *aqua* complex (**1**) resembles the resting state of the enzyme that results from the displacement of the product by a water molecule.¹⁶ In the enzyme crystal structure,^{3,10,16} the carboxylic group of Glu869 located near the active site has been suggested¹⁶ to be in a position where it is ready to accept a proton from the coordinated water molecule, thus generating an anionic species similar to complex **2**, also observed in the desulfo form in the crystal structure.¹⁰ The calculated metal-dithiolate fold angles of

the model complexes flatten from 42.6° in **1** to 12.3° in **2** and 10.4° in **3**. The geometry of complex **2** is very similar¹² to the crystal structure geometry of the active site¹⁰, which has a fold angle of 16.6° . It is interesting to note that although the formal oxidation state of **2** is Mo(VI), the proton abstraction from **1** leaves an overall negative charge on **2**, and the fold angle reduces to accommodate this change. Geometry optimized structure **2** has a sulfido-Mo-O(H) angle of 103.9° , and the oxygen lone pair of the hydroxyl group is in an appropriate orientation to attack the carbonyl carbon of the aldehyde substrate.¹⁶ The orbital plot of the lowest unoccupied molecular orbital (LUMO) of compounds **1** (Figure 9.3) and **2** shows that this orbital is anti-bonding between Mo and the sulfido ligand, as also observed in studies of other model complexes.²⁰ The subsequent hydride attack on the sulfur atom, and therefore, reduction of this orbital, will weaken the Mo and S double bond and ease the formation of a sulfhydryl group - a crucial enzymatic step. As a result of the hydride atom transfer the metal-dithiolate fold angle in the resultant model complex **3** flattens to 10.4° . In the reduced state (Mo (IV)), complex **3**, the highest occupied molecular orbital (HOMO; Figure 9.4) is primarily a metal in-plane orbital that is derived from population of the LUMO in **1** during the two-electron cascade associated with incorporation of an oxygen atom into substrate during catalysis.

Notice that in the oxidized active site model (**1**), the folding of the metal-dithiolate introduces contributions from the dithiolate S_π^+ combination into the redox orbital (LUMO, Figure 9.3), with concomitant decrease in the metal contribution. The S_π^+ orbital has the right symmetry and energy match to mix with the metal in-plane (M_{ip}) orbital upon folding, as confirmed experimentally for bent metallocene dithiolate

compounds.⁵ This orbital also contains significant contributions from the S atom of the sulfhydryl group, that has changed from a double bonded sulfur atom to a single bonded sulfur atom. Thus, the metal-dithiolate fold angle and metal-sulfido/sulfhydryl may geometrically control the electronic structure of the oxidized (**1**) and reduced (**3**) forms of the active site by defining the orientation of the dithiolate sulfur- π (p) orbitals with respect to the metal in-plane (M_{ip}) acceptor orbital and upon reduction of the sulfido to a sulfhydryl group.

Figure 9.4 also shows the second highest occupied molecular orbital (HOMO-1) of **3**, the reduced (Mo(IV)) compound. This orbital is primarily the symmetric combination of the dithiolate sulfur out-of-plane orbitals (S_{π}^{+}) which has an antibonding interaction with the π orbitals of the carbon-carbon double bond. The constrained unsaturated five-membered chelate ring⁷ is essential for raising the energy of the S_{π}^{+} orbitals to have the right symmetry and energy match with metal in-plane orbitals.⁵ The symmetric combination of the sulfur orbitals (S_{π}^{+}) is more destabilized than the antisymmetric combination (S_{π}^{-}) because of the greater interaction with the C=C π -orbital of appropriate symmetry.^{5,21}

The calculated structure for the isolated active site of MOP closely resembles that found for the desulfo form of the oxidized protein.¹⁰ The LUMO acceptor orbital of the oxidized form is poised for hydride attack on the terminal sulfido ligand (Figure 9.3), and the fold angle of the dithiolate ligand decreases upon reduction of the site. These calculations support the proposal that metal-dithiolate fold angle effects⁵ help to buffer the electron density at the metal center.²² Proton abstraction from the *aqua* ligand of the

oxidized site (2) also flattens the fold angle. This latter result suggests that the dithiolate fold angle can fine tune the nucleophilicity of the hydroxide ligand that is *trans* to a dithiolate sulfur atom. Changing the fold angle can also facilitate the attack of hydride on the terminal sulfido ligand by modulating the acceptor properties of the LUMO. Thus, static or dynamic changes in the structure of the protein surrounding the active site can be expected to induce dithiolate fold angle changes that should play an important role in modulating the catalytic reactions of molybdenum and tungsten enzymes.

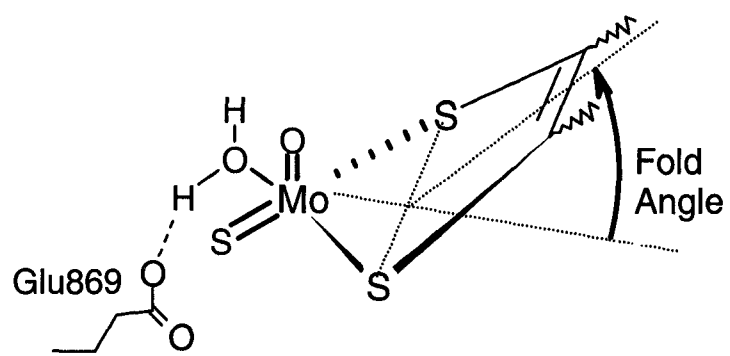


Figure 9.1. The definition of the fold angle along the S-S vector, shown for the proposed active site of aldehyde oxidase (MOP).³

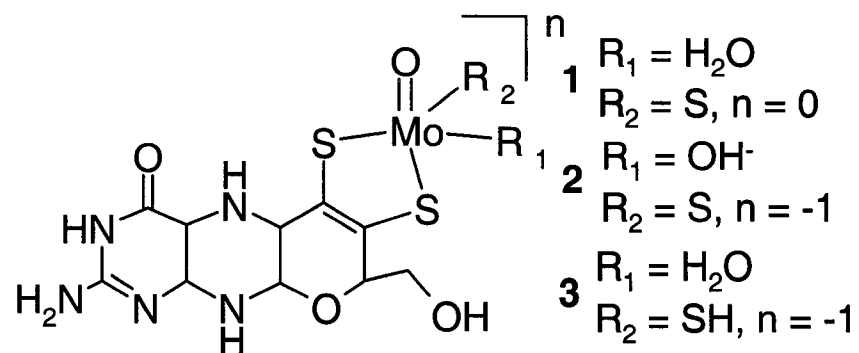


Figure 9.2. Bioinspired computational models 1-3 of the active site of MOP.

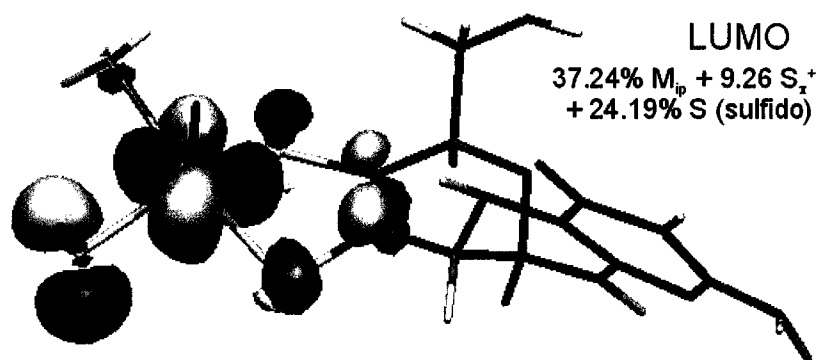


Figure 9.3. The lowest unoccupied molecular orbital (LUMO) of the oxidized active site of complex 1 (fold angle: 42.6°) that accepts two electrons in the reduction half cycle.

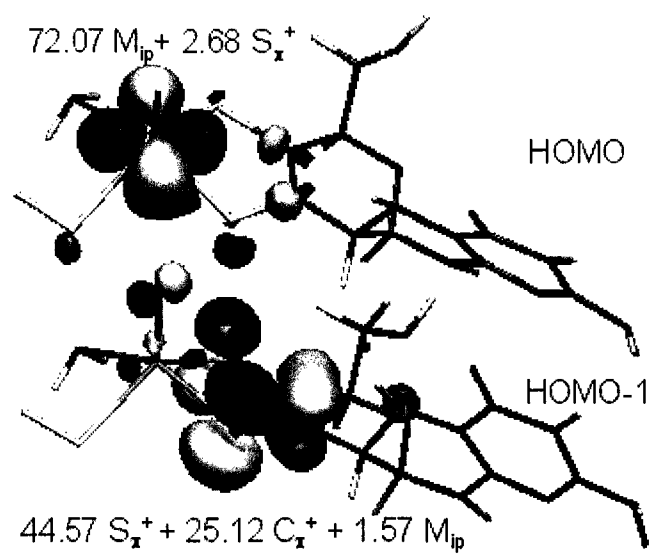


Figure 9.4. The frontier orbitals (highest occupied molecular orbital; HOMO and HOMO-1) of the reduced active site complex 3 (fold angle: 10.4°).

2.0 References

1. Rajagopalan, K.; Johnson, J. L. *J. Biol. Chem.* **1992**, *267* (15), 10199.
2. Sigel, A.; Sigel, H. *Molybdenum and Tungsten: Their Roles in Biological Processes;* Metals Ions in Biological Systems; vol. 39; Dekker: New York, **2002**.
3. Romão, M. J.; Archer, M.; Moura, I.; Moura, J. J.; LeGall, J.; Engh, R.; Schneider, M.; Hof, P.; Huber, R. *Science* **1995**, *270*, 1170.
4. Inscore, F. E.; McNaughton, R.; Westcott, B.; Helton, M. E.; Jones, R.; Dhawan, I. K.; Enemark, J. H.; Kirk, M. L. *Inorg. Chem.* **1999**, *38*, 1401
5. Joshi, H. K.; Cooney, J. J. A.; Inscore, F. E.; Gruhn, N. E.; Lichtenberger, D. L.; Enemark, J. H. *Proc. Natl. Acad. Sci. USA* **2003**, *100* (7), 3719.
6. Peariso, K.; McNaughton, R. L.; Kirk, M. L. *J. Am. Chem. Soc.* **2002**, *124*, 9006.
7. Joshi, H. K.; Inscore, F. E.; Schirlin, J. T.; Dhawan, I. K.; Carducci, M. D.; Bill, T. G.; Enemark, J. H. *Inorg. Chim. Acta* **2002**, *337*, 275.
8. Inscore, F. E.; Rubie, N.; Joshi, H. K.; Kirk, M. L.; Enemark, J. H. manuscript submitted to *Inorg. Chem.*
9. Young, C. G. *JBIC, J. Biol. Inorg. Chem.* **1997**, *2* (6), 810.
10. Rebelo, J.; Dias, J.; Huber, R.; Moura, J.; Romão, M. *JBIC, J. Biol. Inorg. Chem.* **2001**, *6*, 791.
11. Calculations were performed using the ADF (Amsterdam density functional theory calculations) package (release 2000.02). Further details are provided in reference 5.

12. In compounds **1-3**, the cytosine dinucleotide portion of the native cofactor of MOP has been simplified to OH to reduce the computational efforts. On the average, the optimized geometry of **2** differed by less than 2% in bond lengths and 1% in bond angles from the crystal structure geometry (ref 10).
13. The z-axis on Mo points towards the axial oxo ligand, and the x axis is the bisector of the angle formed by the dithiolate sulfurs. The Mo in-plane orbital is dx^2-y^2 ; the sulfur out-of-plane orbitals are Sp_z .
14. Voityuk, A. A.; Albert, K.; Romao, M. J.; Huber, R.; Roesch, N. *Inorg. Chem.* **1998**, *37*, 176.
15. Voityuk, A. A.; Albert, K.; Koestlmeier, S.; Nasluzov, V. A.; Neyman, K. M.; Hof, P.; Huber, R.; Romão, M. J.; Roesch, N. *J. Am. Chem. Soc.* **1997**, *119*, 3159.
16. Romão, M. J.; Rosch, N.; Huber, R. *JBIC, J. Biol. Inorg. Chem.* **1997**, *2*, 782.
17. Hille, R. *Biochim. Biophys. Acta* **1994**, *1184*, 143.
18. Huber, R.; Hof, P.; Duarte, R.; Moura, J.; Moura, I.; Liu, M.; LeGall, J.; Hille, R.; Archer, M.; Romão, M. *Proc. Natl. Acad. Sci. USA* **1996**, *93*, 8846.
19. Ilich, P.; Hille, R. *J. Phy. Chem. B* **1999**, *103*, 5406.
20. Rubie, N. D.; Peariso, K.; Doonan, C.; George, G.; Young, C. G.; Kirk, M. L. *Abstracts of Papers, 224th ACS National Meeting, Boston, MA, United States, August 18-22, 2002*, INOR-001.
21. Guimon, C.; Pfister-Guillouzo, G.; Meunier, P.; Gautheron, B.; Tainturier, G.; Pouly, S. *J. Organomet. Chem.* **1985**, *284*, 299.
22. Westcott, B. L.; Gruhn, N. E.; Enemark, J. H. *J. Am. Chem. Soc.* **1998**, *120*, 3382.

CHAPTER 10: Conclusions and Future Directions

1.0 Model Chemistry

Synthesis, X-ray crystallography, photoelectron spectroscopy, and density functional theoretical studies of minimum molecular models of the active sites of pyranopterindithiolate enzymes have been reported.

Chapter 1 and 2 provided introduction and experimental details. The majority of the compounds reported here have group VI metals stabilized by scorpionate (hydrotris(3,5-dimethylpyrazol-1-yl)borate) and enedithiolate ligands. The photoelectron spectra on these complexes have always provided prominent signatures from the scorpionate ligands that were poorly understood. A detailed discussion of the electronic structure of scorpionate ligands and ene-1,2-dithiolate ligands is provided in Chapter 3. Three bands, A, B, and C, have been identified in the lower energy region in the photoelectron spectra of scorpionate ligands. The general shape of the low energy ionization bands A, B, and C is not greatly effected by the nature of the metal ions as reported here and by others.¹ However, substitutions at the 3, 4 and 5 positions of the pyrazole ring can shift the ionization energies of the bands significantly, as especially shown by the CF₃ substitutions.

The scorpionates discussed in this work are coordinated to the metal through the nitrogen atoms of the pyrazole rings and this σ -bonding is modulated by electron density at the metal center or *vice versa*. The electronic structure of scorpionate ligands presented here includes distinct assignments of σ_{BH} and σ_{N} (*a* and *e*-symmetry) orbitals confirmed experimentally for the first time. The shift in the position of band B can be an

indicator of the extent of σ -bonding of these scorpionate ligands upon coordination with transition metals.² The electronic structure studies of enedithiolate ligands show that they have a symmetric combination of the sulfur out of plane orbitals as their highest occupied molecular orbital. This electronic structure of scorpionate and enedithiolate ligands will help in understanding the electronic structure of scorpionate, and enedithiolate-based transition metal complexes utilized in bioinorganic modeling and organometallic catalysis.

Oxo-Mo(V) dihalide complexes of the type $(Tp^*)MoOX_2$ (where X = F, Cl, Br, I) have been studied in Chapter 4. Theoretically obtained first ionization energies have similar trends as obtained experimentally by photoelectron spectroscopy and EPR. The presence of a $\pi(Mo=O)$ band at similar energies in their photoelectron spectra suggests an electronically isolated $Mo=O$ diatomic core. A strong molybdenum and axial oxo interaction dominates the electronic structure of these and similar other species. The DFT calculations show that the metal-halide covalency increases in these compounds as we go down the halogen group due to the increased number of electrons leading to more diffusion of the electron cloud along the halogen-metal bond. The compound $(Tp^*)MoOI_2$ has the most covalent metal-halogen interaction. Significant differences in the metal-ligand covalency are observed between coordination of molybdenum with the first row element (F) and other elements (Cl, Br, I) in the halogen group resulting in highly covalent bonds in the complexes of the second and higher row halogens. This could suggest that relatively softer second row element sulfur has been selected in the

biological systems for enhanced covalent interaction with metal to relatively harder first row element oxygen in the pyranopterindithiolate cofactor.

The X-ray structures of some metal-dithiolate model complexes were presented in Chapter 5. The most significant structural perturbation observed within the (Tp*)MoO(S-S) system is the fold angle, which exhibits considerable variation among the (Tp*)ME(S-S) and Cp₂Mo(bdt) complexes that have been investigated. For the (Tp*)MoO(S-S) compounds the fold angle varies between 6.9 – 29.5°. Investigation of the crystal packing forces and electronic contributions to the fold angle has been done to assess the role that the fold angle may play in controlling the electronic structure and reactivity of Mo ene-1,2-dithiolate systems. Previous electronic studies and available crystal structures on various Mo(V)/ Mo(IV) dithiolene complexes such as [Cp₂Mo(S-S)]⁺,³⁻⁶ [MoO(S-S)₂]⁻⁷⁻⁹ and [Mo(S-S)₃]⁻¹⁰ revealed that the fold angle generally decreased upon reduction of the Mo center. In a recent anionic and neutral photoelectron spectroscopic and computational study of Cp₂M(bdt) (M = Mo, Ti), [MoO(bdt)₂]⁻ and related compounds, the fold angle was proposed to be electronic in origin and appears to persist in the gas phase.¹¹⁻¹³ The observed variances in fold angle as a function of the metal, axial substitution, and electron donor properties of the dithiolate ligand in (Tp*)MoO(dithiolate) compounds seems electronic in origin. It is proposed that this structural distortion may fine tune the electronic structure and properties of the oxo-Mo(V) dithiolate systems, and also may play a regulatory role in the pyranopterin Mo and W enzymes during catalysis. The postulated role of this fold angle in conjunction with the obtuse O-M-S angles (oxo-gate hypothesis, orbital overlap model)¹⁴ would be to

control the orientation (overlap) of the ene-1,2-dithiolate S $p(\pi)$ donor orbitals with the Mo $4d_{xy}$ redox orbital and concomitantly with the unoccupied metal acceptor orbitals ($d_{xz,yz}$, $d_{x^2-y^2}$, and d_z^2).

The structure of $\text{Cp}_2\text{Mo}(\text{bdt}) (d^2)$ reveals presence of a planar dithiolate. Structural studies of compounds with no electrons in the metal in-plane (metal orbital(s) in the metal-sulfur plane) orbital, are reported and discussed in Chapter 7. A large fold angle has been observed in these cases. Thus, the fold angle of the dithiolate, which is a geometric parameter, is closely related to the electronic occupation of the metal in-plane orbital. This folding could possibly play a role in modulating redox potentials by controlling the Mo effective nuclear charge via S_σ and S_π charge donation into the unfilled Mo acceptor d-orbitals.

The combined photoelectron spectroscopic and density functional theoretical results presented in Chapter 6 support the conclusion that these oxomolybdenum and oxotungsten compounds have considerable metal-sulfur covalency. The assignment of lower energy ionizations to frontier orbitals that contain contributions from dithiolate in-plane or out of plane orbitals has been possible. The results presented in Chapter 6 for compounds $(\text{Tp}^*)\text{MO}(\text{S-S})$ reveal a trend in their first ionization energies which is consistent with the electron withdrawing properties of the substitution on the benzene ring of the dithiolate ligand. The effectively similar ionization potentials for the metal in-plane orbital in groups (a) $(\text{Tp}^*)\text{MO}(\text{bdt})$ (where $M = \text{Mo}, \text{W}$), $\text{Cp}_2\text{Mo}(\text{bdt})$ and (b) $(\text{Tp}^*)\text{MO}(\text{tdt})$ (where $M = \text{Mo}, \text{W}$) indicates that dithiolate can maintain a nearly constant effective nuclear charge on metal center. This property of dithiolate donors has been

previously summarized as “electronic buffering effect”¹⁵ and “dithiolate-folding-effect”¹³ and shown here for transition metals Mo and W relevant to the active site of the pyranopterindithiolate enzymes. The computed total energy involved in the variation of fold angle for a Mo(V), d^1 system is of the order of 23 kcal/mol which compares with the energy of a few hydrogen bonds and can be provided to the pyranopterindithiolate by movements of the protein backbone or breaking of hydrogen bonds. The metal substitution of Mo by W does not significantly change the electronic structure of the metal-dithiolate compounds investigated here.

The synthesis, structural and physical characterization of three $(Tp^*)Mo(NO)(S-S)$ compounds, reported in Chapter 7, have provided an opportunity to investigate the geometric and electronic structure differences of $(Tp^*)MoE(S-S)$ (where $E = O, NO$) systems as a function of axial ligation and remote substituent effects on the ene-1,2-dithiolate ligand. The most significant structural difference is the large fold angle of ene-1,2-dithiolate along S—S axis in the nitrosyl-Mo compounds. Photoelectron spectroscopy and density functional theoretical studies provide insight into the electronic structures of these molybdenum nitrosyls and supports the hypothesis of folding of the dithiolate ligand. This folding of the dithiolate ligands in $(Tp^*)Mo(NO)(S-S)$ compounds minimizes the filled-filled interaction of out of plane metal and sulfur orbitals. The frontier orbitals have significant contributions from dithiolate out of plane and in-plane molecular orbitals and support the assignment of ionizations in the photoelectron spectroscopic studies. Thus, there are sufficient evidences to support the electronic origin of the geometric perturbations of dithiolate folding. This angular perturbation (fold

angle) is sensitive to the electronic occupation of metal in-plane (equatorial) orbital. The reduction potential of these (Tp*)Mo(NO)(S-S) compounds is sensitive to peripheral substitution of the ligand, whereas the first ionization energy is not. This diversity is due to the different orbitals involved in each of these processes.

In Chapter 8, the gas phase photoelectron spectra of Cp₂M(bdt) (where M = Mo, W, Ti), obtained with HeI and HeII photon sources clearly show that under favorable conditions the ionizations from primarily metal based orbitals and primarily S_π-based orbitals can be experimentally distinguished from one another. In addition, an unambiguous demonstration has been made that the symmetric S_π⁺ orbital, which can interact with the in-plane metal orbital upon bending, is more easily ionized than the antisymmetric S_π⁻ orbital. This successful analysis and assignment of the low energy ionizations of compounds Cp₂M(bdt) provides the framework for investigation and direct assignment of the S_π and metal-based ionizations in other metal dithiolate systems that may be more strongly mixed than Cp₂M(bdt) or that may have less favorable separation of their M-S region from the ionizations of other ligands. It is interesting to note that in the case of Cp₂Ti(bdt) the dithiolate ligand can be thought of as a six-electron donor, two electrons from each of the thiolate σ-orbitals and two from the S_π⁺ orbital. Hence, folding of the dithiolate ligand may stabilize an 18-electron complex. This folding effect is in contrast to the nitrosyl group where the transformation from linear to bent coordination transfers a pair of electrons from the metal to a localized orbital on the ligand.¹⁶

2.0 Implications for Enzymes

The variation in the fold angle of the dithiolate ligand reflects the electron occupation in the equatorial in-plane metal orbital.¹⁷ Folding of the dithiolate ligand enables the S_{π} electron density to modulate the electron density in the equatorial plane of the metal, and thus folding can play a significant role in the metal-sulfur anisotropic bonding interaction. This “dithiolate-folding-effect” may be important in stabilizing the multiple oxidation states that result from electron transfer or equatorial oxygen atom transfer (OAT) in pyranopterin Mo/W enzymes (*e.g.* in SO and XO). For example, reduction of the metal in-plane orbital due to the release of an equatorial oxygen atom during OAT should make the dithiolene unit of PDT more planar compared to the fully oxidized enzyme. In this regard, we note that the calculated dithiolate fold angles for the two chemically equivalent, but crystallographically distinct, molybdenum centers in SO (Figure 8.1) of 6.6 and 7.0° (Table 8.1) are smaller than that for the oxidized center of aldehyde oxidoreductase (16.6°), whose oxidized structure has been determined to high resolution (1.28 Å).¹⁸ The exact oxidation state of SO in the crystal structure is not known, but there is evidence for photoreduction of the molybdenum center in the synchrotron beam during data collection.^{19,20} The fold angle studies on model systems support the view that the reported structure of SO¹⁹ is a reduced form of the enzyme. Dithiolate folding can also modify the electropositive nature of the metal center by varying the overlap of sulfur lone pairs with the metal in-plane orbital. The S_{π} orbitals of dithiolate can therefore serve as an essential instrument for the buffering of electron density at the metal center by either involving themselves in strong mixing with an empty

metal orbital, as shown here for the d^0 $\text{Cp}_2\text{Ti}(\text{bdt})$ complex, or by localization of electron density on the S_π orbitals in the presence of a filled metal orbital, as shown here for the d^2 $\text{Cp}_2\text{Mo}(\text{bdt})$ complex. The “ene” nature of the dithiolate appears to be essential for raising the energy of the S_π^+ orbitals for interaction with the metal in-plane orbital. The substitution of Mo by W in $\text{Cp}_2\text{M}(\text{bdt})$ system results in the shift of the metal based ionization to lower ionization energy.

Dithiolate folding may also provide a mechanism for the sulfur- π orbitals of the PDT ligand to act as an effective electron transfer pathway from the in-plane orbitals on the metal center to other redox partners via the pyranopterin. For molybdenum and tungsten enzymes the energies involved in substrate binding, docking with electron transfer partners, and dynamic motions of the protein skeleton, may modulate the dithiolate fold angle and, consequently, the electron distribution, overall reduction potential and reactivity of the metal center.

In Chapter 9, the calculated structure for the isolated active site of MOP closely resembles that found for the desulfo form of the oxidized protein.¹⁸ The LUMO acceptor orbital of the oxidized form is poised for hydride attack on the terminal sulfido ligand (Figure 9.3), and the fold angle of the dithiolate ligand decreases upon reduction of the site. These calculations support the proposal that metal-dithiolate fold angle effects help to buffer the electron density at the metal center. Proton abstraction from the *aqua* ligand of the *oxidized* site also flattens the fold angle. This latter result suggests that the dithiolate fold angle can fine tune the nucleophilicity of the hydroxide ligand that is *trans* to a dithiolate sulfur atom. Changing the fold angle can also facilitate the attack of

hydride on the terminal sulfido ligand by modulating the acceptor properties of the LUMO. Thus, static or dynamic changes in the structure of the protein surrounding the active site can be expected to induce dithiolate fold angle changes that should play an important role in modulating the catalytic reactions of molybdenum and tungsten enzymes.

3.0 Future Directions

The fold angle variations in $(\text{Tp}^*)\text{Mo}(\text{NO})(\text{S-S})$ system, described in Chapter 7, can be studied as a function of the oxidation state of the metal. This would require the chemical or electrochemical reduction of these compounds. These complexes, if isolated and crystallized, could be subjected to X-ray structural studies and could also be an excellent target for EPR studies. Their precursor complexes $(\text{Tp}^*)\text{Mo}(\text{NO})\text{Cl}_2$ have previously been reduced to 17 electron species $[(\text{Tp}^*)\text{Mo}(\text{NO})\text{Cl}_2]^-$ and characterized by spectroscopies including EPR, IR, MS.²¹

Structural studies of the pyranopterindithiolate enzymes in different oxidation states are worth pursuing with the advent of sophisticated X-Ray crystallographic techniques. This may help in elucidating fine details of the active sites as a function of the oxidation state and may provide further insight into the functional role of pyranopterindithiolate cofactor. One example of the structural differences observed in the oxidized and reduced active sites is the X-ray study of the formate dehydrogenase where a folding of the pyranopterindithiolate cofactor has been observed for the oxidized active site.²²

4.0 References

1. Bruno, G.; Centineo, G.; Ciliberto, E.; Di Bella, S.; Fragala, I. *Inorg. Chem.* **1984**, *23* (13), 1832-6.
2. Joshi, H. K.; Inscore, F. E.; Gruhn N. E.; Enemark, J. H. *manuscript in preparation.*
3. Fourmigue, M. *Coord. Chem. Rev.* **1998**, *178-180* (Pt. 1), 823-864.
4. Fourmigue, M.; Domercq, B.; Jourdain, I. V.; Molinie, P.; Guyon, F.; Amaudrut, J. *Chem. Eur. J.* **1998**, *4* (9), 1714-1723.
5. Clerac, R.; Fourmigue, M.; Gaultier, J.; Barrans, Y.; Albouy, P.; Coulon, C. *European Physical Journal B: Condensed Matter Physics* **1999**, *9* (3), 431-443.
6. Domercq, B.; Coulon, C.; Fourmigue, M. *Inorg. Chem.* **2001**, *40* (2), 371-378.
7. Boyde, S.; Ellis, S. R.; Garner, C. D.; Clegg, W. *J. Chem. Soc., Chem. Commun.* **1986**, *20*, 1541-3.
8. Donahue, J. P.; Goldsmith, C. R.; Nadiminti, U.; Holm, R. *J. Am. Chem. Soc.* **1998**, *120* (49), 12869-12881.
9. Lim, B.; Donahue, J.; Holm, R. *Inorg. Chem.* **2000**, *39* (2), 263-73.
10. Cervilla, A.; Llopis, E.; Marco, D.; Perez, F. *Inorg. Chem.* **2001**, *40* (25), 6525-8.
11. Wang, X.-B.; Inscore, F. E.; Yang, X.; Cooney, J. J. A.; Enemark, J. H.; Wang, L.-S. *J. Am. Chem. Soc.* **2002**, *124*, 10182-10191.
12. Joshi, H. K.; Inscore, F. E.; Schirlin, J. T.; Dhawan, I. K.; Carducci, M. D.; Bill, T. G.; Enemark, J. H. *Inorg. Chim. Acta* **2002**, *337*, 275-286.

13. Joshi, H. K.; Cooney, J. J. A.; Inscore, F. E.; Gruhn, N. E.; Lichtenberger, D. L.; Enemark, J. H. *Proc. Natl. Acad. Sci. USA* **2003**, *100* (7), 3719-3724.
14. Inscore, F. E.; McNaughton, R.; Westcott, B.; Helton, M. E.; Jones, R.; Dhawan, I. K.; Enemark, J. H.; Kirk, M. L. *Inorg. Chem.* **1999**, *38*, 1401-1410.
15. Westcott, B.; Gruhn, N.; Enemark, J. *J. Am. Chem. Soc.* **1998**, *120* (14), 3382-3386.
16. Enemark, J. H.; Feltham, R. D. *Coord. Chem. Rev.* **1974**, *13*, 339-406.
17. Joshi, H. K.; Inscore, F. E.; Schirlin, J. T.; Dhawan, I. K.; Carducci, M. D.; Bill, T. G.; Enemark, J. H. *Inorg. Chim. Acta* **2002**, *337*, 275-286.
18. Rebelo, J.; Dias, J.; Huber, R.; Moura, J.; Romao, M. *JBIC, J. Biol. Inorg. Chem.* **2001**, *6* (8), 791-800.
19. Kisker, C.; Schindelin, H.; Pacheco, A.; Wehbi, W.; Garrett, R. M.; Rajagopalan, K. V.; Enemark, J. H.; Rees, D. C. *Cell* **1997**, *91*, 973-983.
20. George, G. N.; Pickering, I. J.; Kisker, C. *Inorg. Chem.* **1999**, *38* (10), 2539-2540.
21. Mcwhinnie, S.; Jones, C.; Mccleverty, J.; Collison, D.; Mabbs, F. *Polyhedron* **1992**, *11* (20), 2639.
22. Boyington, J.; Gladyshev, V.; Khangulov, S.; Stadtman, T.; Sun, P. *Science* **1997**, *275* (5304), 1305-8.

APPENDIX-A1: Structural parameters for (Tp*)MoO(halide)₂

Table A1.1. Structural parameters for (Tp*)MoOX₂ (X= F, Cl, Br) defining the coordination environment of Mo (lengths in (Å) and angles in (°), DFT = DFT Geometry optimization, NA = Not available. Please refer to the Chapter 4 for references).

Refcode/DFT Average Distance (Å)	BEBCOA X = Cl	DOXJAB X = Cl	DFT X = Cl	DFT X = F	DFT X = Br	X-Ray X = Br	X-Ray X = I	DFT X = I
Mo=O	NA	2.072	1.734	1.739	1.735	1.640	1.694	1.735
Mo-X	NA	2.248	2.394	1.950	2.525	2.335	2.736	2.718
Mo- N _{cis}	2.203	2.167	2.143	2.149	2.156	2.167	2.150	2.160
Mo-N _{trans} (TransEffect)	2.219 (0.016)	2.245 (0.078)	2.311 (0.168)	2.289 (0.140)	2.318 (0.162)	2.330 (0.163)	2.357 (0.207)	2.345 (0.185)
∠(X - M - X)	NA	98.7	91.9	89.3	94.2	95.1	94.6	96.0
∠(O - M - X _{av})	NA	95.6	104.9	107	103.8	100.4	96.2	102.3

APPENDIX-A2: [Mo(IV)(mnt)₂(SPh)₂][PPh₄]₄

This appendix discusses the crystal structure and electronic structure of Mo(IV)(mnt)₂(SPh)₂[PPh₄]₄. This compound contains two dithiolate ligands. This sample was synthesized in Dr. S. Sarkar's lab, the Indian Institute of Technology, Kanpur India and sent to us for structural characterization.

1.0 Structural Studies

The crystal structure parameters are given in Table A2.1, key bond lengths and angles are given in Table A2.2 and crystallographic coordinates with thermal parameters are provided in Table A2.3. An ORTEP picture is shown in Figure A3.1.

Table A2.1. Crystal data and structure refinement for [Mo(IV)(mnt)₂(SPh)₂][PPh₄]₄.

Empirical formula	C ₆₈ H ₅₀ MoN ₄ P ₂ S ₆ .CH ₃ CN	
Formula weight	1312.40	
Temperature	173(2) K	
Wavelength	0.71073 Å	
Crystal system	Monoclinic	
Space group	P2(1)/n	
Unit cell dimensions	a = 13.3808(11) Å	α = 90°.
	b = 32.182(3) Å	β = 111.072(2)°.
	c = 15.9971(13) Å	γ = 90°.
Volume	6428.1(9) Å ³	
Z	4	
Density (calculated)	1.356 Mg/m ³	
Absorption coefficient	0.495 mm ⁻¹	
F(000)	2696	
Crystal size	.60 x .16 x .16 mm ³	
Theta range for utilized data	1.27 to 25.58°.	
Limiting Indices	-16 ≤ h ≤ 16, -39 ≤ k ≤ 39, -19 ≤ l ≤ 19	
Reflections utilized	63421	
Independent reflections	12026 [R(int) = 0.1961]	
Completeness to theta = 25.58°	99.5 %	
Refinement method	Full-matrix least-squares on F ²	
Data / restraints / parameters	12026 / 0 / 773	
Goodness-of-fit on F ²	0.685	
Final R indices [I > 2σ(I)]	R1 = 0.0454, wR2 = 0.0687	
R indices (all data)	R1 = 0.1388, wR2 = 0.0859	
Extinction coefficient	0.00000(3)	
Largest diff. peak and hole	0.734 and -0.304 e.Å ⁻³	
RMS difference density	0.071 e.Å ⁻³	

Table A2.2. Important bond lengths (Å) and angles (°) for [Mo(IV)(mnt)₂(SPh)₂][PPh₄]₄.

Mo(1)-S(2)	2.3630(12)
Mo(1)-S(1)	2.3668(12)
Mo(1)-S(3)	2.3689(12)
Mo(1)-S(4)	2.3769(12)
Mo(1)-S(6)	2.4265(11)
Mo(1)-S(5)	2.4505(12)
S(6)-C(61)	1.774(5)
S(4)-C(41)	1.739(4)
S(3)-C(31)	1.733(5)
S(5)-C(51)	1.769(5)
S(2)-C(21)	1.733(4)
S(1)-C(11)	1.737(5)
S(2)-Mo(1)-S(1)	81.42(4)
S(2)-Mo(1)-S(3)	83.02(4)
S(1)-Mo(1)-S(3)	137.98(4)
S(2)-Mo(1)-S(4)	134.29(4)
S(1)-Mo(1)-S(4)	82.04(4)
S(3)-Mo(1)-S(4)	81.51(4)
S(2)-Mo(1)-S(6)	133.48(4)
S(1)-Mo(1)-S(6)	84.82(4)
S(3)-Mo(1)-S(6)	132.22(4)
S(4)-Mo(1)-S(6)	86.64(4)
S(2)-Mo(1)-S(5)	84.30(4)
S(1)-Mo(1)-S(5)	131.72(4)
S(3)-Mo(1)-S(5)	84.78(4)
S(4)-Mo(1)-S(5)	136.18(4)
S(6)-Mo(1)-S(5)	72.56(4)
C(61)-S(6)-Mo(1)	113.45(14)
C(41)-S(4)-Mo(1)	109.00(16)
C(31)-S(3)-Mo(1)	108.74(16)
C(51)-S(5)-Mo(1)	111.43(14)
C(21)-S(2)-Mo(1)	108.83(17)
C(11)-S(1)-Mo(1)	109.11(17)

Table A2.3. Atomic coordinates ($\times 10^4$) and equivalent isotropic displacement parameters ($\text{\AA}^2 \times 10^3$).
 $U(\text{eq})$ is defined as one third of the trace of the orthogonalized U^{ij} tensor.

	x	y	z	U(eq)
Mo(1)	3419(1)	1220(1)	3368(1)	22(1)
S(6)	5225(1)	1255(1)	4467(1)	29(1)
S(4)	4184(1)	896(1)	2403(1)	26(1)
S(3)	2190(1)	663(1)	2858(1)	29(1)
S(5)	3314(1)	1069(1)	4836(1)	30(1)
P(1)	1377(1)	1044(1)	-2199(1)	25(1)
S(2)	1845(1)	1610(1)	3136(1)	30(1)
P(2)	-2740(1)	1547(1)	-212(1)	30(1)
S(1)	3896(1)	1830(1)	2774(1)	29(1)
C(222)	-2026(4)	746(1)	349(3)	34(1)
C(141)	1399(3)	1111(1)	-1085(3)	23(1)
C(146)	2190(4)	1349(1)	-470(3)	32(1)
C(31)	2506(4)	386(1)	2058(3)	30(1)
C(136)	-607(4)	1259(1)	-3438(3)	31(1)
C(42)	3640(3)	261(1)	1195(3)	26(1)
C(131)	43(3)	947(1)	-2939(3)	24(1)
C(32)	1809(4)	48(2)	1603(3)	36(1)
C(142)	656(4)	909(1)	-807(3)	31(1)
C(135)	-1647(4)	1176(2)	-3972(3)	39(1)
N(31)	1243(4)	-209(1)	1244(3)	64(2)
N(41)	3837(3)	83(1)	656(3)	42(1)
C(111)	1901(4)	1505(1)	-2499(3)	28(1)
C(61)	6198(3)	1393(2)	4001(3)	27(1)
C(241)	-1873(4)	1979(1)	-176(3)	30(1)
C(121)	2186(3)	607(1)	-2243(3)	25(1)
C(211)	-3318(4)	1347(1)	-1315(3)	31(1)
C(134)	-2067(4)	784(2)	-4001(3)	43(1)
C(226)	-1252(3)	1292(1)	1395(3)	33(1)
C(66)	6584(4)	1795(2)	4066(3)	46(2)
C(52)	1314(4)	1255(2)	4862(3)	37(1)
C(41)	3374(3)	483(1)	1857(3)	23(1)

C(236)	-3821(4)	1636(1)	962(3)	40(1)
C(123)	3533(4)	106(2)	-1522(3)	44(1)
C(62)	6654(4)	1091(2)	3628(3)	39(1)
C(231)	-3814(4)	1716(1)	118(3)	32(1)
C(235)	-4631(4)	1795(2)	1207(4)	48(2)
C(21)	1947(4)	2079(1)	2643(3)	29(1)
C(116)	2747(4)	1491(2)	-2809(3)	43(1)
C(65)	7416(4)	1890(2)	3771(4)	58(2)
C(122)	2898(4)	436(1)	-1465(3)	33(1)
C(144)	1470(4)	1184(2)	662(3)	39(1)
C(55)	594(5)	443(2)	4554(3)	50(2)
C(132)	-387(4)	553(1)	-2969(3)	33(1)
C(212)	-3061(4)	1504(1)	-2010(3)	41(1)
C(223)	-1419(4)	462(2)	968(3)	46(2)
C(63)	7465(4)	1199(2)	3314(3)	55(2)
C(221)	-1949(3)	1165(1)	558(3)	28(1)
C(245)	-1487(5)	2705(2)	-56(3)	45(1)
C(246)	-2182(4)	2381(2)	-103(3)	35(1)
C(22)	1041(4)	2359(2)	2459(3)	42(1)
C(143)	704(4)	944(1)	65(3)	36(1)
C(11)	2827(4)	2175(1)	2473(3)	31(1)
C(112)	1463(4)	1888(2)	-2429(3)	42(1)
C(126)	2119(4)	450(1)	-3065(3)	37(1)
C(225)	-653(4)	1009(2)	2007(3)	40(1)
C(242)	-874(4)	1903(2)	-191(4)	56(2)
C(232)	-4624(4)	1947(2)	-482(3)	47(2)
C(51)	1992(4)	942(2)	4743(3)	30(1)
C(125)	2760(4)	116(2)	-3108(3)	46(2)
C(12)	2961(4)	2548(2)	2050(3)	50(2)
C(216)	-4119(4)	1042(2)	-1499(3)	46(2)
C(243)	-181(5)	2230(2)	-144(4)	69(2)
C(56)	1622(4)	542(2)	4610(3)	39(1)
C(244)	-491(5)	2631(2)	-65(3)	52(2)
C(214)	-4339(5)	1064(2)	-3042(4)	57(2)
C(233)	-5430(4)	2112(2)	-239(4)	58(2)
C(215)	-4607(4)	899(2)	-2353(4)	54(2)
C(124)	3464(4)	-48(2)	-2330(3)	45(2)

	x	y	z	U(eq)
C(145)	2228(4)	1386(1)	397(3)	43(1)
C(234)	-5410(4)	2037(2)	622(4)	57(2)
N(21)	315(4)	2568(1)	2337(3)	75(2)
C(224)	-745(4)	593(2)	1790(3)	46(2)
C(115)	3171(5)	1851(2)	-3013(3)	63(2)
C(54)	-69(5)	746(2)	4656(3)	60(2)
C(113)	1865(5)	2248(2)	-2665(4)	64(2)
C(53)	287(4)	1153(2)	4816(3)	57(2)
C(133)	-1435(4)	472(2)	-3499(3)	40(1)
C(213)	-3562(5)	1367(2)	-2873(3)	54(2)
C(64)	7849(4)	1594(2)	3395(4)	63(2)

2.0 Theoretical Studies

2.1 Methods

Calculations were performed on $[\text{Mo(IV)(mnt)}_2(\text{SPh})_2][\text{PPh}_4]_4$ using the ADF (Amsterdam density functional theory calculations) package (release 2000.02). Starting geometries were obtained from crystal structure. A generalized gradient approximation, with the exchange correction of Becke¹ and the correlation correction of Lee *et. al.*,² was used for all density functional calculations. All core levels (up to 3d for Mo, up to 1s for C, N, O and S) were treated as frozen orbitals. The calculations employed triple-zeta basis sets with Slater type orbitals and a polarization function for all elements. Calculations on the ground-state molecules were performed in the spin-restricted mode.

3.0 Results

The molecular orientation for all molecular orbital plot is shown in Figure A.2.2. The highest occupied molecular orbital (HOMO) is populated by two electrons and is predominantly metal in character (70 %) with around 6 % contribution from the sulfur p orbitals of coordinated thiophenolates. Oxidation of complex will remove electron from this orbital. Since EPR is a ground state probe, unpaired electron will be in an orbital that will look like orbital in Figure A.2.1 (b).

HOMO -1, shown in Figure A.2.1 (c) is predominantly sulfur based orbital and it has contributions from symmetric combinations of dithiolate out of plane *Sp* orbitals and

in plane (symmetric) combinations of thiophenolate Sp orbitals. The total sulfur contributions in this orbital is 85%.

HOMO -2 (Figure A.2.1 (d) is predominantly antisymmetric combinations of in-plane thiophenolate S (81 %) orbitals.

4.0 References

1. A.D. Becke, Phys. Rev. A., **1988**, 38, 3098-3100.
2. C. Lee, W. Yang, and R.G. Parr, Phys. Rev. B. **1988**, 37, 785.

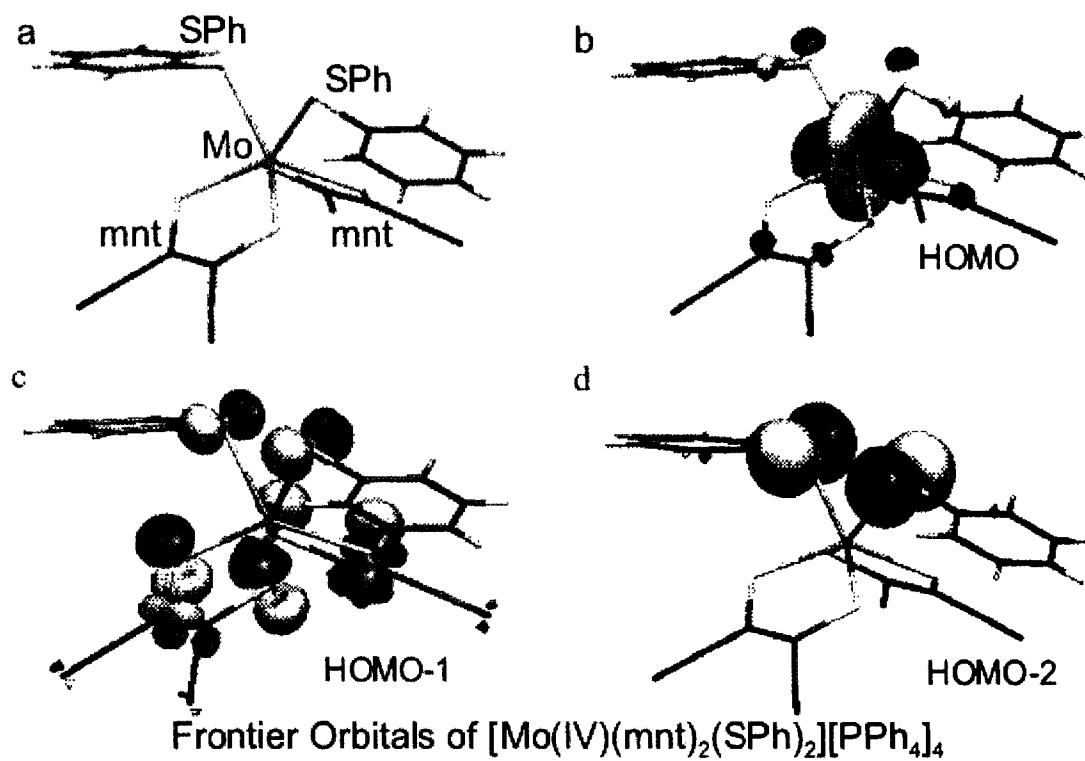


Figure A2.1. (a) The molecular orientation of $[\text{Mo(IV)(mnt)}_2(\text{SPh})_2][\text{PPh}_4]_4$, (b, c and d) The frontier molecular orbitals of $[\text{Mo(IV)(mnt)}_2(\text{SPh})_2][\text{PPh}_4]_4$.

APPENDIX-A3: The Structure of (Tp*)MoO₂(SCH₂Ph)

This appendix discusses the crystal structure of hydrotris(3, 5-dimethylpyrazol-1-yl)borate)-benzylthiolate-oxomolybdenum(VI). The crystal structure parameters are given in Table A3.1, key bond lengths and angles are given in Table A3.2 and crystallographic coordinates with thermal parameters are provided in Table A3.3. An ORTEP picture is shown in Figure A3.1.

Table A3.1. Crystal data and structure refinement for (Tp*)MoO₂(SCH₂Ph).

Empirical formula	C ₂₂ H ₂₉ BMoN ₆ O ₂ S	
Formula weight	548.32	
Temperature	170(2) K	
Wavelength	0.71073 Å	
Crystal system	triclinic	
Space group	<i>P</i> $\bar{1}$	
Unit cell dimensions	a = 8.3742(8) Å	α = 99.188(2)°.
	b = 8.6165(9) Å	β = 100.345(2)°.
	c = 17.6781(18) Å	γ = 102.143(2)°.
Volume	1200.6(2) Å ³	
Z	2	
Density (calculated)	1.517 Mg/m ³	
Absorption coefficient	0.665 mm ⁻¹	
F(000)	564	
Crystal size	.03 x .10 x .20 mm ³	
Theta range for utilized data	2.47 to 25.07°.	
Limiting Indices	-9<=h<=9, -10<=k<=10, -21<=l<=21	
Reflections utilized	12708	
Independent reflections	4257 [R(int) = 0.0551]	
Completeness to theta = 25.07°	99.9 %	
Refinement method	Full-matrix least-squares on F ²	
Data / restraints / parameters	4257 / 129 / 298	
Goodness-of-fit on F ²	1.087	
Final R indices [I>2sigma(I)]	R1 = 0.0555, wR2 = 0.1176	
R indices (all data)	R1 = 0.0759, wR2 = 0.1247	
Largest diff. peak and hole	0.839 and -0.871 e.Å ⁻³	
RMS difference density	0.112e.Å ⁻³	

Table A3.2. Important bond lengths (Å) and angles (°) for (Tp*)MoO₂(SCH₂Ph).

Mo(1)-O(1)	1.701(3)
Mo(1)-O(2)	1.701(3)
Mo(1)-N(31)	2.170(4)
Mo(1)-N(11)	2.289(4)
Mo(1)-N(21)	2.323(4)
Mo(1)-S(1)	2.3824(15)
S(1)-C(7)	1.816(6)
O(1)-Mo(1)-O(2)	103.36(17)
O(1)-Mo(1)-N(31)	94.62(16)
O(2)-Mo(1)-N(31)	94.94(17)
O(1)-Mo(1)-N(11)	167.50(16)
O(2)-Mo(1)-N(11)	88.08(16)
N(31)-Mo(1)-N(11)	79.17(15)
O(1)-Mo(1)-N(21)	87.67(16)
O(2)-Mo(1)-N(21)	167.29(16)
C(7)-S(1)-Mo(1)	110.4(2)
O(1)-Mo(1)-S(1)	97.27(13)
O(2)-Mo(1)-S(1)	100.37(13)
C(1)-C(7)-S(1)	109.7(4)
O(1)-Mo(1)-S(1)-C(7)	132.9(3)
O(2)-Mo(1)-S(1)-C(7)	-122.1(3)

Table A3.3. Atomic coordinates ($\times 10^4$) and equivalent isotropic displacement parameters ($\text{\AA}^2 \times 10^3$). U(eq) is defined as one third of the trace of the orthogonalized Uij tensor.

	x	y	z	U(eq)
Mo(1)	6336(1)	7400(1)	6873(1)	15(1)
S(1)	5557(2)	6538(2)	7999(1)	28(1)
N(31)	6949(5)	9049(5)	6101(3)	18(1)
O(2)	5019(4)	5903(4)	6146(2)	23(1)
N(11)	4215(5)	8700(5)	6861(2)	17(1)
O(1)	8184(4)	6846(4)	6966(2)	22(1)
N(32)	6708(5)	10594(5)	6187(2)	18(1)
N(12)	4484(5)	10362(5)	6962(2)	16(1)
N(22)	7536(5)	11286(5)	7638(2)	18(1)
C(23)	8702(7)	12463(6)	8164(3)	23(1)
N(21)	7760(5)	9796(5)	7758(3)	19(1)
C(15)	2579(6)	8097(6)	6813(3)	17(1)
C(36)	7948(7)	7201(6)	5174(3)	26(1)
C(25)	9067(7)	10089(6)	8368(3)	23(1)
C(14)	1800(6)	9375(6)	6896(3)	20(1)
C(34)	7685(7)	10125(6)	5117(3)	24(1)
C(16)	1808(7)	6323(6)	6683(4)	25(1)
C(13)	3018(6)	10762(6)	6979(3)	17(1)
B(1)	6218(7)	11372(6)	6935(3)	16(1)
C(24)	9665(7)	11759(6)	8641(3)	26(1)
C(35)	7546(6)	8773(6)	5451(3)	20(1)
C(7)	4871(9)	8111(8)	8575(4)	36(1)
C(1)	4759(7)	7721(7)	9358(4)	30(1)
C(33)	7171(6)	11258(6)	5596(3)	19(1)
C(37)	7057(8)	12937(7)	5512(4)	31(1)

	x	y	z	U(eq)
C(17)	2834(7)	12476(6)	7061(3)	25(1)
C(27)	8848(7)	14238(6)	8163(4)	31(1)
C(26)	9710(8)	8780(7)	8684(4)	32(1)
C(5)	5820(8)	8050(8)	10738(4)	35(1)
C(6)	5961(8)	8455(8)	10027(4)	41(2)
C(4)	4535(10)	6968(10)	10809(4)	51(2)
C(3)	3225(13)	6177(10)	10130(5)	80(3)
C(2)	3413(10)	6555(10)	9435(4)	59(2)

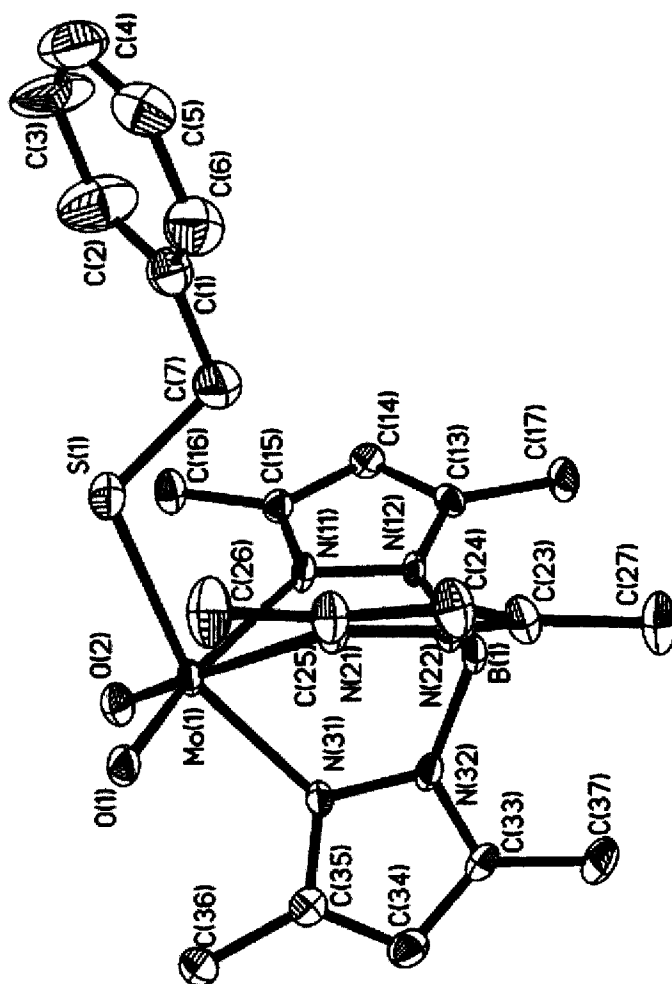


Figure A3.1. The ORTEP drawing of (Tp*)MoO₂(SCH₂Ph). The atoms are drawn as 50% probability ellipsoids. H-atoms have been made arbitrarily small for clarity.

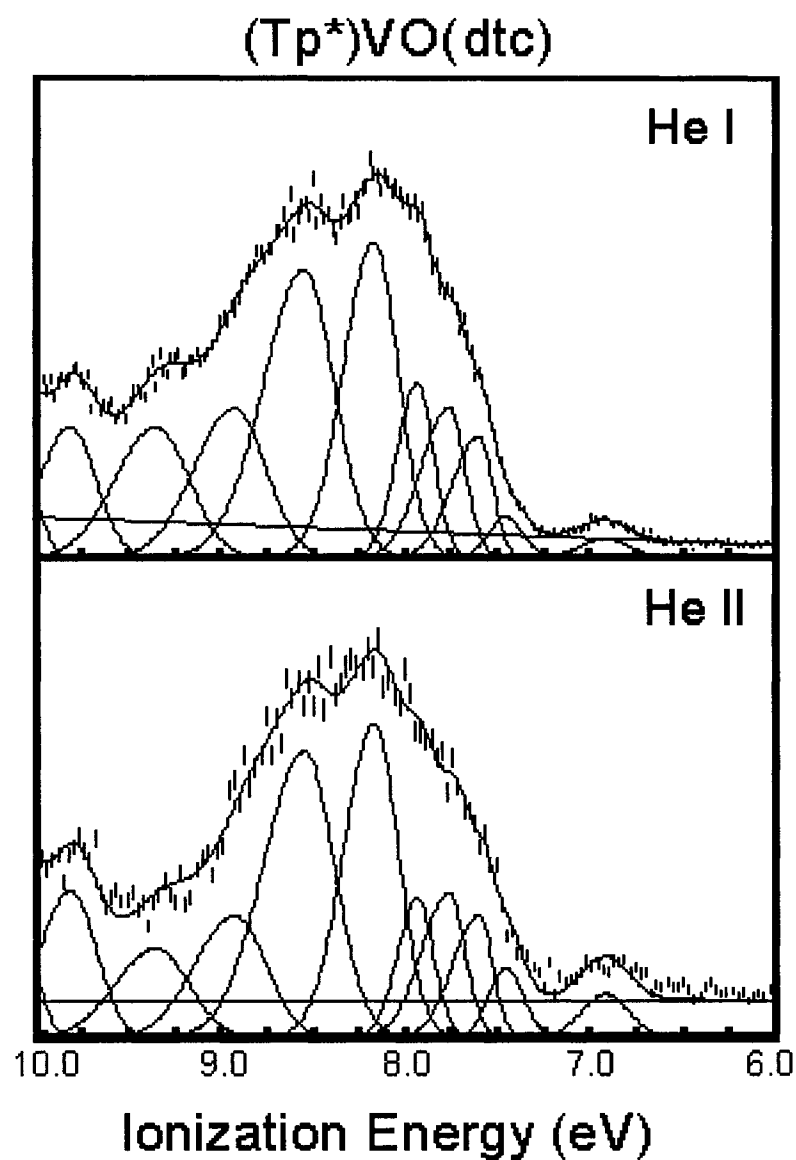
APPENDIX A4. Photoelectron Spectra of (Tp*)VO(dtc)

Figure A.4.1. The He I and He II photoelectron spectra of (Tp*)VO(dtc) (where dtc = S₂CN(CH₃)₂).